

UNIVERSITY OF DELHI, INDIA

DOCTORAL THESIS

**Extraction of Neutrino Oscillation
Parameters using a Simultaneous Fit of
 ν_μ Disappearance and ν_e Appearance data
with the NOvA Experiment**

by

PRABHJOT SINGH

A thesis submitted in partial fulfillment for the
degree of Doctor of Philosophy

in the

Department of Physics and Astrophysics



September, 2019

PROF. BRAJESH C. CHOUDHARY

Ph.D. Supervisor

PROF. BRIAN REBEL

Ph.D. Co-Supervisor


DECLARATION

It is certified that the work presented in this thesis entitled “**Extraction of Neutrino Oscillation Parameters using a Simultaneous Fit of ν_μ Disappearance and ν_e Appearance data with the NOvA Experiment**” has been carried out at the Department of Physics and Astrophysics, University of Delhi, Delhi, under the supervision of Prof. Brajesh C. Choudhary and at Fermi National Accelerator Laboratory, Batavia, IL, U.S.A. under the co-supervision of Prof. Brian Rebel of Fermilab and University of Wisconsin-Madison, U.S.A. This thesis presents the analysis of 8.85×10^{20} protons on target (POT) of data collected by the NOvA experiment. The data collected by the NOvA experiment is analyzed using the three-flavor neutrino oscillation framework, specifically the $\nu_\mu \rightarrow \nu_\mu$ survival and $\nu_\mu \rightarrow \nu_e$ appearance rates are measured.

This work has been done by the candidate himself and to the best of his knowledge, no part of this work has earlier been submitted for any degree or diploma of this or any other university.

Prabhjot Singh
(Candidate)

Prof. Brajesh Chandra Choudhary
(Supervisor)



Prof. Brian Rebel
(Co-Supervisor)

Prof. Sanjay Jain
Head, Department of Physics & Astrophysics
University of Delhi
Delhi 110 007



Department of Physics and Astrophysics

University of Delhi

Delhi 110 007, India

Date:

Certificate of Originality

The research work embodied in this thesis entitled “**Extraction of Neutrino Oscillation Parameters using a Simultaneous Fit of ν_μ Disappearance and ν_e Appearance data with the NOvA Experiment**” has been carried out by me at the **Department of Physics and Astrophysics**, University of Delhi, Delhi, India and **Fermi National Accelerator Laboratory (Fermilab)**, Batavia, I.L., U.S.A. The manuscript has been subjected to plagiarism check by **Turnitin** software. The work submitted for consideration of award of Ph.D. is original.

.....
Prabhjot Singh

Name and Signature of the Candidate

Student Approval Form

Name of the Author	Prabhjot Singh
Department	Department of Physics and Astrophysics
Degree	Doctor of Philosophy
University	University of Delhi
Guide	Prof. Brajesh C. Choudhary
Thesis Title	Extraction of Neutrino Oscillation Parameters using a Simultaneous Fit of ν_μ Disappearance and ν_e Appearance data with the NOvA Experiment
Year of Award	

Agreement

1. I hereby certify that if appropriate, I have obtained and attached hereto a written permission/statement from the owner(s) of each third party copyrighted matter to be included in my thesis/dissertation, allowing distribution as specified below.
2. I hereby grant to the university and its agents the non-exclusive license to archive and make accessible, under the conditions specified below, my thesis/dissertation, in whole or in part in all forms of media, now or hereafter known. I retain all other ownership rights to the copyright of the thesis/dissertation. I also retain the right to use in future works (such as articles or books) all or part of this thesis, dissertation, or project report.

Conditions:

1. Release the entire work for access worldwide	
2. Release the entire work for 'My University' only for: 1 Year 2 Year 3 Year and after this time release the work for access worldwide.	

<p>3. Release the entire work for ‘My University’ only while at the same time releasing the following parts of the work (e.g. because other parts relate to publications) for worldwide access:</p> <ul style="list-style-type: none"> a) Bibliographic details and Synopsis only b) Bibliographic details, synopsis and the following chapters only c) Preview/Table of Contents/24 page only 	
<p>4. View Only (No Downloads) (worldwide)</p>	

.....
Signature of the Scholar

.....
Signature and seal of the Guide

Place:

Date:

Dedication

To my parents Talvinder Singh and Inderjeet Kaur, my brother, Jagjeet Singh, and my sister, Jagpreet Kaur.

Acknowledgements

Here I would like to acknowledge each and every individual, who has directly or indirectly contributed to this long journey of my Ph.D., without whom this work would have been very difficult to accomplish.

Thanks to my Ph.D. supervisor, Prof. Brajesh C. Choudhary for his guidance all along and confidence in me. He has always been caring and protecting. Apart from research guidance, he always made sure that none of my work gets stuck in the University administration. I first met him in the master's program where he taught us particle physics. It was his teaching style which created my interest in particle physics and I decided to continue my career in the same field.

I would also like to thank my supervisor for giving me a lifetime opportunity to visit and work at Fermilab for research-related activities. People at Fermilab are involved in world-class research in the field of experimental particle physics and astronomy. It is a dream for every particle physicist to work at Fermilab. I am also grateful to my supervisor who introduced me to Prof. Brian Rebel who became my co-supervisor at Fermilab. Brian has played a vital role in my life and my career as a particle physicist because whatever I have learned in the field of experimental neutrino physics is because of him. He taught me analysis, enhanced my coding skills, read my NOvA documents and always corrected my numerous mistakes. He taught me how to read and understand plots, to find bugs and to draw conclusions. Other than a co-supervisor, Brian was sort of family-away-from-family when I was stationed at Fermilab for three and a half years from December 2014 to June 2018.

Thanks to Medbh Campbell and Sebastian Bending for their constant help in the analysis. They have played an important role in the development of the analysis framework and the physics analysis.

Thanks to Keith Matera who as a postdoc helped me in the initial stages of the analysis.

Thanks to the members of the FNEX group, Brian Rebel, Keith Matera, Jennifer Thomas, Stefano Germani, Linda Cremonesi, Ryan Nichol, Anna Holin, Medbh Campbell and Sebastian Bending for their insights, comments, and suggestions during group meetings. Thanks to Linda Cremonesi for appreciating and encouraging my work.

Thanks to Patricia Vahle, Christopher Backhouse, Alex Himmel and Jeff Hartnell for their positive suggestions as convenors of the ν_e and ν_μ analysis groups. Thanks to Thomas Coan, Brian Rebel, Matthew Tamsett, Alexander Radovic and Christopher Backhouse for their help and suggestions in my calibration work both as convenors and advisors. Thanks to Alex Sousa, Gavin Davies and Louise Suter for their suggestions in my NSI related work in the NC group meetings as convenors.

Thanks to the members of the housing office, Jacqueline Cyko, Cheryl Bentham, Jeanne Lasusa and Jack Hawkins, for making my accommodation at Fermilab comfortable.

Thanks to Erika Catano-Mur, Fernanda Psihas, Diana Patricia Mendez, Luke Vinton, Justin Vasel, Shiqi Yu for always helping in the analysis related work. Erika Catano-Mur's help in the analysis is most appreciated.

Thanks to Etta Johnson, Stephanie Schuler, Kappy Sherman, Valery Stanley, Linda Granbur, Kimberly Pearce, Dave Anderson, and Enrique for taking care of the salary, visa related-work, and other convenience during my stay at Fermilab.

Thanks to Maury Goodman who on behalf of the NOvA Speakers Committee (NOSC) gave me opportunities to present results of the NOvA experiment in National and International conferences.

Thanks to Kanika Sachdev, Evan Niner and Susan Lein whose Ph.D. thesis I referred for writing my thesis. Thanks to other members of the Fermilab family, Peter Shanahan, Jon Paley, Steve Brice, John Cooper, Cindy Joe, Ting Miao, Barnali Chowdhury, Cristiana Principato, Rick Tesarek and Shaokai Yang who were also around during my thesis journey at Fermilab.

Thanks to Arun Tadepalli, Navaneeth Poonthottathil, Sijith Edayath, Rijeesh Keloth, Siva Prasad, Deepika Grover, Siddhartha Joshi, Jose Sepulveda-Quiroz, Kranti Gunthoti, Jagjeet Singh, Souvik Das, Titas Roy, and Bibhuti Parida were great help at Fermilab. I enjoyed many moments with them. I used to have many conversations, cricket games, lunches, dinners, driving trips, driving lessons and sometimes new things to learn. Arun and Nava always took care of me like a younger brother. I enjoyed numerous coffees with Sijith on the 14th floor of Wilson Hall. We used to talk about many things during coffee. Those conversations saved me from work stress. Thanks to Peter Shanahan and his wife for inviting me and other friends to

New Year lunches every year at their home. I enjoyed those lunches. It was nice of them to invite us when we were away from our family.

Now I would like to acknowledge people at our Department of Physics and Astrophysics, University of Delhi for their important contributions in my Ph.D. thesis journey. Thanks to my thesis committee members, Prof. Samit Mandal and Dr. Supriya Kar for attending my Ph.D. related talks. Thanks to my friends in the office, Rocky Bala Garg, Ajay Kumar, Ram Krishna Sharma, Varun Sharma, Sudha Ahuja, Daljeet Kaur, Sumit Keshri, Ankit Gaur, Arjun Chhetri, Aashaq Shah, and Maitrayee Mandal for physics and fun talks. Thanks to Kundra Prakash, Ganga, Mohammad Yunus, Aamir Husain and Pradhan Ali for taking care of the administrative work.

Thanks to the funding agencies, Department of Science and Technology, Government of India and United States Department of Energy for funding the research project which lead me to this thesis. Thanks to the Department of Physics and Astrophysics, University of Delhi, India and Fermi National Accelerator Laboratory for the resource they provided to finish my thesis. Thanks to the member of the India-Fermilab Neutrino Collaboration for making me a part of this group and for giving me an opportunity to work at Fermilab. Thanks to the NOvA collaboration whose members were always present to help.

Thanks to the Invisibles, Elusives and InvisiblesPlus projects for supporting my visits to Italy and Spain for conferences/schools and opportunity to present my results. My visits to Italy and Spain were memorables and gave me pleasant memories.

Thanks to my family members, my father Talvinder Singh and mother Inderjeet Kaur who always supported me in my education and always allowed me to continue the research I wanted to do. They allowed me to have dreams and inspired me to fulfill them. Thanks to my brother Jagjeet Singh and sister Jagpreet Kaur who are a constant companion in my life. Only because of my brother and sister I was able to go to Fermilab because they took care of our Mother at home.

Again thanks to every individual who helped me in some way or the other in my Ph.D. thesis journey. I appreciate it.

PRABHJOT SINGH

List of Publications

1. **PRD 98, 032012 (2018)** “New constraints on oscillation parameters from ν_e appearance and ν_μ disappearance in the NOvA experiment”.
 - Developed oscillation framework for the analysis of the neutrino oscillation data.
 - Analyzed the $\nu_\mu \rightarrow \nu_\mu$ disappearance and $\nu_\mu \rightarrow \nu_e$ appearance data for the extraction of the Δm_{32}^2 , $\sin^2 \theta_{32}$ and δ_{CP} oscillation parameters.
 - The Ph.D. thesis is based on this paper.
 - The NOvA technical note number 24178 is associated with this published analysis.
2. **PRL 118, 231801 (2017)** - “Constraints on Oscillation Parameters from ν_e Appearance and ν_μ Disappearance in NOvA”.
 - Provided the attenuation and threshold calibration for both the detectors.
 - Contributed in independent cross-checks of the results.
3. **PRL 118, 151802 (2017)** - “Measurement of the Neutrino Mixing Angle θ_{23} in NOvA”.
 - Provided the attenuation and threshold calibration of both NOvA detectors.
 - Contributed in independent cross-checks of the results.
4. **PRD 96, 072006 (2017)** - “Search for active-sterile neutrino mixing using neutral-current interactions in NOvA”.
 - Performed the attenuation and threshold calibrations of the NOvA Near and Far detectors.

This Ph.D. thesis is based on work published in the paper listed as number 1 above. Chapter 4 of this thesis also forms part of the papers listed above in numbers 2, 3 and 4. The Ph.D. candidate also contributed in independent cross-checks of the results of the papers listed in numbers 2 and 3 above.

List of NOvA Technical Notes

1. “**FNEX 2017 Third Oscillation Analyses**”.
 - NOvA document number 24178.
 - Forms chapter number 5 of the Ph.D. thesis.
 - Contributed in the NOvA published paper **PRD 98, 032012 (2018)**.
2. “**FNEX Analyses Framework and NOvA 2016 Oscillation Analyses**”.
 - NOvA document number 24178.
 - Forms chapter number 5 of the Ph.D. thesis.
 - Contributed in the NOvA published paper **PRD 98, 032012 (2018)**.
3. “**The Attenuation and Threshold Calibration of the NOvA detectors**”.
 - NOvA document number 13579 v35.
 - Forms chapter number 4 of the Ph.D. thesis.
 - Contributed in the NOvA published papers **PRL 118, 231801 (2017)**, **PRL 118, 151802 (2017)** and **PRD 96, 072006 (2017)**.
4. “**Acceptance of the NOvA Far Detector for the Cosmic Ray Muons**”.
 - NOvA document number 13623.
 - Forms chapter number 3 of the Ph.D. thesis.

Talks Given

- **Invisibles19 Neutrinos, Dark Matter and Dark Energy Workshop, June 10 - 14, 2019, Valencia, Spain.** Title of the talk “*Neutrino Oscillation Constraints from the NOvA Experiment*”. Talk available at <https://indico.ific.uv.es/event/3427/contributions/10937/>
- **DAE-BRNS High Energy Physics Symposium 2018, December 10 - 14, 2018, IIT-Madras, India.** Title of the talk “*Extracting neutrino oscillation parameters using a simultaneous fit of the ν_e appearance and ν_μ disappearance data in the NOvA experiment*”. Talk available at <https://indico.cern.ch/event/775317/timetable/?print=1&view=standard#42-extracting-neutrino-oscilla>
- **APS Division of Particles and Fields Meeting (DPF 2017) July 31-August 4, 2017, Fermilab, U.S.A.** Title of the talk “*Extracting neutrino oscillation parameters using a simultaneous fit of the ν_e appearance and ν_μ disappearance data in the NOvA experiment*”. Talk available at <https://indico.fnal.gov/event/11999/session/9/contribution/319>

Published Proceedings

- **APS Division of Particles and Fields Meeting (DPF 2017) July 31-August 4, 2017, Fermilab.** Title of the talk “Extracting neutrino oscillation parameters using a simultaneous fit of the ν_e appearance and ν_μ disappearance data in the NOvA experiment”. E-proceedings at <http://www.slac.stanford.edu/econf/C170731/> and at arxiv: <https://arxiv.org/abs/1710.03829>

Posters Presented

- **Invisibles19 School and Workshop - Spain, June 02 - 14, 2019:** “Neutrino Oscillation Constraints from the NOvA Experiment.”
- **Invisibles16 School, SISSA, Trieste, Italy, September 5 - 9, 2016 and Invisibles16 Workshop, Orto Botanico, Padova, Italy, September 12 - 16, 2016:** “Attenuation Calibration of the NOvA Detectors”.
- **38th International Conference on High Energy Physics, ICHEP - Chicago, U.S.A., Aug 03 - 10, 2016:** “Attenuation Calibration of the NOvA Detectors”.
- **49th Fermilab User’s meeting - Fermilab, Batavia, IL, U.S.A., June 14 - 16, 2016:** “Attenuation Calibration of the NOvA Detectors”.
- **48th Fermilab User’s meeting - Fermilab, Batavia, IL, U.S.A., June 10 - 11, 2015:** “Calibration of the NOvA Detectors”.

Ph.D. Registration Details

- **Name:** PRABHJOT SINGH
- **Ph.D. Thesis Title:** Extraction of Neutrino Oscillation Parameters using a Simultaneous Fit of ν_μ Disappearance and ν_e Appearance data with the NOvA Experiment
- **Thesis Supervisor:** Prof. B.C. Choudhary, Department of Physics and Astrophysics, University of Delhi, India
- **Thesis co-Supervisor:** Prof. Brian Rebel, Fermilab and University of Wisconsin-Madison, U.S.A.
- **Department of Affiliation:** Department of Physics and Astrophysics
- **Ph.D. Registration Number:** SF-I/Ph.D./3569
- **Date of Ph.D. Registration:** September 27, 2013

UNIVERSITY OF DELHI, INDIA

Abstract

Faculty of Science

Department of Physics and Astrophysics

Doctor of Philosophy

by PRABHJOT SINGH

This thesis presents the analyses and results of the $\nu_\mu \rightarrow \nu_\mu$ disappearance and $\nu_\mu \rightarrow \nu_e$ appearance due to neutrino oscillations using 8.85×10^{20} protons on target (POT) equivalent of data collected by the NOvA experiment. The data analyzed in this thesis was collected from February 06, 2014 to February 20, 2017. NOvA is an accelerator-based, long-baseline neutrino oscillation experiment and uses the two detector set-up to study the phenomenon of neutrino oscillation using a beam of muon neutrinos produced at Fermilab. One NOvA detector is placed within the Fermilab campus, 100 m underground, at a distance of 1 km from the neutrino source and is called the Near Detector (ND). The ND is 300 ton in mass and smaller in size than the Far Detector (FD) which is 14 kton in mass and is placed 810 km away from the neutrino source in Ash River, Minnesota (MN). Both ND and FD are made of the same material and are functionally identical. The ND being closer to the neutrino source, analyzes the neutrino beam before the neutrinos oscillate and the FD analyzes the neutrinos after oscillations. The ND is used to predict the signal and background expectations in the FD. The similarity in the ND and FD help to reduce the systematic uncertainties in the FD prediction. The combined oscillation fit to the $\nu_\mu \rightarrow \nu_\mu$ disappearance and $\nu_\mu \rightarrow \nu_e$ appearance gives the best fit values of the Δm_{32}^2 , $\sin^2 \theta_{32}$ and δ_{CP} oscillation parameters and are presented in this thesis.

Synopsis

Neutrino physics is one of the exciting fields of fundamental science today. Neutrinos are the most abundant massive fundamental particles in the Universe. Each second billions of neutrinos are passing through our body without being noticed. Neutrinos interact with matter via weak interactions which make neutrinos really hard to detect. There are many sources of neutrinos in the Universe. For example, they are produced in the Big Bang, in the core of our Sun, radioactive processes inside Earth, Supernovae, cosmic ray showers, nuclear reactors and particle accelerators. Along with electrons, positrons and photons, neutrinos were produced just after the Big Bang. Neutrinos from the Big Bang are also known as primordial or relic neutrinos.

Prior to 1930, we did not know about neutrinos. In 1930, Wolfgang Ernst Pauli in order to explain the continuous spectrum of β -decay postulated a new particle and named it the “neutron”. Pauli suggested this new particle should be electrically neutral, have spin $1/2$ and mass of the order of either electron mass or less than 0.01 times of the mass of proton. In 1932, James Chadwick discovered another neutral particle and named it “neutron” for being electrically neutral. The mass of the James Chadwick’s neutron was supposed to be equal to that of a proton. To distinguish Pauli’s light neutron from the James Chadwick’s heavy neutron, the Italian physicist Edoardo Amaldi in a conversation with Enrico Fermi coined the name “neutrino”, which in Italian means “a little neutral one”. The scientific community accepted the name “neutrino” when it was proposed by Enrico Fermi in a conference in Paris in 1932. Pauli also welcomed the new name in the Solvay conference of October 1933 citing Fermi’s name. Neutrinos were detected in 1956 by Clyde L. Cowan and Frederick Reines. Cowan and Reines, used the neutrino (actually anti-neutrino) flux from the nuclear reactors at the Savannah River Plant of the United States Atomic Energy Commission and a large water tank loaded with cadmium chloride as detectors for anti-neutrino interactions and surrounding scintillator detectors for capturing products of the interactions with the protons.

Neutrinos being fundamental particles are part of the Standard Model (SM) of Particle Physics. which defines the properties of the fundamental particles and the interactions among them. In the SM, there are three types of neutrinos associated with three generations of leptons. In any weak interaction reaction, neutrinos are always produced along with a lepton. The three neutrinos are, electron-neutrino

(ν_e), muon-neutrino (ν_μ) and tau-neutrino (ν_τ) In the SM, neutrinos are known to be massless particles. In the 1960s, a number of solar neutrino experiments including the Homestake radiochemical solar neutrino experiment of Ray Davis faced a problem better known as Solar Neutrino Problem (SNP). Nuclear reactions in the core of the Sun produce ν_e . The solar neutrino experiments were able to detect only one-third of the expected solar neutrinos in their detectors. The remaining two-third of the solar neutrinos were missing. In 1998, the Super-Kamiokande (Super-K) experiment, observed a deficit of atmospheric muon neutrinos. Super-K showed that the atmospheric ν_μ , produced by collision of cosmic rays with Earth's atmosphere, transforms to ν_τ . The transformation of neutrinos from one flavor to another is called "neutrino oscillations". In 2001, the Sudbury Neutrino Observatory (SNO) experiment established that the ν_e from the core of the Sun transform to ν_μ and ν_τ on their journey outward from the interior of the Sun, thereby establishing the oscillation of solar neutrinos. The Nobel Prize in Physics of 2015 was awarded jointly to Takaaki Kajita of the Super-K and Arthur B. McDonald of the SNO collaborations for evidence of the neutrino oscillations. The establishment of neutrino oscillations also implies that neutrinos are not massless particles. This observation is important because it established that the SM of particles, which predicts massless neutrinos, is not complete. At present, there are a number of solar, atmospheric, reactor and short- and long-baseline neutrino oscillation experiments operating around the world. The purpose of these experiments is to analyze the neutrino oscillation data in order to measure neutrino properties precisely. One such experiment is the NOvA experiment at Fermilab, which is a long-baseline, accelerator-based neutrino oscillation experiment. NOvA has two detectors and uses a beam of muon neutrinos produced by the Fermilab Main Injector to analyze the oscillation of ν_μ to ν_e . The Near Detector of NOvA measures the beam before neutrinos have any chance to oscillate, and the Far Detector at a distance of 810 km from Fermilab, measures the beam after neutrino oscillations. The content of this Ph.D. thesis is based on the analyses of the neutrino data collected by the NOvA experiment. The structure of the thesis is as follows.

- **Chapter 1** gives a brief summary of the history of neutrino physics. It explains the postulation of neutrino by Pauli in 1930 and the detection of the neutrino in 1956 by Cowan and Reines. The SNP is also explained briefly. The phenomenology of neutrino oscillation from one flavor to another flavor is also explained for two and three flavor neutrino scenarios, both in the absence

and presence of the matter. Special focus on $\nu_\mu \rightarrow \nu_e$ oscillations and $\nu_\mu \rightarrow \nu_\mu$ survival probability is given because these are the two important modes of neutrino oscillation in accelerator-based experiments such as NOvA. The current status of neutrino oscillation parameters inferred from solar, atmospheric, reactor and atmospheric neutrinos is also given. Finally, I conclude Chapter 1 by mentioning some un-resolved questions in the neutrino sector.

- **Chapter 2** explains various aspects of the NOvA experiment in great detail. A brief introduction to the Fermilab accelerator complex is also given which is used for producing the neutrino beams for various experiments, including the NOvA experiment. The production of the muon-neutrino beam is also described. This chapter also discusses the scientific reasoning for keeping NOvA detectors slightly off the main axis of the neutrino beam. NOvA uses two identical detectors, one near the neutrino source within the Fermilab boundary at a distance of 1 km and another one at a distance of 810 km away in Ash River, MN. Both detectors are made up of identical material but are of different sizes. This chapter describes in detail the different parts of the two detectors.
- **Chapter 3** is dedicated to the acceptance studies of the NOvA Far Detector (FD) using cosmic ray muons. The NOvA FD is on the surface of Earth with a very shallow overburden, equivalent to 3.2 meter of water and is constantly exposed to the cosmic ray muons. The NOvA FD sees different numbers of cosmic ray muons from different directions because of the varying thickness of the Earth's atmosphere and the geometry of the detector. The acceptance studies measure the acceptance of the NOvA FD for cosmic ray muons in different directions. Knowing the acceptance of the detectors helps in making the strategy for the calibration process, since the cosmic ray muons are used to calibrated the NOvA detectors.
- **Chapter 4** starts by giving an introduction to the calibration and importance of calibration of the NOvA detectors. In order to infer correct energies of the incident particles in the detectors, it is necessary to calibrate the detectors, such that the response of the detectors to signal light is uniform throughout the volume of the detector as well as over different times. This chapter explains various effects which are needed to correct or account for, including the threshold, shielding and attenuation effects. Description of various steps followed in the attenuation and threshold calibration of both NOvA detectors

using cosmic ray muons is given. At the end of the chapter, I assess the performance of the Near and Far Detector calibrations. NOvA is able to successfully calibrate more than 98% of the near and 99% of the far detector cells. The result presented in the chapter forms part of papers in numbers 2, 3, and 4 in the attached list of publications.

- **Chapter 5** describes the $\nu_\mu \rightarrow \nu_\mu$ disappearance and $\nu_\mu \rightarrow \nu_e$ appearance analyses for the NOvA experiment. An introduction to the analysis framework designed for the data analysis is given in full detail. The extrapolation of signal and background predictions from the near to the far detectors is described. The χ^2 fitting procedure to fit the selected data is introduced. All steps in data analysis, including the event selection, signal and background topologies, neutrino energy estimation, analysis binning and the treatment of systematic uncertainties are described in detail. Finally the results of the analyses are presented and best fit values of the oscillation parameters are given. The result of these analyses are published in **Phys. Rev. D. 98, 032012 (2018)**.
- **Chapter 6** summarizes and concludes the work done in this Ph.D. thesis.

Contents

Dedication	ix
Acknowledgements	xi
Abstract	xxi
Synopsis	xxiii
List of Figures	xxix
List of Tables	xxxii
Abbreviations	xxxiii
Physical Constants	xxxv
Symbols	xxxvii
1 Neutrino Oscillations	1
1.1 Introduction	1
1.2 History	2
1.3 Two Flavor Neutrino Oscillation in Vacuum	5
1.4 Three Flavor Mixing Matrix, U	6
1.5 Three Flavor Neutrino Oscillation in Vacuum	7
1.5.1 Different Mass Hierarchies	8
1.6 The Survival Probability for $\nu_\mu \rightarrow \nu_\mu$ Oscillations	9
1.7 The Appearance Probability for $\nu_\mu \rightarrow \nu_e$ Oscillations	11
1.8 Neutrino Oscillations in Matter	11
1.8.1 The $\nu_\mu \rightarrow \nu_\mu$ Oscillations in Matter	14
1.8.2 The $\nu_\mu \rightarrow \nu_e$ Oscillations in Matter	14
1.9 Status of the Current Neutrino Oscillation Parameters	16
1.9.1 Measurement of the $\sin^2 \theta_{23}$	17
1.9.2 Measurement of the $ \Delta m_{32}^2 $	18

1.9.3	Measurement of the $\sin^2 \theta_{13}$	18
1.9.4	Measurement of the $\sin^2 \theta_{12}$ and Δm_{21}^2	19
1.10	Open Challenges	21
1.10.1	CP Violating Phase, δ_{cp}	21
1.10.2	The Neutrino Mass Ordering	22
1.10.3	Octant of θ_{23}	22
2	The NOvA Experiment	25
2.1	The Fermilab Accelerator Complex	27
2.2	The NuMI Beam	29
2.3	The Off-Axis Concept	30
2.4	Detectors	34
2.4.1	The Near Detector	34
2.4.2	The Far Detector	36
2.4.3	The unit cell	38
2.4.4	Liquid Scintillator	38
2.4.5	Optical Fiber	40
2.4.6	Avalanche photodiodes	41
2.4.7	Polyvinyl Chloride (PVC) modules	42
2.5	Data Acquisition System	43
2.6	Trigger	44
3	Acceptance of the NOvA FD using Cosmic Ray Muons	47
3.1	Introduction	47
3.2	Projected area	48
3.3	Detector efficiency and acceptance	51
3.3.1	Efficiency	51
3.3.1.1	Number of muons as a function of $\cos(\theta)$ and ϕ	53
3.3.1.2	Efficiency as a function of $\cos(\theta)$ and ϕ	55
3.3.2	Acceptance	55
3.4	Detector efficiency and acceptance for tri-cell hit muon tracks	58
3.4.1	Tri-cell hit	58
3.4.2	Number of muons as a function of $\cos(\theta)$ and ϕ for tri-cell hit tracks	59
3.4.3	Acceptance as a function of $\cos(\theta)$ and ϕ for tri-cell hit tracks	62
3.5	Results of the acceptance study	63
4	The Attenuation and Threshold Calibration of the NOvA Detectors	65
4.1	Calibration of the Detectors	65
4.1.1	Coordinates	66
4.1.2	Definitions	67
4.2	Attenuation fits	68
4.2.1	Selection and Calibration steps	68

4.2.2	Threshold and Shielding effects	70
4.2.3	Simulation and Detector Specific Attenuation Fit	72
4.2.4	Functional Form of Attenuation Fit	73
4.2.5	Rolloffs	74
4.2.6	Locally Weighted Scatter Plot Smoothing, LOWESS, Fit	75
4.2.7	Calibrator and Database	77
4.2.8	Near Detector Calibration Performance	78
4.2.9	Far Detector Calibration Performance	79
4.3	Calibration leading to calibration systematics	81
4.4	Summary and results of the attenuation and threshold calibration	82
5	Neutrino Oscillation Analysis	83
5.1	Introduction to the Analysis Framework	84
5.2	ν_μ Disappearance Analysis	86
5.2.1	Signal and Background Event Topologies	86
5.2.2	ν_μ Event Selection	87
5.2.3	Energy Estimation and Analysis Binning	90
5.2.4	ν_μ Selected FD Data	92
5.3	ν_e Appearance Analysis	94
5.3.1	Signal and Background Event Topologies	95
5.3.2	ν_e Event Selection	95
5.3.3	Energy Estimation and Analysis Binning	99
5.3.4	ν_e Selected FD Data	101
5.4	Extrapolation: Constraints from the ND	102
5.4.1	ν_e Signal and Background Extrapolation	103
5.4.2	ν_μ Signal and Background Extrapolation	109
5.5	Fitting Procedure	110
5.5.1	Binned χ^2	110
5.6	Incorporation of Systematic Uncertainties	111
5.6.1	Calibration	112
5.6.2	Normalization	112
5.6.3	Cross sections and GENIE	113
5.6.4	Extrapolation	113
5.6.5	Neutrino Beam Flux	114
5.6.6	Muon and Calorimetric Energy Scales	114
5.6.7	Cherenkov light and light levels	114
5.6.8	Rock Events	115
5.7	Physics Sensitivities	115
5.8	Oscillation Results	117
5.8.1	Oscillation Fit to the FD Data Events	118
5.8.2	Best Fit Oscillation Parameters	121
5.8.3	Analysis Contours	123
5.8.4	Significance of Oscillation Parameters	124

5.9 Summary	126
6 Conclusions	129
A Neutrino Oscillation Phenomenology	133
A.1 Two Flavor Neutrino Oscillation in Vacuum	133
B ν_e Selected FD Data Events	137
C ν_μ Selected FD Data Events	143

List of Figures

- 1.1 A pictorial representation of the neutrino mass squared terms in the case of different ordering. One ordering of the neutrino masses is the Normal Hierarchy in which $m_1 < m_2 < m_3$. The other ordering of the neutrino masses is called the Inverted Hierarchy in which $m_3 < m_1 < m_2$. The colors represent the fraction of different flavors in the given mass eigenstates for varying δ_{cp} . Image from [23]. 9
- 1.2 The survival probability for the $\nu_\mu \rightarrow \nu_\mu$ oscillation is shown as a function of neutrino energy for $\Delta m_{32}^2 = 2.44 \times 10^{-3} \text{ eV}^2$, $\Delta m_{21}^2 = 7.53 \times 10^{-5} \text{ eV}^2$, $\sin^2 \theta_{23} = 0.5$, $\sin^2 \theta_{13} = 0.02$, $\sin^2 \theta_{12} = 0.30$, $\delta_{CP}(\pi) = 1.20$ and $L = 810 \text{ km}$ 10
- 1.3 The appearance probability for $\nu_\mu \rightarrow \nu_e$ oscillation is shown as a function of neutrino energy for $\sin^2 \theta_{23} = 0.5$, $\sin^2 \theta_{13} = 0.02$, $\sin^2 \theta_{12} = 0.30$, $\Delta m_{31}^2 = 2.44 \times 10^{-3} \text{ eV}^2$, $\Delta m_{32}^2 = 2.44 \times 10^{-3} \text{ eV}^2$, $\Delta m_{21}^2 = 7.53 \times 10^{-5} \text{ eV}^2$ and $L = 810 \text{ km}$ 12
- 1.4 Feynman diagram to show the interaction of neutrinos, ν_e , ν_μ and ν_τ with electrons, protons and neutrons present in matter. The three active neutrinos interact with the matter particles by neutral current interactions and the neutrinos maintain their identity after interactions. 13
- 1.5 Feynman diagram to show the interaction of electron-neutrinos, ν_e with electrons present in matter. In this diagram the ν_e interacts with the electrons by the charge current interactions. 13
- 1.6 The effect of matter on $\nu_\mu \rightarrow \nu_\mu$ survival probability is shown as a function of neutrino energy for constant matter density, $\rho = 2.84 \text{ g cm}^{-3}$, $\Delta m_{32}^2 = 2.44 \times 10^{-3} \text{ eV}^2$, $\sin^2 \theta_{23} = 0.5$ and $L = 810 \text{ km}$. As expected, the Earth's matter has no effect on muon-neutrino oscillation due to the absence of muons in matter. 15
- 1.7 The ν_e appearance probabilities for neutrinos and anti-neutrinos as a function of energy is shown for both the NH and IH. The matter potential has opposite effect on the neutrino and anti-neutrino oscillation probabilities. 16
- 1.8 The solar neutrino flux from different nuclear reactions in the Sun is shown as a function of neutrino energies. The percentages shown near neutrino spectrum from different nuclear reactions represent the uncertainty in the neutrino fluxes. Image from [31]. 20

2.1	Locations of the NOvA Near and Far Detectors are shown on a geographical map. The Near Detector is located at the Fermilab site whereas the Far Detector is located in Ash River, Minnesota (MN). Images from [36].	26
2.2	Fermilab accelerator complex consists of linear and circular accelerators. Image from [38].	27
2.3	Production of neutrino beam using a beam of 120 GeV protons from the Main Injector is shown. The neutrino beam is used by the NOvA experiment for the neutrino oscillation studies. Image from [35].	29
2.4	This figure shows the energy of the neutrinos produced at an angle θ , relative to the pion direction. For maximum oscillation sensitivity of ν_μ 's to ν_e 's, NOvA uses off-axis angle of $\theta = 14.6$ milli radian [35].	31
2.5	The simulated neutrino energy spectra at the FD for various values of the off-axis angles compared to the on-axis case. The detectors location at 14.6 milli-radians off-axis gives a narrow neutrino energy spectrum [35].	32
2.6	The figure shows the neutrino flux at a distance of 810 km from pions of energy E_π at an angle θ with respect to the NuMI beam direction [35].	33
2.7	The figure shows the simulated energy spectrum of the ν_μ CC events with and without oscillations, the NC events, the signal ν_e CC events from $\nu_\mu \rightarrow \nu_e$ oscillations and the intrinsic beam ν_e CC events. The intrinsic beam ν_e events from the three body decay shows a broader energy spectrum compared to the oscillated ν_e CC events. Image from [35].	33
2.8	The NOvA ND is situated in an underground cavern at Fermilab. Image from [36].	35
2.9	A schematic of the NOvA ND is shown to display the active and muon catcher regions of the detector. A is the active region, and B is the muon catcher region. The muon catcher region is $\frac{2}{3}$ rd in height to the active region and the same width as the active region. C is the DAQ racks region, D is the stairs and walking area and E is the movable platform. Image from [41]	36
2.10	The NOvA FD situated at Ash River, Minnesota, U.S.A. is shown. The scale of the FD can be seen by comparing it to a person standing next to it, in the bottom left corner of the picture. Image from [36].	37
2.11	The left figure shows a cartoon image of a cell [35] and the right figure shows a real image of cells extruded in PVC module [36].	38
2.12	A small part of the NOvA detector is shown to emphasize the horizontal and vertical orthogonal planes made of the PVC modules.	39
2.13	The figure shows the absorption and emission spectrum of the NOvA optical fiber. The optical fiber captures blue light in the region (400 - 450)nm and shifts it to the green light in the region (490 - 550)nm [35].	41

2.14	The figure shows the front (in the left plot) and back (in the right plot) views of the NOvA APD mounted on a board. Each APD has 32 pixels to readin signal from the NOvA cells. Image from [35]. . . .	42
2.15	The NOvA readout chain is shown. The signal from a NOvA module is readout by an APD and is digitized in the FEB by an ADC unit. The digitized signal from 64 FEBs is read by a DCM unit and is transferred to the buffer nodes for storage [52].	43
2.16	The NuMI beam timing peak is a $10\mu s$ long window from $218\mu s$ to $228\mu s$ in a $500\mu s$ readout window [54].	45
3.1	The zenith, θ , and azimuthal, ϕ , angles for a point $P(\theta, \phi)$ in space with respect to an observer are shown. The angle θ is defined as the angle between the zenith and a line from the observer to the point $P(\theta, \phi)$. The angle ϕ is defined as the angle between the North direction and the line from the observer to point $P(\theta, \phi)$ projected on the horizontal plane in the clockwise direction from North to East. . .	49
3.2	The projected area of the NOvA FD as a function of $\cos\theta$ and ϕ . . .	51
3.3	The number of muons seen by the NOvA FD as a function of $\cos(\theta)$ and ϕ for the “All Muons” (no selection criterion applied).	54
3.4	The number of muons seen by the NOvA FD as a function of $\cos(\theta)$ and ϕ for “All Passing Muons”.	54
3.5	The number of muons seen by the NOvA FD as a function of $\cos(\theta)$ and ϕ for “Stopping Muons”.	55
3.6	The efficiency of the NOvA FD as a function of $\cos(\theta)$ and ϕ for “All Passing Muons”.	56
3.7	The efficiency of the NOvA FD as a function of $\cos(\theta)$ and ϕ for “Stopping Muons”.	56
3.8	The acceptance of the NOvA FD as a function of $\cos(\theta)$ and ϕ for “All Passing Muons”.	57
3.9	The acceptance of the NOvA FD as a function of $\cos(\theta)$ and ϕ for “Stopping Muons”.	57
3.10	A tri-cell hit in a horizontal (y-view) cell.	59
3.11	The number of muons seen by the NOvA FD as a function of $\cos(\theta)$ and ϕ for “All Passing Muons” after the tri-cell selection.	60
3.12	The number of muons seen by the NOvA FD as a function of $\cos(\theta)$ and ϕ for “Stopping Muons” after the tri-cell selection.	60
3.13	Ratio of number of muons with tricell to the “All Passing” sample seen by the NOvA FD as a function of $\cos(\theta)$ and ϕ	61
3.14	Ratio of number of stopping muons with tricell to all “Stopping” muons seen by the NOvA FD as a function of $\cos(\theta)$ and ϕ	61
3.15	The acceptance of the NOvA FD as a function of $\cos(\theta)$ and ϕ for “All Passing Muons” after the tri-cell selection.	62
3.16	The acceptance of the NOvA FD as a function of $\cos(\theta)$ and ϕ for “Stopping Muons” after the tri-cell selection.	63

4.1	A cartoon image to represent the selection of a cell hit under “ xy ” estimator. The red dark cell in the center is selected because the light red neighboring cells have hit as well. Here the path length is estimated by the ratio of the cell width, L_y to the direction cosine c_y .	69
4.2	Top plots are examples of the FD threshold corrections as a function of W and cell number for both the X (left) and Y view (right) cells. Bottom plots are after the empirical fit is applied to the top plots to remove the statistical noise for both the X and Y view cells.	72
4.3	Comparison of the empirical fit, red curve, to the threshold correction and the underlying distribution, black curve for the high gain Far Detector X view, top plots, and Y view, bottom plots, for both W (left) and cell number (right).	73
4.4	A pictorial representation of the NOvA cell to illustrate short- and long-paths for scintillation light to reach the readout via wavelength shifting fiber.	74
4.5	Example here shows the response of a particular ND cell for cosmic data. The blue curve in the left plot is the total attenuation fit including the LOWESS corrections and the red curve is the exponential fit to the cell response. The performance of the attenuation fit and the LOWESS correction is visible as it passes close to all cell hit points. The right figure, for example, shows the LOWESS fit through the residuals for the same ND cell.	76
4.6	Examples of the full attenuation fit including the LOWESS corrections to one ND cell (left) and to one FD cell (right) are shown. The full attenuation fit in the blue curve is also compared to the double exponential fit in red. The attenuation fit including LOWESS corrections performs a better fit to the cosmic data.	77
4.7	The ratios of the reconstructed to the true energies for the ND X-view hits. The red points are the ratios before the attenuation and threshold calibrations are applied and the blue points are after the calibrations are applied. The right plot is the zoomed version of the left plot. One can see the improvements in the ratios of the reconstructed to the true energies after attenuation and threshold calibrations are applied. Even after calibration, some calibration residuals remain. . .	78
4.8	The ratios of the reconstructed to the true energies for the ND Y-view hits. The red points are the ratios before the attenuation and threshold calibrations are applied and the blue points are after the calibrations are applied. The right plot is the zoomed version of the left plot. One can see the improvements in the ratios of the reconstructed to the true energies after attenuation and threshold calibrations are applied. Even after calibration, some calibration residuals remain. . .	79

4.9	The ratios of the reconstructed to the true energies for the FD X-view hits are shown. The red points are the ratios before the attenuation and threshold calibrations are applied and the blue points are after the calibrations are applied. The top left plot is made using the simulated data from period 1 and the top-right plot is made using simulated data from period 3. The bottom plots are simply the zoomed version of the corresponding top plots. One can see the improvements in the ratios of the reconstructed to the true energies after attenuation and threshold calibrations are applied. Even after calibration, some calibration residuals remain.	80
4.10	The ratios of the reconstructed to the true energies for the FD Y-view hits are shown. The red points are the ratios before the attenuation and threshold calibrations are applied and the blue points are after the calibrations are applied. The top left plot is made using the simulated data from period 1 and top the right plot is made using simulated data from period 3. The bottom plots are simply the zoomed version of the corresponding top plots. One can see the improvements in the ratios of the reconstructed to the true energies after attenuation and threshold calibrations are applied. Even after calibration, some calibration residuals remain.	81
5.1	Feynman diagram shows the interaction of ν_μ with a neutron. The ν_μ interacts via CC interaction through an exchange of a charged W boson.	86
5.2	A pictorial representation to shows the signal and one of the backgrounds in the ν_μ disappearance analysis. The signature of a ν_μ CC interactions is a long track of a muon and some activity at the interaction point in the detector. One of the background interaction is also pictured in which a neutrino interaction creates a π^- and a π^0 , and the π^0 decays into two photons.	87
5.3	Comparison of the ν_μ selected ND data events to the ν_μ CC simulated events to show the variable energy binning. Various backgrounds in the ND are also shown. The simulated events are normalized to ND data POT and also normalized to the bin widths.	91
5.4	Comparison of the ν_μ selected ND data events to the ν_μ CC simulated events in different quartiles in order of increasing hadronic energy fractions. The background events are also added.	92
5.5	The ν_μ selected events is shown in the FD for the $\nu_\mu \rightarrow \nu_\mu$ analysis. In total 126 ν_μ events are selected. The neutrino energy spectra of all quartiles are shown.	93
5.6	Neutrino energy spectrum of all ν_μ selected events in the FD is shown. This spectra is the sum of number of neutrinos shown in Fig. 5.5. . .	93
5.7	NOvA event display of one of the ν_μ FD data events for the $\nu_\mu \rightarrow \nu_\mu$ oscillations. A muon is clearly visible as a long straight track and some hadronic activity at the interaction vertex are clear signatures of the ν_μ CC interaction.	94

5.8	Feynman diagram shows the interaction of ν_e inside the FD. The ν_e interacts via CC interaction through exchange of a charged W boson producing an electron and a proton.	95
5.9	A pictorial representation to show a signal and a background in the ν_e appearance analysis. The signature of a ν_e CC interaction is an electromagnetic shower and hadronic activity at the interaction point in the detector. The background shown here is the same from Fig. 5.2.	96
5.10	Comparison of ν_e selected ND data sample to the ν_e selected simulated events. Various backgrounds in the ND are also shown.	100
5.11	Selected ν_e events in the FD for $\nu_\mu \rightarrow \nu_e$ analysis. In total 66 ν_e events are selected. The energy and CVN spectrum of the selected FD events are shown.	101
5.12	NOvA event display of one of the selected ν_e FD data events for the $\nu_\mu \rightarrow \nu_e$ analysis.	102
5.13	The selected data and simulated ν_μ CC events in the ND in reconstructed neutrino energy bins are shown. The ND data and simulated events are used to make the signal prediction in the FD for both the ν_μ disappearance and ν_e appearance analyses.	104
5.14	The ratios of the ND data and simulated ν_μ CC events in reconstructed neutrino energy bins are shown. The ratios of the ND data and simulated events are used in the signal extrapolation from the ND to the FD.	105
5.15	The true and reconstructed neutrino energies of the ND ν_μ CC events selected by the ν_μ selections are shown as a 2D spectrum. The true energy bins are to be weighted by the ratios of the ND data and simulated events shown in Fig. 5.14 to make the predictions in the FD.	106
5.16	The weighted 2D spectrum showing the true and reconstructed neutrino energies of the ND ν_μ CC events selected by the ν_μ selections. The true energy bins are weighted by the ratios of the ND data and simulated events to make the predictions in the FD.	107
5.17	The predicted true energy spectrum, $N_{\nu_\mu}^{\text{Prediction}}(E_j^{\text{true}})$, of the ν_μ CC events selected by the ν_μ selections. The ratios of the $N_{\nu_\mu}^{\text{Prediction}}(E_j^{\text{true}})$ to the reconstructed spectra, $N_{\nu_\mu}^{\text{MC}}$ are used to make the signal predictions in the FD.	108
5.18	The ratios of the ND predicted and simulated ν_μ CC events in true neutrino energy bins are shown. These ratios are used in the signal extrapolation.	108
5.19	The physics sensitivities for both the “ ν_e only” and the combined $\nu_\mu - \nu_e$ fit for the $\sin^2 \theta_{23}$ vs. δ_{cp} parameters are shown using 1, 2, and 3 σ C.L. The sensitivities are generated for the values of the oscillation parameters shown in Table 5.10. Top plots are for the “ ν_e only” fit and the bottom plots are for the combined $\nu_\mu - \nu_e$ fit. The left plots are for the NH and the right plots are for the IH.	117

5.20	Results of the oscillation fit to the FD data events is shown for the $\nu_\mu \rightarrow \nu_\mu$ analysis for all four quartiles. The signal events are shown by the green stacked histogram, the NC beam background by the gray histogram and the cosmic ray background by the yellow histogram. The other stacked histogram is the CC beam background. Most of the beam background and cosmic ray events are in the fourth, least resolution quartile as expected.	119
5.21	Results of the oscillation fit to the FD data events is shown for the $\nu_\mu \rightarrow \nu_\mu$ analysis for all four quartiles. The total best fit prediction is shown by purple line. As expected most of the beam background and cosmic ray events are in the fourth, least resolution quartile. . . .	120
5.22	Result of the oscillation fit to the FD data events is shown for the $\nu_\mu \rightarrow \nu_\mu$ analysis for combined quartiles. The best fit prediction is shown by the purple line. The gray band shows the beam background and the cosmic ray background is shown by the blue band.	120
5.23	Results of the oscillation fit to the FD data events are shown for the $\nu_\mu \rightarrow \nu_e$ analysis for all three CVN and peripheral bins. The signal events are shown by the dark green stacked histograms. The cosmic ray backgrounds are shown by the yellow band. Spectra of different beam CC and NC background components are shown too. As expected, the majority of the cosmic backgrounds are in the peripheral bin.	121
5.24	Results of the oscillation fit to the FD data events are shown for the $\nu_\mu \rightarrow \nu_e$ analysis for all three CVN and peripheral bins. The total best-fit prediction is shown by the purple line. The total expected beam and cosmic backgrounds are shown too. Events in the peripheral bins have energy from 0 to 4.5 GeV and are kept in a single energy bin. As expected, the majority of the cosmic backgrounds are in the peripheral bin.	122
5.25	The FD data analysis contours are shown for the “ ν_e only” fit. Contours in the left plot are for the normal hierarchy and in the right for the inverted hierarchy. The overall best fit point is found for the normal hierarchy having a lower value of the χ^2	124
5.26	The FD data analysis contours are shown for the combined “ $\nu_\mu - \nu_e$ ” fit. Contours in the top plot are for the normal hierarchy and in the bottom plot for the inverted hierarchy. The overall best fit point is found for the normal hierarchy having a lower value of the χ^2	125
5.27	The 1D significance levels for the “ ν_e only” oscillation fit for the δ_{cp} parameter are shown in the top plots and for the $\sin^2 \theta_{23}$ parameter in the bottom plots. The left plots are for the normal hierarchy and the right plots are for the inverted hierarchy.	126
5.28	The 1D significance levels for the “ $\nu_\mu - \nu_e$ joint” oscillation fit for the δ_{cp} parameter are shown in the top plots and for the $\sin^2 \theta_{23}$ parameter in the bottom plots. The left plots are for the normal hierarchy and the right plots for the inverted hierarchy.	127

B.1	Core sample event: run = 18457, subrun = 63, event number = 860083, slice = 23, hadronic energy = 0.76 (GeV), leptonic energy = 0.82 (GeV) and reconstructed neutrino energy = 1.69 (GeV). . . .	137
B.2	Core sample event: run = 19586, subrun = 07, event number = 125513, slice = 29, hadronic energy = 0.33 (GeV), leptonic energy = 1.73 (GeV) and reconstructed neutrino energy = 2.02 (GeV). . . .	138
B.3	Core sample event: run = 22242, subrun = 18, event number = 232856, slice = 30, hadronic energy = 0.30 (GeV), leptonic energy = 1.30 (GeV) and reconstructed neutrino energy = 1.56 (GeV). . . .	138
B.4	Core sample event: run = 23033, subrun = 43, event number = 561297, slice = 35, hadronic energy = 0.55 (GeV), leptonic energy = 0.89 (GeV) and reconstructed neutrino energy = 1.44 (GeV). . . .	139
B.5	Core sample event: run = 23210, subrun = 41, event number = 333628, slice = 36, hadronic energy = 0.02 (GeV), leptonic energy = 2.17 (GeV) and reconstructed neutrino energy = 2.17 (GeV). . . .	139
B.6	Core sample event: run = 25058, subrun = 51, event number = 359, slice = 35, hadronic energy = 0.22 (GeV), leptonic energy = 1.57 (GeV) and reconstructed neutrino energy = 1.74 (GeV).	140
B.7	Core sample event: run = 25399, subrun = 14, event number = 2233, slice = 34, hadronic energy = 0.77 (GeV), leptonic energy = 2.91 (GeV) and reconstructed neutrino energy = 3.85 (GeV).	140
B.8	Peripheral sample event: run = 19348, subrun = 58, event number = 832317, slice = 26, hadronic energy = 0.01 (GeV), leptonic energy = 2.30 (GeV) and reconstructed neutrino energy = 2.30 (GeV).	141
B.9	Peripheral sample event: run = 24880, subrun = 58, event number = 350, slice = 29, hadronic energy = 0.004 (GeV), leptonic energy = 1.68 (GeV) and reconstructed neutrino energy = 1.65 (GeV).	141
B.10	Peripheral sample event: run = 25344, subrun = 29, event number = 4650, slice = 24, hadronic energy = 0.82 (GeV), leptonic energy = 1.16 (GeV) and reconstructed neutrino energy = 2.12 (GeV).	142
C.1	Run = 17953, subrun = 38, event number = 256887, slice = 29, hadronic energy = 0.54 (GeV), leptonic energy = 2.72 (GeV) and reconstructed neutrino energy = 2.81 (GeV).	143
C.2	Run = 18862, subrun = 51, event number = 820267, slice = 37, hadronic energy = 0.09 (GeV), leptonic energy = 0.83 (GeV) and reconstructed neutrino energy = 0.92 (GeV).	144
C.3	Run = 19162, subrun = 18, event number = 275537, slice = 34, hadronic energy = 1.35 (GeV), leptonic energy = 0.54 (GeV) and reconstructed neutrino energy = 1.89 (GeV).	144
C.4	Run = 19588, subrun = 02, event number = 39026, slice = 33, hadronic energy = 0.51 (GeV), leptonic energy = 2.31 (GeV) and reconstructed neutrino energy = 2.82 (GeV).	145

-
- C.5 Run = 21539, subrun = 39, event number = 553083, slice = 26, hadronic energy = 2.01 (GeV), leptonic energy = 1.96 (GeV) and reconstructed neutrino energy = 3.97 (GeV). 145
- C.6 Run = 22241, subrun = 22, event number = 291677, slice = 39, hadronic energy = 0.32 (GeV), leptonic energy = 2.34 (GeV) and reconstructed neutrino energy = 2.65 (GeV). 146
- C.7 Run = 22594, subrun = 10, event number = 134619, slice = 35, hadronic energy = 1.24 (GeV), leptonic energy = 0.82 (GeV) and reconstructed neutrino energy = 2.06 (GeV). 146
- C.8 Run = 22803, subrun = 52, event number = 658433, slice = 39, hadronic energy = 2.64 (GeV), leptonic energy = 0.85 (GeV) and reconstructed neutrino energy = 3.49 (GeV). 147
- C.9 Run = 23203, subrun = 11, event number = 71924 , slice = 28, hadronic energy = 0.18 (GeV), leptonic energy = 0.64 (GeV) and reconstructed neutrino energy = 0.82 (GeV). 147
- C.10 Run = 24706, subrun = 58, event number = 6498 , slice = 30, hadronic energy = 0.44 (GeV), leptonic energy = 1.78 (GeV) and reconstructed neutrino energy = 2.22 (GeV). 148

List of Tables

1.1	The current values of neutrino oscillation parameters are summarized from the global fit [27] to the data from various reactor, solar, atmospheric and accelerator neutrino experiment. Values of parameters which are sensitive to the choice of hierarchy are also presented by NH for normal hierarchy and IH for inverted hierarchy of neutrino masses.	21
2.1	The different components used to make the NOvA scintillator are shown by mass fraction. The main scintillator is pseudocumene. The mineral oil is used as a solvent to blend the scintillator, wavelength shifters and other important agents [50].	40
3.1	Range of θ and ϕ , and area for different surfaces of the NOvA FD. The FD's north surface is 26.55° offset towards west of geographical north, so, the detector's north surface is at $\phi = 333.45^\circ$, the east surface is $\phi = 63.45^\circ$, the south surface is $\phi = 153.45^\circ$ and the west surface is $\phi = 243.45^\circ$	50
3.2	Selection criteria used to select Monte Carlo sample for NOvA FD acceptance study.	52
3.3	The efficiency and acceptance of the NOvA FD.	58
3.4	The efficiency and acceptance of the NOvA FD for tri-cell tracks.	63
3.5	The efficiency and acceptance of the NOvA FD before and after the tri-cell track selection.	64
4.1	This table shows the start and end dates of different data taking periods. The calibration was performed for each period.	66
4.2	Over 98% of the ND and over 99% of the FD cells were successfully calibrated.	82
5.1	Containment selections for the events in the ND. Containment selections make sure that the events have deposited energy in the detector volume.	89
5.2	Containment selections for the events in the FD. Containment selections make sure that the events have deposited energy in the detector volume.	90
5.3	The Number of ND data and simulated events selected by the ν_μ selection.	92

5.4	Number of FD selected events by the ν_{mu} selections in each quartile bin.	94
5.5	The ND specific fiducial and containment selections for the ν_e CC events in the ν_e analysis.	97
5.6	The FD specific prong containment selections for the ν_e CC events in the core sample in terms of the distances from the sides of the detector.	98
5.7	Allowed values of the CVN for the “low”, “mid”, “high” and peripheral CVN bins in the FD. If an event has CVN value in the range lower to upper CVN allowed value then the event would fall in the corresponding CVN bin.	100
5.8	Number of ND data and simulated events selected by the ν_e selection. As expected, the ν_e CC and $\bar{\nu}_e$ CC components increase from the Low to the High CVN bins and the ν_μ CC, $\bar{\nu}_\mu$ CC and NC components decrease.	101
5.9	Number of FD selected events by the ν_e selections in each CVN and peripheral bin.	102
5.10	Values of the oscillation parameters used to make physics sensitivities for the ν_e only and combined $\nu_\mu - \nu_e$ analyses for both the normal (NH) and inverted (IH) hierarchies.	116
5.11	Values of the oscillation parameters used to make the physics sensitivities in addition to the parameter values shown in Table 5.10.	116
5.12	The number of signal and background components are shown from the best oscillation fit to the FD data events selected by the ν_μ selections. In this analysis, 138.05 signal events, 3.43 CC and NC beam background events and 5.82 cosmic ray events are found.	119
5.13	The number of signal and background components are shown from the best oscillation fit to the FD data events selected by the ν_e selections. In this analysis, 46.65 signal events, 9.13 CC, 6.10 NC, and 4.81 cosmic ray background events are found.	122
5.14	The best fit values for the neutrino oscillation parameters obtained from the combined ν_μ and ν_e fit to the FD data events.	123
5.15	For the “ ν_e only” oscillation fit, the δ_{cp} and $\sin^2 \theta_{23}$ values under 1σ confidence intervals are shown for the normal and inverted hierarchies.	124
5.16	For the “ $\nu_\mu - \nu_e$ joint” oscillation fit, the δ_{cp} and $\sin^2 \theta_{23}$ values under 1σ confidence intervals are shown for the normal and inverted hierarchies.	126

Abbreviations

ADC	Analog to D igital C onverter
APD	Avalanche P hoto D iode
CC	Charge C urrent interactions
CMB	Cosmic Microwave B ackground
CNB	Cosmic Neutrino B ackground
CP	Charge- P arity
CRY	Cosmic-ray Shower Library
DCM	Data Concentrator M odule
DONUT	Direct O bservation of the Nu Tau
FD	Far D etector
FEB	Front E nd B oard
FNAL	Fermi National Accelerator L aboratory
GALLEX	Gallium E xperiment
GeV	Giga E lectronvolt
GPS	Global P ositioning S ystem
IH	Inverted H ierarchy
IL	I llinois
IS	Ion S ource
LEP	Large E lectron P ositron collider
LINAC	L inear A ccelerator
LOWESS	L Ocally W Eighted S catter plot S moothering
MI	Main I njector
MINOS	Main I njector N eutrino O scillation S earch

MIP	Minimum Ionizing Particle
MN	Minnesota
MTDU	Master Time Distribution Unit
NC	Neutral Current
ND	Near Detector
NDOS	Near Detector on Surface
NH	Normal Hierarchy
NOνA	NuMI off-axis ν_e Appearance
NuMI	Neutrinos from the Main Injector
PE	Photo-electron
PECorr	Corrected Photo-electron
PMT	Photo Multiplier Tube
PPO	Diphenyloxazole
PVC	Polyvinyl Chloride
QE	Quantum Efficiency
RENO	Reactor Experiment for Neutrino Oscillation
RF	Radio Frequency
RR	Recycler Ring
SAGE	Soviet American Gallium Experiment
SM	Standard Model
SNO	Sudbury Neutrino Observatory
SNP	Solar Neutrino Problem
T2K	Tokai to Kamioka experiment
TEC	Thermo Electric Cooler
USA	United States of America
UV	Ultra Violet light
WLS	Wave Length Shifter
WS	Wavelength Shifter

Physical Constants

Speed of light	$c = 2.997\,924\,58 \times 10^8 \text{ ms}^{-\text{s}}$ (exact)
Unit of energy	$\text{GeV} = 1.6 \times 10^{-19} \text{ Joules (J)}$
Fermi coupling constant	$G_F = 1.166\,3787 \times 10^{-5} \text{ GeV}^{-2}$
reduced Planck constant	$\hbar = 1.054\,571\,726 \times 10^{-34} \text{ J s}$

Symbols

$\frac{dE}{dx}$	energy loss	MeV cm ² g ⁻¹
A_p	total projected area of the FD	m ²
$A_{p,i}(\theta, \phi)$	projected area of i^{th} solid angle bin	m ²
$\mathcal{A}_{s,i}$	area of a given FD side	m ²
E_{true}	true energy deposited by a charged particle in NOvA cells	GeV
E_{mip}	energy deposited by a minimum ionizing particle in NOvA detectors	GeV
ϕ	azimuthal angle	radian
ϵ	efficiency	%
α	solid angle	steradian (sr)
\mathcal{A}	acceptance of NOvA FD	cm ² sr
δ_{CP}	standard charge-parity violation parameter	rad (radians)
θ_{23}	neutrino mixing angle	rad (radians)
θ_{13}	neutrino mixing angle	rad (radians)
θ_{12}	neutrino mixing angle	rad (radians)
e^\pm	electron particle	
μ	muon particle	
τ	tau particle	
ν_e	electron type neutrino	
$\bar{\nu}_e$	electron type anti-neutrino	

ν_μ	muon type neutrino
$\bar{\nu}_\mu$	muon type neutrino
ν_τ	tau type neutrino
$\pi^{0,\pm}$	neutral and charged pions
γ	photon
K	kaon particle

Extraction of Neutrino Oscillation Parameters using a Simultaneous Fit
of ν_μ Disappearance and ν_e Appearance data with the NOvA Experiment

Chapter 1

Neutrino Oscillations

1.1 Introduction

Neutrino physics is one of the exciting fields of fundamental research. Neutrinos are the second most abundant particles in the Universe after photons. Neutrinos were discovered more than 60 years ago, but we still know very little about them. Neutrinos, electrons, positrons and photons were the only particles produced in the first few seconds after the Big Bang and were in thermal equilibrium with each other. The Cosmic Neutrino Background (CNB), also known as relic neutrinos from early Universe, are present in the space just like the Cosmic Microwave Background (CMB). There are a number of sources of neutrinos in the Universe. Other than the Big Bang, neutrinos are produced in the core of our Sun, radioactive processes inside Earth, Supernovae, cosmic ray showers, nuclear reactors and particle accelerators. During the Big Bang, equal amounts of matter and anti-matter were produced but today our Universe is dominated by matter over anti-matter. The baryon-sector (quark-sector) does not explain the dominance of matter. The leptogenesis theory [1] indicates that the asymmetry of matter over anti-matter in the Universe might have been caused by the early neutrinos. The fact that neutrinos might be the reason for the asymmetry of matter over anti-matter makes them interesting for fundamental research. Many experiments around the world such as Super-Kamiokande [2], T2K [3], NOvA [4], are trying to explore the possibility of neutrinos being the key to the existence of matter in the Universe.

1.2 History

The history of neutrino physics started in 1914 when James Chadwick demonstrated using a primitive Geiger counter that the beta (β) spectrum was indeed a continuous spectrum of energies instead of discrete lines of energies as in the case of α and γ decays. An example of α decay process is the decay of Uranium ($^{238}\text{U}_{92}$) to Thorium ($^{234}\text{Th}_{90}$) with an emission of a Helium ($^4\text{He}_2$) nuclei or an α particle,



an example of a γ decay is the decay of Uranium ($^{238}\text{U}_{92}$),



Prior to 1930 the β -decay was simply known to be a two body decay just like an α or a γ decay. An example of β -decay prior to 1930 would be the decay of carbon-14 ($^{14}\text{C}_6$) to nitrogen-14 ($^{14}\text{N}_7$),



The continuous spectrum observed by James Chadwick violated both the energy and momentum conservation which are the fundamental pillars of physics. The continuous spectrum of β decay remained a mystery for many years until 1930 when Wolfgang Ernst Pauli [5] in a letter to a meeting of physicists in Tübingen, Germany, suggested a way to explain the continuous β decay spectrum such that the conservation of energy and momentum are not violated. Pauli suggested the existence of a neutral, spin 1/2 particle in the nuclei which obeys the Pauli exclusion principle. He also suggested that the new particle has to be different from the light quanta and would not travel at the speed of light. He called the new particle “neutron” for being electrically neutral. The Italian physicist Edoardo Amaldi renamed Pauli’s new particle to “neutrino” (ν_e) to distinguish it from James Chadwick “neutron” [6]. According to Pauli, the mass of the neutrino was supposed to be of the order of electron mass, or less than 0.01 times the mass of the proton. The β decay spectrum can now be explained as a three body decay,



in which an emitted electron is accompanied by a neutrino and the sum of the energies of the emitted electron and newly created neutrino remains constant. Pauli also suggested that it would be hard to detect such particles because it would have either same or 10 times more power to go through material than a γ -ray. Enrico Fermi in 1934 [7], [8] proposed a simple description of the spectrum of the β decay. To be consistent with the conservation of energy, Fermi assumed the existence of Pauli's neutrino. Fermi successfully derived the expressions for the life time of the β decay as well as the shape of the spectrum of β decay. The success of the Fermi's theory further strengthened the existence of Pauli's neutrino. The Fermi's theory heavily relied on the existence of neutrino which was not detected experimentally till that time. The first experimental evidence for existence of neutrinos came in 1956 from Clyde L. Cowan and Frederick Reines [9]. Cowan and Reines detected anti-neutrinos ($\bar{\nu}_e$) using the flux of anti-neutrinos from the fission reactor at the Savannah River Plant of the United States Atomic Energy Commission. A hydrogenous liquid scintillator loaded with cadmium chloride was used as a detector for the anti-neutrino interactions. The reactor anti-neutrinos were captured by the protons in the detector volume using the reaction,



The reaction products, positrons (β^+) and neutrons (n) were detected as electrical pulses and constituted the signal. The annihilation of the positron by an electron in the detector volume gives the first pulse which was two back-to-back photons of 511KeV at the same time. The second pulse was a delayed one that came from the capture of the slow neutron by the cadmium mixed in the detector. The energies of the pulses and their time spectrum was used to identify and establish the observed signal as neutrino induced signal. The Cowan and Reines experiment established the existence of neutrinos. In the Standard Model (SM) of particle physics [10], [11], [12], neutrinos are associated with leptons. The SM is a theory of the weak, electromagnetic and strong forces. The SM defines the properties of the fundamental particles and the interactions among them. Neutrinos are always produced and detected via the weak force which makes neutrino detection very challenging. For three generations of leptons there are three associated generations of neutrinos, the electron-flavored neutrino (ν_e), the muon-flavored neutrino (ν_μ) and the tau-flavored neutrino (ν_τ). The second type of neutrino, the muon-neutrino (ν_μ) was detected in 1962 using the Alternating Gradient Synchrotron (AGS) particle accelerator at the Brookhaven National Laboratory [13]. The ν_μ were produced from in-flight decay

of the pions,

$$\begin{aligned}\pi^+ &\rightarrow \mu^+ + \nu_\mu , \\ \pi^- &\rightarrow \mu^- + \bar{\nu}_\mu .\end{aligned}\tag{1.6}$$

It was the first experiment to use a particle accelerator to produce a beam of neutrinos. The possibility of using accelerators for doing high energy neutrino experiment was independently proposed by Pontecorvo [14] and Schwartz [15]. It was shown that accelerators can produce several orders of neutrinos. The pions in equation 1.6 were produced by striking protons, from the accelerator, on the fixed beryllium target. These days, accelerators are commonly used to produce beams of neutrinos for various neutrino experiments. The third type of neutrino, the tau-neutrino (ν_τ) was detected in 2000 by the "Direct Observation of the Nu Tau (DONUT)" collaboration [16] at the Fermi National Accelerator Laboratory (Fermilab) . A beam of 800 GeV protons was produced using Fermilab Tevatron. The interaction of the proton beam in a meter long tungsten beam dump, produced a beam of tau-neutrino from the decay of charmed mesons.

The Sun is a major source of ν_e . The ν_e from the Sun are used for solar neutrino experiments. In the 1960s, the Homestake radiochemical solar neutrino experiment of Ray Davis, faced a problem related to the rate of the solar neutrinos. The ν_e are produced in the nuclear reactions in the core of the Sun. The experiment was only able to detect one third the expected solar neutrinos predicted by the Standard Solar Model (SSM) [17]. There was no account of the remaining solar neutrinos. This problem in the 1960s was known as the Solar Neutrino Problem (SNP) and remained unsolved for around 40 years. The Super-Kamiokande (Super-K) experiment in 1998 [18], observed a deficit of atmospheric muon-neutrinos. The Super-K [19] experiment in Japan is a large size, water Cherenkov neutrino detector containing 50 ktons of pure water to detect neutrinos. The Super-K showed that the atmospheric ν_μ , produced by the collision of the cosmic rays with the Earth's atmosphere, transform to ν_τ on their way from the atmosphere to the surface of the Earth. The Sudbury Neutrino Observatory (SNO) experiment in 2001 [20], also showed that the ν_e produced in the core of the Sun, transform to ν_μ and ν_τ on their way from the core to the surface of the Sun. The SNO experiment observed the interactions of all three flavors of neutrinos from the solar flux and thus established the transformation of the solar ν_e to the ν_μ and ν_τ flavors. The observations of the Super-K and SNO experiment resolved the SNP problem. The Nobel Prize in Physics of 2015 was

awarded jointly to Takaaki Kajita of the Super-K and Arthur B. McDonald of the SNO collaborations for evidence of the neutrino transformations.

The transformation of one flavor of neutrino to another flavor without involving any mediating particle is termed neutrino oscillation. Neutrino oscillation is a quantum mechanical phenomenon in which the interference of different massive neutrino eigenstates leads to oscillation of the flavor neutrino states. The small differences in the masses of the mass eigenstates cause the interference of neutrino states. Neutrino oscillations thus prove that neutrinos are not massless particles as predicted by the SM of particle physics. The SM thus need extensions for incorporating the neutrino masses.

1.3 Two Flavor Neutrino Oscillation in Vacuum

The two approximation flavor neutrino oscillation explains the basis of the neutrino oscillation mechanism very well. In the two neutrino oscillation framework, the flavor eigenstate, $|\nu_\alpha\rangle$ is a quantum state composed of mass eigenstates, $|\nu_i\rangle$. The mixing of mass eigenstates with flavor eigenstates is described by a unitary mixing matrix, U [21] as,

$$|\nu_\alpha\rangle = \sum_{i=1}^2 U_{\alpha i}^* |\nu_i\rangle, \quad (1.7)$$

here U is the Pontecorvo-Maki-Nakagawa-Sakata (PMNS) matrix and is defined in more detail in § 1.4. The mass and flavor eigenstates are orthogonal states. The free particle Hamiltonian (H_o) and the time evolution of the flavor eigenstate ($|\nu_\alpha\rangle_t$) is given by,

$$|\nu_\alpha\rangle_t = e^{-iH_o t} |\nu_\alpha\rangle, \quad (1.8)$$

which leads to the transformation of one flavor state to another. The probability of transformation, $P_{\nu_\alpha \rightarrow \nu_{\alpha'}}(t)$, from one flavor state to another in terms of the mixing matrix and energy E_i of the mass eigenstate is given by,

$$P_{\nu_\alpha \rightarrow \nu_{\alpha'}}(t) = \left| \sum_i U_{\alpha' i} e^{-iE_i t} U_{\alpha i}^* \right|^2. \quad (1.9)$$

For the two flavor neutrino oscillation case, the unitary mixing matrix is parameterized using a single mixing angle, θ , which describes the mixing of flavor states with

mass states,

$$U = \begin{pmatrix} \cos \theta & \sin \theta \\ -\sin \theta & \cos \theta \end{pmatrix}. \quad (1.10)$$

The probability of ν_α flavor state with energy E to transform to $\nu_{\alpha'}$ flavor state after traveling a distance (L) is derived in appendix A and is given by,

$$P_{\nu_\alpha \rightarrow \nu_{\alpha'}}(L, E) = \sin^2(2\theta) \sin^2\left(\frac{\Delta m_{21}^2 L}{4E}\right), \quad (1.11)$$

where $\Delta m_{21}^2 = m_2^2 - m_1^2$, and the probability for a ν_α flavor to survive as a ν_α is given by,

$$P_{\nu_\alpha \rightarrow \nu_\alpha}(L, E) = 1 - \sin^2(2\theta) \sin^2\left(\frac{\Delta m_{21}^2 L}{4E}\right). \quad (1.12)$$

In practical units, the Δm_{21}^2 is in the units of eV^2 , distance, L is in km and neutrino energy, E , is in GeV. The survival and transformation probabilities follow the unitarity condition, such that the sum of both probabilities remain unity,

$$P_{\nu_\alpha \rightarrow \nu_\alpha}(L, E) + P_{\nu_\alpha \rightarrow \nu_{\alpha'}}(L, E) = 1. \quad (1.13)$$

The survival probability is also called the disappearance probability as it gives an estimate of the number of neutrinos disappearing from their initial flavor state. The transformation probability, also called the appearance probability gives an estimate of the number of neutrinos of the new flavor appearing from the transformation of the initial state flavor neutrinos.

1.4 Three Flavor Mixing Matrix, U

For the three-flavor neutrino oscillations, the mixing matrix, U , is a 3×3 unitary matrix and is characterized using three mixing angles, θ_{12} , θ_{23} and θ_{13} , and a CP violating phase (δ_{cp}). The angle θ_{12} describes the mixing of mass eigenstates ν_1 and ν_2 in a given flavor state. Angle θ_{23} describes the mixing of states ν_2 and ν_3 in flavor states and angle θ_{13} tells about the ν_1 and ν_3 mixings. The CP violation phase differentiates the behavior between neutrinos and anti-neutrinos. In the case of neutrino oscillations, the CP violating phase gives the differences in the pattern of neutrino and anti-neutrino oscillation probabilities. If the oscillation probabilities for both the neutrinos and anti-neutrinos are same then the CP phase would be zero.

The mixing matrix [22] takes the following form for three flavor neutrino oscillations and uses the expressions $c_{ij} = \cos \theta_{ij}$ and $s_{ij} = \sin \theta_{ij}$,

$$U = \begin{pmatrix} 1 & 0 & 0 \\ 0 & c_{23} & s_{23} \\ 0 & -s_{23} & c_{23} \end{pmatrix} \begin{pmatrix} c_{13} & 0 & s_{13}e^{-i\delta_{cp}} \\ 0 & 1 & 0 \\ -s_{13}e^{-i\delta_{cp}} & 0 & c_{13} \end{pmatrix} \begin{pmatrix} c_{12} & s_{12} & 0 \\ -s_{12} & c_{12} & 0 \\ 0 & 0 & 1 \end{pmatrix},$$

the combined matrix takes the form,

$$U = \begin{pmatrix} c_{12}c_{13} & c_{13}s_{12} & s_{13}e^{-i\delta_{cp}} \\ -c_{12}s_{13}s_{23}e^{i\delta_{cp}} - c_{23}s_{12} & -s_{12}s_{13}s_{23}e^{i\delta_{cp}} + c_{12}c_{23} & c_{13}s_{23} \\ -c_{12}s_{13}c_{23}e^{i\delta_{cp}} + s_{23}s_{12} & -s_{12}s_{13}c_{23}e^{i\delta_{cp}} - c_{12}s_{23} & c_{13}c_{23} \end{pmatrix} \quad (1.14)$$

$$= \begin{pmatrix} U_{e1} & U_{e2} & U_{e3} \\ U_{\mu1} & U_{\mu2} & U_{\mu3} \\ U_{\tau1} & U_{\tau2} & U_{\tau3} \end{pmatrix}. \quad (1.15)$$

1.5 Three Flavor Neutrino Oscillation in Vacuum

In the case of three-neutrino oscillations, an electron-neutrino (ν_e) may oscillate to a muon-neutrino (ν_μ) or/and to a tau-neutrino (ν_τ). Similarly the ν_μ and ν_τ can transform to the other neutrino flavors. For the case of three-neutrino mixing, the oscillation probability is given by [22],

$$P_{\bar{\nu}_\alpha \rightarrow \bar{\nu}_{\alpha'}} = \delta_{\alpha,\alpha'} - 4 \sum_{j>i} \text{Re} U_{\alpha'j} U_{\alpha j}^* U_{\alpha'i} U_{\alpha i} \sin^2 \frac{\Delta m_{ji}^2 L}{4E} + 2 \sum_{j>i} \text{Im} U_{\alpha'j} U_{\alpha j}^* U_{\alpha'i} U_{\alpha i} \sin^2 \frac{\Delta m_{ji}^2 L}{2E}. \quad (1.16)$$

where $\Delta m_{ki}^2 = m_k^2 - m_i^2$ is the differences in the masses of mass eigenstates. For anti-neutrino oscillations from flavor α to flavor α' , that is, $|\bar{\nu}_\alpha\rangle \rightarrow |\bar{\nu}_{\alpha'}\rangle$, the mixing matrix $U_{\alpha i}$ is changed to its complex conjugate element, $U_{\alpha i}^*$. The oscillation

probability for anti-neutrinos thus takes the following form from [22],

$$P_{\bar{\nu}_\alpha \rightarrow \bar{\nu}_{\alpha'}} = \delta_{\alpha, \alpha'} - 4 \sum_{j>i} \text{Re} U_{\alpha'j} U_{\alpha j}^* U_{\alpha'i}^* U_{\alpha i} \sin^2 \frac{\Delta m_{ji}^2 L}{4E} - 2 \sum_{j>i} \text{Im} U_{\alpha'j} U_{\alpha j}^* U_{\alpha'i}^* U_{\alpha i} \sin^2 \frac{\Delta m_{ji}^2 L}{2E}. \quad (1.17)$$

The difference in the sign of the imaginary terms in equations 1.16 and 1.17 gives the differences in the way neutrinos and anti-neutrinos oscillate. The difference in the neutrino and anti-neutrino oscillations is defined as the charge-parity (CP) asymmetry factor, $\delta_{\alpha\alpha'}^{CP}$. The $\delta_{\alpha\alpha'}^{CP}$ takes the form [22],

$$\delta_{\alpha\alpha'}^{CP} = P_{\nu_\alpha \rightarrow \nu_{\alpha'}} - P_{\bar{\nu}_\alpha \rightarrow \bar{\nu}_{\alpha'}} = 4 \sum_{j>i} \text{Im} U_{\alpha'j} U_{\alpha j}^* U_{\alpha'i}^* U_{\alpha i} \sin^2 \frac{\Delta m_{ji}^2 L}{2E}. \quad (1.18)$$

The $\delta_{\alpha\alpha'}^{CP}$ is same as the δ_{cp} phase defined in § 1.4.

1.5.1 Different Mass Hierarchies

For the three neutrino mixing case, there are three mass-squared differences, Δm_{21}^2 , Δm_{32}^2 and Δm_{31}^2 . Only two mass-squared differences terms are independent because one of the mass-squared differences is the sum of the other two terms. The analysis of the solar neutrino data shows that the Δm_{21}^2 has a positive value, that is $m_2 > m_1$. The existing neutrino data does not reveal the sign of Δm_{31}^2 or Δm_{32}^2 . In the three neutrino oscillation case, two possible signs of Δm_{31}^2 or Δm_{32}^2 exists which correspond to two different orderings for neutrino masses. One is the normal ordering of the masses, sometimes called the Normal Hierarchy, (NH), in which $m_1 < m_2 < m_3$ and the other is the inverted ordering of the masses, sometimes called the Inverted Hierarchy, (IH) which has $m_3 < m_1 < m_2$. Figure 1.1 shows a pictorial representation of the ordering of the neutrino masses. The y-axis represents the mass squared differences and the colors in each mass eigenstate shows the fraction of flavor states mixed in the given mass eigenstates.

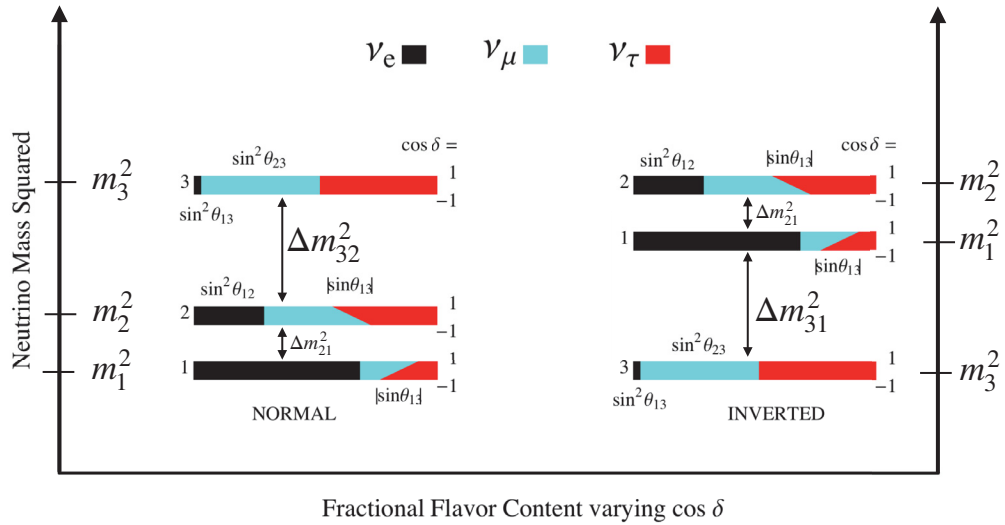


FIGURE 1.1: A pictorial representation of the neutrino mass squared terms in the case of different ordering. One ordering of the neutrino masses is the Normal Hierarchy in which $m_1 < m_2 < m_3$. The other ordering of the neutrino masses is called the Inverted Hierarchy in which $m_3 < m_1 < m_2$. The colors represent the fraction of different flavors in the given mass eigenstates for varying δ_{cp} . Image from [23].

1.6 The Survival Probability for $\nu_\mu \rightarrow \nu_\mu$ Oscillations

Suppose there is a beam of muon-neutrinos (ν_μ) traveling from one point in space to another. After travelling a distance L some of the ν_μ 's will transform to the ν_e 's, some will transform to ν_τ 's and the rest of the neutrinos would remain ν_μ 's. The probability for the surviving neutrinos is called the ν_μ survival probability and is denoted by $P_{\nu_\mu \rightarrow \nu_\mu}$. The ν_μ survival probability [24] is,

$$P_{\nu_\mu \rightarrow \nu_\mu} = 1 - \left[\sin^2 2\theta_{13} \sin^2 \theta_{23} + \cos^4 \theta_{13} \sin^2 2\theta_{23} \right] \sin^2 \left(\frac{\Delta m_{32}^2 L}{4E} \right),$$

the first term in the bracket is sub-dominant due to the small value of the θ_{13} parameter. The survival probability can be explained using two flavor case for small value of θ_{13} and is given in natural units [25] as,

$$P_{\nu_\mu \rightarrow \nu_\mu} = 1 - \sin^2 2\theta_{23} \sin^2 \left(\frac{\Delta m_{32}^2 L}{4E} \right). \quad (1.19)$$

A factor of 1.27 also appears when natural units are converted into practical units. The ν_μ survival probability in practical units thus takes the form,

$$P_{\nu_\mu \rightarrow \nu_\mu} = 1 - \sin^2 2\theta_{23} \sin^2 \left(\frac{1.27 \Delta m_{32}^2 (eV^2) L (km)}{E (GeV)} \right). \quad (1.20)$$

Figure 1.2 shows the ν_μ survival probability as a function of neutrino energy in GeV and uses $\sin^2 \theta_{23} = 0.5$, $\Delta m_{32}^2 = 2.44 \times 10^{-3} eV^2$ and $L = 810$ km from [4] for maximal value of $\sin^2 \theta_{23} = 0.5$. The ν_μ survival probability is mostly sensitive to θ_{23} and Δm_{32}^2 parameters as shown in equation 1.19. The dip in the survival probability curve gives the value of the $\sin^2 2\theta_{23}$ and the location of the dip on the energy axis gives Δm_{32}^2 .

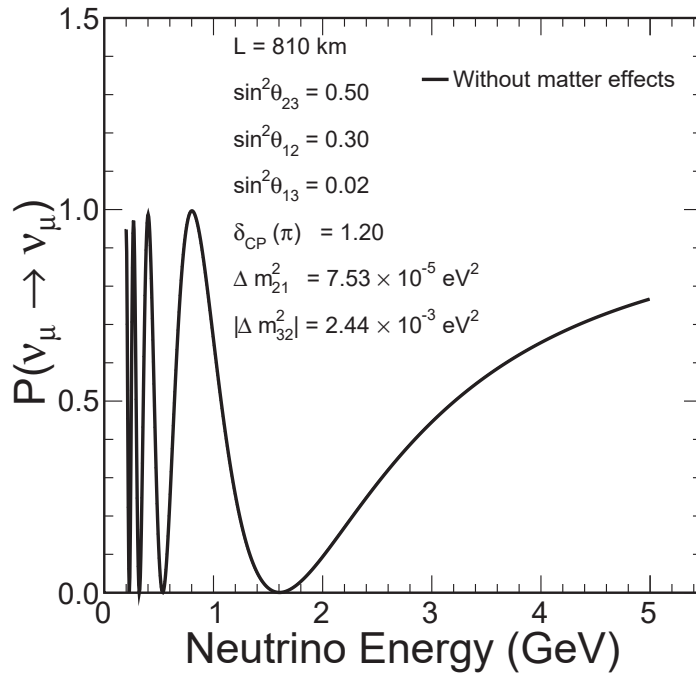


FIGURE 1.2: The survival probability for the $\nu_\mu \rightarrow \nu_\mu$ oscillation is shown as a function of neutrino energy for $\Delta m_{32}^2 = 2.44 \times 10^{-3} eV^2$, $\Delta m_{21}^2 = 7.53 \times 10^{-5} eV^2$, $\sin^2 \theta_{23} = 0.5$, $\sin^2 \theta_{13} = 0.02$, $\sin^2 \theta_{12} = 0.30$, $\delta_{CP}(\pi) = 1.20$ and $L = 810$ km.

1.7 The Appearance Probability for $\nu_\mu \rightarrow \nu_e$ Oscillations

The initial ν_μ 's can transform to ν_e 's after traveling a distance of L km. The oscillation probability for ν_μ to ν_e oscillation is also known as the ν_e -appearance probability and is given as [23],

$$\begin{aligned} P_{\nu_\mu \rightarrow \nu_e} &= \left| \sqrt{P_{atm}} e^{-i\left(\frac{\Delta m_{32}^2 L}{4E} + \delta_{cp}\right)} + \sqrt{P_{sol}} \right|^2 \\ &= P_{atm} + 2\sqrt{P_{atm}} \sqrt{P_{sol}} \cos\left(\frac{\Delta m_{32}^2 L}{4E} + \delta_{cp}\right) + P_{sol}, \end{aligned} \quad (1.21)$$

where P_{atm} is the probability term that contains the Δm_{31}^2 mass squared atmospheric term and P_{sol} contains Δm_{21}^2 mass squared solar term. The P_{atm} and P_{sol} probability terms are given as [23],

$$\begin{aligned} \sqrt{P_{atm}} &= \sin \theta_{23} \sin 2\theta_{13} \sin\left(\frac{\Delta m_{31}^2 L}{4E}\right), \\ \sqrt{P_{sol}} &= \cos \theta_{23} \cos \theta_{13} \sin 2\theta_{12} \cdot \frac{\Delta m_{21}^2 L}{4E}. \end{aligned} \quad (1.22)$$

The appearance probability for $\nu_\mu \rightarrow \nu_e$ oscillation is an important channel for analysis because it is sensitive to many neutrino oscillation parameters especially the small mixing angle, θ_{13} and the CP violating phase, δ_{cp} . The observation of $\nu_\mu \rightarrow \nu_e$ oscillations in neutrino experiments points to the non-zero value of the θ_{13} angle. The estimation of δ_{cp} parameter is also possible by analysis of the $\nu_\mu \rightarrow \nu_e$ and $\bar{\nu}_\mu \rightarrow \bar{\nu}_e$ oscillation data. Figure 1.3 shows the $\nu_\mu \rightarrow \nu_e$ appearance oscillation probability as a function of neutrino energy and with parameters $\sin^2 \theta_{23} = 0.5$, $\sin^2 \theta_{13} = 0.02$, $\sin^2 \theta_{12} = 0.30$, $\Delta m_{31}^2 = 2.44 \times 10^{-3} \text{ eV}^2$, $\Delta m_{32}^2 = 2.44 \times 10^{-3} \text{ eV}^2$, $\Delta m_{21}^2 = 7.53 \times 10^{-5} \text{ eV}^2$ and $L = 810 \text{ km}$. The appearance probability shows distinct features in presence of matter as explained in § 1.8.2.

1.8 Neutrino Oscillations in Matter

Neutrinos traveling through Earth or/and Sun interact with quarks and electrons present in the stable matter. In 1978, L. Wolfenstein [26] discovered that neutrinos face a potential by matter particles which change the oscillation probabilities.

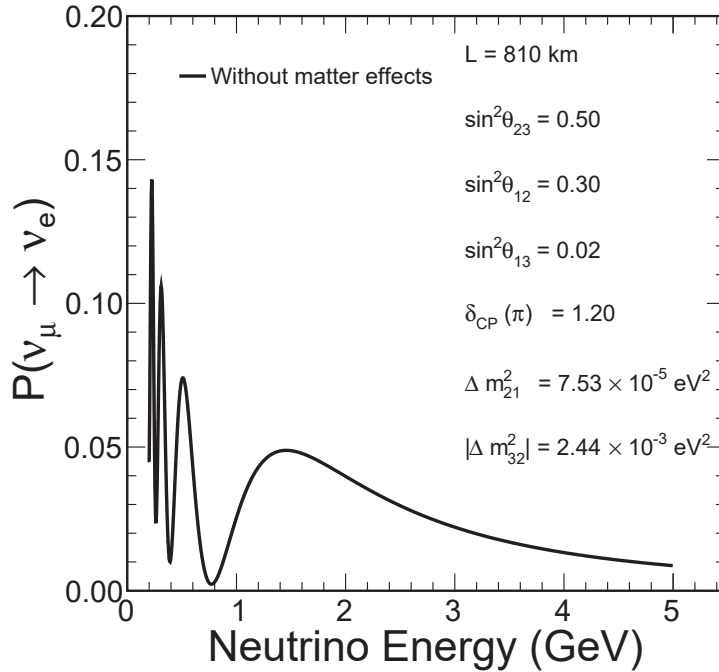


FIGURE 1.3: The appearance probability for $\nu_\mu \rightarrow \nu_e$ oscillation is shown as a function of neutrino energy for $\sin^2 \theta_{23} = 0.5$, $\sin^2 \theta_{13} = 0.02$, $\sin^2 \theta_{12} = 0.30$, $\Delta m_{31}^2 = 2.44 \times 10^{-3} \text{ eV}^2$, $\Delta m_{32}^2 = 2.44 \times 10^{-3} \text{ eV}^2$, $\Delta m_{21}^2 = 7.53 \times 10^{-5} \text{ eV}^2$ and $L = 810 \text{ km}$.

The ν_e , ν_μ and ν_τ interact with matter via both the CC and NC interactions. All three neutrino flavors contribute to the matter potential via NC interactions but only ν_e contribute to the matter potential via CC interactions because of presence of electrons in the matter. The ν_μ and ν_τ do not add any contribution to the matter potential via CC interactions due to absence of muons and taus in the matter. The extra potential due to ν_e plays an important role in modifying the oscillation probabilities. Figures 1.4 and 1.5 shows the Feynman diagrams to illustrate the neutral and charge current interactions. Figure 1.4 shows the neutral current interactions and all three neutrino flavors experience the same potential. Figure 1.5 shows the charge current interaction of ν_e with electrons in matter. The matter potential effects due to NC interactions are common to all three neutrinos and hence show no extra effects on the oscillations of three neutrinos. The potential due to the CC interactions show extra effect on the ν_e oscillation. In the presence of matter the free particle vacuum Hamiltonian, H_0 , becomes an effective Hamiltonian, H_{Eff} , including

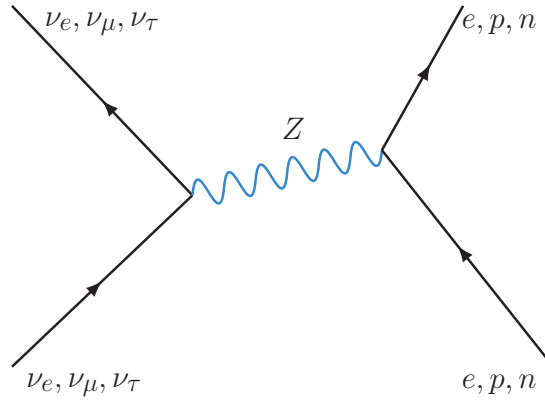


FIGURE 1.4: Feynman diagram to show the interaction of neutrinos, ν_e , ν_μ and ν_τ with electrons, protons and neutrons present in matter. The three active neutrinos interact with the matter particles by neutral current interactions and the neutrinos maintain their identity after interactions.

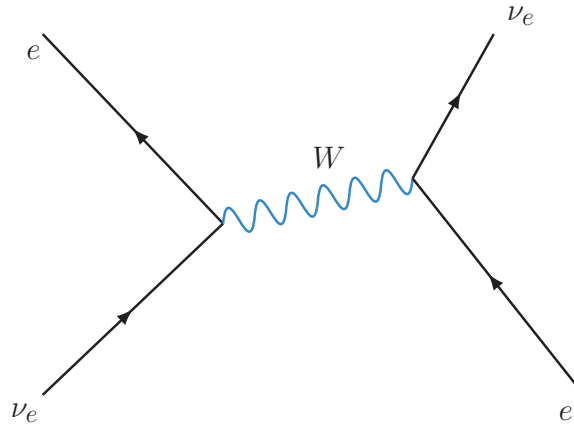


FIGURE 1.5: Feynman diagram to show the interaction of electron-neutrinos, ν_e with electrons present in matter. In this diagram the ν_e interacts with the electrons by the charge current interactions.

effects from matter potential, V ,

$$H_{\text{Eff}} = H_0 + V . \quad (1.23)$$

The Fermi coupling constant, G_F , which describe the strength of the weak force and the density of electrons, N_e , contributes to the matter potential [23],

$$V = \pm\sqrt{2}G_F N_e . \quad (1.24)$$

The matter potential is positive for neutrinos and negative for anti-neutrinos.

1.8.1 The $\nu_\mu \rightarrow \nu_\mu$ Oscillations in Matter

The matter potential modifies the values of the mixing angles and the mass squared differences terms and introduces a function of the matter density. The $\nu_\mu \rightarrow \nu_\mu$ survival probability is similar to equation 1.19 and includes the modified mixing angle, θ_{23}^M and mass squared, $(\Delta m_{32}^2)^M$ terms. The ν_μ survival probability in matter is given as [23],

$$P_{\nu_\mu \rightarrow \nu_\mu} = 1 - \sin^2 2\theta_{23}^M \sin^2 \left(\frac{(\Delta m_{32}^2)^M L}{4E} \right). \quad (1.25)$$

The modified mixing angle and the mass squared difference terms are [23],

$$\sin^2 2\theta_{23}^M = \frac{\sin^2 2\theta_{23}}{\sqrt{\left(\cos 2\theta_{23} - \frac{2VE}{\Delta m_{32}^2} \right)^2 + \sin^2 2\theta_{23}}}, \quad (1.26)$$

$$(\Delta m_{32}^2)^M = \Delta m_{32}^2 \sqrt{\left(\cos 2\theta_{23} - \frac{2VE}{\Delta m_{32}^2} \right)^2 + \sin^2 2\theta_{23}}, \quad (1.27)$$

the opposite sign values of the matter potential causes the matter to have opposite effect on neutrinos and anti-neutrinos. The neutrino oscillations are enhanced in the presence of matter and the anti-neutrino oscillations are suppressed. Figure 1.6 shows the impact of the presence of matter on the $\nu_\mu \rightarrow \nu_\mu$ survival probability and as expected the presence of matter makes nearly no impact on muon oscillations due to the absence of muons in matter.

1.8.2 The $\nu_\mu \rightarrow \nu_e$ Oscillations in Matter

The appearance probability for the $\nu_\mu \rightarrow \nu_e$ oscillations in matter [23] is similar to the ν_e survival probability in the vacuum as given in equation 1.21,

$$\begin{aligned} P_{\nu_\mu \rightarrow \nu_e} &= \left| \sqrt{P_{atm}} e^{-i\left(\frac{\Delta m_{32}^2 L}{4E} + \delta_{cp}\right)} + \sqrt{P_{sol}} \right|^2 \\ &= P_{atm} + 2\sqrt{P_{atm}} \sqrt{P_{sol}} \cos \left(\frac{\Delta m_{32}^2 L}{4E} + \delta_{cp} \right) + P_{sol}, \end{aligned} \quad (1.28)$$

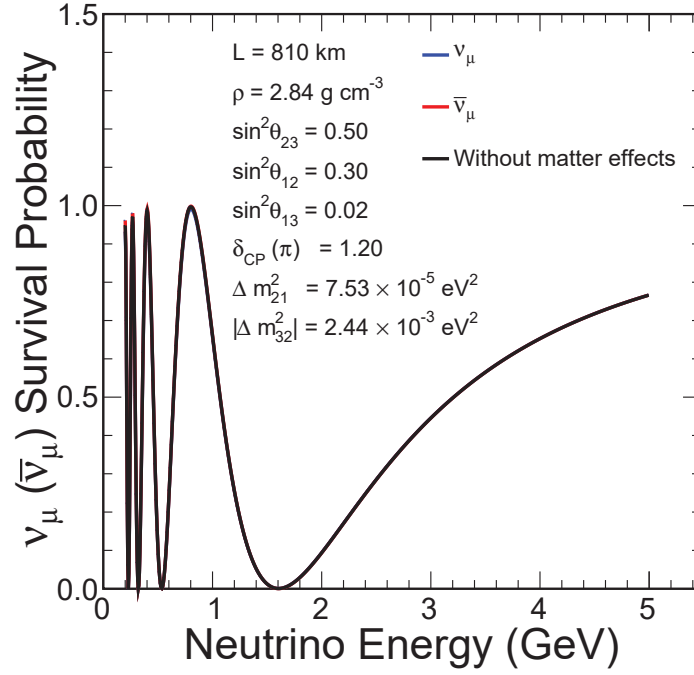


FIGURE 1.6: The effect of matter on $\nu_\mu \rightarrow \nu_\mu$ survival probability is shown as a function of neutrino energy for constant matter density, $\rho = 2.84 \text{ g cm}^{-3}$, $\Delta m_{32}^2 = 2.44 \times 10^{-3} \text{ eV}^2$, $\sin^2 \theta_{23} = 0.5$ and $L = 810 \text{ km}$. As expected, the Earth's matter has no effect on muon-neutrino oscillation due to the absence of muons in matter.

but the P_{atm} and P_{sol} probability terms are modified and become a function of the matter potential, V , [23],

$$\begin{aligned} \sqrt{P_{atm}} &= \sin \theta_{23} \sin 2\theta_{13} \frac{\sin \left(\frac{\Delta m_{31}^2 L}{4E} - \frac{VL}{2} \right)}{\left(\frac{\Delta m_{31}^2 L}{4E} - \frac{VL}{2} \right)} \cdot \left(\frac{\Delta m_{31}^2 L}{4E} \right) \\ \sqrt{P_{sol}} &= \cos \theta_{23} \sin 2\theta_{12} \frac{\sin \left(\frac{VL}{2} \right)}{\left(\frac{VL}{2} \right)} \left(\frac{\Delta m_{21}^2 L}{4E} \right). \end{aligned} \quad (1.29)$$

Figure 1.7 shows the impact of presence of matter on $\nu_\mu \rightarrow \nu_e$ oscillation probabilities for neutrinos and anti-neutrinos, for both the NH and IH. As can be seen, the matter potential has opposite effect on the neutrinos and anti-neutrinos. The neutrino oscillation is enhanced and anti-neutrino oscillation is suppressed in the case of NH, whereas in the case of IH the neutrino oscillation is suppressed and the anti-neutrino

oscillations is enhanced.

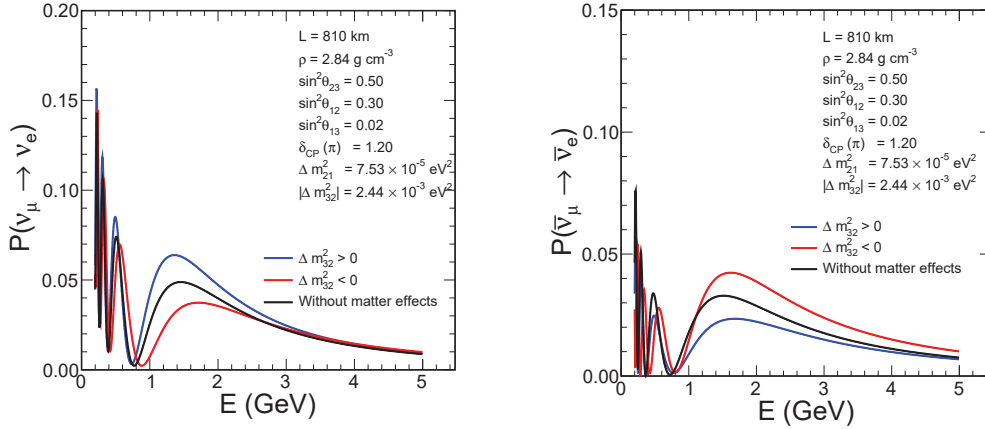


FIGURE 1.7: The ν_e appearance probabilities for neutrinos and anti-neutrinos as a function of energy is shown for both the NH and IH. The matter potential has opposite effect on the neutrino and anti-neutrino oscillation probabilities.

1.9 Status of the Current Neutrino Oscillation Parameters

As explained in § 1.5.1 and 1.4, for the current three-neutrino oscillation scenario, there are three mixing angles, θ_{12} , θ_{13} and θ_{23} , two mass-squared differences, Δm_{21}^2 and Δm_{32}^2 , and one CP violating phase, δ_{cp} , which makes six neutrino oscillation parameters in total. The $\sin^2 2\theta_{23}$ parameter is determined from the survival probabilities of $\nu_\mu \rightarrow \nu_\mu$ and $\bar{\nu}_\mu \rightarrow \bar{\nu}_\mu$ observation because of these oscillation channels are sensitivity to the $\sin^2 2\theta_{23}$ term as was explained in § 1.6. The $\nu_\mu \rightarrow \nu_\mu$ and $\bar{\nu}_\mu \rightarrow \bar{\nu}_\mu$ oscillations help us to figure out if the angle θ_{23} is maximal or not, that is, if the angle $\theta_{23} = 45^\circ$ or not. The values of mixing angles θ_{13} and θ_{23} are obtained from analysis of the $\nu_\mu \rightarrow \nu_e$ and $\bar{\nu}_\mu \rightarrow \bar{\nu}_e$ oscillations in the form, $\sin^2 2\theta_{23} \sin^2 2\theta_{13}$ as was shown in § 1.7. The analysis of neutrino and anti-neutrino oscillations, that is, $\nu_\mu \rightarrow \nu_e$ vs. $\bar{\nu}_\mu \rightarrow \bar{\nu}_e$ helps to determine the sign of the $|\Delta m_{32}^2|$ and the δ_{cp} parameters. The mass hierarchy is explained in § 1.5.1 can be resolved by determining the sign of the parameter $|\Delta m_{32}^2|$. The sign of $|\Delta m_{32}^2|$ can be measured from the matter effects due to ν_e and $\bar{\nu}_e$ traveling long distances through the Earth.

1.9.1 Measurement of the $\sin^2 \theta_{23}$

The current measurements of the $\sin^2 \theta_{23}$ parameter come from the atmospheric and long-baseline accelerator-based neutrino experiments. The primary cosmic rays are highly energetic particles composed of protons, helium, some fraction of electrons, positrons and various stable nuclei up to iron. The interaction of the primary cosmic ray particles with the upper atmosphere of the Earth produces secondary cosmic ray which consists of hadrons, pions and kaons. The pions and kaons decay to produce cascades of muons and neutrinos,

$$\begin{aligned}\pi^+ &\rightarrow \mu^+ + \nu_\mu, \\ \pi^- &\rightarrow \mu^- + \bar{\nu}_\mu.\end{aligned}\tag{1.30}$$

The muons which decay before hitting the Earth's surface produce electrons and electron-neutrinos,

$$\begin{aligned}\mu^+ &\rightarrow e^+ + \nu_e + \bar{\nu}_\mu, \\ \mu^- &\rightarrow e^- + \bar{\nu}_e + \nu_\mu.\end{aligned}\tag{1.31}$$

The muon-neutrinos and electron-neutrinos produced from the collision of cosmic rays with the atmosphere constitute the atmospheric neutrino data. The Super-Kamiokande [2] experiment in Japan, analyzed the atmospheric neutrino data for $\nu_\mu \rightarrow \nu_\mu$ oscillations and finds the best fit value for $\sin^2 \theta_{23} = 0.588_{-0.064}^{+0.031}$. Unlike atmospheric neutrino experiments, the long-baseline accelerator-based experiments use a high energy beam of proton to strike a fixed target to produce hadrons, for example, pions and kaons. The pions and kaons decay in flight to produce beams of muon-type neutrinos or anti-neutrinos as explained in equation 1.30. The accelerator-based experiments analyze $\bar{\nu}_\mu \rightarrow \bar{\nu}_\mu$ to the measure $\sin^2 \theta_{23}$ parameter. The Tokai to Kamioka (T2K) [3] long-baseline accelerator experiment in Japan measures $\sin^2 \theta_{23} = 0.550_{-0.090}^{+0.050}$. The NuMI Off-axis ν_e Appearance (NOvA) [4] experiment in the U.S.A. measures $\sin^2 \theta_{23} = 0.560_{-0.04}^{+0.04}$. A global fit [27] to the combined atmospheric and long-baseline accelerator-based neutrino data gives $\sin^2 \theta_{23} = 0.582_{-0.019}^{+0.015}$. Results from experiments and the global fit to the neutrino data are consistent with maximal $\sin^2 \theta_{23}$, that is, $\sin^2 \theta_{23}$ close to 0.50 or the θ_{23} mixing angle value close to 45° .

1.9.2 Measurement of the $|\Delta m_{32}^2|$

The atmospheric and the accelerator-based neutrino experiments also measure values of the $|\Delta m_{32}^2|$ parameter by fitting $\bar{\nu}_\mu \rightarrow \bar{\nu}_\mu$ oscillation data. The Super-Kamiokande [2] experiment measures $|\Delta m_{32}^2| = 2.50 \times 10^{-3} eV^2$. The T2K [3] experiment used both the neutrino and anti-neutrino disappearance, $\bar{\nu}_\mu \rightarrow \bar{\nu}_\mu$ oscillations to measure $|\Delta m_{32}^2| = 2.54 \times 10^{-3} eV^2$. The NOvA [4] experiment used the neutrino oscillations in the disappearance channel, that is, $\nu_\mu \rightarrow \nu_\mu$ for measuring $|\Delta m_{32}^2|$ parameter and finds $|\Delta m_{32}^2| = 2.44 \times 10^{-3} eV^2$. The global fit [27] to combined data from atmospheric and accelerator experiments gives $|\Delta m_{32}^2| = 2.525 \times 10^{-3} eV^2$.

1.9.3 Measurement of the $\sin^2 \theta_{13}$

The best fit value of $\sin^2 \theta_{13}$ comes from the reactor neutrino data. The nuclear reactors are abundant sources of the electron anti-neutrinos ($\bar{\nu}_e$). The $\bar{\nu}_e$ produced in the nuclear reactors are detected in the neutrino detectors after they have travelled some distance. The $\bar{\nu}_e \rightarrow \bar{\nu}_e$ survival channel is used to measure the θ_{13} parameter using the $\bar{\nu}_e \rightarrow \bar{\nu}_e$ oscillation probability [28],

$$P_{\bar{\nu}_e \rightarrow \bar{\nu}_e} = 1 - \sin^2 2\theta_{13} \sin^2 \left(\frac{1.27 \Delta m_{31}^2 L}{E} \right). \quad (1.32)$$

The reactor anti-neutrinos after oscillation are detected using inverse beta decay process,

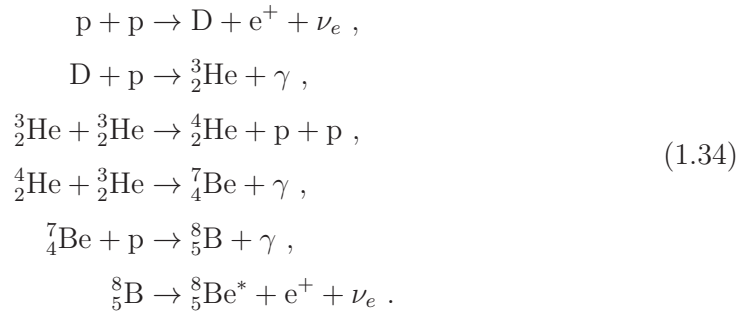
$$\bar{\nu}_e + p \rightarrow e^+ + n. \quad (1.33)$$

The Daya Bay reactor neutrino experiment [29] in China, uses six nuclear plants of the Ling Ao and Daya Bay nuclear plant facility as sources of $\bar{\nu}_e$ and eight anti-neutrino detectors to detect $\bar{\nu}_e$ after they have travelled from the source. The Daya Bay experiment makes measurements of the anti-neutrino oscillations of $\bar{\nu}_e \rightarrow \bar{\nu}_e$ and find the best fit value of $\sin^2 \theta_{13}$ parameter. The value measured is $\sin^2 \theta_{13} = 0.0215$, that is, $\theta_{13} = 8.43^\circ$. The Double Chooz [28] reactor neutrino experiment in France the uses Chooz nuclear power plant facility as source of $\bar{\nu}_e$ and a set of two detectors to detect $\bar{\nu}_e$ after $\bar{\nu}_e \rightarrow \bar{\nu}_e$ oscillations. The Double Chooz experiment finds $\sin^2 \theta_{13} = 0.023$ which gives the value of the mixing angle, $\theta_{13} = 8.73^\circ$. The Reactor Experiment for Neutrino Oscillation (RENO) [30] in South Korea uses six nuclear power reactors in the Hanbit Nuclear Power facility as source of $\bar{\nu}_e$ and a set of two

detectors to detect $\bar{\nu}_e$ after $\bar{\nu}_e \rightarrow \bar{\nu}_e$ oscillations. The RENO experiments find the best fit value of the $\sin^2 \theta_{13} = 0.022$ or mixing angle, $\theta_{13} = 8.53^\circ$. Finally the global fit [27] to the combined data from reactor experiments finds $\sin^2 \theta_{13} = 0.0224$ and $\theta_{13} = 8.61^\circ$.

1.9.4 Measurement of the $\sin^2 \theta_{12}$ and Δm_{21}^2

The best fit values of the $\sin^2 \theta_{12}$ and Δm_{21}^2 parameters come from the analysis of the solar neutrino data. The Sun is the most abundant source of electron-neutrinos in our Solar system, ν_e , which are produced during various nuclear reactions in the core of the Sun. The most important ones are the neutrinos from the proton-proton (pp) and 8-Boron (^8B) reactions,



The ν_e produced in the pp reactions are of lower energy having $E < 0.42$ MeV [31] and constituent 91% of the total solar neutrino flux. The low energy of the ν_e from the pp reaction make it difficult to detect them. Most of the solar neutrino experiments focus on detecting the flux of ν_e from the ^8B reaction which constituents less than 1% of the total neutrino flux but have energies around 14 MeV [32]. Figure 1.8 shows the flux of the ν_e from different nuclear reactions in Sun.

The solar neutrinos, ν_e , can oscillate either to ν_μ or ν_τ on their way from Sun to the Earth. The surviving ν_e from the Sun are used to find the values of the solar mixing angle, θ_{12} and mass-squared difference term, Δm_{21}^2 . The ^8B solar neutrino flux is detected using electron scattering. The Super-K detects the surviving ν_e from the sun. The ν_e surviving probability [19] is given by,

$$P_{\nu_e \rightarrow \nu_e} = 1 - \sin^2 \theta_{12} \cos^4 \theta_{13} \sin^2 \left(\frac{\Delta m_{21}^2 L}{4E} \right) . \tag{1.35}$$

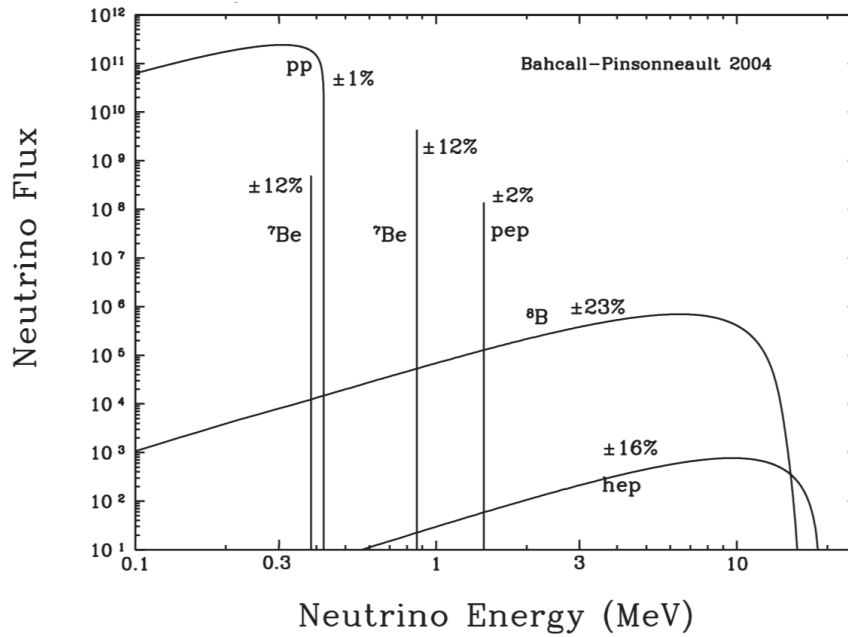


FIGURE 1.8: The solar neutrino flux from different nuclear reactions in the Sun is shown as a function of neutrino energies. The percentages shown near neutrino spectrum from different nuclear reactions represent the uncertainty in the neutrino fluxes. Image from [31].

The Super-Kamiokande experiment fits the solar data and finds $\sin^2 \theta_{12} = 0.334$, that is, $\theta_{12} = 35.30^\circ$. The Global fit [27] to data from various solar neutrino experiments finds $\sin^2 \theta_{12} = 0.310$, or $\theta_{12} = 33.82^\circ$ and mass-squared difference, $\Delta m_{21}^2 = 7.39 \times 10^{-5} \text{eV}^2$. The Particle Data Group (PDG) [33] finds $\Delta m_{21}^2 = 7.37 \times 10^{-5} \text{eV}^2$.

Table 1.1 summarizes the current values of the oscillation parameters from global fit [27] to the combined data from various atmospheric, reactor, solar and accelerator neutrino oscillation experiments.

1.10 Open Challenges

A number of questions remain unanswered related to the oscillation of neutrinos from one flavor to another. The most important ones are questions related to the CP violating phase (δ_{cp}), the sign of the $|\Delta m_{32}^2|$, that is, the ordering of the masses of the neutrinos and the octant of the θ_{23} parameter.

Parameters	Best fit values
$\Delta m_{21}^2 (10^{-5} \text{eV}^2)$	7.39
$ \Delta m_{31}^2 (10^{-3} \text{eV}^2) $ (NH)	2.525
$ \Delta m_{31}^2 (10^{-3} \text{eV}^2) $ (IH)	-2.512
$\sin^2 \theta_{12}$	0.310
θ_{12}°	33.82°
$\sin^2 \theta_{23}$ (NH)	0.582
θ_{23}°	49.70°
$\sin^2 \theta_{23}$ (IH)	0.582
θ_{23}°	49.70°
$\sin^2 \theta_{13} (10^{-2})$ (NH)	2.240
θ_{13}°	8.61°
$\sin^2 \theta_{13} (10^{-2})$ (IH)	2.263
θ_{13}°	8.65°

TABLE 1.1: The current values of neutrino oscillation parameters are summarized from the global fit [27] to the data from various reactor, solar, atmospheric and accelerator neutrino experiment. Values of parameters which are sensitive to the choice of hierarchy are also presented by NH for normal hierarchy and IH for inverted hierarchy of neutrino masses.

1.10.1 CP Violating Phase, δ_{cp}

The long-baseline experiments play an important role in measuring the values of the CP violating phase, δ_{cp} . The difference in matter effects on the ν_e compared to the $\bar{\nu}_e$ oscillations in the $\nu_\mu \rightarrow \nu_e$ and $\bar{\nu}_\mu \rightarrow \bar{\nu}_e$ channels helps to measure the δ_{cp} parameter. Long-baseline experiments can easily change the polarity of their beams to produce neutrino and anti-neutrino beams and hence are used in study of CP violation. The Super-Kamiokande [2] experiment measures $\delta_{cp} = 1.33\pi$ assuming normal hierarchy at 90% C.L. The T2K [3] experiment excludes δ_{cp} values of 0 or π at 90% confidence level (C.L.), that is, the exclusion of CP conservation at 90% C.L. The allowed values of δ_{cp} by T2K at 90% C.L. are $-0.94\pi \leq \delta_{cp} \leq -0.14\pi$ for NH and $-0.47\pi \leq \delta_{cp} \leq 0.40\pi$ for the IH. NOvA [4] finds the best fit value for $\delta_{cp} = 1.21\pi$ and the 68% C.L. at $0 \leq \delta_{cp} \leq 0.12\pi$ and $0.91 \leq \delta_{cp} \leq 2\pi$ for the

NH. There are several allowed values of the δ_{cp} parameter from different experiments including the CP conservating value of 0 or π . The precise value of δ_{cp} still remains an open challenge.

1.10.2 The Neutrino Mass Ordering

The ordering of the neutrino masses is another unsolved puzzle. Again the long-baseline experiments play an important role in the determination of the ordering. The Super-Kamiokande experiment slightly prefers normal mass hierarchy and disfavors inverted mass hierarchy at 93% C.L. [2]. The T2K experiment too has a weak preference for the normal ordering of neutrino masses [3]. The NOvA experiment [4] disfavors inverted hierarchy at 95% C.L, that is, at 2σ level. The global fit [27] also slightly hint towards normal ordering and disfavors inverted ordering at more than 3.4σ confidence level. Though most of the experiments have slight preference for the normal ordering of the neutrino masses, the ordering of neutrino masses still remains an open question.

1.10.3 Octant of θ_{23}

The value of $\sin^2 \theta_{23} = 0.5$, that is, the mixing angle, $\theta_{23} = 45^\circ$ is called the maximal mixing. The maximal value of θ_{23} implies that the ν_μ and ν_τ flavors have equal admixture in the ν_3 neutrino mass eigenstate. If $\sin^2 \theta_{23} < 0.5$ then the θ_{23} is said to lie in the lower octant and if $\sin^2 \theta_{23} > 0.5$ then the θ_{23} is in the upper octant. Some of the long-baseline experiments show that the $\sin^2 \theta_{23}$ value is consistent with maximum mixing as explained in § 1.9.1. The possibility of θ_{23} to fall in either of the octants is also under 1σ confidence levels. The precise value of θ_{23} and thus its octant remains unanswered and needs to be determined which is important for the neutrino mixing symmetries [34].

Chapter 2

The NOvA Experiment

The NuMI Off-axis ν_e Appearance experiment (NOvA), is an accelerator-based long-baseline neutrino experiment, designed to study the oscillations of muon neutrinos and anti-neutrinos. It uses two detectors and a beam of muon neutrinos produced by the Fermi National Accelerator complex, situated in Batavia, IL, U.S.A. NuMI itself is an acronym, standing for Neutrinos from the Main Injector which is Fermilab's flagship accelerator.

This chapter draws most of its information from the NOvA Technical Design Report (TDR) [35].

The NOvA Near Detector (ND) is located 100m underground at a distance of 1 km from the neutrino source within the Fermilab complex, whereas the Far Detector (FD) is located on the surface of the Earth, at a distance of 810 km in Ash River, MN, U.S.A. Since the FD is situated on the surface of the Earth with a very shallow overburden, equivalent to 3.2 meter of water, it is constantly exposed to cosmic ray muons.

The ND detects the beam neutrinos before they have chance to oscillate while the FD detects neutrinos after they have oscillated. Being on the surface, the FD also collects the cosmic ray data. Figure 2.1 [36] shows the locations of the ND and the FD on a geographical map. Neutrino oscillations can be observed through ν_μ disappearance and the ν_e appearance. The FD at a distance of 810 km from the target sits at the first maximum for ν_μ disappearance which implies that the ν_μ to ν_e oscillations are also at a maximum at the FD location. NOvA is a second generation

long-baseline neutrino oscillation experiment at Fermilab. The MINOS experiment [37] was the first generation long-baseline accelerator-based experiment at Fermilab and finished taking data in May 2018.



FIGURE 2.1: Locations of the NOvA Near and Far Detectors are shown on a geographical map. The Near Detector is located at the Fermilab site whereas the Far Detector is located in Ash River, Minnesota (MN). Images from [36].

The NOvA collaboration consists of more than 240 scientists, engineers and Ph.D. students from about 50 institutions in Brazil, Colombia, the Czech Republic, India, Russia, the United Kingdom and the United States of America. The experiment receives support from the U.S. Department of Energy, the U.S. National Science Foundation, the Department of Science and Technology, India and funding agencies of other participating countries.

The ND construction finished in August 2014 and the FD construction finished in October 2014. Since then both the detectors have continuously collected data.

The ND, is constructed as identical in structure to the FD as possible. Its function is to predict the expected rate of event types and their energy spectra in the FD in

absence of oscillation. Differences seen between the events in the two detectors are attributed to oscillations.

The ND measures the neutrino content of the beam at Fermilab, characterizes the detector response to neutrino events, and helps in performing crucial background studies. The NOvA detectors are optimized to observe electromagnetic (EM) showers from the interactions of ν_e in the detector. The neutrino beam spectra at the Near and Far Detectors are not identical, because the ND sees a line source being 1 km from the target, while the FD sees a point source from 810 km.

2.1 The Fermilab Accelerator Complex

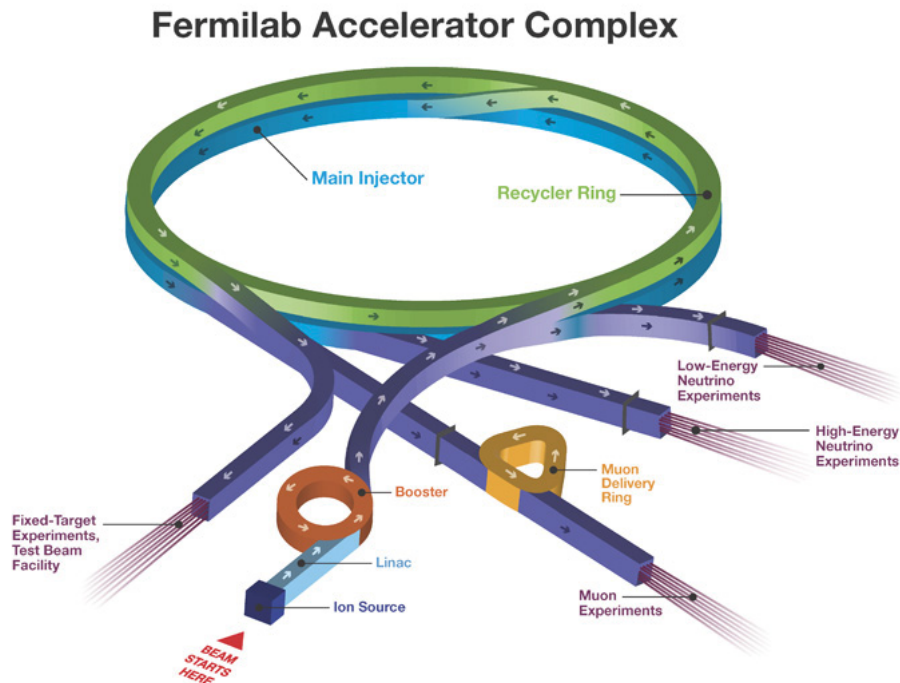


FIGURE 2.2: Fermilab accelerator complex consists of linear and circular accelerators. Image from [38].

A picture of Fermilab's accelerator complex is shown in Figure 2.2. This section draws its information from a number of sources [35], [38], [39], [40], [41] and [42].

The 120 GeV beam of protons is produced using Fermilab's accelerator complex. The complex provides beam for various neutrino experiments including NOvA [43], MINERvA [44], MicroBooNE [45], Muon g-2 [46], Mu2e [47] etc. The complex has two main circular accelerators, the Booster and the Main Injector (MI). The Booster produces a 8 GeV low energy proton beam for low energy neutrino experiments, for example, MiniBooNE and MicroBooNE. The MI produces a 120 GeV proton beam for high energy neutrino experiments, such as NOvA and MINERvA.

The acceleration process starts at the Ion Source (IS) where H^- ions are produced from hydrogen gas. The H^- ions are first accelerated to 35 keV energy and are passed to the Radio Frequency (RF) cavity where H^- ions are accelerated to 750 keV by the electrostatic field in the RF cavity. The 750 keV H^- ions are fed into a linear accelerator (LINAC). The LINAC is a straight line accelerator of about 150 m length. It accelerates H^- beam from 750 keV to 400 MeV energy using a series of oscillating electric potentials and provides input to the Booster. The electrons from H^- ions are stripped off by passing them through carbon foils before they are passed to the Booster. The H^- ions become H^+ ions or protons after the electrons are stripped off. The 400 MeV protons are injected into the Booster.

The Booster is a circular accelerator with a 452m circumference. The Booster uses a series of RF cavities to accelerate protons from 400 MeV to 8 GeV energy. The Booster provides input to the Recycler Ring (RR) which is a storage ring and makes batches of protons to increase the beam intensity. Each batch contains about 4×10^{12} protons. The circumference of the RR is about 3.3km, approximately seven times the circumference of the Booster. Six batches of protons are transferred from Booster to the RR. The six batches of protons are decelerated in the RR to a lower momentum orbit by reducing the frequency of the RF cavities. Since the diameter of the RR is about 7 times compared to the Booster, a seventh batch of protons can be introduced in the RR. The momentum difference of the seventh batch and the first six batches make them to slip azimuthally in a different momentum orbit with respect to each other such that the RF keeps them packed and the process is called slip-stacking [42]. Before the next injection of a proton batch happens from Booster to the RR, the seventh batch aligns itself azimuthally to the sixth batch. The process of slip-stacking is repeated until there are 12 batches. The slip-stacking process is used to increase the intensity of the proton beam.

Twelve batches of protons produced by the slip-stacking process makes a single spill of protons and contains about 5×10^{13} protons. The beam from the RR is extracted to the MI, which accelerates the beam from an energy of 8 GeV to 120 GeV, by using a series of RF cavities at 53 MHz frequency. A spill of 5×10^{13} protons lasts for about $10\mu\text{s}$ in the MI. The duty cycle of the MI is 1.3 seconds and maintains the time difference between consecutive spill to be same as the 1.3 seconds duty cycle time. Finally proton beam in spills, where each spill is $10\mu\text{s}$ long and consecutive spills are 1.3 s apart is delivered to the NOvA target to produce beam of neutrino for the experiment.

2.2 The NuMI Beam

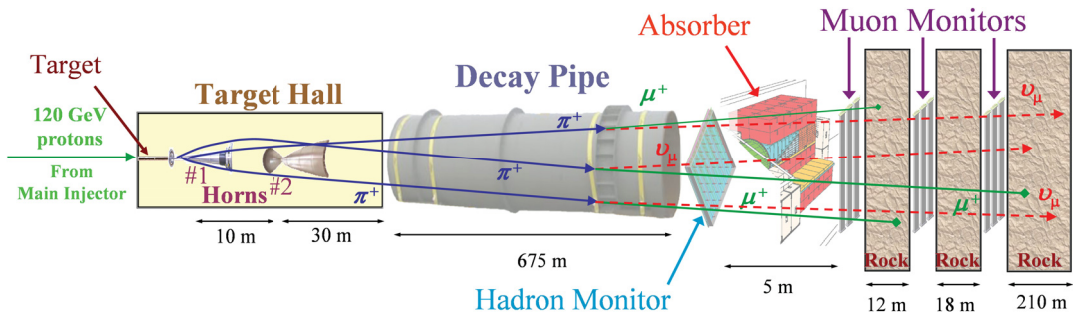


FIGURE 2.3: Production of neutrino beam using a beam of 120 GeV protons from the Main Injector is shown. The neutrino beam is used by the NOvA experiment for the neutrino oscillation studies. Image from [35].

Figure 2.3 shows the pictorial representation of the neutrino beam production with NuMI. This section gives a summary of the NuMI beamline and more information can be found in NOvA TDR [35]. The 120 GeV protons from the MI strike a fixed neutrino target. The neutrino target is made of a series of graphite fins enclosed within a stainless steel pipe. A couple of graphite fins were replaced by berilium fins during the last 18% of the data collection. This change from graphite to berilium made negligible difference in the neutrino flux. In total, the target is 0.95 meter-long and corresponds to ~ 1.8 pion interaction lengths in graphite [48]. The length of the target is sufficient for interactions of majority of the incoming protons from the beam and also avoids absorption of the low energy pions due to the structure of the target. The collision of the proton beam and the graphite target produces pions and kaons. The charged pions and kaons are focused into a thin beam by

using a set of two, nickel plated aluminium magnetic horns, parabolic in shape, each about 3m long and pulsed at 200 kA current. The beam of pions and kaons are directed through an evacuated decay pipe of 675m in length and 2m in diameter. In the decay pipe, the pions and kaons decay to produce muons and muon neutrinos, $\pi^+ \rightarrow \mu^+ + \nu_\mu$ and $K^+ \rightarrow \mu^+ + \nu_\mu$. The remaining protons and mesons are absorbed in the hadron absorber made of concrete with a water cooled aluminium core. The 240m of Earth shielding, which separates the absorber and the ND Hall, absorbs the muons from the pion and kaon decays. Once the muons are absorbed we are left with a beam of muon neutrinos. The ν_μ CC interactions of ν_μ in the rock can produce μ . To produce a beam of muon anti-neutrinos ($\bar{\nu}_\mu$), the polarity of the magnetic horn current is changed to a negative value. The negative polarity of the magnetic horn current focuses the π^- and K^- which decay to produce beams of anti-neutrinos by following the same process as described above.

2.3 The Off-Axis Concept

The NOvA experiment uses the off-axis concept which leads to production of a narrow, nearly monoenergetic flux of neutrinos as seen by the NOvA detectors. Both the ND and the FD are placed such that the center of the detectors are approximately 14.6 milli-radians off-axis from the NuMI beam direction. For a muon neutrino produced in the reaction, $\pi^+ \rightarrow \mu^+ + \nu_\mu$, the energy of the neutrino (E_ν) at an off-axis angle, θ is given by [49]

$$E_\nu = \frac{2\gamma}{1 + \gamma^2\theta^2} \times E_{cm}, \quad (2.1)$$

where γ is defined by the ratio of the pion energy to the rest mass of pion, that is, $\gamma = \frac{E_\pi}{m_\pi}$ and E_{cm} is the center of mass neutrino energy in the rest frame of the pion given by [49]

$$E_{cm} = \frac{m_\pi}{2} \left(1 - \frac{m_\mu^2}{m_\pi^2} \right). \quad (2.2)$$

Combining the definition of γ and E_{cm} , the neutrino energy is given by

$$E_\nu = \left(1 - \frac{m_\mu^2}{m_\pi^2} \right) \frac{1}{1 + \gamma^2\theta^2} \times E_\pi, \quad (2.3)$$

where $m_\mu = 105.66$ MeV and $m_\pi = 139.57$ MeV are the rest masses of the muon and pion. Substituting the masses of the muon and pion, the muon neutrino energy from the decay of pion comes to

$$E_\nu = \frac{0.43E_\pi}{1 + \gamma^2\theta^2}. \quad (2.4)$$

The energy of muon neutrino as a function of pion energy for different values of the off-axis angles is shown in Figure 2.4.

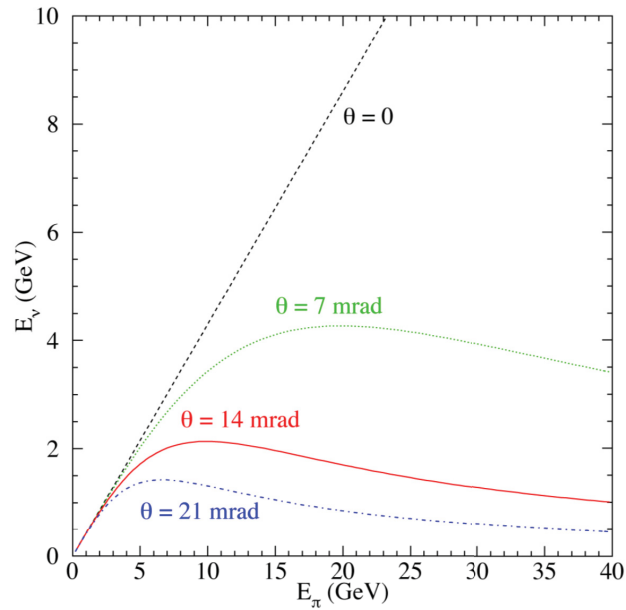


FIGURE 2.4: This figure shows the energy of the neutrinos produced at an angle θ , relative to the pion direction. For maximum oscillation sensitivity of ν_μ 's to ν_e 's, NOvA uses off-axis angle of $\theta = 14.6$ milli radian [35].

The simulated neutrino energy spectra at the FD for various values of the off-axis angles compared to the on-axis case are shown in Figure 2.5. The detector location at 14.6 milli-radians off-axis gives a narrow neutrino energy spectrum peaked at 2 GeV.

The flux of neutrinos at an off-axis angle θ , at a distance L from the neutrino source, in a detector of area A , is given by [35]

$$F_\nu = \left(\frac{2\gamma}{1 + \gamma^2\theta^2} \right)^2 \frac{A}{4\pi L^2}, \quad (2.5)$$

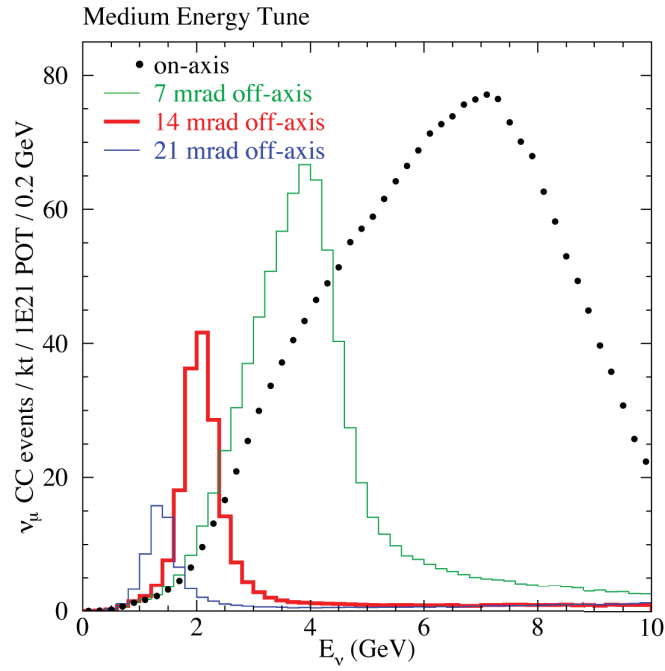


FIGURE 2.5: The simulated neutrino energy spectra at the FD for various values of the off-axis angles compared to the on-axis case. The detectors location at 14.6 milli-radians off-axis gives a narrow neutrino energy spectrum [35].

and is shown in Figure 2.6.

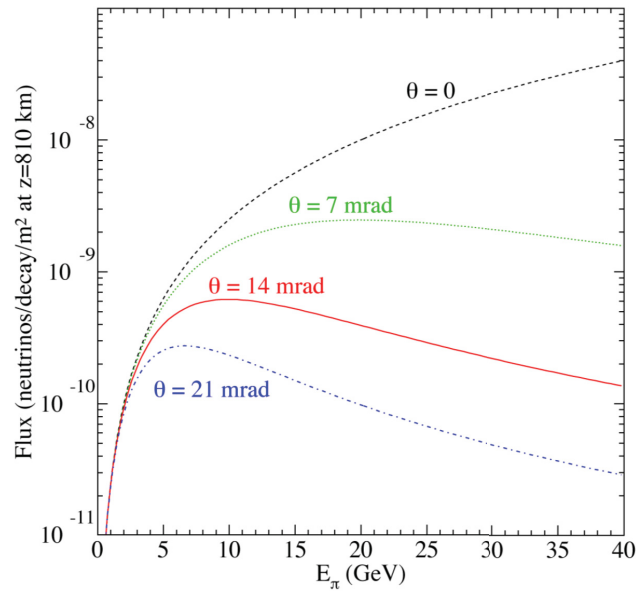


FIGURE 2.6: The figure shows the neutrino flux at a distance of 810 km from pions of energy E_π at an angle θ with respect to the NuMI beam direction [35].

Figure 2.4 shows that at an off-axis angle of 14.6 milli-radians, the neutrino energy does not vary much as function of the energy of the parent pion and the energy of neutrinos remain close to 2 GeV. Figure 2.6 also shows that the flux of neutrinos does not show a strong dependence on the energy of the pions for the 14.6 milli-radians off-axis angle. The narrow beam reduces the high energy neutral current background events from the high energy tail. The narrow beam also helps to distinguish intrinsic ν_e background events from the signal ν_e events. The intrinsic ν_e come from a three body decay of $\mu^+ \rightarrow e^+ + \nu_e + \bar{\nu}_\mu$ and exhibit a broader spectrum as shown by the blue line in Figure 2.7 compared to the signal ν_e events shown by the red shaded region.

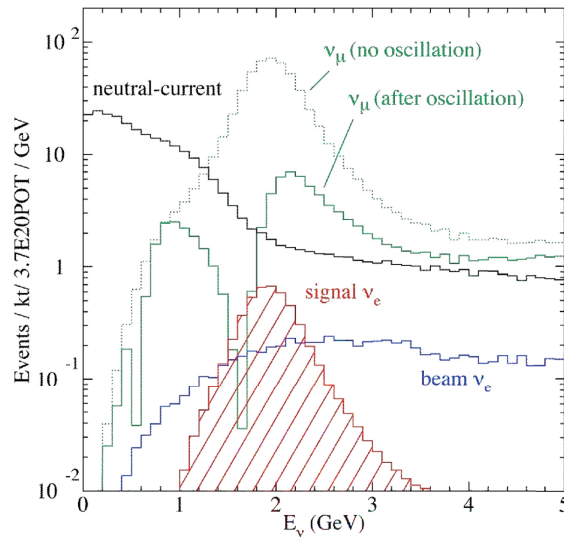


FIGURE 2.7: The figure shows the simulated energy spectrum of the ν_μ CC events with and without oscillations, the NC events, the signal ν_e CC events from $\nu_\mu \rightarrow \nu_e$ oscillations and the intrinsic beam ν_e CC events. The intrinsic beam ν_e events from the three body decay shows a broader energy spectrum compared to the oscillated ν_e CC events. Image from [35].

2.4 Detectors

The NOvA Near and Far Detectors are functionally identical, low density, tracking calorimeters filled with liquid scintillator as the active detector medium. The detectors are made of Polyvinyl Chloride (PVC) extrusions. More details regarding the PVC extrusions is in § 2.4.7. The basic unit of the NOvA detectors is called

a cell and is described in detail in § 2.4.3. The detectors are 65% active by mass and effective for the development of the electro-magnetic showers while rejecting the background events. PVC extrusions are made such that each extrusion has 16 cells. Two such extrusions are glued together to make 1 PVC module containing 32 cells. The PVC modules are glued together to make PVC planes. The ND and the FD are constructed using horizontal and vertical arrangements of the PVC planes. The horizontal and vertical planes give the X and Y coordinates of the energy deposition in a cell by a charge particle. The depth of the detector in the direction of the neutrino beam gives the Z coordinate. This arrangement of horizontal and vertical planes along with the depth of the detectors helps to create 3 dimensional tracks of charged particles traversing through the detectors. Planes in the ND and the FD contains different numbers of PVC modules as explained in the following subsections.

2.4.1 The Near Detector



FIGURE 2.8: The NOvA ND is situated in an underground cavern at Fermilab. Image from [36].

The NOvA ND shown in Figure 2.8 is situated 100m underground in a cavern at Fermilab about 1 km from the NuMI target. The ND consist of two regions. The first is an active region to contain the vertices of neutrino interactions, shown as region A in Figure 2.9 and the second is a muon catcher region to identify and contain muons, shown as region B in Figure 2.9.

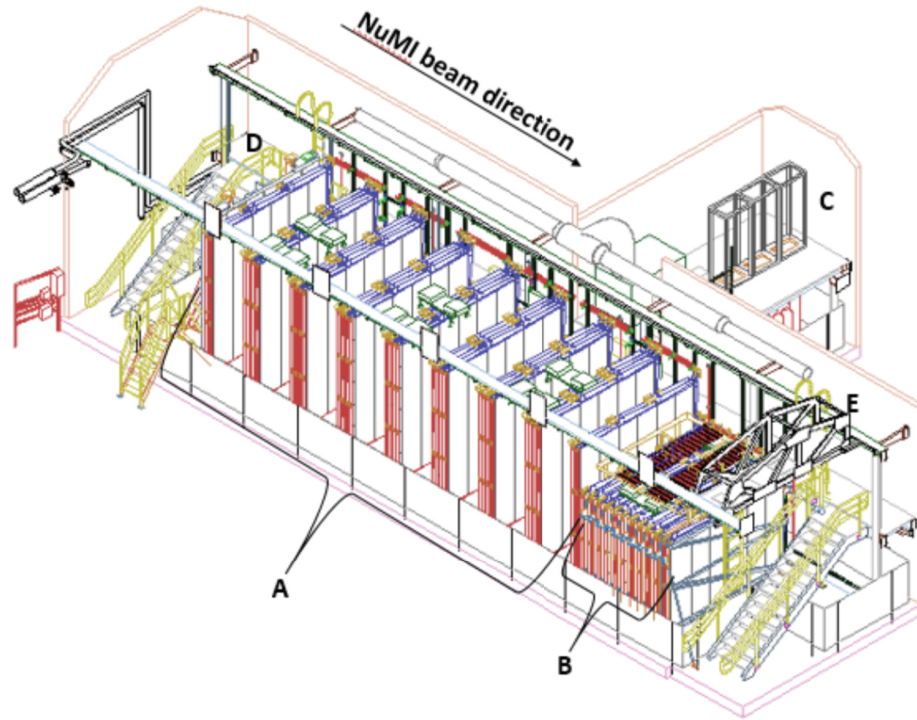


FIGURE 2.9: A schematic of the NOvA ND is shown to display the active and muon catcher regions of the detector. A is the active region, and B is the muon catcher region. The muon catcher region is $\frac{2}{3}$ rd in height to the active region and the same width as the active region. C is the DAQ racks region, D is the stairs and walking area and E is the movable platform. Image from [41]

Each PVC plane in the active region consists of 3 PVC modules which have 96 PVC cells. In total, the active region has 192 such PVC planes containing a total of 18,432 cells. Out of 18,432 cells, half are in the horizontal orientation and the other half are in the vertical orientation. Region B of the ND is the muon catcher region. To contain muons, the muon catcher region consists of 10 planes of stainless steel, each having a thickness of ~ 10 cm and 22 planes of PVC modules as the active detector. The muon catcher region follows the structural sequence of a horizontal plane, a steel plane and a vertical plane. The horizontal planes in the muon catcher region contains only 2 PVC modules which corresponds to $\frac{2}{3}$ rd of the height of the

PVC planes in the active region. The vertical planes in the muon catcher region contains all 3 PVC modules, so that, the muon catcher region has the same width as the active region. The height of the steel planes is also $\frac{2}{3}$ rd of the height of the PVC planes in the active regions and the width the same as the PVC planes in the active region. In total, 192 planes from the active region, 11 horizontal and 11 vertical planes from the muon catcher region makes a total of 20,192 cells. In terms of measurable dimensions, the ND is 15.9m long. It consists of 12.8m of active region and 3.1m of muon catcher region. The width and height of the active region is $4.1\text{m} \times 4.1\text{m}$ and of the muon catcher region is $4.1\text{m} \times 2.7\text{m}$. The shorter height of the muon catcher region is because of 2 PVC horizontal modules unlike 3 modules in the active region. The ND re-uses muon catcher region of the Near Detector on Surface (NDOS) prototype detector which was build before the ND. The NDOS was 3 modules wide and 2 modules tall and hence the muon catcher region of the ND is shorter in height. In terms of mass, the ND is 300 tons out of which 130 tons are the liquid scintillator, 78 tons are steel planes and the remaining 92 tons are PVC.

2.4.2 The Far Detector

The NOvA FD is situated on the surface of Earth, 14.6 milli-radians off the NuMI beam axis, at a distance of 810 km from the NuMI target in Ash River, Minnesota (MN), U.S.A. The FD is a 14 kton structure out of which 65% (9.1 kton) is the liquid scintillator and the remaining 45% (6.3 kton) is PVC. The dimensions of the FD are $15.6\text{m} \times 15.6\text{m} \times 60\text{m}$ (height \times width \times depth). Each FD PVC plane is $15.6\text{m} \times 15.6\text{m}$ (height \times width) and are 6.6cm wide. The length of each FD unit PVC cell is 15.5m. The depth of the FD along the direction of the beam is 60m. The scale of the FD compared to a person can be seen in Figure 2.10. Each FD PVC plane consists of 12 PVC modules or 384 cells. There are in total 896 PVC planes in the FD, out of which 448 are horizontal and the remaining 448 are vertical planes. The FD is assembled in units of blocks, consisting of 32 planes each. Two blocks are combined together to make a single diblock. There are 14 diblocks in the FD which make a total of 344,064 cell units.

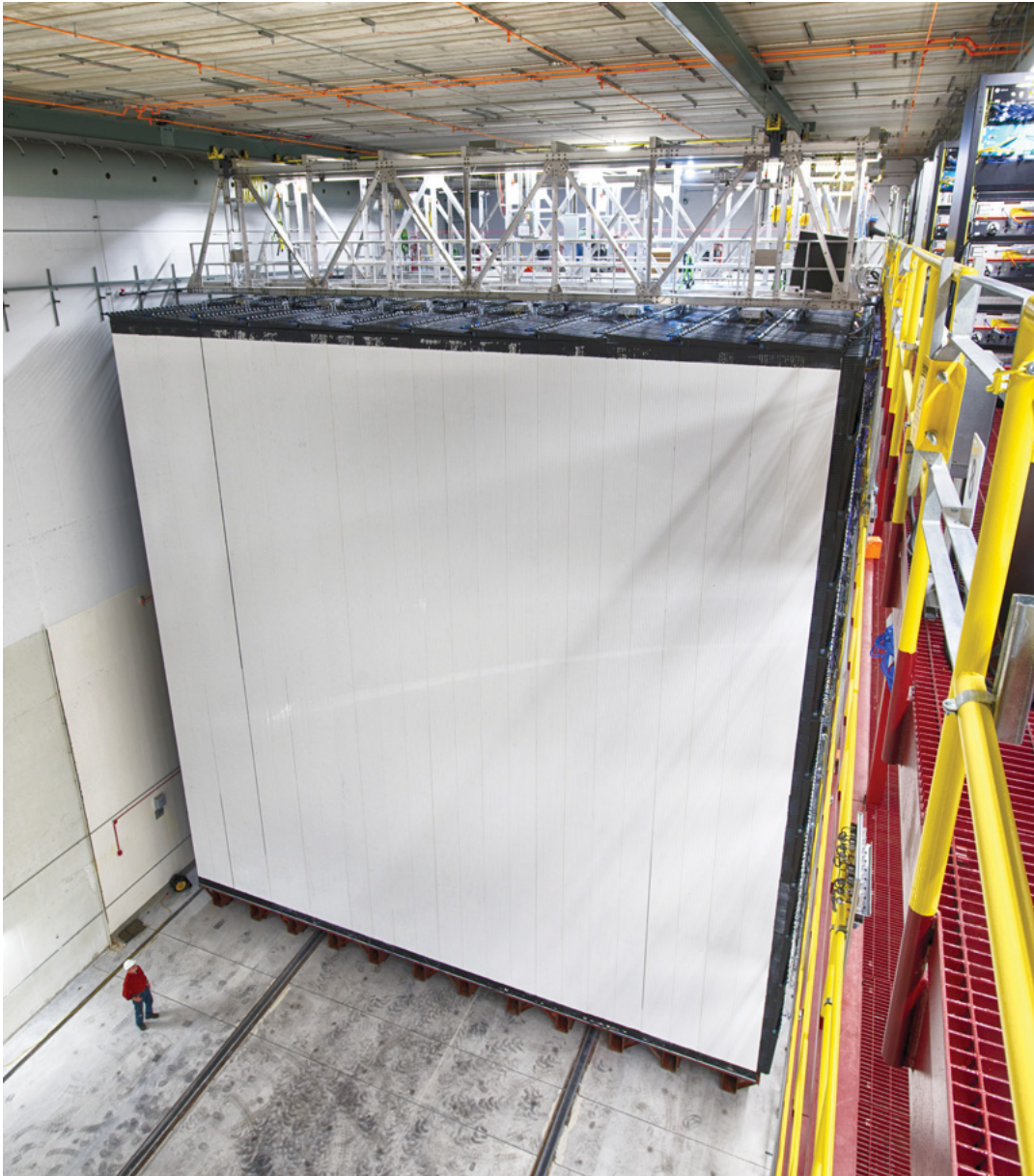


FIGURE 2.10: The NOvA FD situated at Ash River, Minnesota, U.S.A. is shown. The scale of the FD can be seen by comparing it to a person standing next to it, in the bottom left corner of the picture. Image from [36].

2.4.3 The unit cell

As shown in Figure 2.11, the cells are made of white PVC modules, cuboidal in shape and having a cross-sectional area of $3.9\text{cm} \times 6.6\text{cm}$. The 6.6cm side is in the direction of the NuMI beam and is called the depth dimension of the cell. The cells are 15.5m long for the FD and 3.9m for the ND. The cells are the basic units

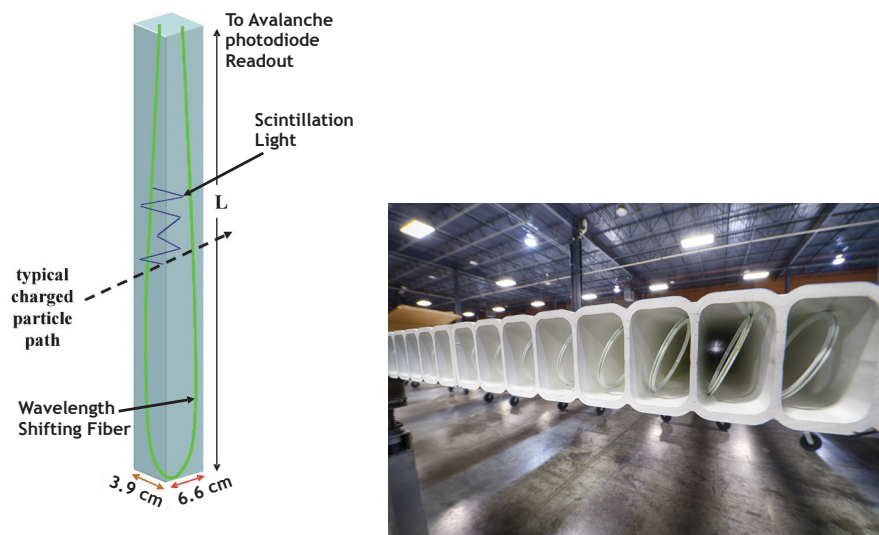


FIGURE 2.11: The left figure shows a cartoon image of a cell [35] and the right figure shows a real image of cells extruded in PVC module [36].



FIGURE 2.12: A small part of the NOvA detector is shown to emphasize the horizontal and vertical orthogonal planes made of the PVC modules.

which are filled with the mineral oil as the solvent for the liquid scintillator. Details about the liquid scintillator used in cells are given in § 2.4.4. Each cell contains an optical fiber which is used to capture the scintillator light signal in the cell and transfers the light to the Avalanche photodiodes (APD), for the conversion of the light signal to electric charge for further processing. Figure 2.12 shows a subsection of the orthogonal horizontal and vertical cells in different planes.

2.4.4 Liquid Scintillator

The NOvA scintillator is made of three major components [50]. First, the scintillating material that emits light in the ultraviolet (UV) region of light spectrum. Second, the wavelength shifting (WS) components to shift the scintillation light from lower to higher wavelength which are required for capture by the optical fiber in the cells. Third, the mineral oil that blends all other components to make scintillator. The main scintillation agent is pseudocumene (1,2,4 - Trimethylbenzene or $C_6H_3(CH_3)_3$) which emits light in the UV range of (270 - 320)nm. The pseudocumene is a flammable, colorless organic compound, which when dissolved in mineral oil works as a scintillator. The output light from the pseudocumene excites the WS PPO (2,5 - Diphenyloxazole or $C_{15}H_{11}NO$). The PPO, 0.11% in mass, is an organic scintillator and is used as a wavelength shifter which shifts light from lower wavelength to higher wavelength so that the WLS fiber can capture high wavelength light. The excited PPO re-emits light in the higher wavelength region of (340 - 380)nm. The output light from the PPO excites bis-MSB (1,4-bis-(o-methyl-styryl)-benzene). The bis-MSB, 0.0016% in mass, is another wavelength shifter used in the liquid scintillator. The bis-MSB emits lights in the higher wavelength range of (390 - 440)nm. Finally the light is captured by the optical fiber in the cell and transported to the APD. An anti-static agent, Stadis-425, is also added to the scintillator at 3ppm level to make scintillator semi-conductive to prevent any potential fire-hazard due to charge buildup. An anti-oxidant agent, vitamin E, is also added to the scintillator mixture to prevent the yellowing of the scintillator, which otherwise degrades the transparency of the scintillator over time.

The NOvA scintillator is approximately 94.91% mineral oil, 4.98% pseudocumene and 0.11% wavelength shifters. Table 2.1 shows the composition of NOvA scintillator by percentage of mass fraction.

2.4.5 Optical Fiber

The NOvA experiment uses S-type Kuraray Y11(200) wavelength shifting fiber (WLS) [35] of 0.7mm diameter for the collection and transfer of light to the APD. The WLS fiber captures the scintillation light in the blue region (400 - 450 nm) and shifts it to higher wavelength green region (490 - 550 nm) using Y11(200) dye as a

Component	Purpose	Mass Fraction
Mineral Oil	Solvent	94.91%
Pseudocumene	Scintillator	4.98%
PPO	Wavelength shifter	0.11%
bis-MSB	Wavelength shifter	0.0016%
Stadis-425	Anti-static agent	0.001%
Vitamin E	Anti-oxidant	0.001%
Total		100.0%

TABLE 2.1: The different components used to make the NOvA scintillator are shown by mass fraction. The main scintillator is pseudocumene. The mineral oil is used as a solvent to blend the scintillator, wavelength shifters and other important agents [50].

wavelength shifting agent. Figure 2.13 shows the absorption and emission spectrum of the NOvA optical fiber.

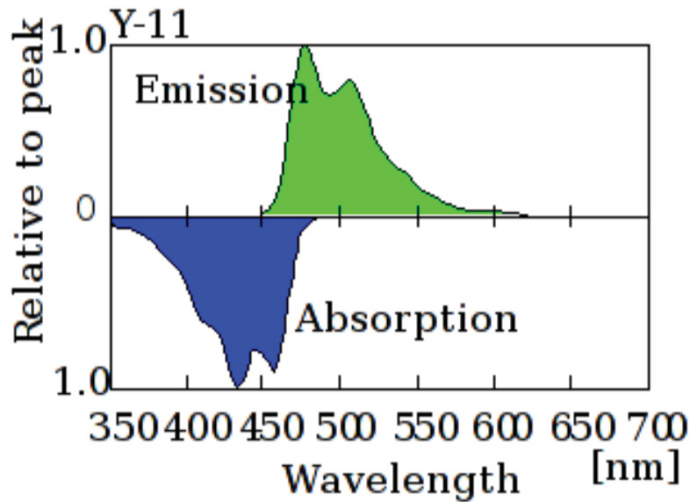


FIGURE 2.13: The figure shows the absorption and emission spectrum of the NOvA optical fiber. The optical fiber captures blue light in the region (400 - 450)nm and shifts it to the green light in the region (490 - 550)nm [35].

The light below 490nm is attenuated in the fiber because of the overlay of the absorption and emission spectrum of the fiber. The length of the optical fibers used is more than twice the length of the NOvA cells and is looped at the bottom of the cell in a U-shape as shown in Figure 2.11. Both ends of the fiber terminates to

a single pixel of the 32 pixel APD. The termination of both ends of the fiber into the same pixel increases the light collection of the optical fiber by roughly twice the amount compared to a single fiber. The optical fiber uses the concept of total internal reflection to transfer light to the APDs. The WLS fiber is a double cladded fiber to protect the fiber core against scintillator penetration [35]. The inner core of the optical fiber is made up of polystyrene of refractive index 1.59. The core is enclosed by an outer cladding which is made up of fluorinated-polymer of lower refractive index 1.42 and inner acrylic cladding of refractive index 1.49.

2.4.6 Avalanche photodiodes

Avalanche photodiodes (APD) are photo sensitive, high speed semi-conductor diodes. The APDs operate in reverse bias mode which helps in the generation of electron multiplication giving rise to the avalanche of electrons. A photon incident on an APD creates an electron - hole pair via the photo-electric effect. The generated electrons under the effect of an electric field are further accelerated and create more electron - hole pairs via ionization giving rise to an avalanche of electrons. NOvA uses a custom variant of the Hamamatsu manufactured S8550 APDs [35]. The APDs are chosen by NOvA for their high quantum efficiency (QE) of 85%. The QE is the ratio of the photoelectrons produced to the incident photons, that is, for every 100 photons, 85 photoelectrons are produced. The QE of the NOvA APDs is uniform over the range of the scintillation light (490 - 550 nm) produced by the WLS fiber. The high QE is required to detect the faint light signal from the far-end of the 15.5m long NOvA cells. The high QE allows detection of a minimum of 20 photoelectrons from the far end of the cells [35]. The noise levels of the APDs are maintained at or around 10 photoelectrons [35].

Figure 2.14 shows the front and back views of an APD mounted on a carrier board. Each APD has an array of 32 pixels to detect the light. The two ends of the optical fiber from each NOvA cell terminate to a single pixel of the APD. The APDs are operated at a temperature of -15° C to keep the noise level down due to the dark currents in the APD. Each APD has its own thermo electric cooler (TEC) unit which maintains a temperature of -15° C. The heat from the TEC is removed using chilled water. All NOvA APDs are operated at a high voltage of around 425 V to maintain a gain of 140.

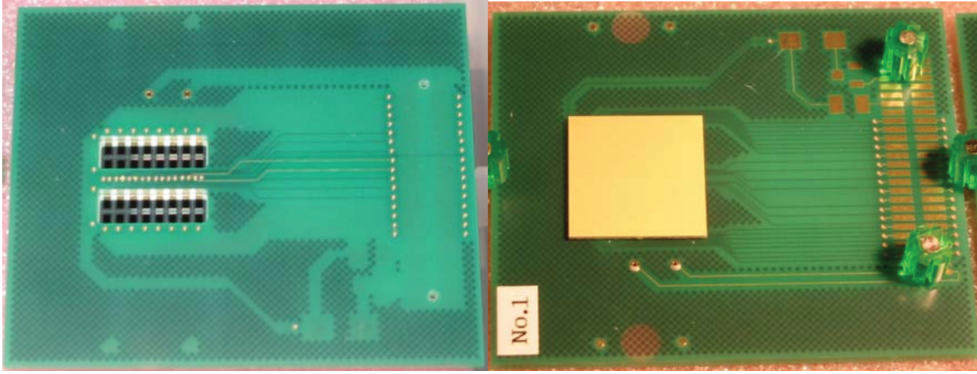


FIGURE 2.14: The figure shows the front (in the left plot) and back (in the right plot) views of the NOvA APD mounted on a board. Each APD has 32 pixels to readin signal from the NOvA cells. Image from [35].

2.4.7 Polyvinyl Chloride (PVC) modules

The PVC modules are the structural units of both NOvA detectors. They provide supportive structure to contain the liquid scintillator. The PVC modules make up nearly 30% of the NOvA detector by mass. A picture of a PVC module is shown in Figure 2.11. The PVC modules are coated with titanium dioxide (TiO_2) which increases the reflectivity of the PVC modules to $\sim 90\%$ [51] for the 430nm wavelength scintillation light from the liquid scintillator. The inner walls of the PVC extrusions between the cells is 3.3mm in thickness and the outer walls to connect two PVC modules is 4.8mm in thickness. The corners of the PVC cells are rounded to reduce the stress on the corners. The PVC extrusions are arranged in a group of 16 cells and two PVC extrusions are glued side by side to make one PVC module of 32 cells. This way each PVC module outputs the signal light to a single APD of 32 pixels. A front end board (FEB) is mounted on one end of each PVC module. The FEB provides the electronic, voltage, APD, cooling units and analog-to-digital converters (ADC) to digitize the signal from APD. A group of 64 FEBs sends signal information to a single data concentrator module (DCM) which stores the signal information for data acquisition.

2.5 Data Acquisition System

This section draws information from [35], [40] and [52]. A brief summary of the data acquisition system (DAQ) is presented here. The electrical pulses (or signal) from

an APD of a 32 cell NOvA module is readout by an FEB, where the signal is time stamped and digitized using an ADC. The digitized electrical signal from 64 FEBs are fed to a single DCM unit as shown in Figure 2.15. In total 168 units of DCM

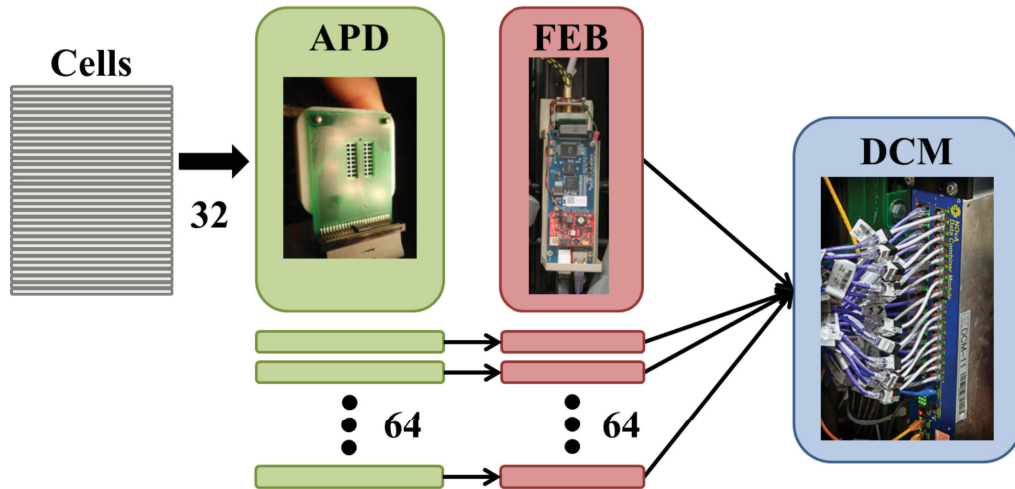


FIGURE 2.15: The NOvA readout chain is shown. The signal from a NOvA module is readout by an APD and is digitized in the FEB by an ADC unit. The digitized signal from 64 FEBs is read by a DCM unit and is transferred to the buffer nodes for storage [52].

are used to readout the data in the FD. The FD has 14 diblocks and each diblock is readout using 12 DCMs. Six of the 12 DCMs are used to read the horizontal planes and other six are used to read the vertical planes. The DCM organizes the data from the FEBs into $5\mu\text{s}$ long time window called micro-slices. The $5\mu\text{s}$ micro-slices are summed up to make 5ms long milli-slices. The DCM transfer the 5ms milli-slices to an array of buffer nodes, such that, the same 5ms milli-slices from all DCMs reaches the same buffer node. The energy deposited in a cell is recorded as a hit with a time stamp, if it is above a certain energy threshold. The master time distribution unit (MTDU) is used to synchronize all NOvA readouts to an external clock which is connected to a high precision global positioning system (GPS) receiver. Fermilab's accelerator network is connected to the MTDU. When a spill happens at Fermilab, the MTDU converts the accelerator time stamp to NOvA time. The spill is transmitted to both the detectors. When the spill is received at the detectors, the buffer nodes start to search the milli-slices for hits in the beam spill time and store the selected hits to permanent storage. The beam spills at the FD are recorded for a $500\mu\text{s}$ time window centered at the beam spill of $10\mu\text{s}$. The NOvA experiment also uses a cosmic activity trigger to record cosmic data for a

$500\mu\text{s}$ time window at a time. The cosmic data is used for the attenuation, energy and timing calibrations, the detector response studies and in the prediction of the cosmic ray background for the oscillation analysis. The ND sees multiple neutrino interactions in a given beam spill. The separation of the hits from different neutrino interactions demand more precise timing resolution in the ND compared to the FD. More details regarding the timing resolution of the ND can be found in [53]. As the FD is located on the surface of Earth and is dominated by cosmic ray data, a series of cosmic rejection selections including containment and low transverse momentum fraction with respect to the NuMI beam direction are used to select neutrino-like events and to reject the cosmic events. The timing distribution of the final events passing the cosmic rejection selections is used to determine the timing peak of the NuMI beam. The beam timing falls in the $10\mu\text{s}$ window from $218\mu\text{s}$ to $228\mu\text{s}$ in a $500\mu\text{s}$ window as shown in Figure 2.16.

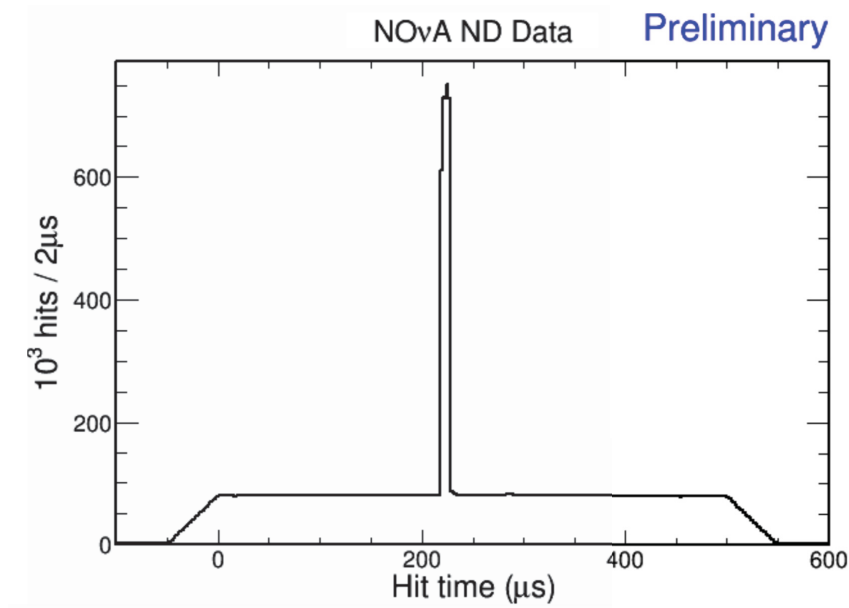


FIGURE 2.16: The NuMI beam timing peak is a $10\mu\text{s}$ long window from $218\mu\text{s}$ to $228\mu\text{s}$ in a $500\mu\text{s}$ readout window [54].

2.6 Trigger

There are two distinct tasks of the NOvA readout system. The first one is to record the activity in the detectors caused by the beam neutrinos. The second task is to

collect cosmic ray events between the beam spills, for calibration and monitoring of the detector. The NOvA experiment has simple detectors and does not demand a complicated trigger system to store interesting events. Details of the NOvA trigger system, described here, are summarized in [35] and [41].

An activity based trigger is not a viable option in case of the NOvA experiment, because the FD is located on the surface of the Earth, exposed to 120 kHz rate of cosmic ray activity and only 1.93×10^{-19} neutrino events per POT in the neutrino mode and 1.05×10^{-19} events per POT in the anti-neutrino mode. Because of very high cosmic ray background rate, it is not possible for the activity based trigger to select neutrino events from cosmic ray backgrounds. To collect the beam neutrinos, the experiment saves 100% of the data at the buffering stage and waits for spill trigger information before making a decision to store events of interest to permanent locations. At Fermilab, the beam spill is time stamped by the NOvA timing system. Both detectors are precisely synchronized before receiving the beam trigger.

The FEB continuously digitizes and time stamps the data in un-triggered mode. The time stamped data collected at the FEB is compared to the NuMI timing to know if an event occurred in or out of the beam spill time. The collected data is held at the buffering locations, provided by the DAQ system, before it is decided to store or reject the data permanently. The data is held for up to 20 seconds at the buffering node while waiting for the spill trigger message from the accelerator time stamp. The spill trigger message must reach the buffering node to match the spill time stamp to the time stamp of the collected data otherwise the data can be lost. There are no other selections applied for the in-spill data. All events occurring in a $500\mu\text{s}$ window centered at the $10\mu\text{s}$ beam spill are stored and recorded. The events collected in the $500\mu\text{s}$ window but outside the $10\mu\text{s}$ beam spill are the cosmic events.

Chapter 3

Acceptance of the NOvA FD using Cosmic Ray Muons

3.1 Introduction

The primary cosmic rays are highly energetic charged particles composed of protons, α -particles, some fraction of electrons, positrons and various stable nuclei up to iron. The charged cosmic ray particles are deflected by the magnetic fields of the galaxies and, the solar system, which results in almost isotropic cosmic ray flux in the outer space. The Earth is constantly bombarded by them. When cosmic rays hit atoms in the upper atmosphere they produce showers of secondary particles consisting pions (π) and kaons (K). The π and K decay to produce muons and neutrinos,

$$\begin{aligned} \pi^+ &\rightarrow \mu^+ + \nu_\mu, & \pi^- &\rightarrow \mu^- + \bar{\nu}_\mu, \\ K^+ &\rightarrow \mu^+ + \nu_\mu, & K^- &\rightarrow \mu^- + \bar{\nu}_\mu. \end{aligned} \quad (3.1)$$

Those muons which decay before reaching to the surface of Earth, produce electrons and electron-neutrinos through following decay processes,

$$\mu^+ \rightarrow e^+ + \nu_e + \bar{\nu}_\mu, \quad \mu^- \rightarrow e^- + \bar{\nu}_e + \nu_\mu. \quad (3.2)$$

Muons are the dominant charged particles at the surface of the Earth from cosmic ray interactions. The FD is located on the surface of the Earth and hence is constantly bombarded with cosmic ray muons from all directions along with π , e^- , γ .

Both NOvA detectors (FD and ND) are calibrated using cosmic-ray muons which stop inside the detector because the energy loss, dE/dx , of stopping muons is very well known from the Bethe-Bloch formula [33]. A 1m window 2m from the end of the stopping muon track in the detector is used for calibration because in this window dE/dx of cosmic ray muon is close to minimum ionizing [55].

The FD sees different numbers of cosmic ray muons in different directions due to the varying thickness of the Earth's atmosphere and the geometry of the detector. The thickness or mass of the Earth's atmosphere increases as we move away from the zenith direction, reaching the highest value along the horizon. Due to the varying thickness of the Earth's atmosphere, the majority of the muons reach the surface of the Earth from the zenith direction. The muon count decreases as we move away from the zenith direction.

The knowledge of detector's capability to accept cosmic ray muons is called its "acceptance". The analysis of the detector's acceptance as a function of zenith angle, θ , and azimuthal angle, ϕ , enable us to optimize the selection of the cosmic ray muons used in the calibration. Fig. 3.1 shows the θ and ϕ directions with respect to an observer at the NOvA FD.

In this chapter, we study quantities that are used to determine the acceptance of the FD. We also describe the procedure to calculate the acceptance and the selection of the cosmic ray sample.

3.2 Projected area

Cosmic ray muons originating from different directions see different projections of the surface of the NOvA FD. Muons coming directly from the zenith ($\theta = 0^\circ$), can only see the top surface of the FD. Similarly, those coming from the horizon can only see the side surfaces. The first step in the acceptance study is to calculate the projected area, which is obtained by taking the dot product of the vector normal to

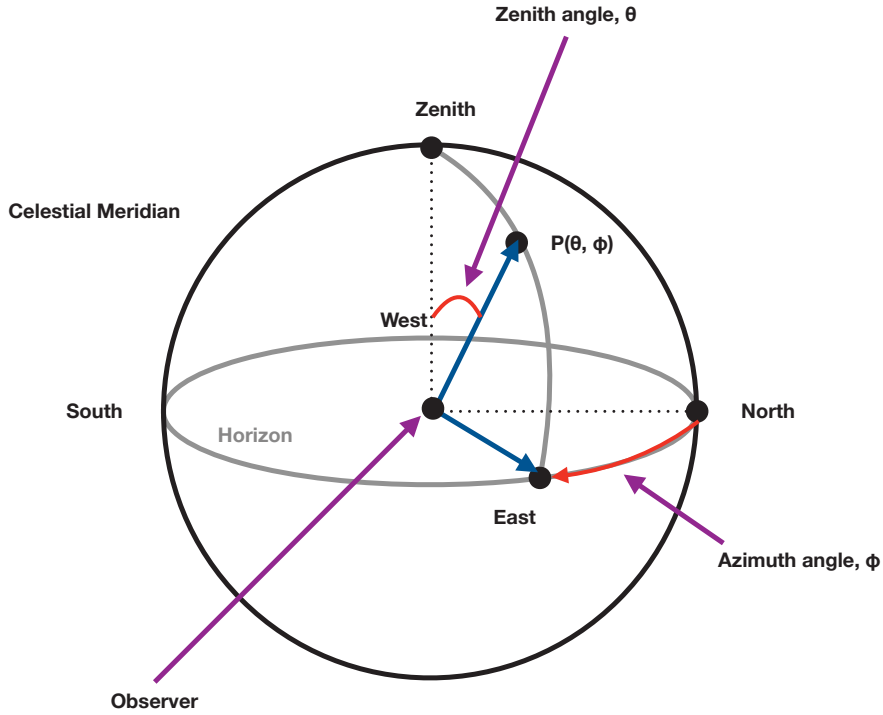


FIGURE 3.1: The zenith, θ , and azimuthal, ϕ , angles for a point $P(\theta, \phi)$ in space with respect to an observer are shown. The angle θ is defined as the angle between the zenith and a line from the observer to the point $P(\theta, \phi)$. The angle ϕ is defined as the angle between the North direction and the line from the observer to point $P(\theta, \phi)$ projected on the horizontal plane in the clockwise direction from North to East.

the detector's surface and the incoming direction of the cosmic ray muon.

$$A_p = \sum_i A_{p,i}(\theta, \phi) = \sum_{s,i} \mathcal{A}_{s,i} \cdot \vec{U}_s \cdot \vec{V}(\theta, \phi),$$

where A_p is the total projected area of the detector, $A_{p,i}(\theta, \phi)$ is the projected area of i^{th} solid angle bin, $\mathcal{A}_{s,i}$ is the area for a given side, \vec{U}_s are the components of the unit vector normal to the surface of the detector for side s and $\vec{V} = (\sin \theta \sin \phi, \cos \theta, \sin \theta \cos \phi)$ are the components of the direction of the momentum of the incoming particle. We do not calculate the projected area for the bottom surface because it is facing the Earth and no cosmic ray muons are entering from the bottom surface of the detector.

The areas of the FD surfaces are shown in Table 3.1. Different surfaces of the FD cover different ranges of θ and ϕ as shown in Table 3.1.

Surface	Area ($\times 10^6 \text{ cm}^2$)	θ°	ϕ°
East	9.233	[0, 180]	[333.45, 153.45]
West	9.233	[0, 180]	[153.45, 333.45]
North	2.400	[0, 180]	[243.45, 63.45]
South	2.400	[0, 180]	[63.45, 243.45]
Top	9.233	[0, 90]	[00.00, 360.00]

TABLE 3.1: Range of θ and ϕ , and area for different surfaces of the NOvA FD. The FD's north surface is 26.55° offset towards west of geographical north, so, the detector's north surface is at $\phi = 333.45^\circ$, the east surface is $\phi = 63.45^\circ$, the south surface is $\phi = 153.45^\circ$ and the west surface is $\phi = 243.45^\circ$.

For the bin by bin calculation of the projected area we plot a 2D histogram of the ϕ angle, on the x-axis and the cosine of the θ angle, that is $\cos(\theta)$, on the y-axis for equal solid angle bins. The $\cos(\theta)$ bins simplify our calculations in terms of the solid angle which is defined as $\sin\theta d\theta d\phi = d(\cos\theta)d\phi$. This study uses 360 bins in the range $0^\circ \leq \phi \leq 360^\circ$ and 100 bins in the range $0 \leq \cos\theta \leq 1$. Here $d(\cos\theta)d\phi$ represents a bin of the $\cos(\theta)$ vs ϕ histogram, hence every bin is a solid angle (α). The α for each bin is 1.75×10^{-4} sr. Each bin of this histogram can be filled with the value of the projected area. The projected area of the FD is shown in Fig. 3.2. The FD's north surface is 26.55° offset towards west of geographical north, so, the detector's north surface is at $\phi = 333.45^\circ$, the east surface is $\phi = 63.45^\circ$, the south surface is $\phi = 153.45^\circ$ and the west surface is $\phi = 243.45^\circ$.

The total projected area of the NOvA FD is $3.75 \times 10^{11} \text{ cm}^2$ which is calculated by adding the projected areas in all solid angle bins. The projected area decreases

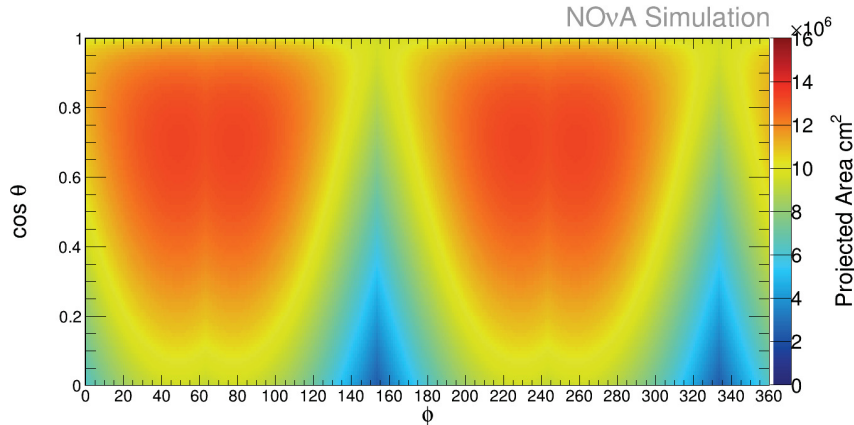


FIGURE 3.2: The projected area of the NOvA FD as a function of $\cos \theta$ and ϕ .

near $\phi = 153.45^\circ$ and $\phi = 333.45^\circ$ as these are the detector's south and north surfaces respectively and have smaller cross-sections than the east and west surfaces. The projected area also decreases near $\cos \theta = 0^\circ$ because $\cos \theta = 0^\circ$ is the horizon direction and in this direction cosmic-ray muon count rate is very low as explained in § 3.1.

3.3 Detector efficiency and acceptance

The acceptance study is performed using the Monte Carlo sample of cosmic ray muon events in the FD. In total six million cosmic ray muons were generated using the Cosmic-ray Shower Library (CRY) generator [56] and using all 14 di-blocks of the FD.

3.3.1 Efficiency

The probability of detecting and reconstructing a cosmic ray muon is defined as the efficiency, ϵ . It is calculated by taking the ratio of the number of muons passing a particular selection criterion to the total number of muons seen by the detector in a given solid angle. The following selection criteria have been applied to find the efficiency of the NOvA FD. The effect of each of the selection requirement on the

number of muons is described in Table 3.2.

Selection Name	Number of muons passing cumulative cuts	efficiency (ϵ) %
All Muons	6211475	100
Track Z Length	5754597	92.6
$\cos(\theta)$	5036713	81.1
Entering Muon	3466460	55.8
Good Step	3360646	54.1
Stopping Muons	1278882	20.6

TABLE 3.2: Selection criteria used to select Monte Carlo sample for NOvA FD acceptance study.

Here “All Muons” imposes no selection criterion on the number of muons seen by the detector. This number is used as a denominator in the efficiency calculation.

The “Track Z Length” selection requires that the difference between the start point and the end point of the cosmic ray muon track should be greater than 50 cm in the z-direction. This selection makes sure that the track will cross more than 8 NOvA planes. This condition is very important for good reconstruction of the track because the more planes a track crosses the better the lever arm for tracking.

The “ $\cos(\theta)$ ” selection selects only those cosmic ray muon tracks for which $\cos(\theta) < 0.95$ i.e. $\theta > 18^\circ$. This cut avoids those tracks which are coming from near the zenith. The cosmic ray muons that are coming from near the zenith do not cross enough planes in the detector and hence are not reconstructed well. Both “Track Z Length” and “ $\cos(\theta)$ ” requirement removes tracks that do not cross enough planes in the detector but they differ in the sense that the “ $\cos(\theta)$ ” selection removes tracks only coming from near the zenith and the “Track Z Length” selection removes those tracks which are coming from the geographical east and west directions as well.

The “Entering Muon” selection requires the starting point of the cosmic ray muons to be within 10 cm from the edge of the detector. This condition makes sure that the events selected enter the detector, as expected for the cosmic ray muons.

The “Good Step” selection removes a track if it has a few large steps as compared to the rest. A step is defined as the distance between consecutive trajectory points along a track. For every track a distribution of steps is obtained and if the biggest step in the distribution is more than four times the median of the distribution of sizes then the track is rejected. Tracks having a few large step sizes compared to the rest are poorly reconstructed.

The “Stopping Muons” selection selects only those muons which stop in the detector. It requires the end point of the track to be greater than 50 cm from the edge of the detector. Stopping muons are very important for absolute energy calibration of the NOvA detectors because their energy loss, dE/dx , is very well known from the Bethe-Bloch formula [33].

In this study, the above selections from Table 3.2 except “Stopping Muons” selection are collectively defined as the “All Passing Muons” selection. In the following subsections, various acceptance and efficiency histograms are created for “All Passing Muons” and “Stopping Muons” selections.

3.3.1.1 Number of muons as a function of $\cos(\theta)$ and ϕ

For the efficiency calculation, 2D histogram of $\cos(\theta)$ vs ϕ for “All Muons” is made, as shown in Fig. 3.3. Then the selection criteria are applied and again a 2D histogram of $\cos(\theta)$ vs ϕ is made, as shown in Figs. 3.4 and 3.5. The bin by bin efficiency is found from the ratio of the first histogram to the second.

In these plots we can see that there are gaps at around $\phi = 63.45^\circ$ and $\phi = 243.45^\circ$. We also see in these figures that the number of the cosmic ray muons decreases as $\cos(\theta)$ approaches 0, i.e. θ approaches 90° . This effect is enhanced in the case of “All Passing Muons” and “Stopping Muons” because of the selection criteria.

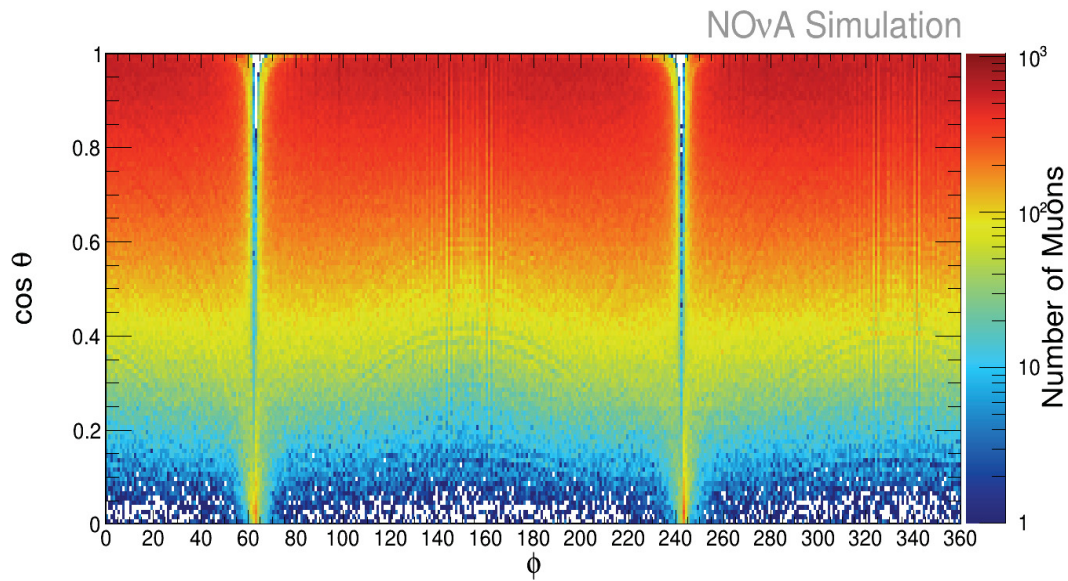


FIGURE 3.3: The number of muons seen by the NOvA FD as a function of $\cos(\theta)$ and ϕ for the “All Muons” (no selection criterion applied).

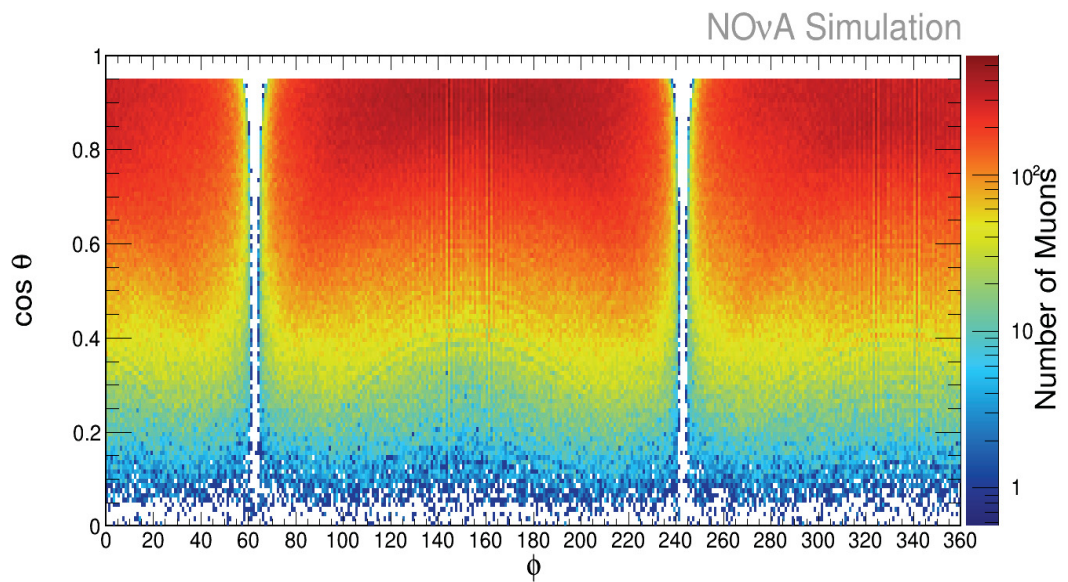


FIGURE 3.4: The number of muons seen by the NOvA FD as a function of $\cos(\theta)$ and ϕ for “All Passing Muons”.

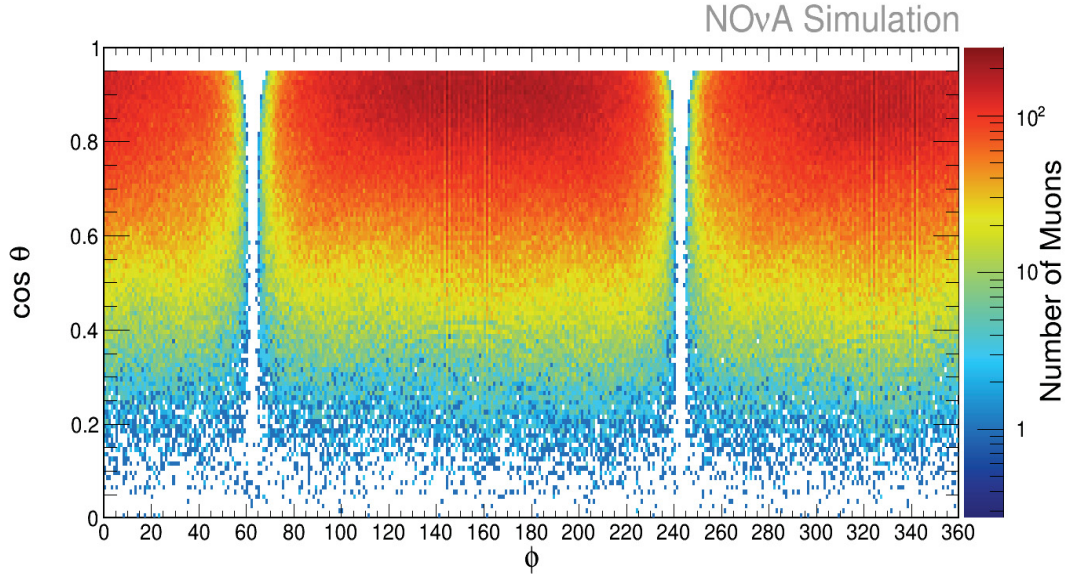


FIGURE 3.5: The number of muons seen by the NOvA FD as a function of $\cos(\theta)$ and ϕ for “Stopping Muons”.

There is a deficiency of the stopping muons for $\cos(\theta) < 0.2$ i.e. $\theta > 80^\circ$ and a high statistics of the stopping muons is observed for $\cos(\theta) > 0.6$ i.e. $\theta < 53^\circ$

3.3.1.2 Efficiency as a function of $\cos(\theta)$ and ϕ

Bin by bin efficiency plots for “All Passing Muons” and “Stopping Muons” as a function of $\cos(\theta)$ and ϕ are shown in Figs. 3.6 and 3.7 respectively, which are obtained by taking the ratio of the Figs. 3.4 and 3.5 to Fig. 3.3 respectively.

3.3.2 Acceptance

The acceptance, \mathcal{A} , is defined as the product of the projected area seen by an incoming cosmic ray muon from a given direction, the probability of detecting and reconstructing the cosmic ray muon and the solid angle of the given direction [57].

$$\mathcal{A}(\theta, \phi) = A_p(\theta, \phi) \times \epsilon(\theta, \phi) \times \alpha(\theta, \phi) , \quad (3.3)$$

where, $\mathcal{A}(\theta, \phi)$ is the acceptance, $A_p(\theta, \phi)$ is the projected area, $\epsilon(\theta, \phi)$ is the efficiency and $\alpha(\theta, \phi)$ is the solid angle for a (θ, ϕ) bin.

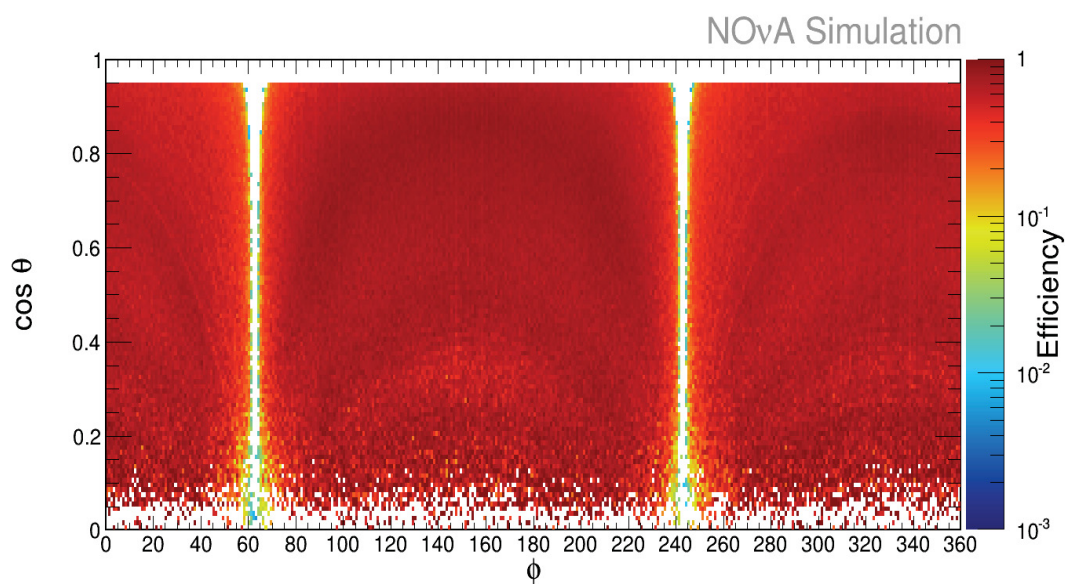


FIGURE 3.6: The efficiency of the NOvA FD as a function of $\cos(\theta)$ and ϕ for “All Passing Muons”.

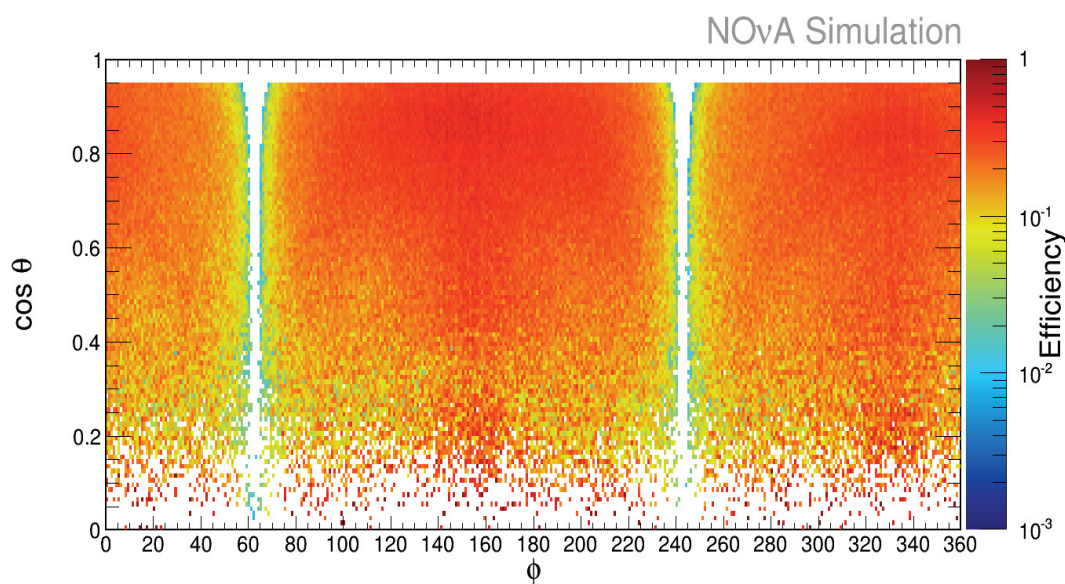


FIGURE 3.7: The efficiency of the NOvA FD as a function of $\cos(\theta)$ and ϕ for “Stopping Muons”.

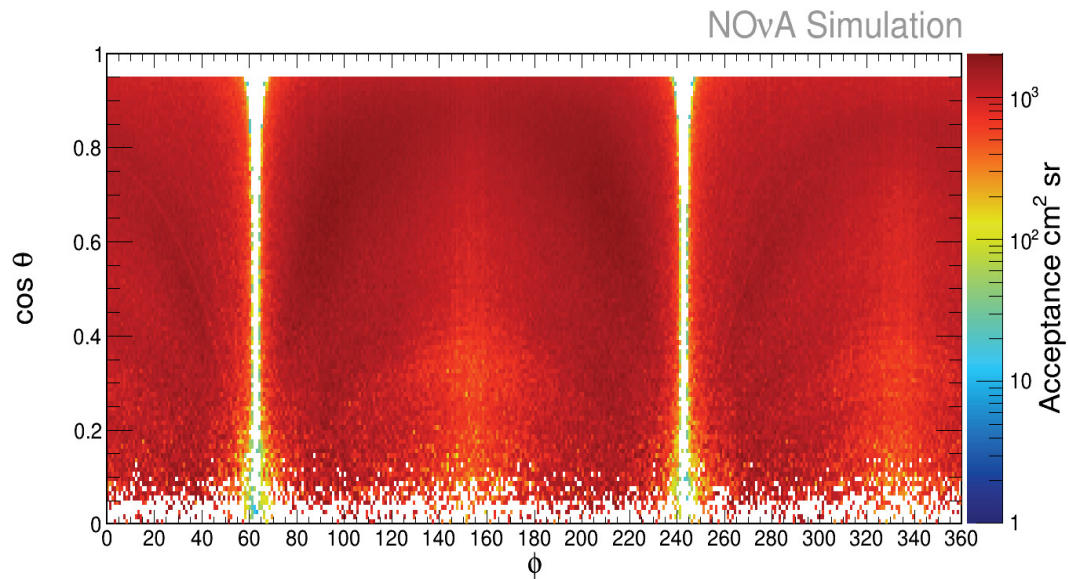


FIGURE 3.8: The acceptance of the NOvA FD as a function of $\cos(\theta)$ and ϕ for "All Passing Muons".

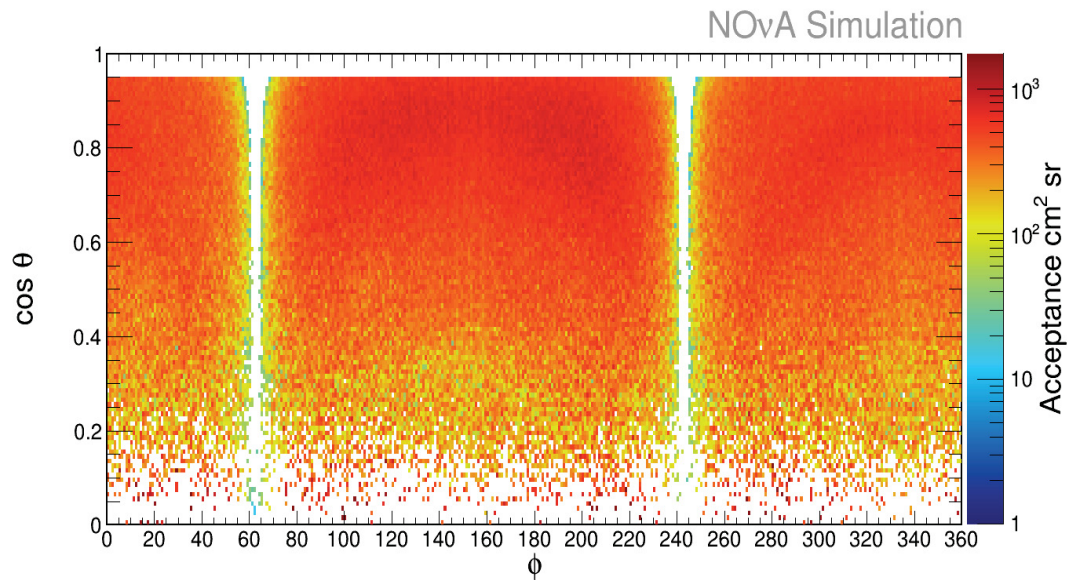


FIGURE 3.9: The acceptance of the NOvA FD as a function of $\cos(\theta)$ and ϕ for "Stopping Muons".

The acceptance for "All Passing Muons" and "Stopping Muons" cases are shown in Figs. 3.8 and 3.9 respectively. The total acceptance is $3.63 \times 10^7 \text{ cm}^2 \text{sr}$ for "All Passing Muons" selection and is $1.08 \times 10^7 \text{ cm}^2 \text{sr}$ for "Stopping Muons".

Selection Name	Number of muons $\times 10^6$	ϵ %	\mathcal{A} (cm^2sr) $\times 10^7$
All Muons	6.20	100.00	6.44
All Passing Muons	3.36	54.20	3.63
Stopping Muons	1.28	20.60	1.08

TABLE 3.3: The efficiency and acceptance of the NOvA FD.

Table 3.3.2 tells us that we are left with around 54% of the muons after “All Passing Muons” selection and we lose an additional 34% of the muons after “Stopping Muons” selection is applied. Fig. 3.6 shows that the efficiency is as high as almost 100% in many bins around $\phi = 153.45^\circ$ (North face) and around $\phi = 333.45^\circ$ (South face). Similarly, the overall efficiency after “Stopping Muons” selection is around 20% but it is higher than this in many bins around $\phi = 153.45^\circ$ and around $\phi = 333.45^\circ$ as shown in Fig. 3.7.

3.4 Detector efficiency and acceptance for tri-cell hit muon tracks

3.4.1 Tri-cell hit

For the calibration it is important to know the direction of the incoming muon track and the path length of each hit in a NOvA cell. If reconstruction is not very good, it is hard to say from where the muon track entered and exited the cell and an accurate path length can not be obtained. For example, if a cell in y-view has both its neighbors hit then from the direction cosine of the track with the x, y, or z axes, we can say that the track entered through the upper wall and exited through the lower wall. Such hits are known as tri-cell hits and one such hit is shown in Fig. 3.10. Tricell hits remove some dependence on reconstruction effects that might skew the pathlength determination. In Fig. 3.10, the red hit in the center is a tri-cell hit because both its pink neighbors are hit. L_y , C_x and C_y are the width of the cell,

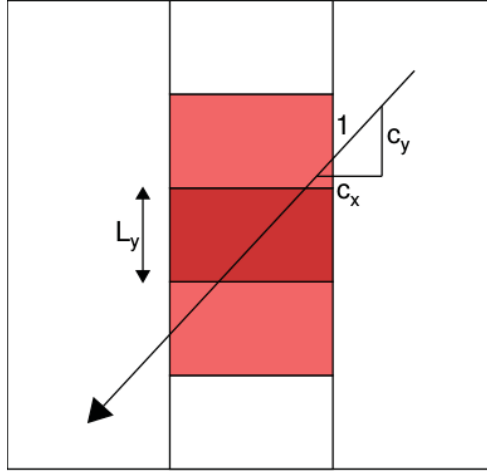


FIGURE 3.10: A tri-cell hit in a horizontal (y-view) cell.

direction cosine of the track with x-axis and direction cosine of the track with y-axis. The path length can be obtained in terms of L_y , C_x and C_y . Here the path length is L_y/C_y . This selection can also help us to get rid of noise hits which are mainly single cell hits and follows no pattern in the detector.

3.4.2 Number of muons as a function of $\cos(\theta)$ and ϕ for tri-cell hit tracks

A muon track having at least one hit as a tri-cell hit is defined as a tri-cell track. To find the efficiency and acceptance for the tri-cell tracks, all selection criteria described in §3.3.1 are used along with the requirement that the track have at least one tricell hit.

The number of muons as a function of $\cos(\theta)$ and ϕ after tri-cell hit selection are shown in Figs. 3.11 and 3.12 for “All Passing Muons” and “Stopping Muons” respectively. By taking the ratio of the number of muons before and after the tricell hit requirement for “All Passing Muons” and “Stopping Muons”, we observe that number of muons decreases in the range $\phi \in (100, 190)$, $\phi \in (290, 20)$ and $\cos(\theta) < 0.70$ i.e. $\theta > 45^\circ$ as shown in Figs. 3.13 and 3.14. The reduction of number of muons in some ranges of ϕ and $\cos(\theta)$ means that in order to calibrate detector in these directions we will need to loosen the tricell hit requirement.

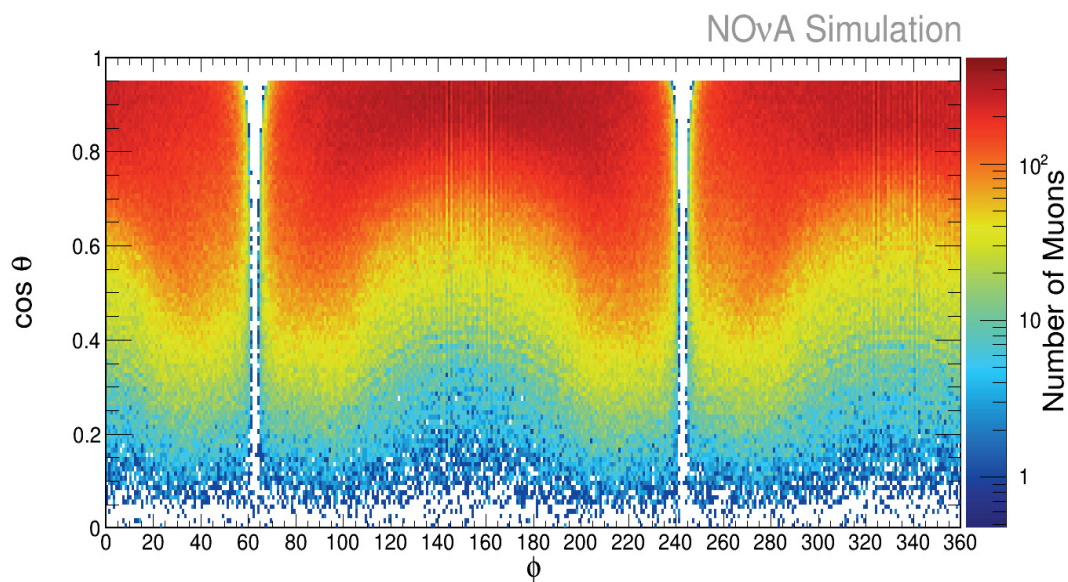


FIGURE 3.11: The number of muons seen by the NOvA FD as a function of $\cos(\theta)$ and ϕ for “All Passing Muons” after the tri-cell selection.

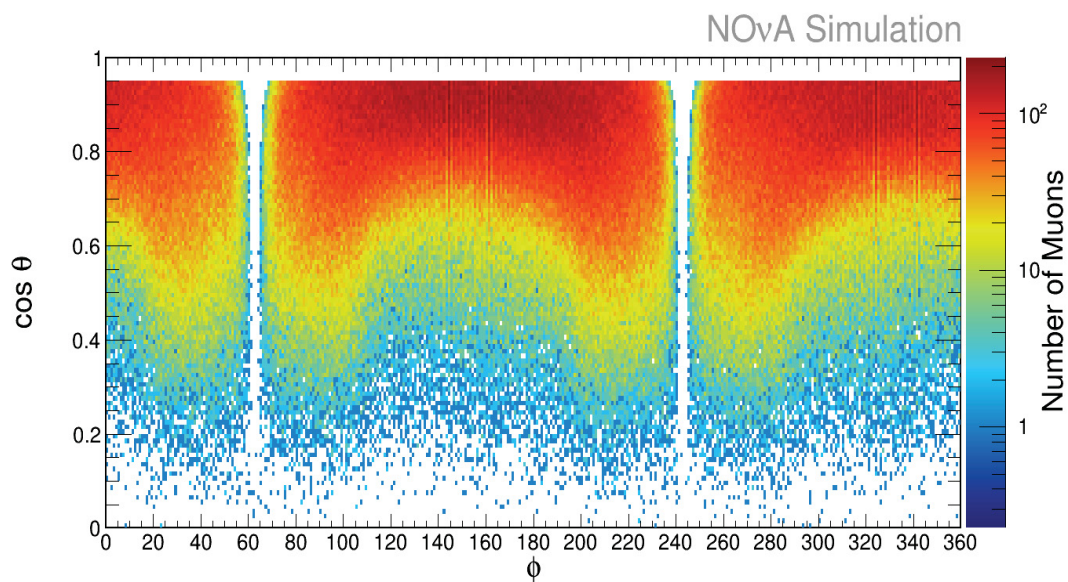


FIGURE 3.12: The number of muons seen by the NOvA FD as a function of $\cos(\theta)$ and ϕ for “Stopping Muons” after the tri-cell selection.

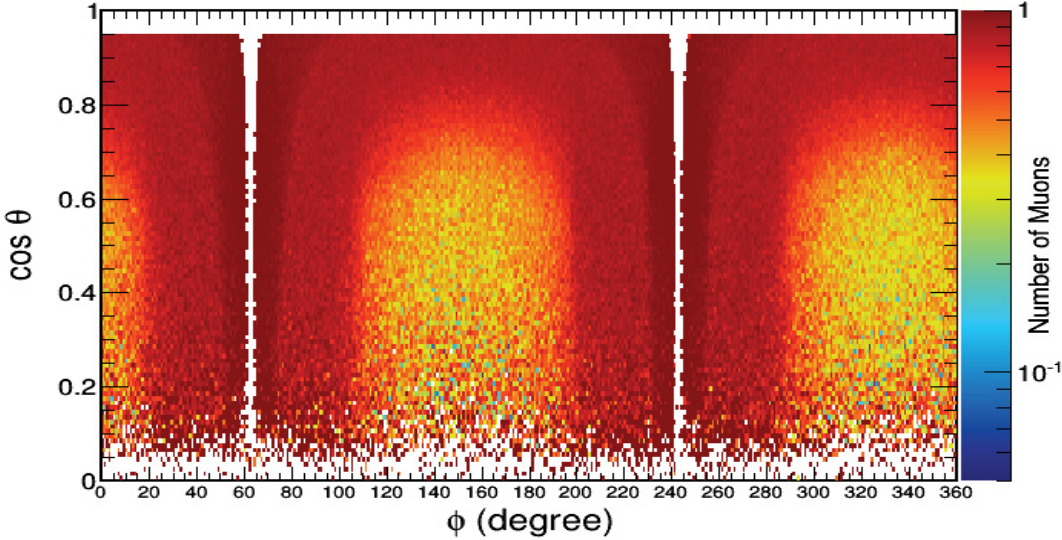


FIGURE 3.13: Ratio of number of muons with tricell to the “All Passing” sample seen by the NOvA FD as a function of $\cos(\theta)$ and ϕ .

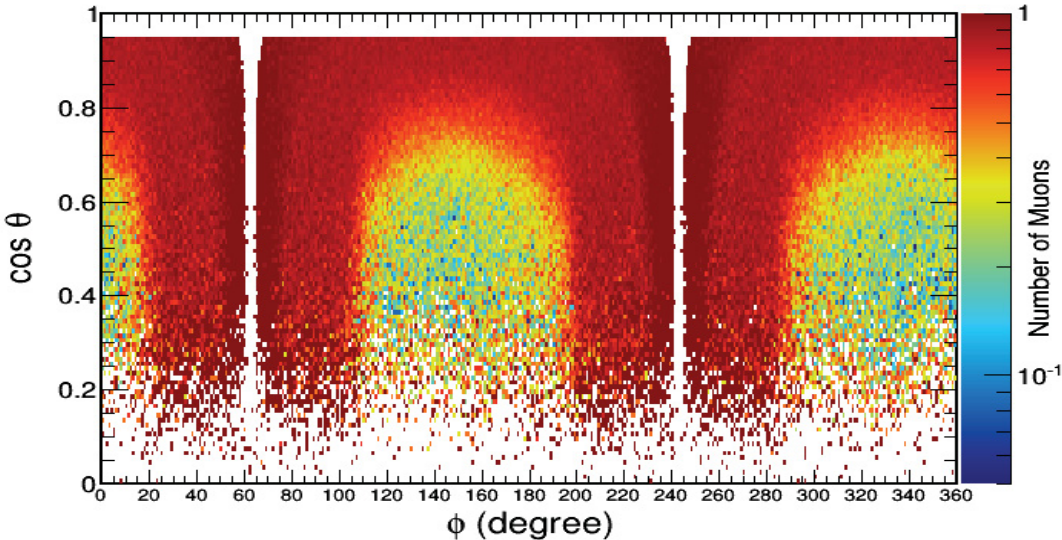


FIGURE 3.14: Ratio of number of stopping muons with tricell to all “Stopping” muons seen by the NOvA FD as a function of $\cos(\theta)$ and ϕ .

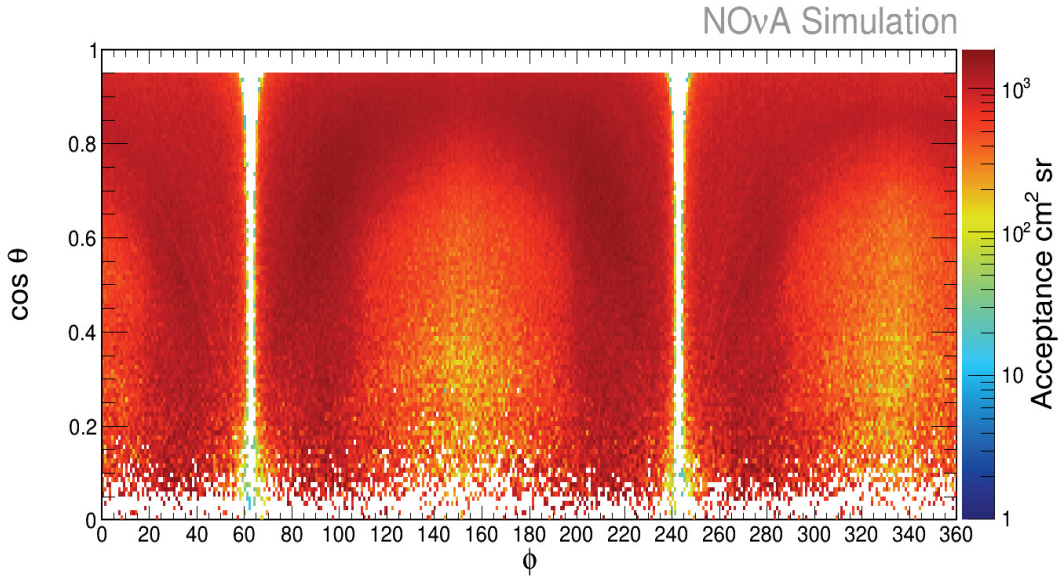


FIGURE 3.15: The acceptance of the NOvA FD as a function of $\cos(\theta)$ and ϕ for “All Passing Muons” after the tri-cell selection.

3.4.3 Acceptance as a function of $\cos(\theta)$ and ϕ for tri-cell hit tracks

The acceptance as a function of $\cos(\theta)$ and ϕ after tri-cell hit selection is shown in Figs. 3.15 and 3.16 for “All Passing Muons” and “Stopping Muons” respectively. After the tri-cell selection the total acceptance for all the bins is $2.67 \times 10^7 \text{ cm}^2 \text{ sr}$ for “All Passing Muons” and is $0.74 \times 10^7 \text{ cm}^2 \text{ sr}$ for “Stopping Muons”.

These plots in Figs. 3.15 and 3.16 are helpful to identify the directions in θ and ϕ where tri-cell tracks are more common and thus can be used in the calibration. The bins where acceptance values are high can be calibrated using tri-cell tracks whereas the bins where acceptance is low can be calibrated by loosening the tri-cell hit requirement.

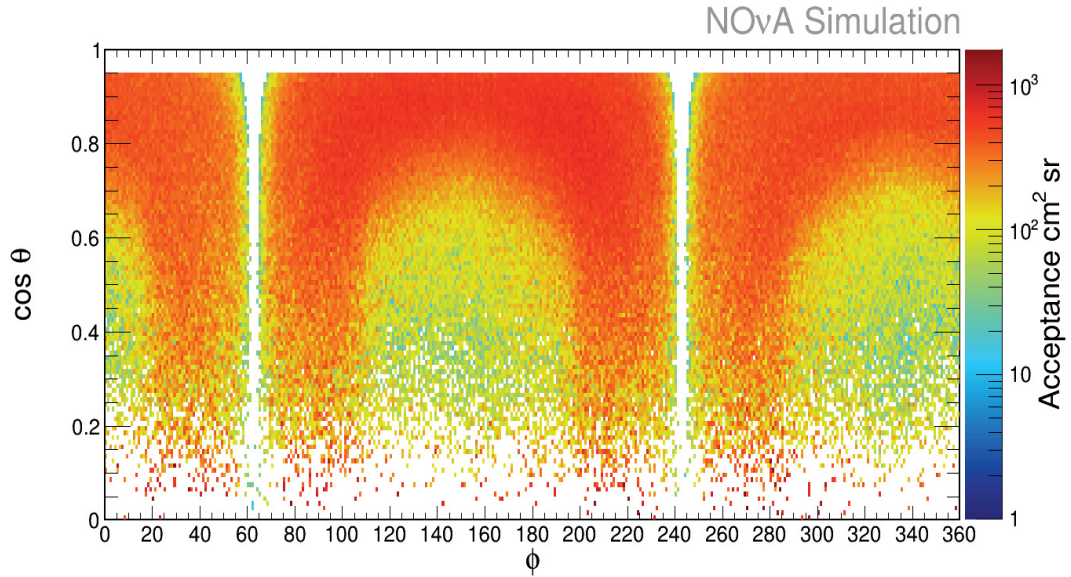


FIGURE 3.16: The acceptance of the NOvA FD as a function of $\cos(\theta)$ and ϕ for “Stopping Muons” after the tri-cell selection.

Selection Name	Tricell selection	Number of muons $\times 10^6$	ϵ %	\mathcal{A} ($cm^2 sr$) $\times 10^7$
All Muons	no	6.20	100.00	6.44
All Passing Muons	yes	2.59	41.80	2.67
Stopping Muons	yes	0.95	15.30	0.74

TABLE 3.4: The efficiency and acceptance of the NOvA FD for tri-cell tracks.

3.5 Results of the acceptance study

The total projected area of the FD is found to be 3.75×10^{11} cm^2 . The overall efficiency and acceptance of “All Passing Muons” and “Stopping Muons” before and after the tri-cell track selection is shown in Table 3.5. The $\epsilon_{\mathcal{A}}$ in the table is the fraction of the total acceptance for selection criteria. Table 3.5 indicates that we lose around 15% acceptance for “All Passing Muons” and 5% acceptance for “Stopping Muons” after the tri-cell track selection.

Selection Name	Tricell selection	Number of muons $\times 10^6$	ϵ %	\mathcal{A} (cm^2sr) $\times 10^7$	ϵ_A %
All Muons	no	6.20	100.0	6.44	100.0
All Passing Muons	no	3.36	54.2	3.63	56.4
	yes	2.59	41.8	2.67	41.5
Stopping Muons	no	1.28	20.6	1.08	16.8
	yes	0.95	15.3	0.74	11.5

TABLE 3.5: The efficiency and acceptance of the NOvA FD before and after the tri-cell track selection.

Most of the loss in the number of muons, efficiency and acceptance is in the range $\phi \in (100, 190)$, $\phi \in (290, 20)$ and $\cos(\theta) < 0.70$ i.e. $\theta > 45^\circ$.

Chapter 4

The Attenuation and Threshold Calibration of the NOvA Detectors

4.1 Calibration of the Detectors

Any charged particle traversing through NOvA scintillator produces scintillation light as explained in Chapter 2. The scintillation light is captured by the wavelength shifting fiber and is transferred to the APD. The scintillation light is attenuated while traveling through the fiber, that is, some amount of the scintillation light is lost between the point of light capture in fiber to the APD readout. Due to the attenuation of the light, the original energy of the incident particle can be miscalculated. To find the correct energy of the incident particle, the attenuation corrections are applied. The cosmic ray muons are used in estimating attenuation corrections. The cosmic ray muons are also used in energy calibration because they provide a consistent source of energy across detectors.

The main objective of the attenuation calibration is to make the response of the detector to a minimum ionizing particle uniform across the detector, no matter where the energy deposition occurs in the detectors. If that is not done, the detector's response to any two charged particles of the same energy would be different if they deposit energies in different parts of the detectors. In other words, the attenuation calibration corrections make the spatial response of the detector uniform. To do

this, the calibration constants are created and are used to estimate the number of photo-electrons (PE) as a result of deposited energy in NOvA cell and to produce the corrected photon-electron (PECorr) count. The results of the attenuation calibrations are used as inputs in the relative calibration whose objective is to convert PECorr to physical units of energy in GeV. The details of relative calibration are beyond the scope of this thesis work.

For analysis and calibration, all ND and FD data are divided into different periods. A period is an interval of time and is defined by different conditions of the experiment such as a long shutdown accelerator period, a change in horn current, displacement of target etc. Table 4.1 shows the start and end dates of different periods.

Period	Start Date	End Date
1	August 2014	May 2015
2	May 2015	October 2015
3	October 2015	June 2016

TABLE 4.1: This table shows the start and end dates of different data taking periods. The calibration was performed for each period.

Each period is further sub-divided into different epochs. An epoch is also a period of time and a new epoch begins whenever data analysis begins with a new set of calibration data. The attenuation and threshold calibration are performed for each epoch separately.

This chapter describes various steps involved in the attenuation calibration technique and the strategy followed for the attenuation fit. Different strategies followed for the Data and Monte Carlo calibration and are also discussed in this chapter.

4.1.1 Coordinates

The axis of the detector along the direction of the beam is labeled as \mathbf{z} axis, the vertical axis as \mathbf{y} and the horizontal axis as \mathbf{x} axis in the offline coordinate system. The center of the front face of the detector is the origin of the offline coordinate system. All distances are measured in centimeters (cm).

The cell number, V , and the distance along the cell length, W , are also used as the coordinates. Here W , is not the distance from the cell readout, it is an alias for the

x and y axes. For example, $W = 0$ is the center of the cell. More positive values of W indicate distances closer to the readout and more negative values of W represent distances farther from the readout. Throughout the attenuation and threshold calibration work, W is extensively used because it is independent of different views of the detector.

4.1.2 Definitions

- ADC – is the analog to digital conversion of the energy deposited by a charged particle in a NOvA cell, The ADC value is used to finally determine the number of scintillation photons produced and the energy deposited by the charged particle in NOvA cells. The ADC values are a fundamental parameter in the experiment to know and register the information about particles in NOvA detectors.
- PE – stands for photoelectrons produced by the energy deposition of a charged particle in NOvA cells. PE is an uncalibrated unit and approximately represents the peak of the ADC distribution. PE is an input to the attenuation and threshold calibration.
- PECorr – is the corrected number of photo-electrons obtained by applying attenuation and threshold corrections to the PE value. PECorr values are adjusted such that at the center of a cell, i.e. $W = 0$ and $1 \text{ PE} = 1 \text{ PECorr}$. The determination of PECorr value requires a reconstructed W value.
- GeV – is a unit of the energy deposited by a charged particle in the scintillator. The GeV value is obtained from the PECorr value. The correction due to the dead material of the detector, e.g. the PVC, are adjusted in the GeV value to get the final energy estimates.
- MIP – is the energy deposited by a minimum ionizing particle, i.e. a muon, in the cell along the z -direction, i.e. the depth of the cell. The MIP value is determined from a flat scaling of the GeV value of a charged particle.
- Raw digits – are the digitized signal from the cells including the time-stamp and ADC value of the event.

- Cell hit – is defined as an activity in a cell caused by energy deposition by a charged particle.
- Bad channel – any faulty cell due to some damage in the APD is called bad.

The offline calibration process converts raw digits into cell hits and saves them in production files. In this conversion, the cell numbering system is converted into the offline plane, cell, and coordinate values. The reconstructed hits are then generated using cell hits in the Calibration package which is a collection of NOvA code for the calibration purpose.

4.2 Attenuation fits

4.2.1 Selection and Calibration steps

The process of attenuation calibration begins by selecting suitable cell hits from cosmic muon ray tracks. After selecting suitable cell hits, we make plots of uncorrected photo-electrons per pathlength i.e. PE/cm, as a function of distance from the read-out, W . A channel by channel attenuation correction is determined and performed using plots of PE/cm vs. W . Here pathlength refers to the distance traveled by a charged particle through a NOvA cell and channel refers to a NOvA cell itself. We normalize PE by pathlength to eliminate the effect of reconstruction efficiency for different distributions of pathlengths of tracks from different angles, especially due to the presence of dead cells. Dead cells are cells which due to some reasons are not functioning, e.g. may be due to some maintenance work, or maybe a cell was masked because it became too noisy, etc. The inclusion of a correction due to normalization of PE by pathlength also sharpens the PE/cm distribution being used in calibration.

For a reliable estimate of the pathlength, all hits are not suitable for the calibration purpose. The selection of cell hits starts with 3-dimensional (3D) reconstructed tracks. The bad channels along the reconstructed tracks are removed.

For the estimation of pathlengths, different estimators are used, called “ xy ”, “ z ” and “ avg ”. Each of these estimators are explained in the following text. If a channel has each of its neighbor channels hit in the same plane, say Y-view, i.e. horizontal

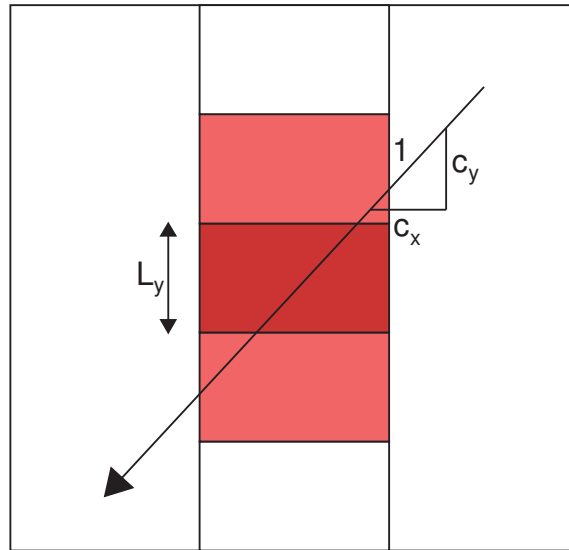


FIGURE 4.1: A cartoon image to represent the selection of a cell hit under “ xy ” estimator. The red dark cell in the center is selected because the light red neighboring cells have hit as well. Here the path length is estimated by the ratio of the cell width, L_y to the direction cosine c_y .

channels, then we know that the track entered the detector from the top wall and exited the lower wall. Such hits which have each of its neighbors a hit in the same plane are called tri-cell hits. The dark red cell in Fig. 4.1 illustrates a tri-cell hit. In this case, the pathlength is just the width of the cell divided by the direction cosine, c_y . This selection also removes the noise hits which are random in detector because noise hits do not follow any pattern and not give hits in the neighboring cells. This selection of hits is called the “ xy ” estimator because it requires hits in the x or y direction. Dead hits are also adjusted in this criteria if “hit, dead, hit, hit” pattern is followed. Another pathlength estimator is the “ z ” estimator and requires the same cell number hits in the neighboring planes in the same view. The “ z ” estimator is used in the cases where there are too many dead neighboring channels. In this case, the pathlength is the depth of the cell divided by the direction cosine c_z .

All suitable cell hits are collected for each estimator and cell combination by the Calibration package. The success of the calibration depends on the statistics of the hits in a channel. The “ xy ” sample is selected if there are at least 5,000 entries or cosmic hits in a channel. If the entries in a channel are less than 5,000 then “ z ”

sample is used. If there are too few hits in a channel then the “*avg*” estimator is used. The “*avg*” estimator relaxes the requirement for a channel to have hits in the neighboring channels. The case of the “*avg*” estimator usually happens for the cell in the corner of the detectors.

After selection of a statistically enriched sample of cosmic hits and the estimator, the hits are arranged into 2D histograms of PE/cm vs. W space. Once we make 2D histograms of PE/cm vs. W space, we take profiles of the 2D histogram to make 1D histograms of the average value of PE/cm as a function of W . Before we apply attenuation corrections, there are two more effects we need to account for as explained below in § 4.2.2.

4.2.2 Threshold and Shielding effects

Large divergences between the true and calibrated energies are observed in the FD simulation. The longer cell lengths of the FD and detector’s mass are traced to be the reason behind the differences between the true and calibrated energies.

When energy is deposited in a cell, it may only be registered as a signal in the APD if photons are produced above a threshold. If a particle deposit energy far from the readout, the photons are attenuated and the signal will not get above threshold unless the energy deposition has high fluctuation in the number of photons. Similarly, if a particle has deposited too little energy but has a high fluctuation in the number of photons, it can make the signal go above the threshold. The threshold correction tries to correct the effect of this high fluctuation. The self-shielding means the energy deposited by the MIP particles is not spatially uniform across the detectors. Only the high energy cosmic ray muons can reach the bottom of the FD. This means that there is more energy deposited per unit length at the bottom of the FD compared to the top region. The shielding corrections tries to correct the differences in the detector response between the bottom and top regions of the FD.

If we do not correct for the threshold and self-shielding effects, the attenuation fit is biased which can lead to errors in finding the real energies of the charged particles.

To correct for the threshold and self-shielding effects, correction factors are created for each cell hit based on the simulated truth information. These correction factors

are called threshold and self-shielding factors and are applied before attenuation corrections are applied.

The simulated truth information is used to make the combined threshold and self-shielding correction factor for each view and cell combination as a function of position along the cell length,

$$T = \frac{PE}{\lambda} \cdot \frac{E_{true}}{E_{mip}}, \quad (4.1)$$

where T is the “threshold and self-shielding” correction factor, PE is the simulated photo-electrons seen at the readout APD, λ is the Poisson mean number of simulated photons created in the scintillator, E_{true} is the true energy deposited by the charged particles in each cell and E_{mip} is the expected energy deposited by a MIP particle in the cell without shielding effect and based on the pathlength through the cell. This way the threshold correction is taken care of by using simulated PE with and without fluctuations, via λ which depends on the true deposited energy. The self-shielding corrections are taken care of via simulated energy deposition and no shielding approximation.

Equation 4.1 is used to generate a cell by cell, combined threshold, and self-shielding correction. The simulated cosmic sample has lower statistics in each cell for the threshold and shielding corrections. The lower statistics generate large statistical fluctuations in each cell. To remove the statistical fluctuations as shown in top plots in Fig. 4.2, the 2D space is fit by a polynomial function. The polynomial fit removes the statistical fluctuations and results in a smooth distribution of correction factor as shown by bottom plots in Fig. 4.2. The polynomially fitted distribution is then further used to generate attenuation corrections. Fig. 4.2 shows the distribution of the correction factor for each view and cell combination before and after an empirical fit is applied. Figs. 4.3 are made by taking the profiles of distributions shown in Figs. 4.2. The profiles are the threshold and self-shielding correction factors as a function of cell number and position along the cell length for each X and Y view cells. These correction factors are applied to the simulated and data, PE/cm distributions before the fit are performed to make the attenuation corrections.

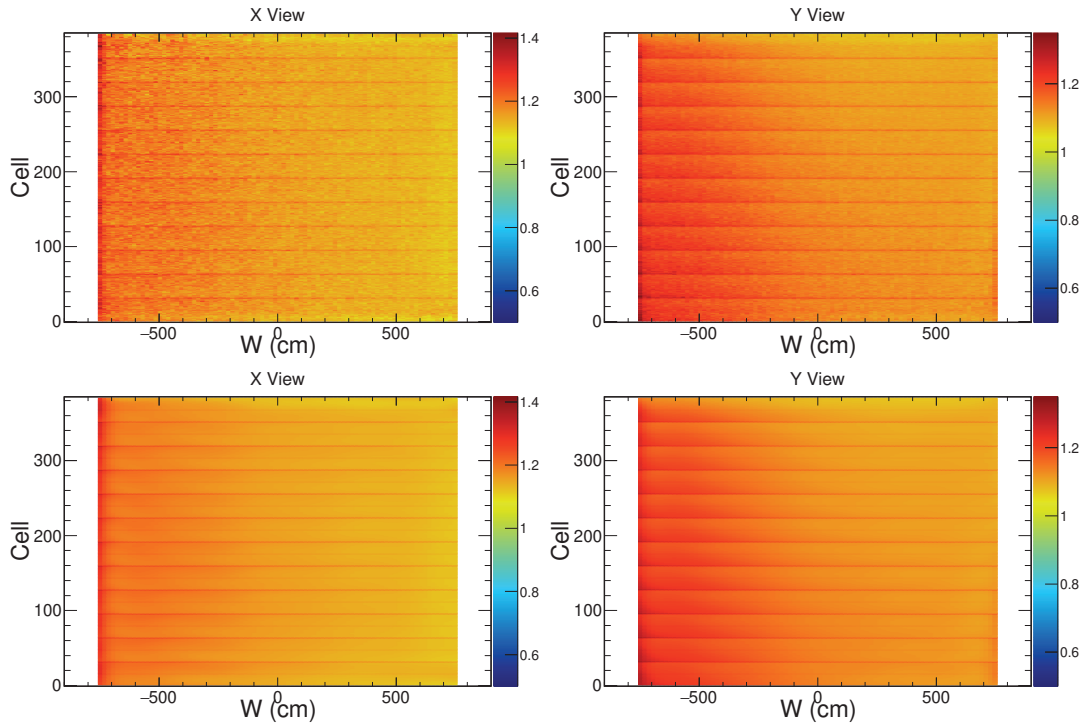


FIGURE 4.2: Top plots are examples of the FD threshold corrections as a function of W and cell number for both the X (left) and Y view (right) cells. Bottom plots are after the empirical fit is applied to the top plots to remove the statistical noise for both the X and Y view cells.

4.2.3 Simulation and Detector Specific Attenuation Fit

The ND and FD data and simulation samples are calibrated using different strategies. For each sample, tri-cell hits are used as explained in § 4.2.1. The simulated cosmic sample is much smaller than the cosmic data and in the simulation, the detector is approximately uniform from plane to plane. So, for the FD and ND simulation, hits are collated by view and cell instead of plane and cell unlike for the data.

For the cosmic data, the FD and ND planes are not assumed to be uniform but there is enough data to calibrate each NOvA cell individually. For the cells in the ND muon catcher, the hits for the cosmic data are collated by view and cell because of lack of cosmic data due to different structures of the muon catcher region. The hits in the muon catcher region fail the tri-cell hit requirement which reduces the cosmic statistics. All the X-view cells are collated as a single plane to calibrate and the same strategy is used to calibrate the Y-view muon catcher cells.

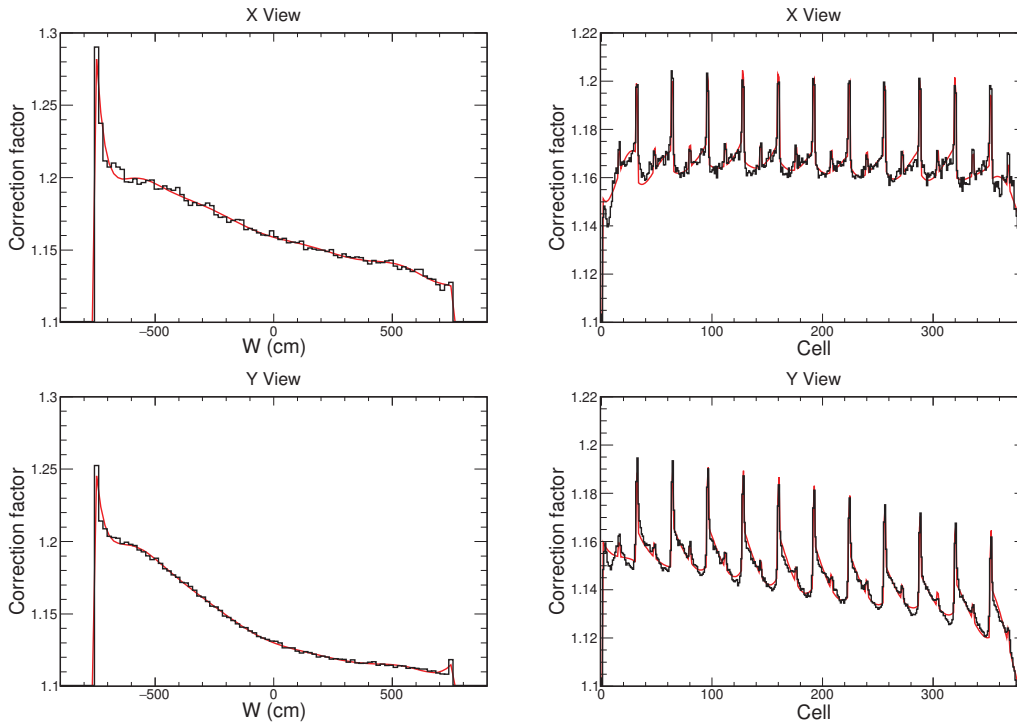


FIGURE 4.3: Comparison of the empirical fit, red curve, to the threshold correction and the underlying distribution, black curve for the high gain Far Detector X view, top plots, and Y view, bottom plots, for both W (left) and cell number (right).

4.2.4 Functional Form of Attenuation Fit

The scintillation light captured by the WLS fiber is transferred to the readout. The light captured can reach the readout using a short path or a long path as shown in Fig. 4.4.

The attenuation fit takes into account both the short and long-path lengths of the scintillation light. The profiles of the PE/cm vs. W are fit to the following form,

$$y = C + A \left(\exp\left(\frac{W}{X}\right) + \exp\left(-\frac{L+W}{X}\right) \right), \quad (4.2)$$

where y is the cell response to scintillation light, L is the length of NOvA cell, and A , C and X are free parameters in the attenuation fit. Parameter X gives the attenuation length of the fiber, C estimates the minimum response of the cell and A measures the amplitude of the detector's response.

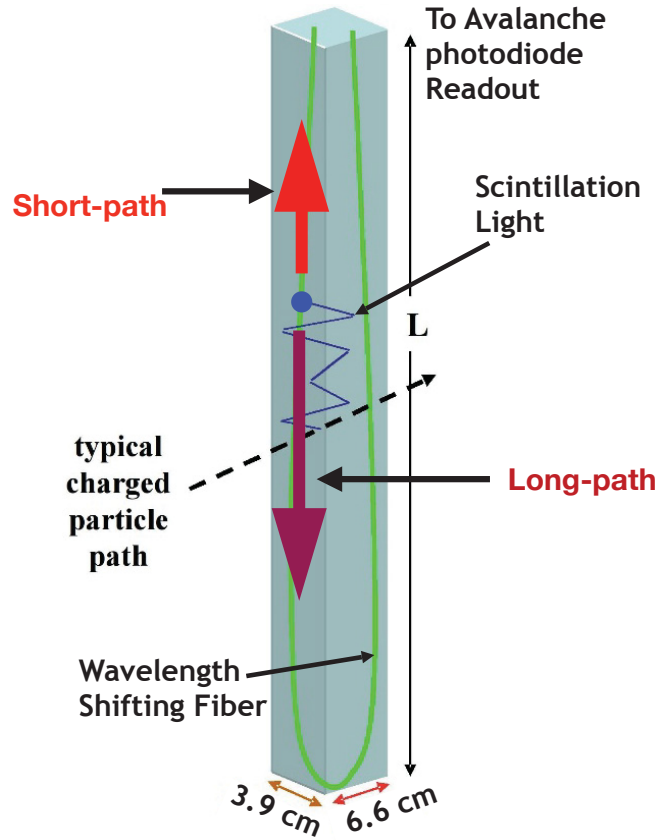


FIGURE 4.4: A pictorial representation of the NOvA cell to illustrate short- and long-paths for scintillation light to reach the readout via wavelength shifting fiber.

The attenuation fit describes the response of the central part of the NOvA FD and ND very well. Initially attenuation fit is applied between $[-150, +150]$ cm for the ND cells, $[-150, +150]$ cm for Y-view ND muon catcher cells, $[-150, +50]$ cm for the X-view ND muon catcher cells and $[-750, +750]$ cm for the X and Y view FD cells.

4.2.5 Rolloffs

The end parts of both the ND and FD cell in data shows noticeable “rolloffs” which are either absent or less noticeable in simulations. The rolloffs are found to follow a quartic polynomial functional form of the type W^4 . The end part of the cell response to light follows,

$$y = \begin{cases} 1 - \alpha_R(W - W_R)^4 & W > +W_R \\ 1 & \text{otherwise} \\ 1 - \alpha_L(W - W_L)^4 & W < -W_L \end{cases} \quad (4.3)$$

here W_L is the left end, that is, the far end positions on the cells. The W_R is the right end, that is, close to the APD. Parameters α_L and α_R are the magnitudes of the rolloffs. These parameters are left free in the fit. The rolloff functional form is found to not properly fit the rolloff behavior of the end parts of the cells, instead, a better fit described in next § 4.2.6 is used to mitigate the response of the end part of the cells.

4.2.6 Locally Weighted Scatter Plot Smoothing, LOWESS, Fit

All cells show quartic behavior at the end of cells. Some cells show large residuals and do not follow any consistent pattern. The main reason may lie with the position of the WLS fiber in the cells. The fiber is supposed to be at the corners of cells but the fiber may twist and can lie at the center of the cell during filling of the mineral oil through detector commissioning. The position of the fiber may be slightly different in different cells along the length of the cell. The central location of the fiber may lead to more light compared to the location at the corner and high residuals in some cells.

To remove the inconsistencies at the end of the cells, the residuals from the attenuation fit are fitted with locally weighted scatter plot smoothing, LOWESS. The LOWESS curve at each W point is formed using the weighted mean of the deviations (w_i). The w_i weight is created for each neighbor point W_i in the vicinity of point W . Here W is the distance from the readout and also called a control point. The neighbor point W_i should be within a pre-defined σ range for the LOWESS to work. The following tri-cube function is the weighting function in the LOWESS fit,

$$w_i = \begin{cases} \left(1 - \left|\frac{W - W_i}{\sigma}\right|^3\right)^3 & \text{for } |W - W_i| < \sigma \\ 0 & \text{for } |W - W_i| \geq \sigma \end{cases} \quad (4.4)$$

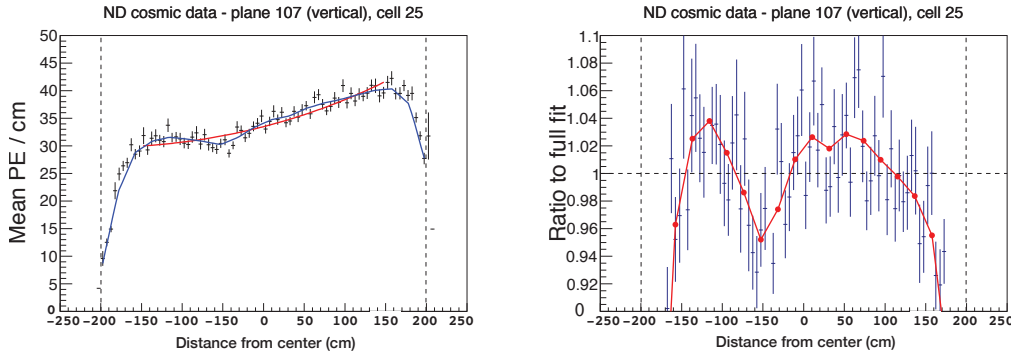


FIGURE 4.5: Example here shows the response of a particular ND cell for cosmic data. The blue curve in the left plot is the total attenuation fit including the LOWESS corrections and the red curve is the exponential fit to the cell response. The performance of the attenuation fit and the LOWESS correction is visible as it passes close to all cell hit points. The right figure, for example, shows the LOWESS fit through the residuals for the same ND cell.

Here σ is selected to be 30 cm as the distance of measurements which influences each control point.

The LOWESS fit finds a best-fit point to the collection of neighboring points to the control point. The best fit line is found by minimizing the squares of distances between the neighboring points and the line. The best fit line represents the response of the cell at location W as $y = m*W + c$. Here y represents the LOWESS correction to the cell response. Parameters c and m are the intercept and slope of the best fit line respectively.

Twenty control points are used in the LOWESS fit to make corrections in the final response of the cell. Fig. 4.5 shows an example of a cell response which is fit using LOWESS corrections. In this example, large deviations (10%) are being fitted.

Even after an application of attenuation fit including LOWESS corrections, some cells having large residuals such that they can not be classified as calibrated cells. One of the reasons is the lack of cosmic hit statistics in that cell. To call a NOvA cell calibrated, a parameter called χ^2 which is the mean deviation of the data points from the fit in quadrature is calculated during the attenuation and LOWESS fit. If the value of the χ^2 , exceeds a value of 0.2 for a cell, the attenuation and LOWESS fits are marked bad and the cell is flagged as uncalibrated.

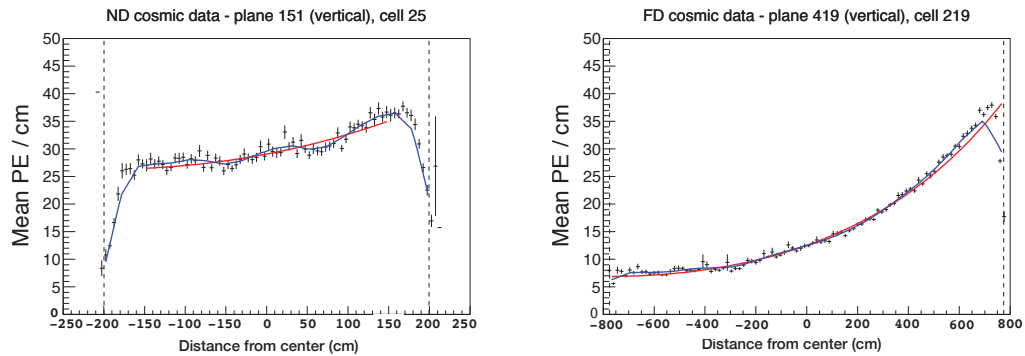


FIGURE 4.6: Examples of the full attenuation fit including the LOWESS corrections to one ND cell (left) and to one FD cell (right) are shown. The full attenuation fit in the blue curve is also compared to the double exponential fit in red. The attenuation fit including LOWESS corrections performs a better fit to the cosmic data.

The fit from equation 4.2 is combined with the LOWESS corrections to make the final attenuation fit. The blue curve in Fig. 4.6 show examples of ND and FD cells which are fitted using full attenuation fit including the LOWESS corrections and are compared to the double exponential fit in the red curve. The application of the attenuation fit including the LOWESS has much better performance both in the central part of the cells and at the ends of the cells. Example in Fig. 4.6 show only a particular ND and FD cell. The rest of the cells can be found at the NOvA official webpage

http://nusoft.fnal.gov/nova/calibration/Attenuation_Calibration/SecondAna/Period3/Epoch3b/ and http://nusoft.fnal.gov/nova/calibration/Attenuation_Calibration/.

Here cells that are well-calibrated are green, cells that are missing any data are black and cells in which the fit failed are yellow and red.

4.2.7 Calibrator and Database

In the NOvA software, the Calibrator package fits the cosmic data in the cells and finds the attenuation constants and the list of 20 LOWESS points. The calibration constants are obtained from the Calibration package and are stored in the NOvA database in the form of two tables `calib_atten_consts` and `calib_atten_points`. Here the `calib_atten_consts` stores the free parameters from the full attenuation fit

and `calib_atten_points` stores the 20 LOWESS points for each NOvA cell, having every row with information for each cell.

The Calibration package also stores the quality of the attenuation fit to the NOvA database such that if a cell is not properly calibrated then the Calibration package will not return the information about the un-calibrated cell during reconstruction stages. Calibrator package also stores and returns the MIP and GeV information of a cell hit.

4.2.8 Near Detector Calibration Performance

To access the performance of the attenuation and threshold calibration, the true and reconstructed energies of the simulated cell hits across the detector are compared before and after calibration corrections are applied.

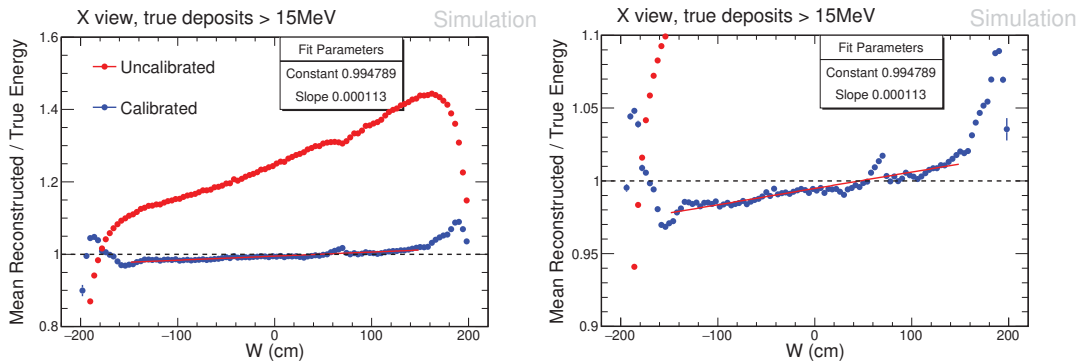


FIGURE 4.7: The ratios of the reconstructed to the true energies for the ND X-view hits. The red points are the ratios before the attenuation and threshold calibrations are applied and the blue points are after the calibrations are applied. The right plot is the zoomed version of the left plot. One can see the improvements in the ratios of the reconstructed to the true energies after attenuation and threshold calibrations are applied. Even after calibration, some calibration residuals remain.

The performance of the ND attenuation and threshold calibrations are shown in Fig. 4.7 for the X-view cells and in Fig. 4.8 for Y-view cells. The y-axis on the plots shows the ratio of the mean reconstructed energies to the true energies as a function of position along the cell length. The red points are the ratio before calibrations are applied and the blue points are after calibrations are applied. The red points clearly show if cell hits are not calibrated then the reconstructed energies show

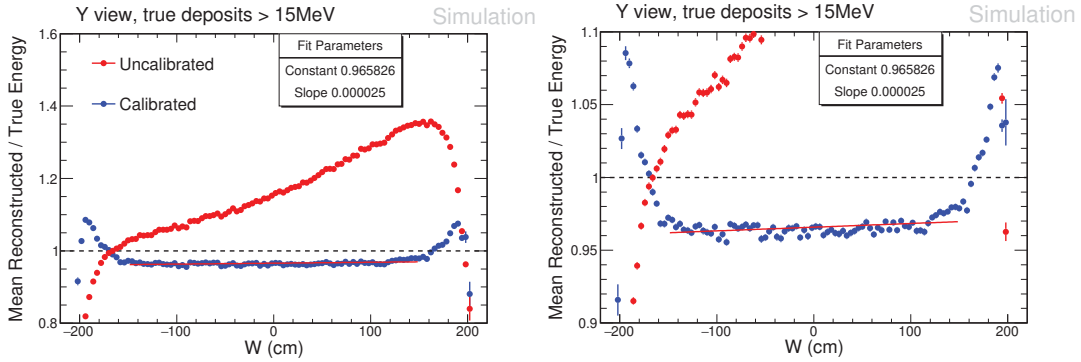


FIGURE 4.8: The ratios of the reconstructed to the true energies for the ND Y-view hits. The red points are the ratios before the attenuation and threshold calibrations are applied and the blue points are after the calibrations are applied. The right plot is the zoomed version of the left plot. One can see the improvements in the ratios of the reconstructed to the true energies after attenuation and threshold calibrations are applied. Even after calibration, some calibration residuals remain.

large divergence from the true simulated energies. The blue points show successful improvement in the ratios of the reconstructed to the true energies.

The ND X view hits after calibration shows a 4% variation in the slope of the ratios from the far end of the cells to the near end. Here near end is the closest point to the readout and the far end is the farthest away from the readout. The Y-view hits after calibration show less than 1% variation in the slope of the ratios from the far end to the near end of the cell. The Y-view hits also show a 4% offset in the ratios of the reconstructed to the true energies.

Fig. 4.7 show a bump in the ratio of the reconstructed to the true energy near $W = 60$ cm. The bump in the ratios is due to the edge of the X-view muon catcher cells as the X-view cells in the ND are two-third the length of the main body cells. In Fig. 4.8 there is no such bump because the Y-view cells in the muon catcher are of the same length as the main body cells and hence no cell edge effect is seen.

4.2.9 Far Detector Calibration Performance

The performance of the FD calibration is shown in Fig. 4.9 for the X-view cells and in Fig. 4.10 for the Y-view cells.

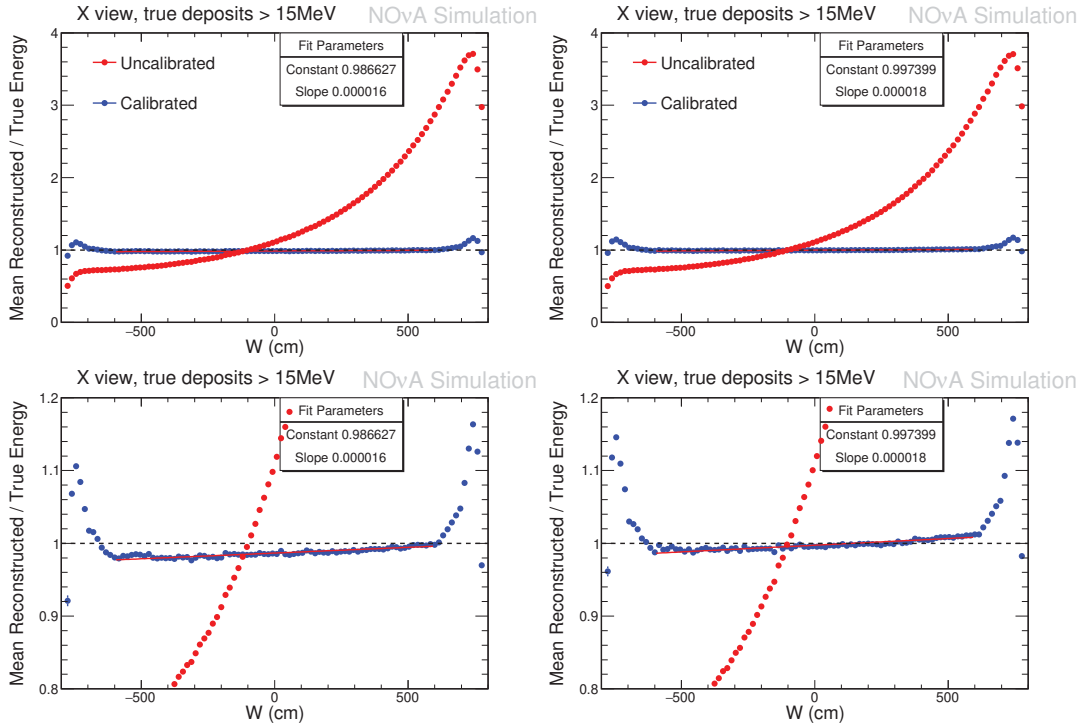


FIGURE 4.9: The ratios of the reconstructed to the true energies for the FD X-view hits are shown. The red points are the ratios before the attenuation and threshold calibrations are applied and the blue points are after the calibrations are applied. The top left plot is made using the simulated data from period 1 and the top-right plot is made using simulated data from period 3. The bottom plots are simply the zoomed version of the corresponding top plots. One can see the improvements in the ratios of the reconstructed to the true energies after attenuation and threshold calibrations are applied. Even after calibration, some calibration residuals remain.

The red points in these plots are again the ratios of the reconstructed to true energies before attenuation and threshold calibrations are applied and blue points are after the calibrations are applied.

Figs. 4.9 and 4.10 show the improvement in the ratios of the reconstructed to the true energies of the X-view and Y-view hits after attenuation and threshold calibrations are applied. The zoomed version of the X-view hits in Fig. 4.9 shows a 2% variation in the slope of the ratios from the far end of the cells to the near end of the cells.

The zoomed version of the Y-view hits in Fig. 4.10 shows less than 1% variation in the slope of the ratios from the far end of the cells to the near end but a clear 4% offset effect remains even after the application of the attenuation and threshold calibrations.

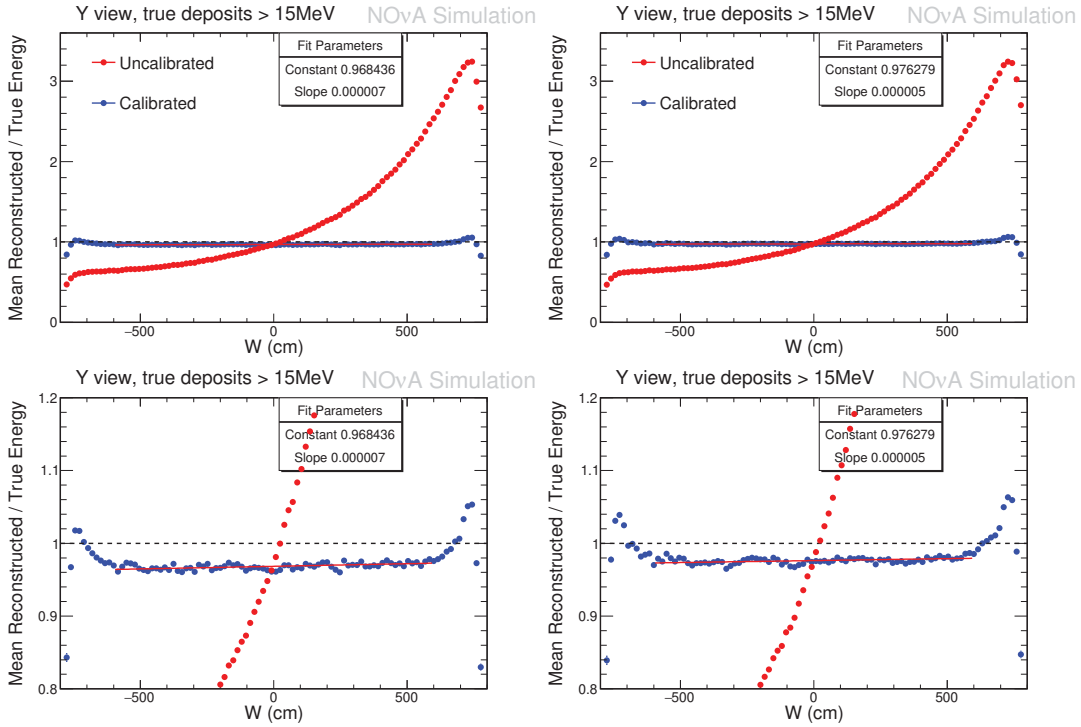


FIGURE 4.10: The ratios of the reconstructed to the true energies for the FD Y-view hits are shown. The red points are the ratios before the attenuation and threshold calibrations are applied and the blue points are after the calibrations are applied. The top left plot is made using the simulated data from period 1 and top the right plot is made using simulated data from period 3. The bottom plots are simply the zoomed version of the corresponding top plots. One can see the improvements in the ratios of the reconstructed to the true energies after attenuation and threshold calibrations are applied. Even after calibration, some calibration residuals remain.

4.3 Calibration leading to calibration systematics

The attenuation and threshold calibration of the near and far detectors is affected by various sources of systematic uncertainty. The calibration residuals, for example the slope and offsets shown in § 4.2.8 and § 4.2.9, lead to systematic uncertainties. The attenuation and threshold calibration systematic uncertainties are quantified using the true energy information from the simulations.

Variations in the offset and the slope of the ratios of the reconstructed to true energies of the cell hits along the length of the cells are used to create datasets to calculate the calibration systematics. Higher-order polynomial functions are used for the shapes and offsets of the ratios to make the functional form to describe the

residuals of the attenuation and threshold calibrations. The calibration functional forms are then used to make files having neutrino events for each view of the detector. The analysis groups then use these functional forms in the analysis. More details regarding the calibration systematics will be given in the analysis chapter of this thesis.

4.4 Summary and results of the attenuation and threshold calibration

The details of the NOvA attenuation and threshold calibration are explained in this chapter. Both the ND and the FD cells are successfully calibrated to remove the effects of the attenuation, shielding, and threshold. The attenuation constants were successfully generated and used in this and various other NOvA analyses. The FD has 344,064 NOvA cells and the ND has 18,592 cells. Table 4.2 show that over 98% ND and over 99% of the FD cells are successfully calibrated. The remaining cells could not be calibrated properly because of the lack of cosmic data in those cells.

Detectors	Number of Total Cells	Number of Calibrated Cells	% of Calibrated Cells
ND	18592	18312	98.5
FD	344064	341311	99.2

TABLE 4.2: Over 98% of the ND and over 99% of the FD cells were successfully calibrated.

Chapter 5

Neutrino Oscillation Analysis

This chapter describes the analyses of the $\nu_\mu \rightarrow \nu_\mu$ survival and the $\nu_\mu \rightarrow \nu_e$ appearance data using the NuMI beamline of Fermilab. A combined fit to the ν_μ disappearance and ν_e appearance data is performed to extract the values of $\sin^2 \theta_{23}$, Δm_{32}^2 and δ_{cp} . The combined fit to the ν_μ disappearance and ν_e appearance data is also called the joint fit. The ν_μ disappearance data are sensitive to the Δm_{32}^2 and $\sin^2 \theta_{23}$ parameters. The ν_e appearance data are sensitive to the Δm_{32}^2 , $\sin^2 \theta_{23}$ and δ_{cp} parameters. The benefit of performing a joint fit is that it finds the values of the Δm_{32}^2 , $\sin^2 \theta_{23}$ and δ_{cp} simultaneously. This analysis includes the NuMI beam data collected from February 06, 2014 to February 20, 2017. The exposure collected in these three years is 9.48×10^{20} protons on target (POT). The data taking started when the FD was not fully constructed. The exposure is modified to account for the changing size of the FD during construction. The 9.48×10^{20} POT in total is equivalent to 8.85×10^{20} POT for the 14kton mass of the completed FD. The signal and background prediction using simulated events are normalized to the collected POT for the oscillation analysis.

This chapter includes an introduction to the analysis framework designed to analyze the neutrino data. Various details of the ν_μ analysis including the signal and background topologies, the selections used for ν_μ events in the ND and FD, the beam and cosmic backgrounds and ν_μ constraints from the ND are explained in § 5.2. Details of the ν_e analysis including the event topologies, event selections, background rejections, and ND constraints are explained in § 5.3. The extrapolation technique used to predict signal and background events in the FD using constraints from the ND is described in § 5.4. The binned χ^2 procedure used to extract the neutrino oscillation

parameters is described in § 5.5. The incorporation of systematic uncertainties is described in § 5.6. The physics sensitivities using the “ ν_e only” and “ $\nu_\mu - \nu_e$ joint” fit for the $\sin^2 \theta_{23}$ and δ_{cp} parameters are shown in § 5.7. The final oscillation results are shown in § 5.8.

5.1 Introduction to the Analysis Framework

An analysis framework has been developed to fit the spectra of neutrino energies selected at the FD. The framework measures the values of the neutrino oscillation parameters from by fitting the FD data. The neutrino flux is simulated using GEANT4 [58], which models the geometry of the NuMI beam-line for hadrons produced from the collisions of the 120 GeV protons on the target. The focusing and decay of hadrons into neutrinos is also simulated at this step. The simulated flux is used as an input to GENIE [59, 60] to simulate neutrino interactions with various materials in the NOvA detectors and their surroundings. The GENIE simulation toolkit generates neutrino events for various nuclear targets, neutrino flavors and a range of neutrino energies. Finally, a model of the NOvA detector in GEANT4 is used to simulate the detector’s response to the particles produced by the interaction of neutrinos. The simulation accounts for the scintillation and Cherenkov radiation in the detector volume. The process of light transport from the NOvA cells to the readout and the digitization process is also simulated. Simulation files are generated for both the ND and the FD. In the ND, the NuMI beam contains 93.8% ν_μ , 5.3% $\bar{\nu}_\mu$ and 0.9% $\nu_e + \bar{\nu}_e$. For the FD, three kinds of files are generated. First, the files to mimic the beam neutrino flux. In the no-oscillation case, the ν_μ s from the ND remain ν_μ s in the FD. The second kind of files, called flux-swap files, have the ν_μ s swapped with ν_e s. These files predict the $\nu_\mu \rightarrow \nu_e$ signal for the ν_e appearance analysis and ν_e CC background for the ν_μ disappearance analysis. Finally, the third kind of files have swapped the beam ν_μ s for ν_τ s. These files predict the ν_τ backgrounds in the FD resulting from $\nu_\mu - \nu_\tau$ oscillations.

In the analysis of the neutrino data, we perform several steps. The first step is to select the ν_μ CC and ν_e CC events in the ND and the FD. The ν_μ CC interactions are the signal for the ν_μ disappearance analysis and ν_e CC interactions in the FD are signals for the ν_e appearance analysis. The beam ν_e CC, the NC interactions, and the cosmic activity are the backgrounds for both analyses. The purpose of the

selections is to remove the background events and to retain the signal events. In our analysis framework, we take the simulated files and apply all selections to keep events that are useful for the oscillation analysis. The process of applying selections is called “skimming”. During the skimming step, we also divide events into various categories called datasets. The data and simulated events are kept separately. The events selected by the ν_μ CC selections are kept separately from the events selected by the ν_e CC selections. The events are also separated for different interaction types, for example, the ν_μ CC, the $\bar{\nu}_\mu$ CC, the ν_e CC, the $\bar{\nu}_e$ CC, the ν_τ CC, the $\bar{\nu}_\tau$ CC, the NC and the cosmic events. The true information about the interaction type from the simulation is used to distinguish different interactions in the simulated events. The skimming process helps to reduce the memory size of the analysis by removing unwanted information which reduces the consumption of computing resources.

The second step in the analysis is to use the selected sample in the ND to make the signal and background predictions in the FD. The process of making the signal and background predictions in the FD using ND data and simulated samples is called extrapolation. Extrapolation not only makes the predictions in the FD but also helps in the reduction of the systematic effects in the FD due to functionally identical near and far detectors. The systematic effects which are present both in the ND and FD are reduced during extrapolation. The systematic uncertainties from different effects are included in the oscillation fit to the FD data. The fit to the FD data is used to determine the best values of the oscillation parameters.

The next step in the analysis is to make sensitivity plots for Δm_{32}^2 , $\sin^2 \theta_{23}$ and δ_{cp} by using the simulated events. The sensitivity plots help us to know the power of the experiment to determine the desired oscillation parameters. Finally, the analysis contours are made around the best fit values of the oscillation parameters obtained from the fit to the FD data.

In this analysis, we follow a blind analysis approach which means we do not look at the selected data events in the FD until we are satisfied with the predictions and the incorporation of the systematic uncertainties. Only when the collaboration is satisfied, we compare the FD predictions with the FD data and make contours.

5.2 ν_μ Disappearance Analysis

For the ν_μ disappearance analysis, we search for ν_μ s in the FD after the ν_μ beam has oscillated between the ND to the FD. The NC interactions in the FD and the cosmic ray muons are the main backgrounds for the ν_μ disappearance analysis.

5.2.1 Signal and Background Event Topologies

The surviving ν_μ interact via CC and NC interactions inside the FD. The signal ν_μ CC interaction produces a muon and hadronic activity at the interaction vertex. The Feynman diagram in Fig. 5.1 shows the interaction of a ν_μ with a neutron via exchange of a charged W boson. Fig. 5.2 pictorially shows the expected signature

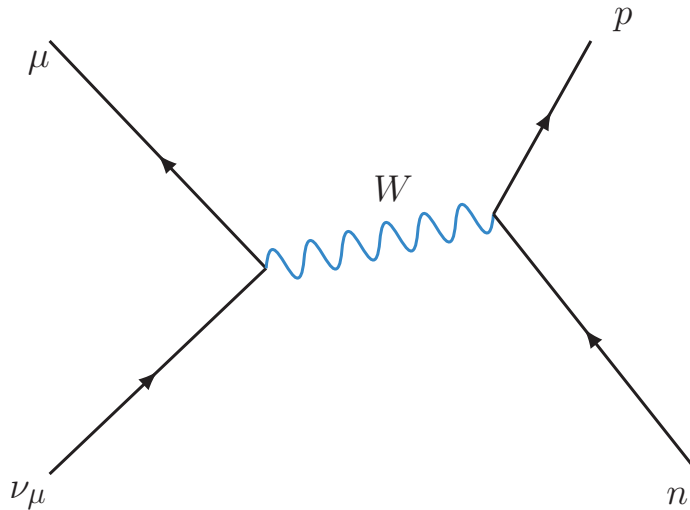


FIGURE 5.1: Feynman diagram shows the interaction of ν_μ with a neutron. The ν_μ interacts via CC interaction through an exchange of a charged W boson.

of a signal and a background event in the FD.

The muon from the signal ν_μ , being a minimum ionizing particle, leaves a long track in the FD and the hadronic activity gives a short hadronic shower near the interaction vertex. The long muon track is a distinctive signature of ν_μ interaction. The more momentum a muon has, the longer the resulting track is in the detector. Such events are unambiguously signal ν_μ CC. If the neutrino interaction produces a low energy μ then the signal μ would be hard to distinguish from the backgrounds. A neutrino interaction shown in the bottom picture in Fig. 5.2. creates a π^- and π^0 ,

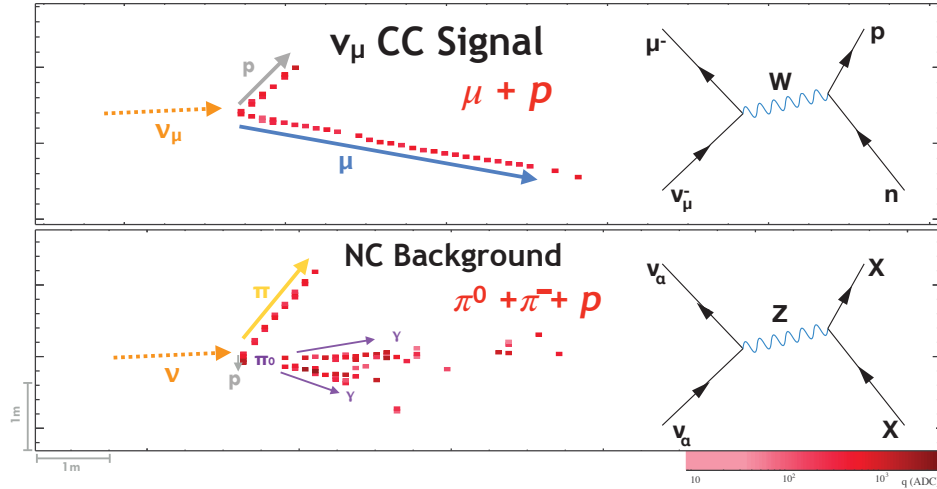


FIGURE 5.2: A pictorial representation to show the signal and one of the backgrounds in the ν_μ disappearance analysis. The signature of a ν_μ CC interactions is a long track of a muon and some activity at the interaction point in the detector. One of the background interaction is also pictured in which a neutrino interaction creates a π^- and a π^0 , and the π^0 decays into two photons.

and the π^0 decays in two photons (γ). The π^- has very similar dE/dx to the μ^- [61] and travels a short distance in the detector. The π^- can look like a low energy μ^- in the detector. The two γ s produce electromagnetic (EM) showers in the detector which look like some activity near the interaction vertex. The combination of a track from π^- and activity due to π^0 can mimic the signal ν_μ CC and therefore classify as a background event.

5.2.2 ν_μ Event Selection

The energy deposition in NOvA cells which we call cell hits are clustered to reconstruct candidate neutrino events [62]. The data are taken for a $500\mu\text{s}$ window centered on the $10\mu\text{s}$ NuMI beam spill window. These data are further divided into slices that are collections of hits close in time and space. There are usually 50 to 70 slices per $500\mu\text{s}$ window. Out of the $500\mu\text{s}$ window, $488\mu\text{s}$ of the data are rejected as out of spill data. This helps us to remove any events which are not in the NuMI beam window. Selections using the track information and the slice information are used to remove the cosmic activity in the remaining $12\mu\text{s}$ window. A deep-learning classifier, called the Convolutional Visual Network (CVN) [63], is trained over cosmic and simulated beam samples. The CVN finds the ν_μ CC events. The higher

the value of the CVN variable, the more likely the slice contains a ν_μ CC interaction. For this analysis, the CVN values are required to be greater than 0.5. The FD events are passed through a Boosted Decision Tree (BDT) [64], which helps to distinguish candidate ν_μ CC events from the cosmic muons. The BDT is trained over simulated and cosmic samples over several variables including the direction, position, and length of the tracks, the CVN value of the slice and the fraction of hits in a slice out of all hits in a $500\mu\text{s}$ window. The slices having CVN value of greater than 0.5 are allowed in this analysis. The following selections are used in the ν_μ analysis.

Data Quality: These selections ensure that the detector was working properly during data taking. They also ensure the quality of the data and reconstruction. We require at least 21 cell hits associated with a slice but less than 400 hits to ensure the slice has a valid Reconstructed Muon Identification (ReMID) value. The ReMID is used to find the presence of a muon in a slice. The trigger should have at least a cosmic track which ensures that the cosmic reconstruction worked and is also used in the cosmic veto to remove cosmic events. There should be at least one track with a valid ReMID value. For reconstruction, we require a slice to have hits in more than 4 continuous planes. The continuous planes selection also removes vertical tracks which are largely from cosmic muons. The cosine of the angle between the beam direction and the event track should be greater than 0.5 to remove cosmic muons and to retain events coming from the NuMI beam.

Containment: These selections are required to ensure that the energy deposited by the ν_μ CC event is within the detector volume, and are also needed to remove cosmic events in the FD and rock muons in the ND. Table 5.1 and Table 5.2 list the containment selections for the ND and the FD respectively.

In Table 5.1, the Kalman Forward Cell is the number of cells from the endpoint of the projection of the Kalman track to the edge of the detector in the forward direction including the muon catcher. The Kalman Backward Cell is the number of cells from the start point of the projection of the Kalman track to the edge of the detector in the backward direction including the muon catcher. The Minimum and Maximum Planes define the number of planes to be present in a slice. The other

Name of the Selection	Value (Unit)
Minimum Kalman Forward Cell	> 5 cells
Minimum Kalman Backward Cell	> 10 cells
Minimum Plane	> 1 planes
Maximum Plane	< 212 planes
Maximum Track Start Z Position	< 1100 cm
Maximum Track Stop Z Position	< 1275 cm
Start and Stop of Showers in X	≥ -180 cm
Start and Stop of Showers in X	≤ 180 cm
Start and Stop of Showers in Y	≥ -180 cm
Start and Stop of Showers in Y	≤ 180 cm
Start and Stop of Showers in Z	≥ 20 cm
Start and Stop of Showers in Z	≤ 1525 cm
Start and Stop of Tracks in Z to be not in muon catcher	≤ 1275 cm
Number of non-muon tracks in Muon Catcher	0

TABLE 5.1: Containment selections for the events in the ND. Containment selections make sure that the events have deposited energy in the detector volume.

selections make sure that the start and stop of the showers and Kalman tracks are well within the detector boundaries in all directions. We also require no non-muon tracks in the muon catcher.

In Table 5.2, the Cosmic Forward Cell is the number of cells from the endpoint of the cosmic track to the edge of the detector in the forward direction and the Cosmic Backward Cell is the number of cells from the start point of the cosmic track to the edge of the detector in the backward direction. The rest of the selections make sure that the events are well within the detector boundaries. The cosmic ray muons being charged particles are removed because they start activity right from the edges of the detectors.

Name of the Selection	Value (Unit)
Minimum Kalman Forward Cell	> 6 cells
Minimum Kalman Backward Cell	> 6 cells
Minimum Cosmic Forward Cell	> 0 cells
Minimum Cosmic Backward Cell	> 7 cells
Minimum Plane to Front	> 1 plane
Maximum Plane to Back	< 1 plane
Distance to FD Top	\geq 60 cm
Distance to FD Bottom	\leq 12 cm
Distance to FD East	\geq 16 cm
Distance to FD West	\leq 12 cm
Distance to FD Front	\geq 18 cm
Distance to FD Back	\leq 18 cm

TABLE 5.2: Containment selections for the events in the FD. Containment selections make sure that the events have deposited energy in the detector volume.

5.2.3 Energy Estimation and Analysis Binning

The maximum neutrino energy of 5 GeV is used in the ν_μ analysis. We keep neutrinos with energies greater than 5 GeV but the oscillation fit is done using the neutrino energy spectrum up to 5 GeV. Any events above 5 GeV are ignored in the oscillation fit for this analysis but can be used to extend this analysis if required. The neutrino energy, E_ν , in a slice is found from the sum of the hadronic, E_h , and muon, E_μ , energies. The muon energy is calculated from the length of the muon track and the hadronic energy from the hits in the slice which are not part of the muon track. The neutrino energy resolution for the ν_μ CC events is 9.1% in the FD and 11.8% in the ND. The presence of the active muon catcher degrades the neutrino energy resolution in the ND. The precise measurement of Δm_{32}^2 and $\sin^2 \theta_{23}$ parameters depend on the energy resolution of the ν_μ CC events near the oscillation dip region that is, near the disappearance maxima of 1.6 GeV. In this analysis, we use two types of binning. The first one has to do with the neutrino energy binning and the

second one has to do with the hadronic energy resolution. In the first method, we use variable neutrino energy binning having 0.1 GeV wide bins near the disappearance maxima and wider bins in the regions away from the disappearance maxima. In the second approach, we divide the whole ND and FD samples into four quartiles in order of increasing hadronic energy resolutions [65]. The quartiles are made using equally populated samples of events. The division of samples by quartiles helps to shift beam NC and cosmic events into the last quartile bin which has the maximum hadronic energy fraction and the worst neutrino energy resolution. The ν_μ energy resolution in the FD in the four quartile bins is 6.2%, 8.2%, 10.3%, and 12.3% respectively. Fig. 5.3 shows the comparison of the ND data sample to the total ν_μ simulated sample including the backgrounds. The simulated events in the plot are the sum of the beam ν_μ and $\bar{\nu}_\mu$ CC components. The ν_e and $\bar{\nu}_e$ CC and NC are the background components. The variable energy binning having the finer and coarser bins is shown too. Fig. 5.4 show different quartiles in order of increasing hadronic

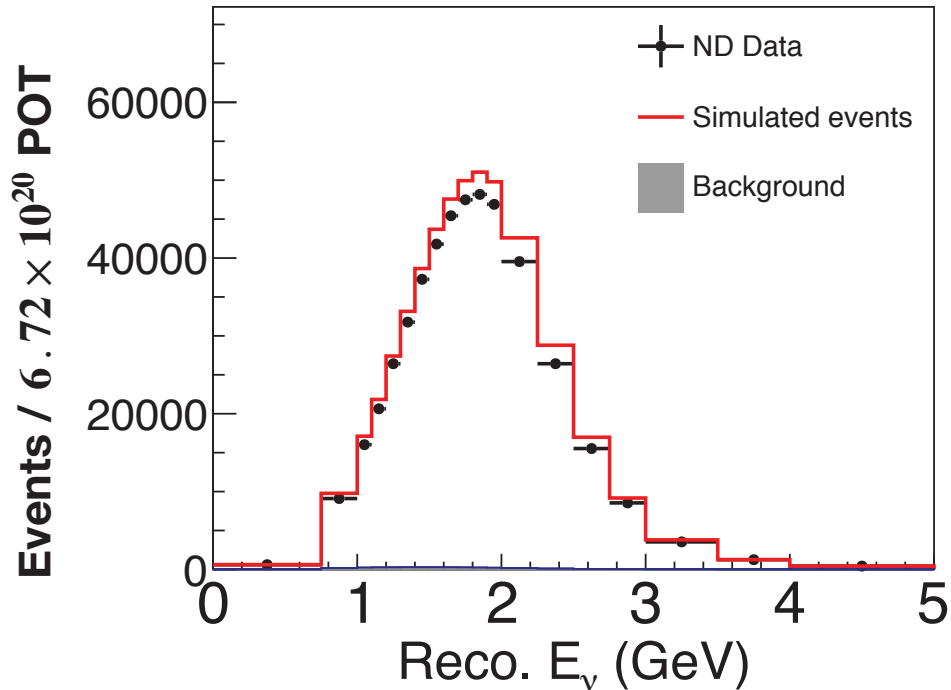


FIGURE 5.3: Comparison of the ν_μ selected ND data events to the ν_μ CC simulated events to show the variable energy binning. Various backgrounds in the ND are also shown. The simulated events are normalized to ND data POT and also normalized to the bin widths.

energy fractions made from Fig. 5.3. The number of ND data and simulated events

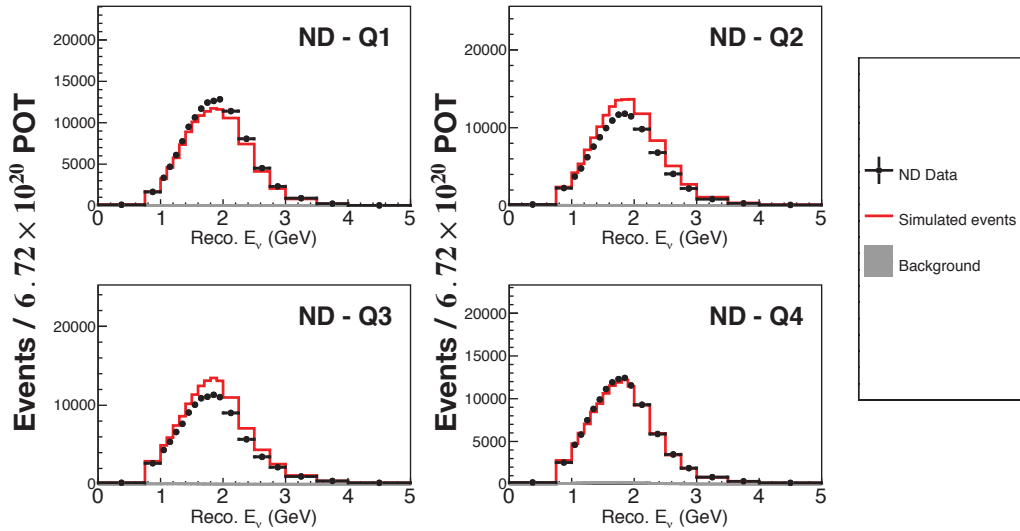


FIGURE 5.4: Comparison of the ν_μ selected ND data events to the ν_μ CC simulated events in different quartiles in order of increasing hadronic energy fractions. The background events are also added.

selected by the ν_μ selections are shown in Table 5.3. The ν_e and $\bar{\nu}_e$ CC, the NC backgrounds accumulates in the third and fourth quartiles.

ND Sample	Events				
	Q1	Q2	Q3	Q4	All Quartiles
Data	167897	157071	155013	162549	642530
ν_μ CC	149165.87	180919.07	176031.0	154545.69	660661.63
$\bar{\nu}_\mu$ CC	6803.40	4381.25	4034.68	2226.17	17445.50
ν_e CC	0.09	1.42	5.18	51.33	58.02
$\bar{\nu}_e$ CC	0	0	0.13	1.59	1.72
NC	128.27	276.90	668.40	3211.0	4284.57
Total MC	156097.63	185578.64	180739.38	160035.78	682451.43

TABLE 5.3: The Number of ND data and simulated events selected by the ν_μ selection.

5.2.4 ν_μ Selected FD Data

For the $\nu_\mu \rightarrow \nu_\mu$ analysis 126 ν_μ events in the FD are selected by the ν_μ selection. We expect $720.3^{+67.4}_{-47.0}$ (syst.) events in the absence of neutrino oscillation. The

disappearance of the ν_μ from the expected numbers is clear evidence of neutrino oscillation. Fig. 5.5 shows the neutrino energy spectrum of the selected 126 ν_μ events for each quartile. Fig. 5.6 shows the neutrino energy spectrum of all 126 ν_μ events. Table 5.4 shows the number of selected events in the FD by the ν_μ selection

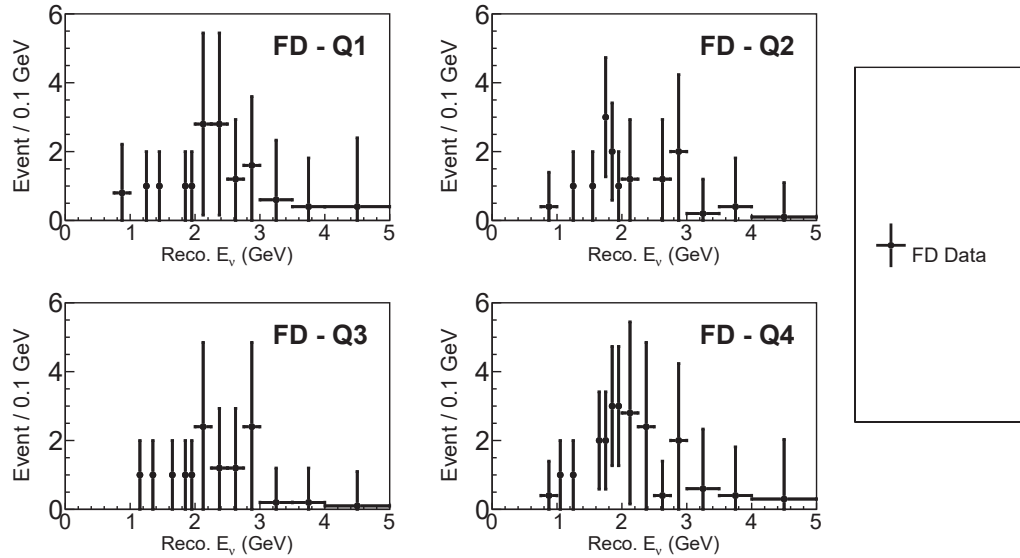


FIGURE 5.5: The ν_μ selected events is shown in the FD for the $\nu_\mu \rightarrow \nu_\mu$ analysis. In total 126 ν_μ events are selected. The neutrino energy spectra of all quartiles are shown.

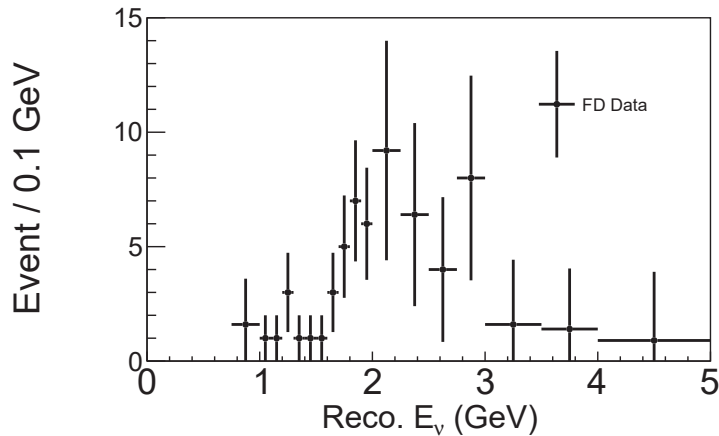


FIGURE 5.6: Neutrino energy spectrum of all ν_μ selected events in the FD is shown. This spectra is the sum of number of neutrinos shown in Fig. 5.5.

in each quartile bins. One of the ν_μ selected events in the FD is shown in Fig. 5.7. A clear straight long track shows the presence of the muon in the slice and some

Sample	Events				
	Q1	Q2	Q3	Q4	All quartiles
FD Data	36	24	26	40	126

TABLE 5.4: Number of FD selected events by the ν_{μ} selections in each quartile bin.

small hadronic activity near the neutrino interaction vertex. A few more ν_{μ} selected FD data events are shown in Appendix C.

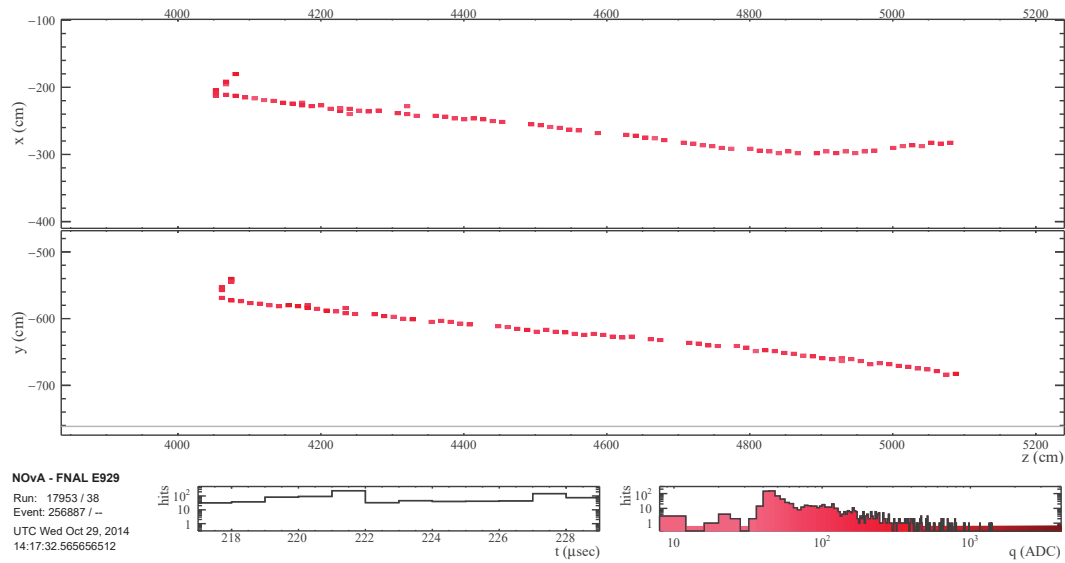


FIGURE 5.7: NOvA event display of one of the ν_{μ} FD data events for the $\nu_{\mu} \rightarrow \nu_{\mu}$ oscillations. A muon is clearly visible as a long straight track and some hadronic activity at the interaction vertex are clear signatures of the ν_{μ} CC interaction.

5.3 ν_e Appearance Analysis

For the ν_e appearance analysis, we search for ν_e s in the FD after the ν_{μ} s produced in the beam oscillated into ν_e s on their way from the ND to the FD. For the ν_e analysis, the NC interactions, and cosmic activity are the backgrounds. The intrinsic ν_e s from the NuMI beam also contribute an important background in the analysis.

5.3.1 Signal and Background Event Topologies

The appearing ν_e s interact via CC and NC interactions inside the FD. The ν_e CC interaction produces an electron and hadronic activity at the interaction vertex. The Feynman diagram in Fig. 5.8 shows the interaction of a ν_e with a neutron via exchange of a charged W boson producing an electron and a proton. Fig. 5.9

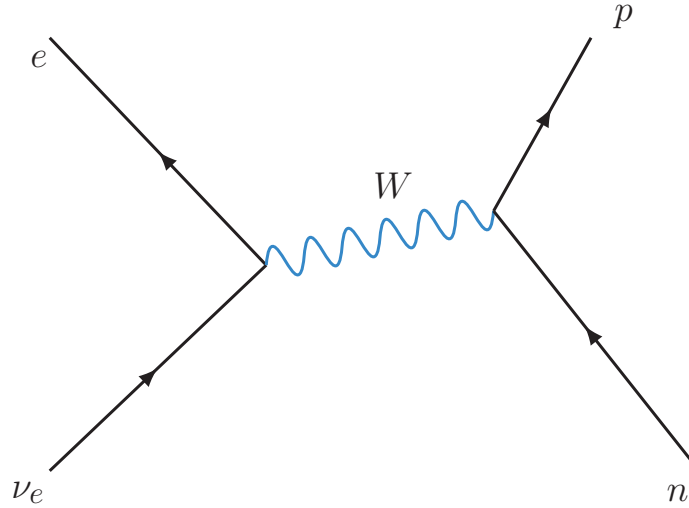


FIGURE 5.8: Feynman diagram shows the interaction of ν_e inside the FD. The ν_e interacts via CC interaction through exchange of a charged W boson producing an electron and a proton.

shows the expected signature of a signal and a background event in the FD. The electron from the signal ν_e interacts electromagnetically in the detector, producing an electromagnetic shower. The NC background shown in Fig. 5.9 is the same NC interaction from Fig. 5.2.

5.3.2 ν_e Event Selection

The purpose of the ν_e event selections is to find the sample of ν_e CC events and to reduce the backgrounds. For the ν_e analysis, the same cell hit and clustering mechanism is used as was explained for the ν_μ disappearance analysis in § 5.2.2. The ν_e CC events are selected for which the ν_e score under the same CVN technique is more than 0.75. Events passing the ν_e selections make the “core” sample in both near and far detectors. Other than the core sample, we also make a sample of FD events that have high ν_e CVN values but fail containment and cosmic rejection

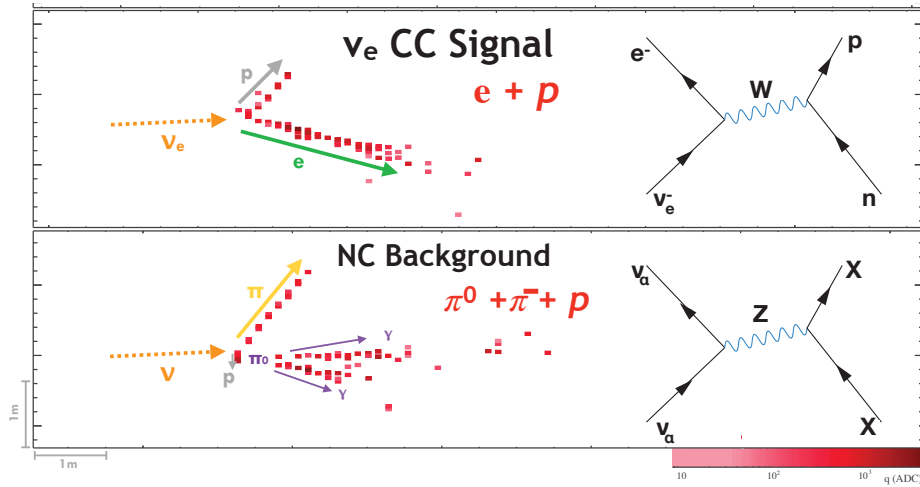


FIGURE 5.9: A pictorial representation to show a signal and a background in the ν_e appearance analysis. The signature of a ν_e CC interaction is an electromagnetic shower and hadronic activity at the interaction point in the detector. The background shown here is the same from Fig. 5.2.

selections. This sample is called the “peripheral” sample. The high value of the CVN ensures that the events in the peripheral sample are ν_e CC like-events and not from cosmic activity. As the events in the peripheral sample are not fully contained, we keep all the peripheral events in a single neutrino energy bin. The core sample is divided into 0.5 GeV bins from 0 to 4.5 GeV reconstructed neutrino energy in the ND and from 1 to 4 GeV in the FD. The addition of the peripheral sample to the core sample increases accumulated exposure of the total sample by 17.4%. The following selections are used in the ν_e analysis:

Data Quality: These selections ensure the quality of the data and the reconstruction. The ND and the FD have the same data quality selections. The data quality requires a slice to have less than 8 cell hits per plane to avoid sudden bursts of light in a front end board (FEB) which may indicate some failure in the FEB.

ND specific requirements: These selections are applied to the slices and events only in the ND. The coordinates of the vertex of any interaction are to be in a fiducial volume as shown in Table 5.5. The start and end of the showers should be fully contained in the detector volume as shown in Table 5.5. There should be no hits in the first five planes of the ND to make sure the event is away from the detector

boundaries. The number of cell hits in a slice should be between 20 to 200 to ensure that the reconstruction has enough hits to properly reconstruct the event. The ν_e having energies up to 4.5 GeV are allowed in the ν_e oscillation fit. The prong length in a slice should be between 100 cm to 500 cm to ensure the interaction is contained in the detector. Events having a ν_e CVN value more than 0.75 are allowed in this ν_e analysis.

Name of the Selection	Value (Unit)
Minimum vertex x-coordinate	≥ -100 cm
Maximum vertex x-coordinate	≤ 160 cm
Minimum vertex y-coordinate	≥ -160 cm
Maximum vertex y-coordinate	≤ 100 cm
Minimum vertex z-coordinate	≥ -150 cm
Maximum vertex z-coordinate	≤ 900 cm
Start and stop of showers in x-direction	≥ -170 cm
Start and stop of showers in x-direction	≤ 170 cm
Start and stop of showers in y-direction	≥ -170 cm
Start and stop of showers in y-direction	≤ 170 cm
Start and stop of showers in z-direction	≥ 100 cm
Start and stop of showers in z-direction	≤ 1225 cm

TABLE 5.5: The ND specific fiducial and containment selections for the ν_e CC events in the ν_e analysis.

FD specific requirements: These selections are applied to the slices and events only in the FD. The selections for the core and peripheral samples are slightly different. We require the events to pass at least 4 di-blocks of the FD for reconstruction. Cosmic vetos are applied to reject cosmic events before the reconstruction stages. For the core sample, the neutrino energies from 1 GeV to 4 GeV are allowed. We require the number of cell hits in a slice to be in the range of 30 hits to 150 hits. The length of the longest prong, which is the primary electromagnetic shower and the candidate ν_e CC event, is to be in the range 100 cm to 500 cm. Table 5.6 shows

the prong containment selections in terms of the distance of the prongs from the boundaries of the detector.

Name of the Selection	Value (Unit)
Distance from the top boundary	> 63 cm
Distance from the bottom boundary	> 12 cm
Distance from the east side of the detector	> 12 cm
Distance from the west side of the detector	> 12 cm
Distance from the front side of the detector	> 18 cm
Distance from the back side of the detector	> 18 cm

TABLE 5.6: The FD specific prong containment selections for the ν_e CC events in the core sample in terms of the distances from the sides of the detector.

We also apply selections on the transverse momentum, p_t , to reject cosmic events which are not aligned with the beam direction. The transverse momentum selection is termed as p_t/p and is the fraction of the transverse momentum in a slice. The p_t/p selection depends on the position in the detector. All events having $p_t/p < 0.58$ are allowed. If the maximum y-coordinate of the events is less than 590 cm then events having p_t/p value in the range 0.58 to 0.80 are allowed to fall in the core sample. If the maximum y-coordinate is less than 350 cm then the events should have $p_t/p > 0.8$ to pass the selections. In all other cases, the events fail the p_t/p selection. For the core sample, we also apply the backward selection, which removes cosmic ray generated photons entering from the back boundary of the detector. If the distance of the prong from the back side of the detector is more than 200 cm, then the event passes backward selection. Here we define “sparseness asymmetry” that is the asymmetry in the planes having zero hits at the start and the end of the shower. If the shower length is within 200 cm from the back side of the detector then events having sparseness asymmetry value < -0.1 are allowed to pass the backward selection. Any event which fails the above-defined selection criteria for the core sample becomes a candidate for the peripheral sample, subject to another set of selection requirements. In the FD as well, events need to have ν_e CVN value more than 0.75. Events in the peripheral sample have the same data quality and cosmic

veto selections. The peripheral events are allowed to have neutrino energies up to 4.5 GeV. The peripheral sample is made only in the FD. Events in the peripheral sample need to have a ν_e CVN value more than 0.95 which ensures they are signal-like events. Any slice, whether in the core sample or in the peripheral sample, within 100 ns and 500 cm from another slice is rejected in this analysis to remove cosmic backgrounds because cosmic-ray backgrounds are found to be close to other cosmic ray muons in time and space.

5.3.3 Energy Estimation and Analysis Binning

The reconstructed neutrino energy, E_ν^{reco} , in a candidate ν_e CC event is estimated using a polynomial function of the reconstructed hadronic, E_h , and leptonic, E_{em} , energies in the event. The reconstructed leptonic energy is the calibrated energy which belongs to the cells in the electromagnetic shower of the events. The reconstructed hadronic energy is the calibrated slice energy which is not in the electromagnetic shower. The reconstructed neutrino energy in a candidate ν_e CC event is given as [66],

$$E_\nu^{\text{reco}} = aE_{em} + bE_h + cE_{em}^2 + dE_h^2. \quad (5.1)$$

Here coefficients a and c represent the contribution or fraction of the electromagnetic shower, and b and d represent the contribution or fraction of the hadronic shower in the reconstructed ν_e energy. A quadratic fit to the 2D distribution of hadronic and leptonic energies yield values of parameters as given in [66],

$$E_\nu^{\text{reco}} = 0.996E_{em} + 0.869E_h + 0.025E_{em}^2 + 0.504E_{had}^2. \quad (5.2)$$

The sample events in the FD are divided into reconstructed energy bins as well as the CVN value bins. Each CVN bin has different signal and background components. The energy bins are uniformly divided into 0.5 GeV bins. The core sample is divided into three CVN bins, “low”, “mid” and “high”. The peripheral sample is added as a fourth CVN bin in the FD. The allowed values for the CVN bins are shown in Table 5.7. Three CVN bins and six energy bins from 1 GeV to 4 GeV for the core sample gives 18 bins, each of 0.5 GeV width. The peripheral sample is only kept in a single energy bin of width from 1 GeV to 4.5 GeV. In total, the ν_e analysis uses 19 analysis bins. Fig. 5.10 shows the comparison of the selected ND data sample to the selected ν_e simulated samples, including the backgrounds. The three CVN bins

CVN bin	Lower CVN value	Upper CVN value
Low	0.75	0.87
Mid	0.87	0.95
High	0.95	1.00
Peripheral	0.95	1.00

TABLE 5.7: Allowed values of the CVN for the “low”, “mid”, “high” and peripheral CVN bins in the FD. If an event has CVN value in the range lower to upper CVN allowed value then the event would fall in the corresponding CVN bin.

and the reconstructed energy bins are shown too. The solid green histogram shows simulated true ν_μ CC events by the ν_e selections, the solid pink shows the ν_e CC and solid blue are the NC events. The ND data events are shown by black points. The low CVN bin has the least ν_e CC component and the high CVN bin has the most ν_e CC component as expected from the ν_e CVN value. The higher the CVN value, the more ν_e CC component. The high CVN bin also has the least ν_μ CC and NC background components. The ND simulated events are normalized to the ND data exposure of 6.72×10^{20} POT. The number of ND data and simulated events selected by the ν_e selections are shown in Table 5.8. The ν_e and $\bar{\nu}_e$ CC events increase from the low to the high CVN bins. The ν_μ and $\bar{\nu}_\mu$ CC and NC events decrease.

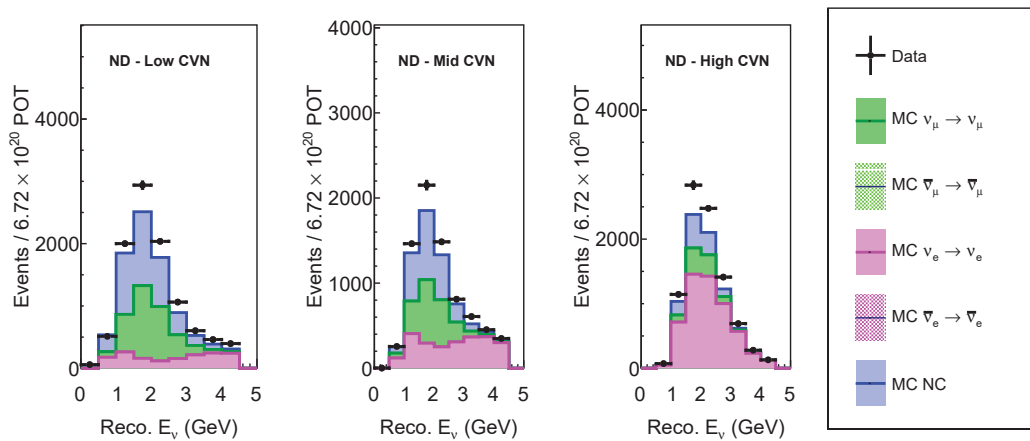


FIGURE 5.10: Comparison of ν_e selected ND data sample to the ν_e selected simulated events. Various backgrounds in the ND are also shown.

ND Sample	Events			
	Low CVN	Mid CVN	High CVN	All CVNs
Data	10063	7575	9039	26677
ν_μ CC	3350.39	2077.87	990.02	6418.28
$\bar{\nu}_\mu$ CC	37.77	14.95	5.27	57.99
ν_e CC	1560.60	2411.24	5563.30	9535.15
$\bar{\nu}_e$ CC	152.53	252.48	409.09	814.11
NC	3889.03	2341.71	1245.63	7476.37
Total MC	8990.33	7098.25	8213.32	24301.9

TABLE 5.8: Number of ND data and simulated events selected by the ν_e selection. As expected, the ν_e CC and $\bar{\nu}_e$ CC components increase from the Low to the High CVN bins and the ν_μ CC, $\bar{\nu}_\mu$ CC and NC components decrease.

5.3.4 ν_e Selected FD Data

For the $\nu_\mu \rightarrow \nu_e$ analysis, 66 ν_e events in the FD are selected by the ν_e selections. Fig. 5.11 shows the neutrino energy spectrum of the selected 66 ν_e events for the three CVN bins and the fourth peripheral bin. Table 5.9 shows the number of the

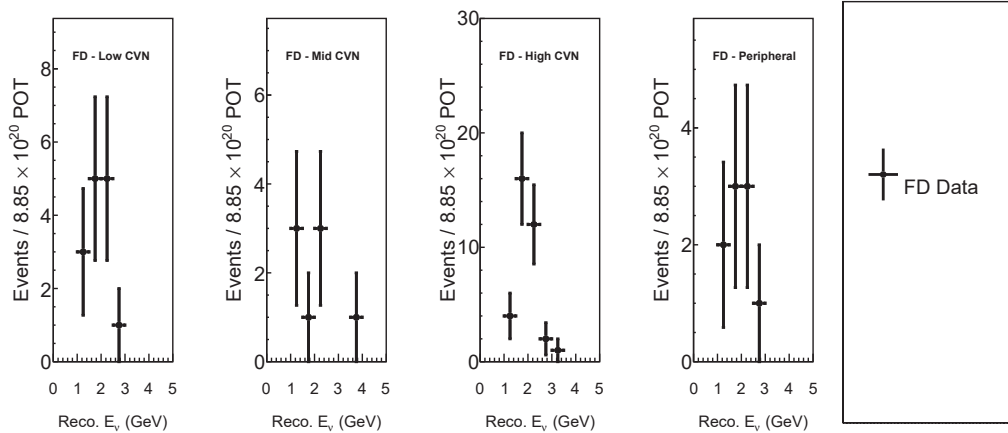


FIGURE 5.11: Selected ν_e events in the FD for $\nu_\mu \rightarrow \nu_e$ analysis. In total 66 ν_e events are selected. The energy and CVN spectrum of the selected FD events are shown.

selected events in the FD by the ν_e selections in each CVN bins. The majority of the data events are selected in the High CVN bin. The contribution from the peripheral bin is 13.6%, almost same as the Mid CVN bin.

One of the ν_e selected FD data events is shown in Fig. 5.12. One can very clearly see the electromagnetic shower and some hadronic activity near the neutrino interaction

Sample	Events				
	Low	Mid	High	Peripheral	All
FD Data	14	8	35	9	66

TABLE 5.9: Number of FD selected events by the ν_e selections in each CVN and peripheral bin.

vertex. Appendix B shows the NOvA event displays of few more ν_e select FD data events.

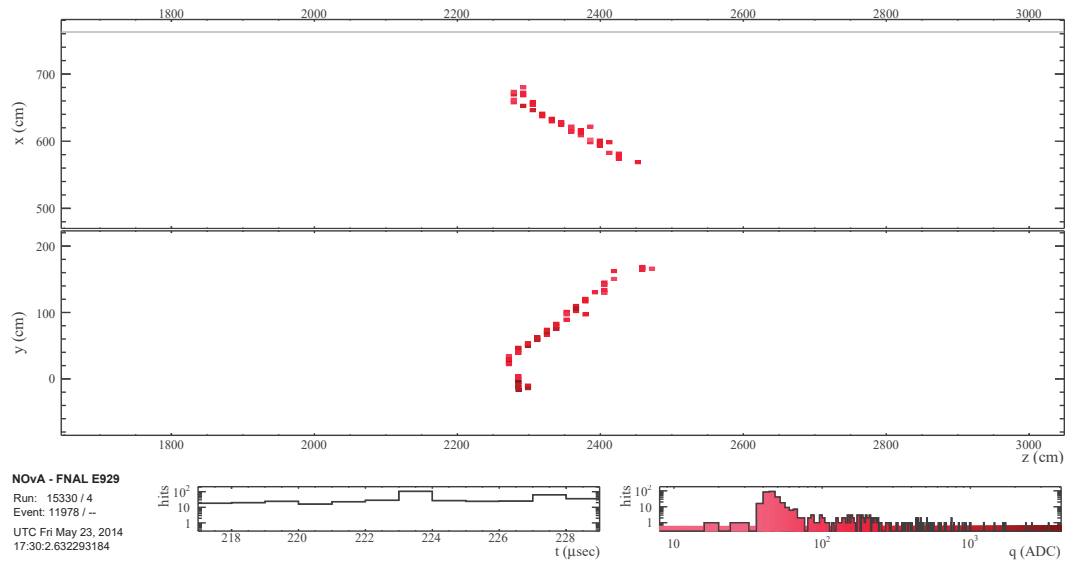


FIGURE 5.12: NOvA event display of one of the selected ν_e FD data events for the $\nu_\mu \rightarrow \nu_e$ analysis.

5.4 Extrapolation: Constraints from the ND

The ND has no ν_μ disappearance and ν_e appearance events because there is no oscillation from ν_μ to ν_e into the ND. The ND has only the beam ν_μ CC, $\bar{\nu}_\mu$ CC, ν_e CC, $\bar{\nu}_e$ CC and the NC events. The simulated spectra in the ND is used to make the signal and background predictions in the FD for both the ν_e appearance and ν_μ disappearance analyses.

5.4.1 ν_e Signal and Background Extrapolation

For the $\nu_\mu \rightarrow \nu_e$ analysis, the signal in the FD is the ν_e CC events that come from the oscillation of beam ν_μ CC events. All other neutrino interactions constitute backgrounds in the FD. So, for the ν_e appearance analysis, the events in the ND selected by the ν_e selections can only help to make predictions of the background events. The signal prediction in the FD is made by using the ν_μ CC events in the ND. Here we assume that the variations in the ν_e CC spectrum in the FD are related to the variations in the ν_μ CC spectrum in the ND because the signal ν_e CC comes from the oscillation of the ν_μ CC observed in the ND.

To make the predictions for the signal events, the simulated ν_μ CC events in the ND are selected using the true information about the neutrino flavor coming from the simulation. The true information is associated with every simulated event from the generation state. For the signal prediction, we start by selecting the ND data and simulated ν_μ CC events. The ND data and simulated events are kept in reconstructed neutrino energy bins as shown in Fig. 5.13

Using the reconstructed energy bins, we make ratios, $R^{\nu_\mu, ND}(E_i^{\text{reco}})$ of the ND data and simulated ν_μ CC events. The ratios are defined as,

$$R^{\nu_\mu, ND}(E_i^{\text{reco}}) = \frac{N^{\text{data}}(E_i^{\text{reco}})^{\nu_\mu}}{N^{\text{MC}}(E_i^{\text{reco}})^{\nu_\mu}}, \quad (5.3)$$

where the ν_μ subscript on the left and right sides represents ν_μ CC interactions selected by the ν_μ selection for each reconstructed energy bin (E_i^{reco}). The bin by bin ratios of the ND data and simulated events are shown in Fig. 5.14. The ratios, $R^{\nu_\mu, ND}(E_i^{\text{reco}})$, are used to make the signal extrapolation weights from the ND to the FD. This method of using the ND data and simulated events for making a signal prediction is called the data-driven method as it uses the ND data events. To make the extrapolation weights, we first make a 2D spectrum of true and reconstructed neutrino energies of the ND ν_μ CC events selected by the ν_μ selections as shown in Fig. 5.15. Each 2D true and reconstructed energy bin in Fig. 5.15 is represented by $N_{\nu_\mu}^{\text{MC}}(E_j^{\text{true}}, E_i^{\text{reco}})$.

The reconstructed energy ratios, $R^{\nu_\mu, ND}(E_i^{\text{reco}})$, are applied as weights to all true energy bins corresponding to the i^{th} reconstructed bin as shown in Fig. 5.16. The

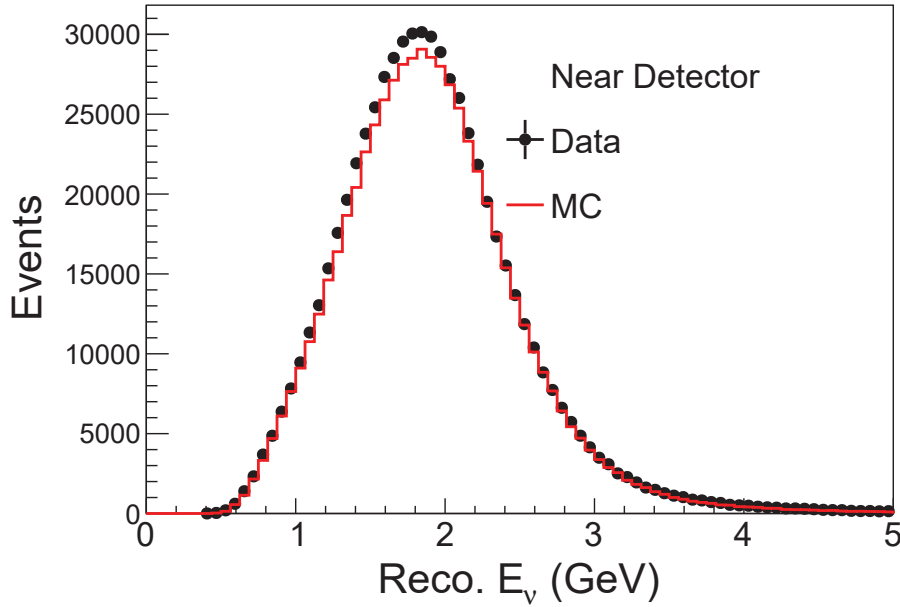


FIGURE 5.13: The selected data and simulated ν_μ CC events in the ND in reconstructed neutrino energy bins are shown. The ND data and simulated events are used to make the signal prediction in the FD for both the ν_μ disappearance and ν_e appearance analyses.

reconstructed energy bins are summed for each true energy bin to make the true data-driven spectrum of ν_μ CC events. The true energy spectrum is called the “predicted” spectrum in the ND and is denoted by $N_{\nu_\mu}^{\text{Prediction}}(E_j^{\text{true}})$,

$$N_{\nu_\mu}^{\text{Prediction}}(E_j^{\text{true}}) = \sum_{\substack{\text{Reco. events in } j^{\text{th}} \\ \text{true energy bin}}} R^{\nu_\mu, ND}(E_i^{\text{reco}}) \times N_{\nu_\mu}^{\text{MC}}(E_j^{\text{true}}, E_i^{\text{reco}}), \quad (5.4)$$

and is shown in Fig. 5.17.

The ratio of the $N_{\nu_\mu}^{\text{Prediction}}(E_j^{\text{true}})$ to the true $N_{\nu_\mu}^{\text{MC}}(E_j^{\text{true}})$ is denoted by $R^{\nu_\mu, ND}(E_j^{\text{true}})$ and is given as,

$$R^{\nu_\mu, ND}(E_j^{\text{true}}) = \frac{N_{\nu_\mu}^{\text{Prediction}}(E_j^{\text{true}})}{N_{\nu_\mu}^{\text{MC}}(E_j^{\text{true}})}, \quad (5.5)$$

The bin by bin ratios $R^{\nu_\mu, ND}(E_j^{\text{true}})$ are shown in Fig. 5.18. The distribution of ratios in Fig. 5.18 is smooth compared to ratios in Fig. 5.14.

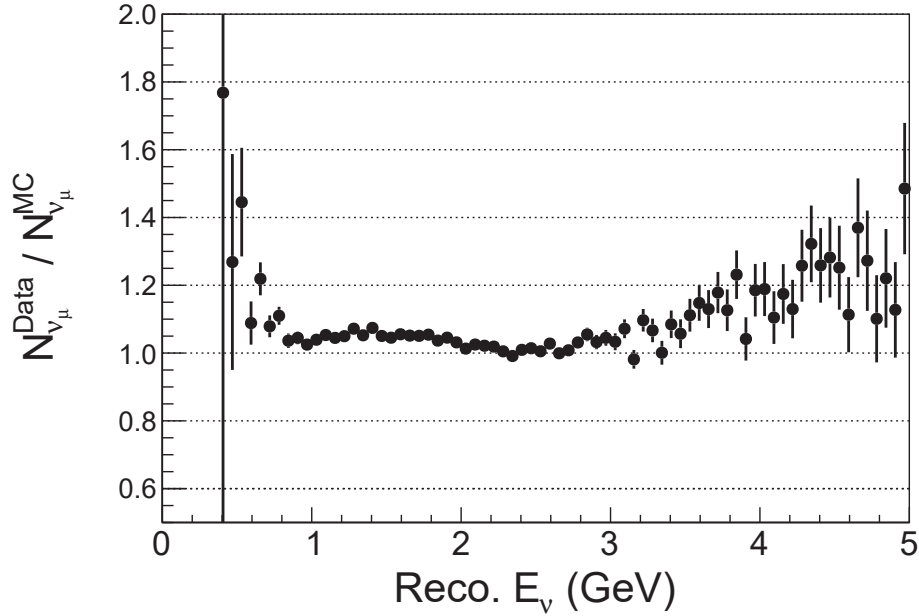


FIGURE 5.14: The ratios of the ND data and simulated ν_μ CC events in reconstructed neutrino energy bins are shown. The ratios of the ND data and simulated events are used in the signal extrapolation from the ND to the FD.

The ratios in Fig. 5.18 are used as extrapolation weights for predicting the ν_e appearance signal. If a simulated event in the FD has true energy in the j^{th} bin then it receives $R^{\nu_\mu, ND}(E_j^{\text{true}})$ as the extrapolation weight. The extrapolation weights are added to a large list of weights which includes weights from various systematic uncertainties. To find the predicted number of events in the FD for the $\nu_\mu \rightarrow \nu_e$ oscillations, $F_{\nu_\mu \rightarrow \nu_e}^{\text{Prediction}}(E_i^{\text{reco}})$, in reconstructed energy bin, i , we weight each FD simulated event, that is $F_{\nu_\mu \rightarrow \nu_e}^{\text{MC}}$, having true energy, E_j^{true} , by the extrapolation weight, $R^{\nu_\mu, ND}(E_j^{\text{true}})$ and the oscillation probability, $P_{\nu_\mu \rightarrow \nu_e}(E_{\text{event}}^{\text{true}})$ of each $\nu_\mu \rightarrow \nu_e$ oscillated event. Finally we sum all the events falling in reconstructed energy bin, i , to predict the total number of ν_e appearance signal events. Equation 5.6 shows the expression we use to predict the ν_e appearance signal events,

$$F_{\nu_\mu \rightarrow \nu_e}^{\text{Prediction}}(E_i^{\text{reco}}) = \sum_{\substack{\text{Events in } i^{\text{th}} \\ \text{reco. energy bin}}} F_{\nu_\mu \rightarrow \nu_e}^{\text{MC}} \times R^{\nu_\mu, ND}(E_j^{\text{true}}) \times P_{\nu_\mu \rightarrow \nu_e}(E_{\text{event}}^{\text{true}}). \quad (5.6)$$

For the background predictions, the ND has no $\nu_\mu \rightarrow \nu_e$ appearance signal events.

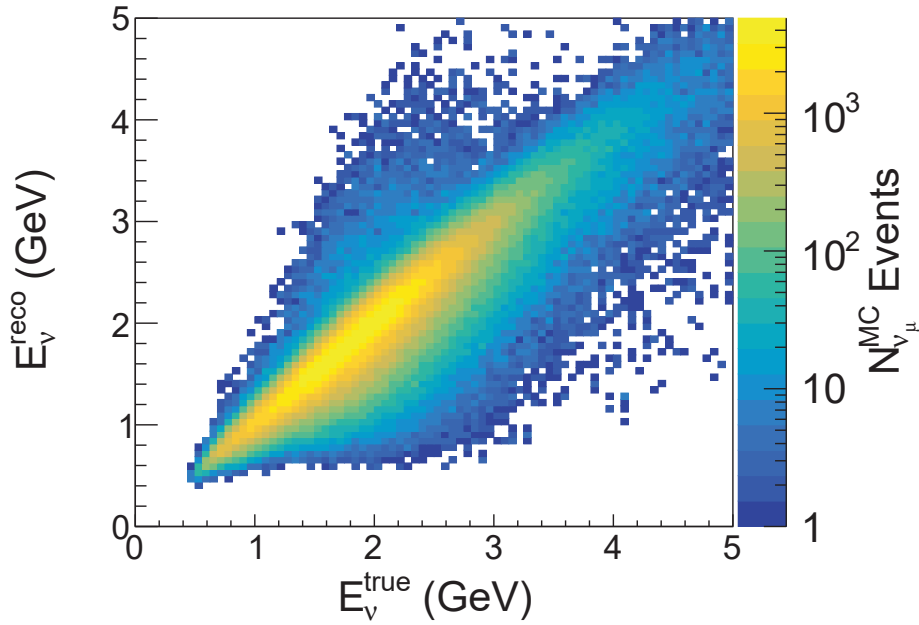


FIGURE 5.15: The true and reconstructed neutrino energies of the ND ν_μ CC events selected by the ν_μ selections are shown as a 2D spectrum. The true energy bins are to be weighted by the ratios of the ND data and simulated events shown in Fig. 5.14 to make the predictions in the FD.

The ND has only ν_μ CC, ν_e CC and NC components from the beam. The ν_e CC events from the beam are denoted by ν_e^{beam} . Any events in the ND are some kind of background to the analysis. The events selected by the ν_e selections are used to make the background predictions for the ν_e appearance analysis. We start by adding all the beam components in the ND. So, for the ν_e analysis we have,

$$N^{\text{MC}}\left(E_i^{\text{reco}}\right)_{\nu_e} = \sum_{k=1}^3 N_k^{\text{MC}}\left(E_i^{\text{reco}}\right)_{\nu_e}, \quad (5.7)$$

here $N^{\text{MC}}\left(E_i^{\text{reco}}\right)_{\nu_e}$ are the sum of all simulated (MC) background events selected by the ν_e selections in reconstructed bin, E_i^{reco} . The $N_k^{\text{MC}}\left(E_i^{\text{reco}}\right)_{\nu_e}$ is the background component for $k = \{\nu_e^{\text{beam}}, \nu_\mu, \text{NC}\}$. Now we identify deficits or excesses in these backgrounds by taking the ratios of the simulated events to the selected ND data events. For the ν_e analysis we have,

$$R^{\nu_e, \text{ND}}\left(E_i^{\text{reco}}\right)_{\nu_e} = N^{\text{Data}}\left(E_i^{\text{reco}}\right)_{\nu_e} / N^{\text{MC}}\left(E_i^{\text{reco}}\right)_{\nu_e}. \quad (5.8)$$

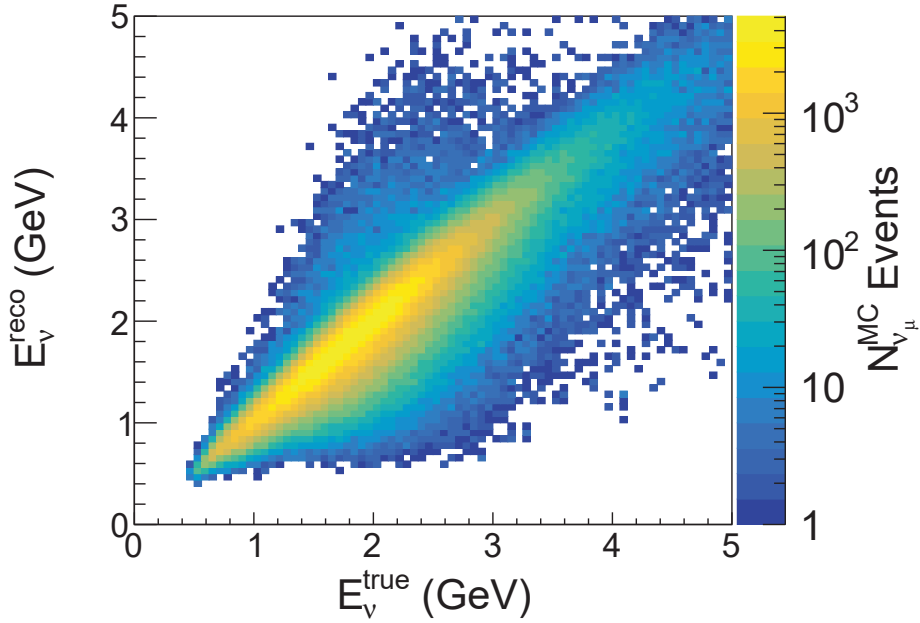


FIGURE 5.16: The weighted 2D spectrum showing the true and reconstructed neutrino energies of the ND ν_μ CC events selected by the ν_μ selections. The true energy bins are weighted by the ratios of the ND data and simulated events to make the predictions in the FD.

We use the ratios to make the predictions of the background components by weighting the simulated background events in the FD by the background extrapolation weights and the oscillation probabilities for the background components. For the ν_e analysis, the background prediction is,

$$F_k^{\text{Prediction}}(E_i^{\text{reco}}) = \sum_{\substack{\text{Events in } i^{\text{th}} \\ \text{reco. energy bin}}} F_k^{\text{MC}} \times R^{\nu_e, \text{ND}}(E_i^{\text{reco}})_{\nu_e} \times P_k^{\text{osc}}(E_{\text{event}}^{\text{true}}), \quad (5.9)$$

here the $F_k^{\text{Prediction}}(E_i^{\text{reco}})$ is the total number of predicted events of background type k in the reconstructed energy bin, i for the ν_e selections. The F_k^{MC} are the simulated background events in the FD and $P_k^{\text{osc}}(E_{\text{event}}^{\text{true}})$ is the oscillation probability from ND to the FD for the background component.

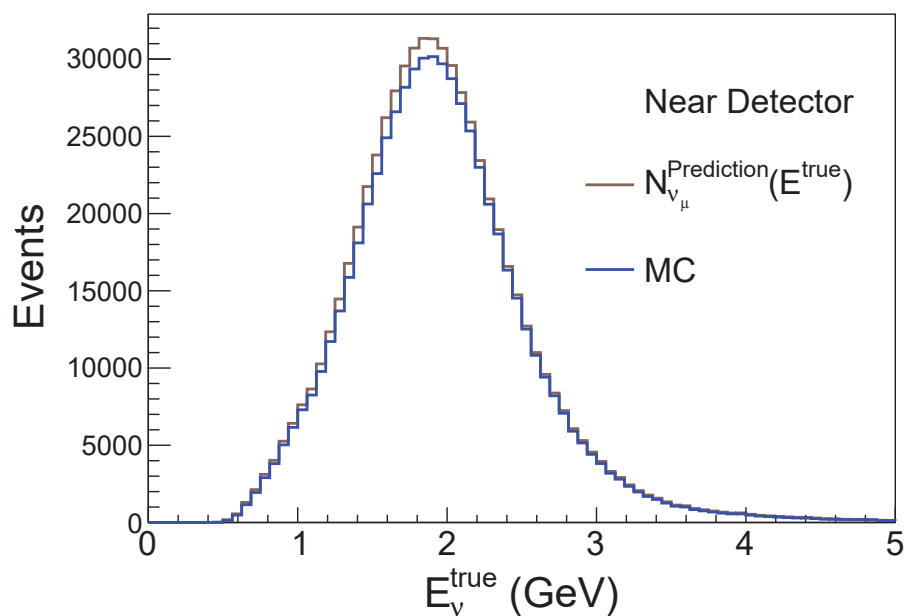


FIGURE 5.17: The predicted true energy spectrum, $N_{\nu_\mu}^{\text{Prediction}}(E_j^{\text{true}})$, of the ν_μ CC events selected by the ν_μ selections. The ratios of the $N_{\nu_\mu}^{\text{Prediction}}(E_j^{\text{true}})$ to the reconstructed spectra, $N_{\nu_\mu}^{\text{MC}}$ are used to make the signal predictions in the FD.

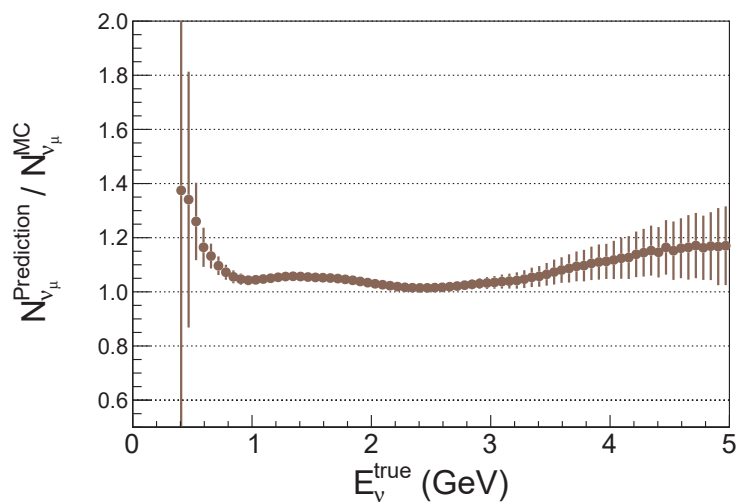


FIGURE 5.18: The ratios of the ND predicted and simulated ν_μ CC events in true neutrino energy bins are shown. These ratios are used in the signal extrapolation.

The total prediction in the FD can be obtained by adding the signal and background predictions. For the ν_e analysis the total predictions in the FD is,

$$F^{\text{Prediction}}\left(E_i^{\text{reco}}\right) = F_{\nu_\mu \rightarrow \nu_e}^{\text{Prediction}}\left(E_i^{\text{reco}}\right) + \sum_{k=\{\nu_e^{\text{beam}}, \nu_\mu, \text{NC}\}} F_k^{\text{Prediction}}\left(E_i^{\text{reco}}\right). \quad (5.10)$$

5.4.2 ν_μ Signal and Background Extrapolation

For the $\nu_\mu \rightarrow \nu_\mu$ disappearance analysis, the ν_μ CC events in the FD which survive the oscillation constitute the signal events. So, the ν_μ CC events in the ND can be used to make the ν_μ CC signal prediction in the FD.

The ratios in Fig. 5.18 are used as extrapolation weights for predicting the ν_μ signal events for the ν_μ disappearance analysis. For finding the prediction of the ν_μ disappearance signal events, the ν_e selections are replaced by the ν_μ selections in the FD for selecting ν_μ CC events. The oscillation weights used are $P_{\nu_\mu \rightarrow \nu_\mu}\left(E_{\text{event}}^{\text{true}}\right)$. The prediction of ν_μ signal events is given by,

$$F_{\nu_\mu \rightarrow \nu_\mu}^{\text{Prediction}}\left(E_i^{\text{reco}}\right) = \sum_{\substack{\text{Events in } i^{\text{th}} \\ \text{reco. energy bin}}} F_{\nu_\mu \rightarrow \nu_\mu}^{\text{MC}} \times R^{\nu_\mu, \text{ND}}\left(E_j^{\text{true}}\right) \times P_{\nu_\mu \rightarrow \nu_\mu}\left(E_{\text{event}}^{\text{true}}\right). \quad (5.11)$$

For the background predictions, as was explained in the introduction of the extrapolation § 5.4, the ND has no $\nu_\mu \rightarrow \nu_\mu$ disappearance signal events. The ND has only ν_μ CC, ν_e CC and NC components from the beam. We assume the backgrounds in the ND are same as in the FD and just apply a single prediction weight to all background events. For the ν_μ disappearance the total simulated background sample is obtained by,

$$N^{\text{MC}}\left(E_i^{\text{reco}}\right)_{\nu_\mu} = \sum_{k=\{\nu_e^{\text{beam}}, \nu_\mu, \text{NC}\}} N_k^{\text{MC}}\left(E_i^{\text{reco}}\right)_{\nu_\mu}. \quad (5.12)$$

For identifying backgrounds for the ν_μ analysis we have,

$$R^{\nu_\mu, \text{ND}}\left(E_i^{\text{reco}}\right)_{\nu_\mu} = N^{\text{Data}}\left(E_i^{\text{reco}}\right)_{\nu_\mu} / N^{\text{MC}}\left(E_i^{\text{reco}}\right)_{\nu_\mu}. \quad (5.13)$$

For the ν_μ analysis, the background prediction is simply obtained by replacing the selections ν_e by the ν_μ . For the ν_μ analysis the prediction of the background component is,

$$F_k^{\text{Prediction}}\left(E_i^{\text{reco}}\right) = \sum_{\substack{\text{Events in } i^{\text{th}} \\ \text{reco. energy bin}}} F_k^{\text{MC}} \times R^{\nu_\mu, ND}\left(E_i^{\text{reco}}\right)_{\nu_\mu} \times P_k^{\text{osc}}\left(E_{\text{event}}^{\text{true}}\right). \quad (5.14)$$

For the ν_μ analysis the total signal and background prediction in the FD is,

$$F^{\text{Prediction}}\left(E_i^{\text{reco}}\right) = F_{\nu_\mu \rightarrow \nu_\mu}^{\text{Prediction}}\left(E_i^{\text{reco}}\right) + \sum_{k=\{\nu_e^{\text{beam}}, \nu_\mu, \text{NC}\}} F_k^{\text{Prediction}}\left(E_i^{\text{reco}}\right). \quad (5.15)$$

5.5 Fitting Procedure

In this analysis, we calculate χ^2 at various points in the oscillation space for the ν_μ disappearance, ν_e appearance and the joint $\nu_\mu - \nu_e$ fits. In all cases, we use MINUIT [67] to minimize χ^2 from the fit to the data. MIGRAD [67] is used to extract the errors on the values of the oscillation parameters from the oscillation fit. Systematic uncertainties are added in the oscillation fit and are allowed to freely float in the fit. The systematic uncertainties increase the χ^2 by adding a small term to it which we call a pull term. A systematic uncertainty adds a pull term to the χ^2 only if the fit requires a non-zero central value of the uncertainty. FD data contours are produced once the best fit values of the oscillation parameters are obtained from the fit of the FD data. To make the contours, the χ^2 are calculated at various grid points in the oscillation space of oscillation parameters, for example, the $\sin^2 \theta_{23}$ and Δm_{32}^2 for the ν_μ disappearance and $\sin^2 \theta_{23}$ and δ_{cp} for the ν_e appearance and the combined $\nu_\mu - \nu_e$ fits. In the oscillation fit, we minimize the effect of the other oscillation parameters, θ_{13} , θ_{12} and Δm_{21}^2 , by keeping them fixed in the fit.

5.5.1 Binned χ^2

For the calculation of χ^2 , we distribute FD events in energy bins and calculate χ^2 for each bin. This method is called ‘‘binned χ^2 ’’. In the end, the χ^2 from all bins are added to measure the overall χ^2 of the fit. Each selected event in energy bins is weighted by the oscillation probabilities and the systematic uncertainties. At each

iteration of the oscillation fit, χ_i^2 is calculated for each energy bin using,

$$\chi_i^2 = 2 \times \left(F_i^{\text{Predicted}} - F_i^{\text{Data}} + F_i^{\text{Data}} \ln \frac{F_i^{\text{Data}}}{F_i^{\text{Predicted}}} \right), \quad (5.16)$$

where F_i^{Data} is the number of FD data events in energy bin i . The $F_i^{\text{Predicted}}$ are the number of predicted FD events.

5.6 Incorporation of Systematic Uncertainties

There are various sources of systematic uncertainties which indicate what we do not know about physics and our detectors. The simulations are used to estimate the effects of systematic uncertainties. The systematic uncertainties are added as nuisance parameters in the oscillation fit. For making the sensitivities and the data contours, the systematic uncertainties add a penalty term to the χ^2 evaluation. The contribution from the systematic uncertainties to the χ^2 evaluation is

$$\chi_{\text{syst.}}^2 = \sum_j^{\text{syst.}} \chi_j^2 = \sum_j^{\text{syst.}} \frac{(\epsilon_j - \langle \epsilon_j \rangle)^2}{\sigma_{\epsilon_j}^2}, \quad (5.17)$$

where $\chi_{\text{syst.}}^2$ is the total contribution from all systematics added in the oscillation fit, χ_j^2 is the penalty contribution from a particular systematic uncertainty denoted by index j , ϵ_j is the converged value of the systematic uncertainty after the oscillation fit, $\langle \epsilon_j \rangle$ is the expected central value for the systematic uncertainty and σ_{ϵ_j} is the 1σ uncertainty on the central value. The systematic uncertainties are added as free parameters in the oscillation fit. The sum of the χ^2 values from equation 5.16 over all reconstructed energy bins in the spectrum and equation 5.17 over all systematic uncertainties, make the total χ^2 in a fit. The fitter minimizes the total χ^2 to find the best fit values of the oscillation parameters and the converged values of the systematic uncertainties.

In this analysis, there are many sources of systematic uncertainty that are taken into account. These systematic uncertainties are divided into broad categories, for example, the neutrino beam flux, the neutrino cross-sections, the calibration of the detectors, the GENIE model, the detector response to light, normalization, and signal and background extrapolations. Some of the systematic uncertainties are not important because they have very little or no effect on the neutrino energy

spectra. Only the largest systematic uncertainties are taken into account in the final oscillation fit to the data. Before we add the systematic uncertainties in the final fit, we ran several tests to make sure that the oscillation fitter can fit systematic uncertainties. For these tests, we used the sample of simulated events and made fake data. In the fake data, we kept information like the reconstructed energies and the event identification. Unlike in the simulation, the true information about the events is not retained. For the tests, we add 1σ systematic uncertainty in the fake data and also add it as a free parameter in the fit. As the fit runs, the fitter tries to minimize the χ^2 value to get the best fit values of the oscillation parameters and the systematic uncertainty. We ran these tests for each systematic uncertainty. These tests give us confidence in fitter performance.

In the following subsections, a brief description of all systematic uncertainties is given.

5.6.1 Calibration

The calibration uncertainties are evaluated using the discrepancies in the simulated and data events after the calibrations are applied. The calibration uncertainties are evaluated from the variation of the detector response to light for the calibrated X and Y view cells as shown in Figs. 4.7 and 4.8 for the ND and Figs. 4.9 and 4.10 for the FD. The slopes and offsets in the detector response are fitted with a polynomial function to evaluate the calibration uncertainties. The calibration uncertainties are divided into two categories, the absolute calibration, which is correlated between the ND and the FD and the relative calibration, which is uncorrelated between the two detectors. We take uncertainty on the absolute and relative calibrations of 5% each.

5.6.2 Normalization

The uncertainties in the calculation of the mass of the detectors, POT accounting, reconstruction efficiencies of detectors and simulation of the pile-up of beam events in the ND due to its closeness to the neutrino source are added in quadrature to estimate the normalization effects. A Normalization systematic uncertainty of 3.5% is added in the analysis to account for the above effects. The normalization systematic uncertainty is divided into two categories, the absolute normalization, which is

applied to both the ND and the FD, and the relative normalization, which is applied only to the FD spectrum. The absolute normalization more or less cancels during the extrapolation of the signal and background samples from the ND to the FD.

5.6.3 Cross sections and GENIE

The reweighting framework of GENIE [60] provides the estimates for various neutrino cross-section uncertainties. Some modifications using the NOvA ND data are also incorporated along with GENIE suggestions in the estimation of the cross-section uncertainties. The weights suggested by the GENIE authors are applied to either enhance or suppress quasi-elastic (QE) and resonance events. The uncertainty on the shape of the meson exchange current (MEC) interactions [68] is also taken into account and the GENIE corrections to NC and CC interactions are also applied. A 2% uncorrelated uncertainty on the ratio of the ν_e to ν_μ cross-sections [3] is applied. A 2% anti-correlated uncertainty between the ν_e and $\bar{\nu}_e$ [3] is also applied.

5.6.4 Extrapolation

As explained earlier, the selected sample in the ND is used to make the signal and background predictions in the FD. The difference in the sizes of the ND and the FD leads to differences in the signal and background predictions if the extrapolation is done using different sections of the ND (e.g. the east/west/top/bottom) compared to the whole ND body. For the background prediction using sub-sections of the ND, the maximum relative difference to the background predictions comes to be 1.2% for the core sample and 1.3% for the peripheral sample. For the signal predictions, the ν_μ CC selected sample in the ND is used to make the prediction of the ν_e signal in the FD. The ν_μ CC sample in the ND is weighted to match the kinematics of the ν_e simulated sample in the FD. The weighting of the ND ν_μ CC sample leads to a maximum difference of 2.0% for the core and 3.0% for the peripheral sample.

5.6.5 Neutrino Beam Flux

There are two types of neutrino flux systematic uncertainties considered in this analysis, the hadron production, which has to deal with the uncertainties in the

production of the muon and kaon in the simulation and the beam transport, which deals with the uncertainties in the simulation and actual working conditions of the NuMI beam. The beam transport uncertainty includes uncertainties from the target and horn positions, the beam position, the beam spot size, and the horn current. The effect of each of these uncertainties is less than 5% both at the ND and the FD.

5.6.6 Muon and Calorimetric Energy Scales

The muon and calorimetric energy scale systematic uncertainty affects the ND and the FD differently. These systematic uncertainties are divided into absolute and relative uncertainties. The absolute uncertainty is correlated between the ND and the FD. The relative uncertainty is uncorrelated between the two detectors.

The muon energy shifts are applied to the muon track lengths before evaluating the energy associated with the muon tracks. The absolute muon energy scale shift is 0.94% for all events. An additional 0.69% shift is added to the muon track parts falling in the muon catcher region in the ND. The relative muon energy scale shift is 0.27% for most of the events and an additional 0.75% shift is added to the muon track segment falling in the muon catcher region.

The studies of the detector's response to the energy deposited by protons in the ND simulation and data leads to a 5% smaller calorimetric energy response in the data compared to the simulation. This difference in the simulation and data is considered as a 5% absolute calorimetric energy scale systematic uncertainty. A 5% relative calorimetric energy scale systematic uncertainty is also added in the oscillation fits.

5.6.7 Cherenkov light and light levels

When a charged particle passes through the NOvA scintillator it produces scintillation light, which is the main detection light mode in NOvA, and also produces Cherenkov light. At short wavelengths (200 - 400 nm), most of the Cherenkov light produced in the NOvA detector is indistinguishable from the scintillation light which affects the estimate of the detector's response to the light. To account for uncertainties in the light level, a $\pm 10\%$ shift is added to the light level. The Cherenkov

model is modified to shift down the proton response by 2.6% without changing the muon response. Protons in the hadronic system produce no Cherenkov light, which can lead to miscalibration in the hadronic part if only scintillation light is assumed at the simulation level.

5.6.8 Rock Events

The interactions of the beam neutrinos in the rock before entering the FD causes the rock event contamination. The rock event contamination is a very small effect, approximately 0.15 events and is added in the final oscillation fit with an uncertainty of 100%.

5.7 Physics Sensitivities

Physics sensitivities are estimated before we look at the FD data events. To estimate sensitivities, we make use of the fake data method. The process of making fake data was explained in § 5.6. This approach of making the fake data sample from the simulated sample helps us to make both the predictions at the FD and the physics sensitivities for the oscillation parameters we are interested in. In this analysis, we make sensitivities for the ν_e only and combined $\nu_\mu - \nu_e$ fits. To estimate sensitivities, we first start by generating a 2D space of the oscillation parameters, for example, $\sin^2 \theta_{23}$ and δ_{cp} parameters. In this oscillation space, we select oscillation points at regular intervals both in $\sin^2 \theta_{23}$ and δ_{cp} directions. We call these oscillation points the grid points. Every grid point has fixed values of the $\sin^2 \theta_{23}$ and δ_{cp} parameters. After we have the 2D oscillation space, we generate fake data for the desired values of the oscillation parameters. Table 5.10 shows the values of Δm_{32}^2 , $\sin^2 \theta_{23}$ and δ_{cp} parameters used to generate the fake data. The values of other oscillation parameters used to make the predictions and sensitivities are shown in Table 5.11.

To make sensitivities for the “ ν_e only” fit, we add Δm_{32}^2 as a nuisance parameter in the fit but for making sensitivities for the combined $\nu_\mu - \nu_e$ fits, we add Δm_{32}^2 as a free parameter in the fit. After we make the 2D space of $\sin^2 \theta_{23}$ and δ_{cp} parameters, we fit the fake data at every grid point using the χ^2 fit explained in § 5.5.1. A successful

Analysis	Hierarchy	$\Delta m_{32}^2 (10^{-3}) \text{eV}^2 / c^4$	$\sin^2 \theta_{23}$	$\delta_{cp} (\pi)$
ν_e only	NH	2.43	0.48	1.44
	IH	-2.50	0.55	1.38
$\nu_\mu - \nu_e$ joint	NH	2.43	0.48	1.44
	IH	-2.50	0.56	1.56

TABLE 5.10: Values of the oscillation parameters used to make physics sensitivities for the ν_e only and combined $\nu_\mu - \nu_e$ analyses for both the normal (NH) and inverted (IH) hierarchies.

Oscillation Parameters	Δm_{21}^2 ($\times 10^{-5} \text{eV}^2 / c^4$)	$\sin^2 \theta_{12}$	$\sin^2 \theta_{13}$	ρ (g/cm^3)
Values	$7.53^{+0.18}_{-0.18}$	$0.307^{+0.013}_{-0.012}$	$0.0210^{+0.0011}_{-0.0011}$	2.84

TABLE 5.11: Values of the oscillation parameters used to make the physics sensitivities in addition to the parameter values shown in Table 5.10.

oscillation fit at every grid point generates a χ^2 value at that point leading to a 2-dimensional space of $\sin^2 \theta_{23}$ and δ_{cp} parameters filled with χ^2 values. We also run an overall best fit job by adding $\sin^2 \theta_{23}$ and δ_{cp} along with Δm_{32}^2 as free parameters. This fit gives an overall best fit value of χ^2 . Now, we add the overall best χ^2 value to the 2D map of χ^2 values for the $\sin^2 \theta_{23}$ and δ_{cp} parameters. In the next step, we take the differences of the overall minimum χ^2 value to the χ^2 values at every grid point and make another 2D space of $\sin^2 \theta_{23}$ and δ_{cp} parameters filled with differences of the χ^2 values, that is, the $\Delta\chi^2$ values. Now we have a 2D map of $\Delta\chi^2$ values at each grid point of the $\sin^2 \theta_{23}$ and δ_{cp} space. The $\Delta\chi^2$ map enables the creation of the final sensitivity lines and confidence levels (C.L.). In the oscillation space, the grid points which have $\Delta\chi^2$ values less than 2.30 fall at a distance of 1σ from the best fit point and make the 1σ C.L. region. The grid points having $\Delta\chi^2 < 6.18$ falls under the 2σ C.L. and points having $\Delta\chi^2 < 11.83$ falls under the 3σ C.L. The same procedure is followed to make the final analysis contours. For the final data contours, we use real FD data instead of the fake data. Fig. 5.19 shows the physics sensitivities for both the “ ν_e only” and combined $\nu_\mu - \nu_e$ fit. The top plots are for the “ ν_e only” fit and the bottom plots are for the combined $\nu_\mu - \nu_e$ fit. The left plots are for the NH and the right plots are for the IH.

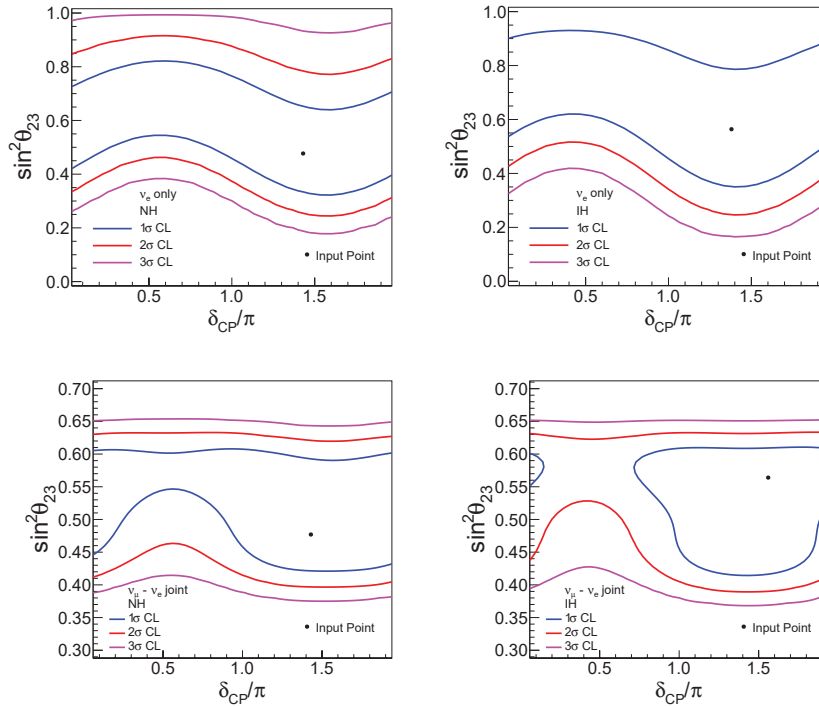


FIGURE 5.19: The physics sensitivities for both the “ ν_e only” and the combined $\nu_\mu - \nu_e$ fit for the $\sin^2 \theta_{23}$ vs. δ_{CP} parameters are shown using 1, 2, and 3 σ C.L. The sensitivities are generated for the values of the oscillation parameters shown in Table 5.10. Top plots are for the “ ν_e only” fit and the bottom plots are for the combined $\nu_\mu - \nu_e$ fit. The left plots are for the NH and the right plots are for the IH.

5.8 Oscillation Results

For the final results, we follow a blind analysis process in which we take a look at the selected FD data events only after developing all necessary tools of the analysis. Before we look at the final FD data events we make sure that the constraints from the ND to make the predictions are working successfully. We also assess the impact of the systematic uncertainties on the simulated sample. We make sure that the oscillation fitting procedure to extract the oscillation parameters is in place and is working successfully. After we are sure that all parts of the analysis are in place, we present all necessary studies to the collaboration and ask their permission to finally look at the FD data events. This process has been named box opening by the collaboration.

As part of the final results, we look at the FD data events selected by the ν_e and

ν_μ analyses. The oscillation fit to the selected FD data events to extract the best fit values of the oscillation parameters is also part of the results. The oscillation fit does not only give the best fit values of the oscillation parameters but also give us quantitative information about the expected signal and background events. Results of the combined $\nu_\mu - \nu_e$ oscillation fit to the FD data are also presented. Finally we also present 2D contours for the $\sin^2 \theta_{23}$ and δ_{cp} oscillation parameters for the ν_e only and combined $\nu_\mu - \nu_e$ fit. We also present 1D contours of the $\sin^2 \theta_{23}$ and δ_{cp} parameters for the extraction of the significance of the results.

5.8.1 Oscillation Fit to the FD Data Events

We ran two types of oscillation fits to the FD data for the extraction of $\sin^2 \theta_{23}$ and δ_{cp} parameters. One is the “ ν_e only” fit, in which we let the $\sin^2 \theta_{23}$ and δ_{cp} parameters to float freely in the fit and use values of other oscillation parameters from external experiments [69]. The systematic uncertainties are added in the fit as nuisance parameters. We use $\Delta m_{21}^2 = (7.53_{-0.18}^{+0.18}) \times 10^{-5} \text{eV}^2/c^4$, $\Delta m_{32}^2 = (2.500_{-0.005}^{+0.005}) \times 10^{-3} \text{eV}^2/c^4$, $\sin^2 \theta_{12} = 0.307_{-0.012}^{+0.013}$, and $\sin^2 \theta_{13} = 0.0210_{-0.0011}^{+0.0011}$. For the matter density of the Earth for the NuMI beam, we use a constant matter density of $\rho = 2.84 \text{ g/cm}^3$. For the combined fit we let Δm_{32}^2 be a free parameter in the fit. The ν_μ disappearance fit is sensitive to the Δm_{32}^2 and $\sin^2 \theta_{23}$ parameters. The ν_e appearance fit is sensitive to the $\sin^2 \theta_{23}$ and δ_{cp} parameters. The benefit of performing a joint fit is that it finds the values of the Δm_{32}^2 , $\sin^2 \theta_{23}$ and δ_{cp} at the same time. Fig. 5.20 shows the best oscillation fit to the ν_μ selected FD data events for all quartiles including the signal and background events. The $\nu_\mu \rightarrow \nu_\mu$ and the $\bar{\nu}_\mu \rightarrow \bar{\nu}_\mu$ are considered as signal events, the NC beam background events are shown by the gray histogram, the cosmic ray events by the yellow histogram and the rest of the spectra are various beam CC backgrounds. Table 5.12 shows the number of the signal and background events. For the ν_μ analysis, the best oscillation fit gives 138.05 signal, 0.84 CC beam background, 2.58 NC beam background and 5.82 cosmic ray events. In total 147.29 simulated events are found from the oscillation fit compared to 126 data events. The different signal and background components from Fig. 5.20 are rearranged in Fig. 5.21 such that the $\nu_\mu \rightarrow \nu_\mu$ and the $\bar{\nu}_\mu \rightarrow \bar{\nu}_\mu$ are added to make a single plot shown by purple line. All beam background components are added into a single gray plot and the cosmic ray background is the blue band. The different

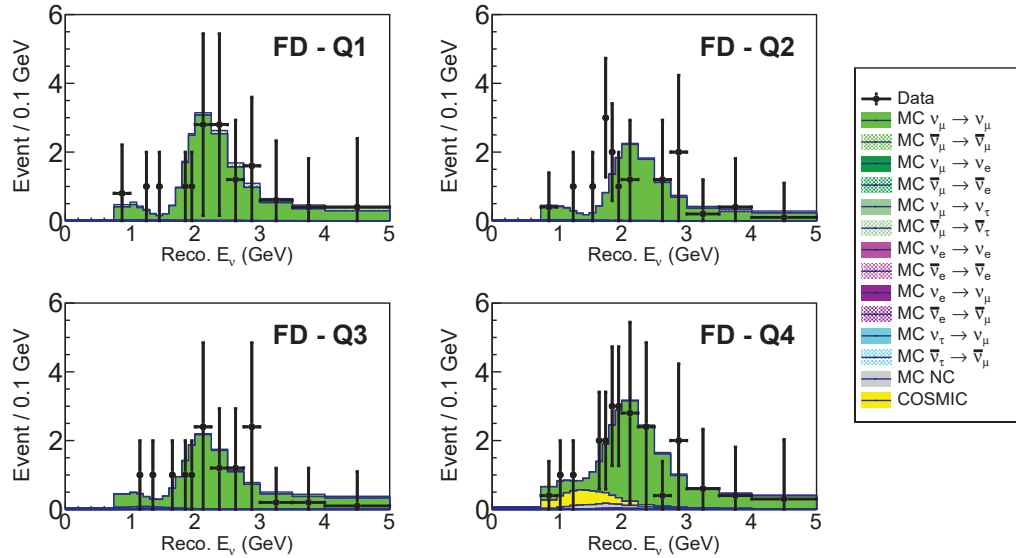


FIGURE 5.20: Results of the oscillation fit to the FD data events is shown for the $\nu_\mu \rightarrow \nu_\mu$ analysis for all four quartiles. The signal events are shown by the green stacked histogram, the NC beam background by the gray histogram and the cosmic ray background by the yellow histogram. The other stacked histogram is the CC beam background. Most of the beam background and cosmic ray events are in the fourth, least resolution quartile as expected.

Components	Events
Data	126
Signal	138.05
Beam background (CC)	0.84
Beam background (NC)	2.59
Cosmic ray background	5.82
Total signal + backgrounds	147.29

TABLE 5.12: The number of signal and background components are shown from the best oscillation fit to the FD data events selected by the ν_μ selections. In this analysis, 138.05 signal events, 3.43 CC and NC beam background events and 5.82 cosmic ray events are found.

signal and background components from all four quartiles are added into a single combined stacked histogram and are shown in Fig. 5.22.

Fig. 5.23 shows the best oscillation fit to the ν_e selected FD data events for all CVN

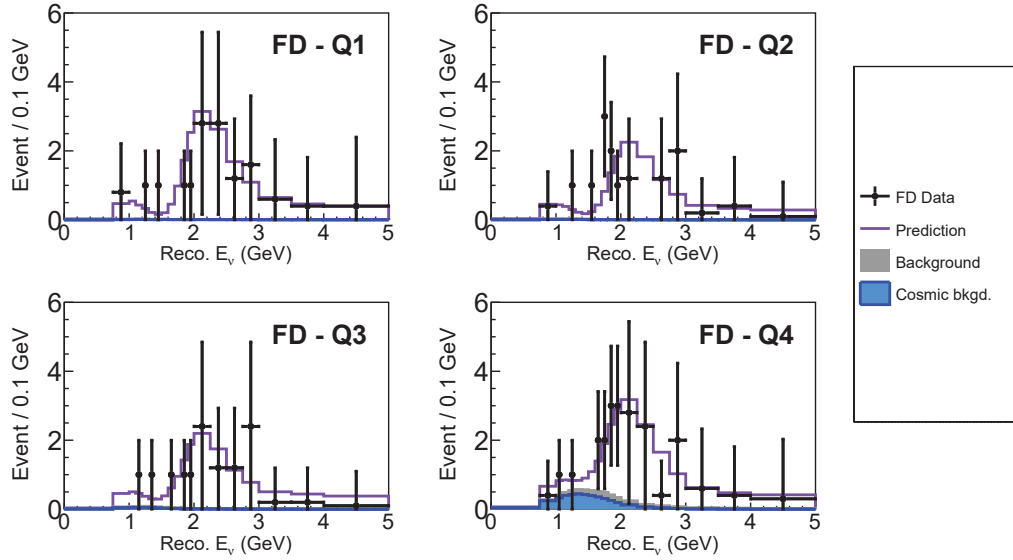


FIGURE 5.21: Results of the oscillation fit to the FD data events is shown for the $\nu_\mu \rightarrow \nu_\mu$ analysis for all four quartiles. The total best fit prediction is shown by purple line. As expected most of the beam background and cosmic ray events are in the fourth, least resolution quartile.

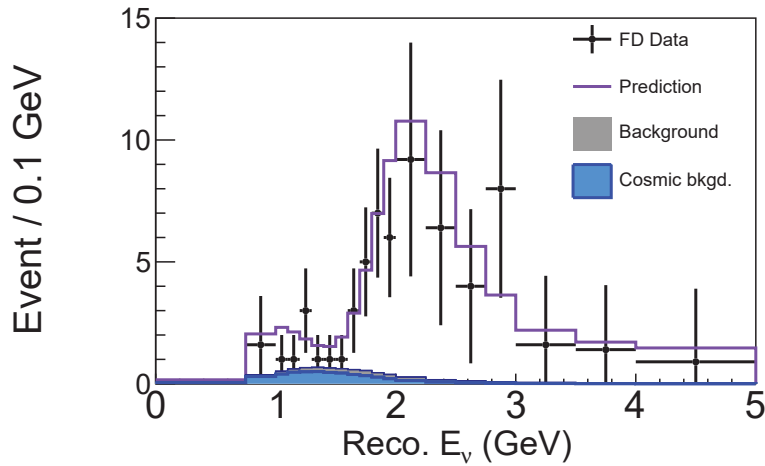


FIGURE 5.22: Result of the oscillation fit to the FD data events is shown for the $\nu_\mu \rightarrow \nu_\mu$ analysis for combined quartiles. The best fit prediction is shown by the purple line. The gray band shows the beam background and the cosmic ray background is shown by the blue band.

and peripheral bins. The signal, CC and NC beam background, and cosmic ray event backgrounds are shown as stacked histograms. The $\nu_\mu \rightarrow \nu_e$ and the $\bar{\nu}_\mu \rightarrow \bar{\nu}_e$ are the signal events. The cosmic ray backgrounds are shown by the yellow band. Spectra of different beam CC and NC background components are shown too. Table 5.13

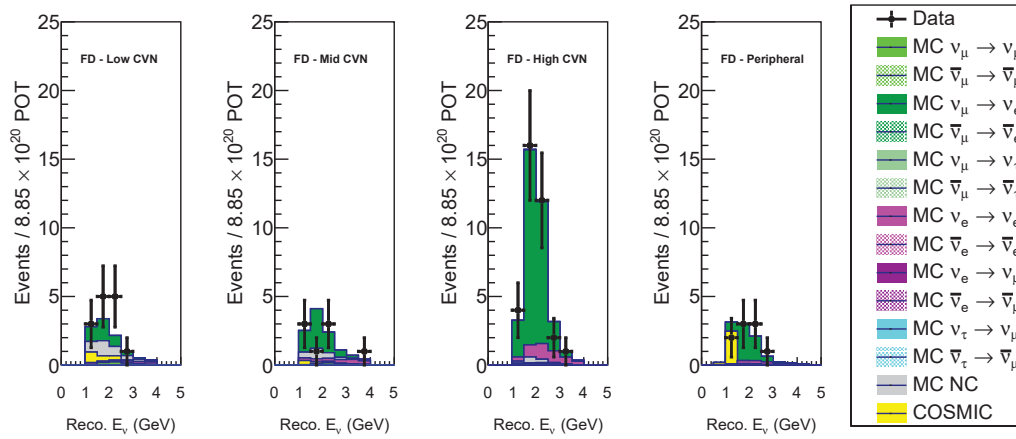


FIGURE 5.23: Results of the oscillation fit to the FD data events are shown for the $\nu_\mu \rightarrow \nu_e$ analysis for all three CVN and peripheral bins. The signal events are shown by the dark green stacked histograms. The cosmic ray backgrounds are shown by the yellow band. Spectra of different beam CC and NC background components are shown too. As expected, the majority of the cosmic backgrounds are in the peripheral bin.

shows the number of the signal and background events. For the ν_e analysis, the best oscillation fit gives 46.65 signal, 9.13 CC beam background, 6.10 NC background and 4.81 cosmic ray events. In total 66.69 predicted events are found from the oscillation fit for 66 data events. Different signal and background components from Fig. 5.23

Components	Events
Data	66
Signal	46.65
Beam background (CC)	9.13
Beam background (NC)	6.10
Cosmic ray background	4.81
Total signal + backgrounds	66.68

TABLE 5.13: The number of signal and background components are shown from the best oscillation fit to the FD data events selected by the ν_e selections. In this analysis, 46.65 signal events, 9.13 CC, 6.10 NC, and 4.81 cosmic ray background events are found.

are rearranged in Fig. 5.24. The total best fit prediction to the data which is a sum

of $\nu_\mu \rightarrow \nu_e$ and the $\bar{\nu}_\mu \rightarrow \bar{\nu}_e$ is shown by the purple line. All beam CC and NC background events are added into a single gray band and the cosmic backgrounds are shown by the blue histogram. Events in the peripheral bins have energies from 0 to 4.5 GeV and are kept in a single energy bin.

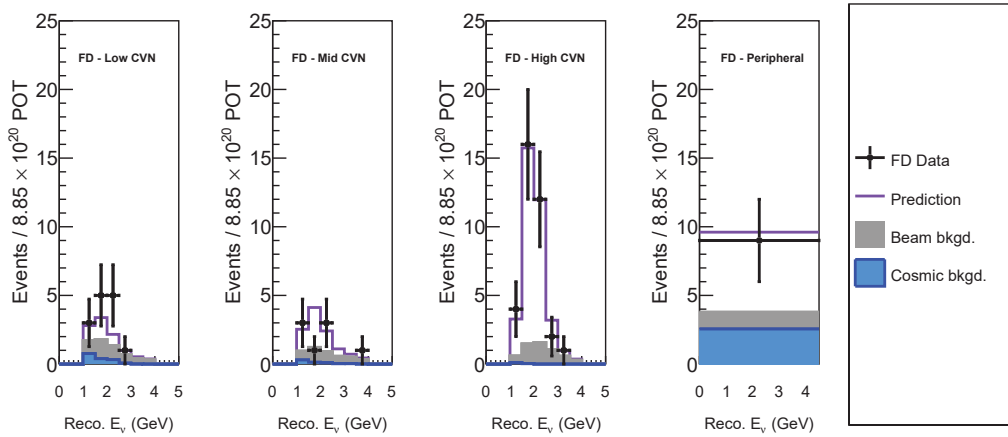


FIGURE 5.24: Results of the oscillation fit to the FD data events are shown for the $\nu_\mu \rightarrow \nu_e$ analysis for all three CVN and peripheral bins. The total best-fit prediction is shown by the purple line. The total expected beam and cosmic backgrounds are shown too. Events in the peripheral bins have energy from 0 to 4.5 GeV and are kept in a single energy bin. As expected, the majority of the cosmic backgrounds are in the peripheral bin.

5.8.2 Best Fit Oscillation Parameters

Table 5.14 shows the best fit values of the oscillation parameters, Δm_{32}^2 , $\sin^2 \theta_{23}$ and δ_{cp} obtained from the oscillation fit to the ν_e only and combined ν_μ and ν_e FD data presented in § 5.8.1. The overall best fit values are found from the combined $\nu_\mu - \nu_e$ fit in the NH having χ^2 value of 89.37 for 94 number degrees of freedom (ndof).

Analysis	Hierarchy	$\Delta m_{32}^2 (10^{-3}) eV^2/c^4$	$\sin^2 \theta_{23}$	$\delta_{cp} (\pi)$	$\chi^2/ndof$
ν_e only	NH	2.43	0.47	1.27	14.52/17
	IH	-2.48	0.82	1.94	14.89/17
$\nu_\mu - \nu_e$ joint	NH	2.35	0.50	1.28	89.37/94
	IH	-2.50	0.56	1.52	89.44/94

TABLE 5.14: The best fit values for the neutrino oscillation parameters obtained from the combined ν_μ and ν_e fit to the FD data events.

5.8.3 Analysis Contours

Using real FD data, we make 2-dimensional (2D) contours in the $\sin^2 \theta_{23}$ and δ_{cp} oscillation space. The 2D analysis contours help us to locate the best fit values of the oscillation parameters. The 2D analysis contours also tell us about the confidence in the results via 1σ , 2σ and 3σ regions. The 2D contours also help us to exclude certain regions of the oscillation space. To make contours we follow the procedure explained in § 5.7 using grid points in the $\sin^2 \theta_{23}$ and δ_{cp} oscillation space. A fit to the far detector data is run at every grid point in the oscillation parameter space. At the grid points, $\sin^2 \theta_{23}$ and δ_{cp} are fixed. Systematic uncertainties are also added in the fit as nuisance parameters. In this analysis, we make two types of contours, one for the “ ν_e only” fit, in which we use Δm_{32}^2 as a fixed parameter from external experiments [69] and use only the ν_e selected FD data neutrino energy spectrum as shown in Fig. 5.25. Analysis contours are made for both the normal and inverted hierarchies. The best fit values for the “ ν_e only” fit are $\sin^2 \theta_{23} = 0.48$ and $\delta_{cp} = 1.27\pi$ for the normal hierarchy and $\sin^2 \theta_{23} = 0.82$ and $\delta_{cp} = 1.94\pi$ for the inverted hierarchy. The overall best fit is in the normal hierarchy with a lower χ^2 value of 14.52 compared to the inverted hierarchy fit having a χ^2 value of 14.89.

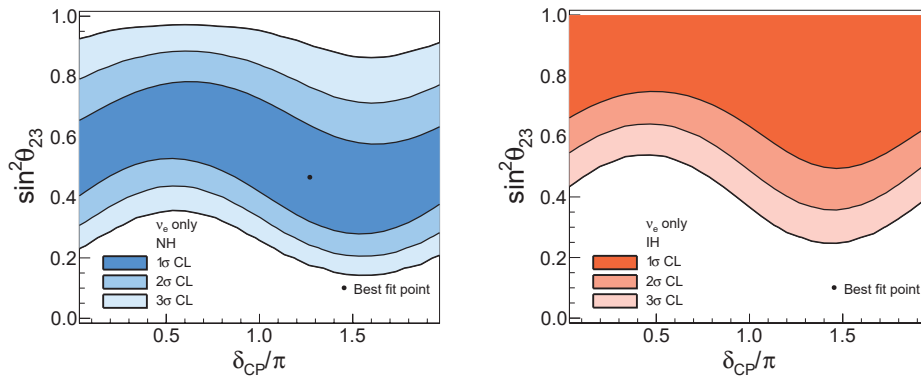


FIGURE 5.25: The FD data analysis contours are shown for the “ ν_e only” fit. Contours in the left plot are for the normal hierarchy and in the right for the inverted hierarchy. The overall best fit point is found for the normal hierarchy having a lower value of the χ^2 .

For the combined $\nu_\mu - \nu_e$ contours, at each grid point in $\sin^2 \theta_{23}$ and δ_{cp} oscillation space, we also add Δm_{32}^2 as free parameter which can take different values at different grid points based on the best fit at those grid points. Fig. 5.26 shows the contours for the combined $\nu_\mu - \nu_e$ fit for the $\sin^2 \theta_{23}$ and δ_{cp} oscillation parameters. The

combined $\nu_\mu - \nu_e$ contours constrain more space than the “ ν_e only” contours. The best fit values of the oscillation parameters shown in Fig. 5.26 are already quoted in Table 5.14.

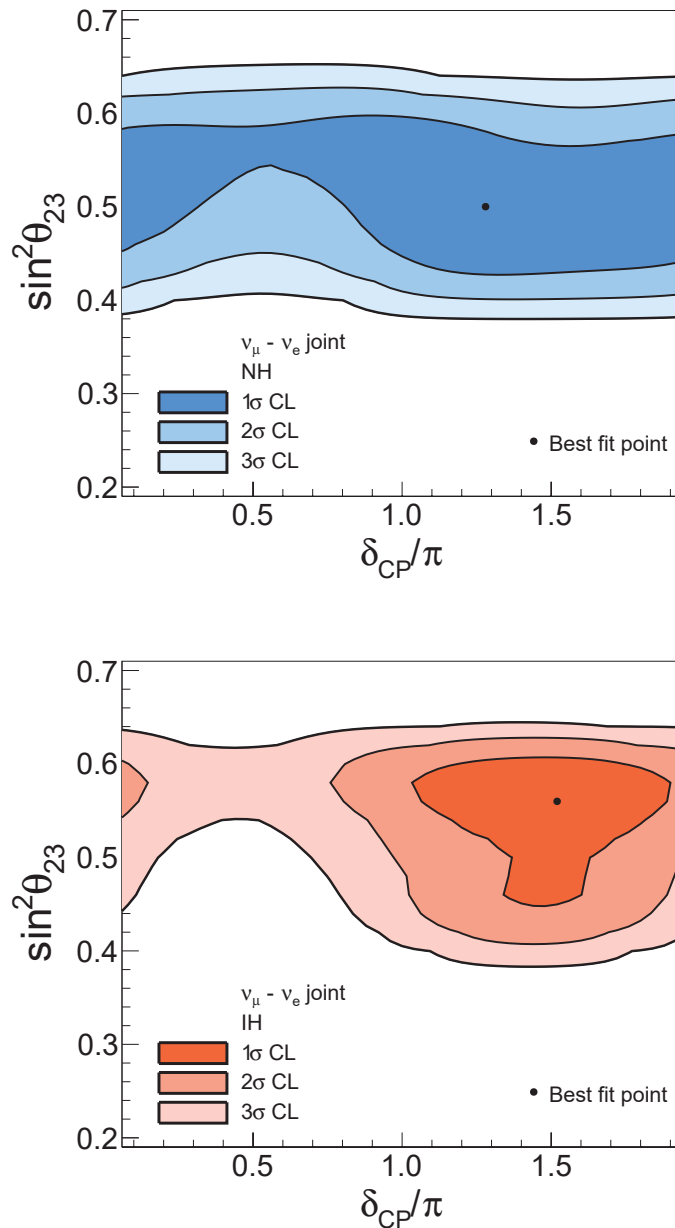


FIGURE 5.26: The FD data analysis contours are shown for the combined “ $\nu_\mu - \nu_e$ ” fit. Contours in the top plot are for the normal hierarchy and in the bottom plot for the inverted hierarchy. The overall best fit point is found for the normal hierarchy having a lower value of the χ^2 .

5.8.4 Significance of Oscillation Parameters

The significance levels for single oscillation parameters are made by marginalization over other oscillation parameters. In this analysis, we make significance levels for the δ_{cp} and $\sin^2 \theta_{23}$ for the “ ν_e only” oscillation fit as well as for the “ $\nu_\mu - \nu_e$ joint” fit. Significance levels (σ) for single parameters are defined using $\Delta\chi^2$ values. The $\Delta\chi^2 < 1.0$ forms 1σ levels, $\Delta\chi^2 < 4.0$ makes 2σ and $\Delta\chi^2 < 9.0$ gives 3σ lines. Fig. 5.27 shows the 1D significance levels for the “ ν_e only” oscillation fit for the δ_{cp} and $\sin^2 \theta_{23}$ oscillation parameters for both normal and inverted hierarchies. The results of the 1D significance levels for the “ ν_e only” are presented in Table 5.15.

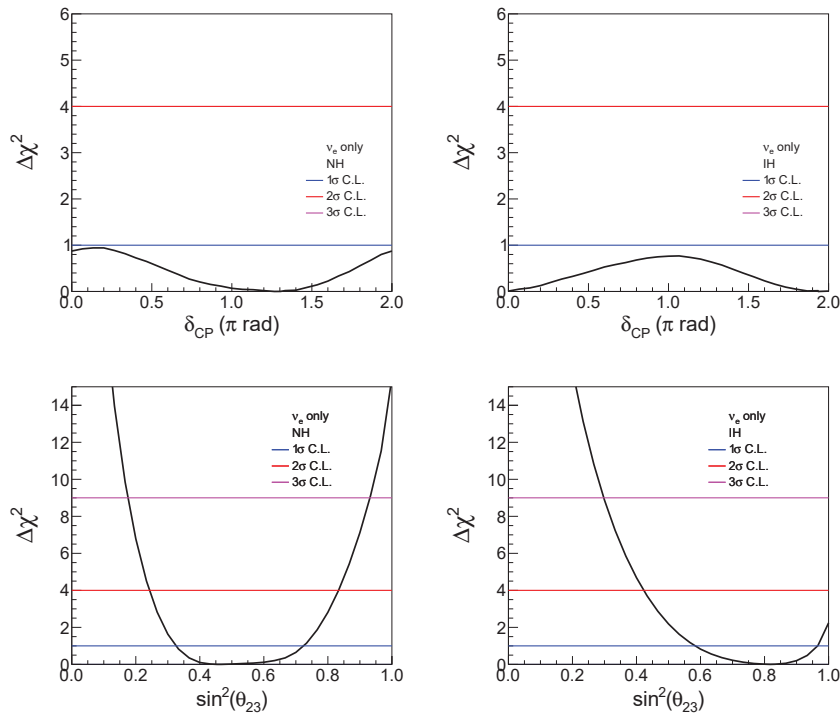


FIGURE 5.27: The 1D significance levels for the “ ν_e only” oscillation fit for the δ_{cp} parameter are shown in the top plots and for the $\sin^2 \theta_{23}$ parameter in the bottom plots. The left plots are for the normal hierarchy and the right plots are for the inverted hierarchy.

Fig. 5.28 shows the 1D significance levels and Table 5.16 shows the results of the 1D levels for the “ $\nu_\mu - \nu_e$ joint” fit. The 1D significance levels show that the inverted hierarchy is rejected at more than 1σ level.

Parameters	1 σ confidence intervals	
	Normal hierarchy	Inverted hierarchy
$\sin^2 \theta_{23}$	[0.33, 0.72]	[0.58, 0.97]
δ_{cp} (π)	[0, 2]	[0, 2]

TABLE 5.15: For the “ ν_e only” oscillation fit, the δ_{cp} and $\sin^2 \theta_{23}$ values under 1σ confidence intervals are shown for the normal and inverted hierarchies.

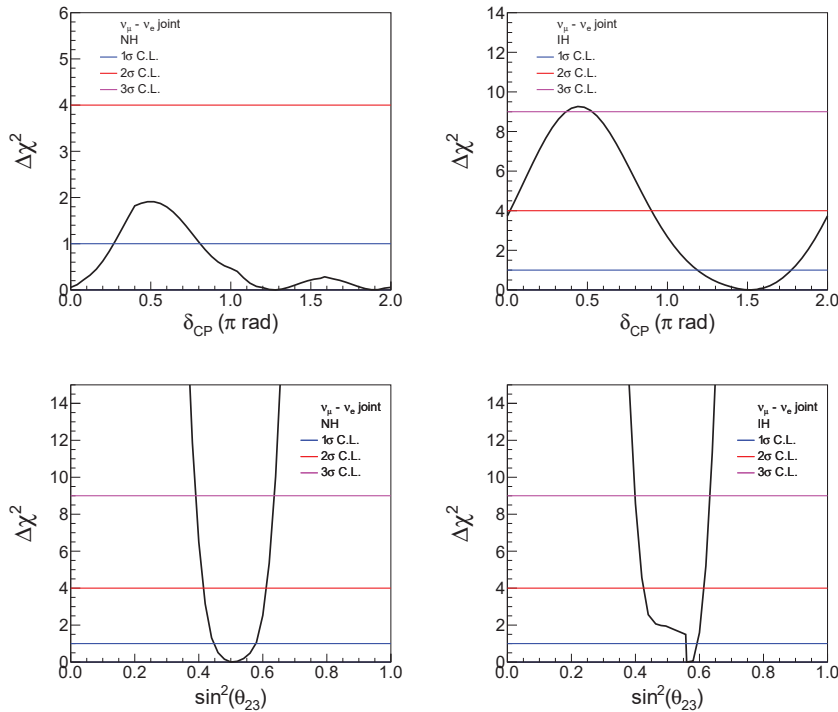


FIGURE 5.28: The 1D significance levels for the “ $\nu_\mu - \nu_e$ joint” oscillation fit for the δ_{cp} parameter are shown in the top plots and for the $\sin^2 \theta_{23}$ parameter in the bottom plots. The left plots are for the normal hierarchy and the right plots for the inverted hierarchy.

5.9 Summary

The joint fit to the ν_μ disappearance and ν_e appearance data collected by the NOvA experiment favors normal ordering of the neutrino masses. The $\sin^2 \theta_{23}$ is very close to the maximal mixing value. The oscillation results presented here are consistent with the official results [4]. This analysis observes the same 126 $\nu_\mu \rightarrow \nu_\mu$ survival and same 66 $\nu_\mu \rightarrow \nu_e$ appearance events in the FD as by the official ones. The 1σ

Parameters	1 σ confidence intervals	
	Normal hierarchy	Inverted hierarchy
$\sin^2 \theta_{23}$	[0.45, 0.58]	[0.56, 0.59]
$\delta_{cp} (\pi)$	[0, 0.27], [0.81, 2.0]	[1.19, 1.77]

TABLE 5.16: For the “ $\nu_\mu - \nu_e$ joint” oscillation fit, the δ_{cp} and $\sin^2 \theta_{23}$ values under 1 σ confidence intervals are shown for the normal and inverted hierarchies.

levels of $\sin^2 \theta_{23}$ and δ_{cp} for both results are also consistent. This analysis finds 1 σ levels as $\sin^2 \theta_{23} \in [0.45, 0.58]$ and $\delta_{cp}(\pi) \in [0, 0.27] \cup [0.81, 2.0]$. The official results finds 1 σ levels as $\sin^2 \theta_{23} \in [0.43, 0.51] \cup [0.52, 0.60]$ and $\delta_{cp}(\pi) \in [0, 0.12] \cup [0.91, 2.0]$. The best fit values found are $\sin^2 \theta_{23} = 0.50$ and $\delta_{cp}(\pi) = 1.28\pi$ compared to the official values of $\sin^2 \theta_{23} = 0.56$ and $\delta_{cp}(\pi) = 1.21\pi$.

Chapter 6

Conclusions

This thesis presents the analysis of 8.85×10^{20} protons on target (POT) of data collected by the NOvA experiment from February 06, 2014 to February 20, 2017. The data collected by the NOvA experiment is analyzed using the three-flavor neutrino oscillation framework, specifically the $\nu_\mu \rightarrow \nu_\mu$ survival and $\nu_\mu \rightarrow \nu_e$ appearance rates are measured.

NOvA is a long-baseline, accelerator-based neutrino oscillation experiment. It uses two detectors to collect and analyze the neutrino oscillation data. The NOvA experiment uses a beam of muon neutrinos produced at Fermilab. The muon-neutrino beam is first observed by the 300 ton Near Detector (ND), 1km from the neutrino source on the Fermilab site. The ND is used to analyze the composition of the neutrino beam. The result is used to predict the signal and beam background events in the 14 kilotons, Far Detector (FD), 810km from the Fermilab at Ash River, Minnesota. The ν_μ beam oscillates to ν_e and ν_τ on its way from the ND to the FD. The FD is used to analyze the oscillated neutrino beam to make precise measurements of the neutrino oscillation parameters, $|\Delta m_{32}^2|$, $\sin^2 \theta_{32}$, $\sin^2 \theta_{31}$ and δ_{CP} . At present we do not know the sign of the parameter $|\Delta m_{32}^2|$, that is, whether $\Delta m_{32}^2 > 0$ or $\Delta m_{32}^2 < 0$. The octant of the θ_{32} , that is, whether $\theta_{32} > 45^\circ$ (upper octant) or $\theta_{32} < 45^\circ$ (lower octant) or $\theta_{32} = 45^\circ$ (maximal mixing) are important for the $\nu_\mu - \nu_\tau$ symmetries [34]. If the value of the δ_{CP} phase is non-zero and large enough, then leptogenesis [1] can explain the dominance of matter over anti-matter in the universe.

During this thesis, I was involved in various aspects of the experiment including the physics analysis. I carried out the acceptance study of the NOvA FD with cosmic ray

muons. The FD is situated on the surface of the Earth and is constantly exposed to the cosmic ray muons from all directions. The FD sees a different number of cosmic ray muons from different directions because of the geometry of the detector and the thickness of the atmosphere in different directions. The cosmic ray muons are used to calibrate NOvA detectors. The knowledge of the acceptance of the FD for the cosmic ray muons helps in making selections for the calibration. I was involved in performing the attenuation calibration for both ND and FD detectors. Any charged particle traversing through the scintillator material in the detector produces scintillation light. The light is captured by the wavelength shifting fiber and is transferred to the APD. The light in the WLS fiber attenuates from the point of capture to the readout end. If attenuation effects are not corrected for, it leads to an inaccurate measurement of energy. The purpose of the attenuation calibration is to provide constants and formulae such that the amount of energy deposited in the detector by an incident charged particle can be corrected, no matter where the deposition occurred in the detector. The attenuation calibration successfully removed significant spatial variations in the detector response. Over 98% of the channels in the ND and the FD were successfully calibrated.

I was also involved in the development of the analysis framework to analyze the $\nu_\mu \rightarrow \nu_e$ appearance and $\nu_\mu \rightarrow \nu_\mu$ survival channels. The framework was developed to implement the signal and background selections in the ND and the FD and make predictions of those events in the FD by extrapolating the selected ν_μ CC, ν_e CC and NC events from the ND. The framework was used to fit the oscillation data to extract values of the parameters $|\Delta m_{32}^2|$, $\sin^2 \theta_{32}$ and δ_{CP} . I contributed to making physics sensitivities and deriving real data contours for the parameters $\sin^2 \theta_{32}$ and δ_{CP} . The $\nu_\mu \rightarrow \nu_\mu$ survival depends primarily on $|\Delta m_{32}^2|$ and $\sin^2 \theta_{32}$. The $\nu_\mu \rightarrow \nu_e$ appearance channel depends on Δm_{32}^2 , $\sin^2 \theta_{13}$, $\sin^2 \theta_{32}$ and δ_{CP} . In this thesis, I analyzed $\nu_\mu \rightarrow \nu_e$ oscillations and also made combined fit to the $\nu_\mu \rightarrow \nu_\mu$ oscillations. The joint fit to the disappearance and appearance channels increases the power of the experiment to make precise measurements compared to using individual channels. For the ν_e appearance, 66 data events were observed with a prediction of 66.68 events, out of which 15.23 were beam and 4.81 were cosmic ray background events. For the ν_μ disappearance, 126 data events were observed with 147.29 total predicted events out of which 3.43 were beam and 5.82 were cosmic ray background events. A χ^2 fit to the combined data gave best fit values of $\sin^2 \theta_{32} = 0.50$ (0.56) for the NH (IH) and $\delta_{CP}(\pi) = 1.28$ (1.52) for the NH (IH),

with the allowed regions of $\sin^2 \theta_{32} \in [0.45, 0.58]$ ($[0.56, 0.59]$) for the NH (IH) and $\delta_{CP}(\pi) \in [0, 0.27] \cup [0.81, 2.0]$ ($[1.19, 1.77]$) for the NH (IH), at 1σ C.L.

The NOvA experiment plans to run until 2025. The experiment is currently collecting data, both in the neutrino and the anti-neutrino modes. At present, NOvA has collected 8.85×10^{20} POT in the neutrino mode and 12.33×10^{20} POT in the anti-neutrino mode. Results from the analyses of the neutrino and anti-neutrino data are published in [70].

Appendix A

Neutrino Oscillation Phenomenology

A.1 Two Flavor Neutrino Oscillation in Vacuum

The eigen states of the weak interaction Hamiltonian, H_0 , are called the flavor eigen states, $|\nu_\alpha\rangle$, or the weak interaction states or the flavor neutrinos. The neutrinos are produced and detected as flavor eigen states. The eigen states of the mass matrix are the mass eigen states, $|\nu_i\rangle$. The mass eigen states have small but different values of the masses which are the cause of neutrino oscillation. Neutrino oscillation is a quantum mechanical phenomenon in which neutrino flavor eigen states change their flavors from one type to another with time without any interaction from the outer world. In the quantum picture, the flavor eigen states are superposition of mass eigen states and are connected via a unitary mixing matrix, U [21].

$$|\nu_\alpha\rangle = \sum_{i=1}^2 U_{\alpha i}^* |\nu_i\rangle, \quad (\text{A.1})$$

the mixing matrix follows the unitary condition,

$$\sum_i U_{\alpha' i} U_{\alpha i}^* = \delta_{\alpha\alpha'}, \quad (\text{A.2})$$

the flavor and mass eigen states are orthogonal states,

$$\begin{aligned} \langle \nu_{\alpha'} | \nu_\alpha \rangle &= \delta_{\alpha'\alpha} \\ \langle \nu_i | \nu_j \rangle &= \delta_{ij}. \end{aligned}$$

The mass states are eigen states of the free particle Hamiltonian, follows the Hamiltonian energy equation and gives the energy, E_i of the eigen state,

$$H_0|\nu_i\rangle = i\frac{\partial|\nu_i\rangle}{\partial t} = E_i|\nu_i\rangle, \quad (\text{A.3})$$

In plane wave approximation, the evolution of flavor eigen state is given as,

$$\begin{aligned} |\nu_\alpha\rangle_t &= e^{-iH_0t}|\nu_\alpha\rangle \\ &= \sum_{\alpha'} |\nu_{\alpha'}\rangle \langle \nu_{\alpha'} | e^{-iH_0t} | \nu_\alpha \rangle \\ &= \sum_{\alpha'} \langle \nu_{\alpha'} | e^{-iH_0t} | \nu_\alpha \rangle |\nu_{\alpha'}\rangle. \end{aligned}$$

The probability of transformation from one flavor, $|\nu_\alpha\rangle_t$ to another flavor, $|\nu_{\alpha'}\rangle_t$ is given by the square of the transformation amplitude,

$$\begin{aligned} P_{\nu_\alpha \rightarrow \nu_{\alpha'}}(t) &= \left| \langle \nu_{\alpha'} | \nu_\alpha \rangle_t \right|^2 \\ &= \left| \langle \nu_{\alpha'} | e^{-iH_0t} | \nu_\alpha \rangle \right|^2 \\ &= \left| \langle \nu_{\alpha'} | \sum_i |\nu_i\rangle \langle \nu_i | e^{-iH_0t} | \nu_\alpha \rangle \right|^2 \\ &= \left| \sum_i \langle \nu_{\alpha'} | e^{-iH_0t} | \nu_i \rangle \langle \nu_i | \nu_\alpha \rangle \right|^2 \\ &= \left| \sum_i \langle \nu_{\alpha'} | e^{-iE_i t} | \nu_i \rangle \langle \nu_i | \nu_\alpha \rangle \right|^2 \\ &= \left| \sum_i e^{-iE_i t} \langle \nu_{\alpha'} | \nu_i \rangle \langle \nu_i | \nu_\alpha \rangle \right|^2. \end{aligned}$$

The unitarity nature of the mixing matrix, U and the orthogonality condition of the flavor and mass eigen states give,

$$\begin{aligned} \langle \nu_{\alpha'} | \nu_i \rangle &= U_{\alpha'i} \\ \langle \nu_i | \nu_\alpha \rangle &= U_{\alpha i}^*, \end{aligned}$$

using the orthogonality condition, the transformation probability becomes,

$$P_{\nu_\alpha \rightarrow \nu_{\alpha'}}(t) = \left| \sum_i U_{\alpha'i} e^{-iE_i t} U_{\alpha i}^* \right|^2. \quad (\text{A.4})$$

For a two flavor case, the mixing of the mass eigen states in flavor states is explained using a mixing angle, θ . The mixing matrix for two flavor case is simply a rotational matrix,

$$U = \begin{pmatrix} \cos \theta & \sin \theta \\ -\sin \theta & \cos \theta \end{pmatrix} = \begin{pmatrix} U_{\alpha 1} & U_{\alpha 2} \\ U_{\alpha' 1} & U_{\alpha' 2} \end{pmatrix}, \quad (\text{A.5})$$

expanding summation over two flavors and substituting the elements of the mixing matrix,

$$\begin{aligned} P_{\nu_\alpha \rightarrow \nu_{\alpha'}}(t) &= \left| U_{\alpha' 1} e^{-iE_1 t} U_{\alpha 1}^* + U_{\alpha' 2} e^{-iE_2 t} U_{\alpha 2}^* \right|^2 \\ &= \left| -\sin \theta e^{-iE_1 t} \cos \theta + \cos \theta e^{-iE_2 t} \sin \theta \right|^2 \\ &= \left| \sin \theta \cos \theta (e^{-iE_2 t} - e^{-iE_1 t}) \right|^2 \\ &= \sin^2 \theta \cos^2 \theta (e^{iE_2 t} - e^{iE_1 t}) (e^{-iE_2 t} - e^{-iE_1 t}) \\ &= \frac{1}{4} \sin^2 2\theta \left(1 - e^{i(E_2 - E_1)t} - e^{-i(E_2 - E_1)t} + 1 \right) \\ &= \frac{1}{4} \sin^2 2\theta \left[2 - 2 \left(\frac{e^{i(E_2 - E_1)t} + e^{-i(E_2 - E_1)t}}{2} \right) \right] \\ &= \frac{1}{2} \sin^2 2\theta \left[1 - \cos(E_2 - E_1)t \right] \\ &= \frac{1}{2} \sin^2 2\theta \cdot 2 \sin^2 \left(\frac{(E_2 - E_1)t}{2} \right) \\ P_{\nu_\alpha \rightarrow \nu_{\alpha'}}(t) &= \sin^2 2\theta \sin^2 \left(\frac{(E_2 - E_1)t}{2} \right). \end{aligned}$$

The energy eigen values of the weak Hamiltonian for equation A.3 in terms of the momentum, p^2 , and mass, m_i of the particle is,

$$E_i = \sqrt{p^2 + m_i^2},$$

for the ultra relativistic neutrinos, the energy eigenvalues are $E_i \simeq p + \frac{m_i^2}{2E}$. For neutrinos with different masses but same initial momentum, the differences in the energy is,

$$E_2 - E_1 = \frac{m_2^2 - m_1^2}{2E} = \frac{\Delta m_{21}^2}{2E}, \quad (\text{A.6})$$

the transformation oscillation probability becomes,

$$P_{\nu_\alpha \rightarrow \nu_{\alpha'}}(t) = \sin^2 2\theta \sin^2 \left(\frac{\Delta m_{21}^2 t}{4E} \right),$$

in natural units [25] for calculational easiness, the values of the fundamental constants such as the speed of light c and reduced Planck constant, \hbar are set to unity. In natural units the time and distance have same dimensions, that is, $t = L$ (L is the distance from the source of neutrinos to detection of neutrinos). The transformation oscillation probability simplifies to,

$$P_{\nu_\alpha \rightarrow \nu_{\alpha'}}(L, E) = \sin^2 2\theta \sin^2 \left(\frac{\Delta m_{21}^2 L}{4E} \right). \quad (\text{A.7})$$

The unitarity condition makes it easy to find the survival oscillation probability, $P_{\nu_\alpha \rightarrow \nu_\alpha}(L, E)$, for any flavor using,

$$P_{\nu_\alpha \rightarrow \nu_\alpha}(L, E) = 1 - P_{\nu_\alpha \rightarrow \nu_{\alpha'}}(L, E),$$

the survival oscillation probability for a neutrino flavor α to remain α after travelling a distance, L , having energy, E , is,

$$P_{\nu_\alpha \rightarrow \nu_\alpha}(L, E) = 1 - \sin^2 2\theta \sin^2 \left(\frac{\Delta m_{21}^2 L}{4E} \right). \quad (\text{A.8})$$

Appendix B

ν_e Selected FD Data Events

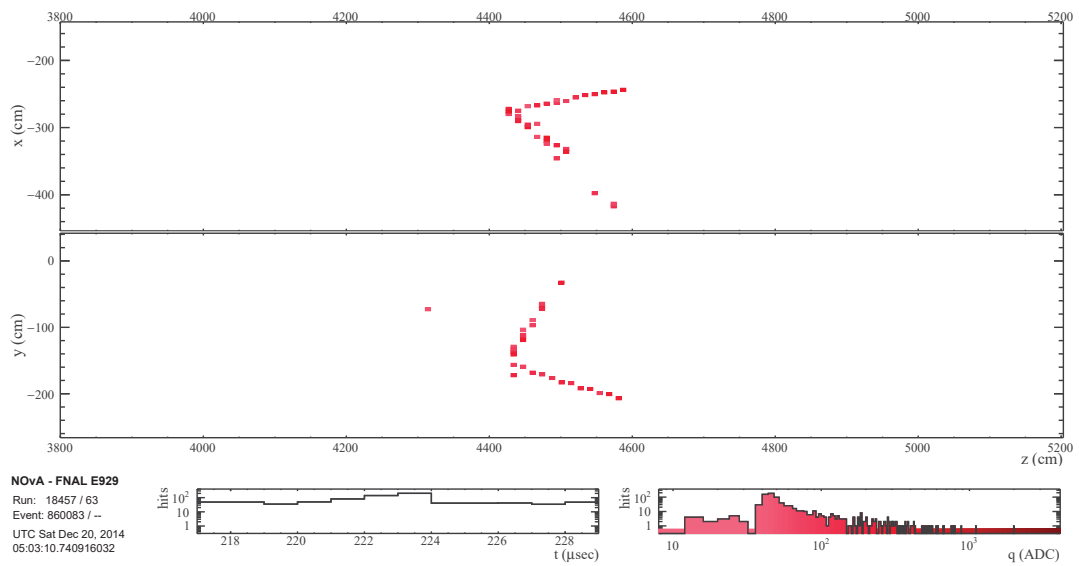


FIGURE B.1: Core sample event: run = 18457, subrun = 63, event number = 860083, slice = 23, hadronic energy = 0.76 (GeV), leptonic energy = 0.82 (GeV) and reconstructed neutrino energy = 1.69 (GeV).

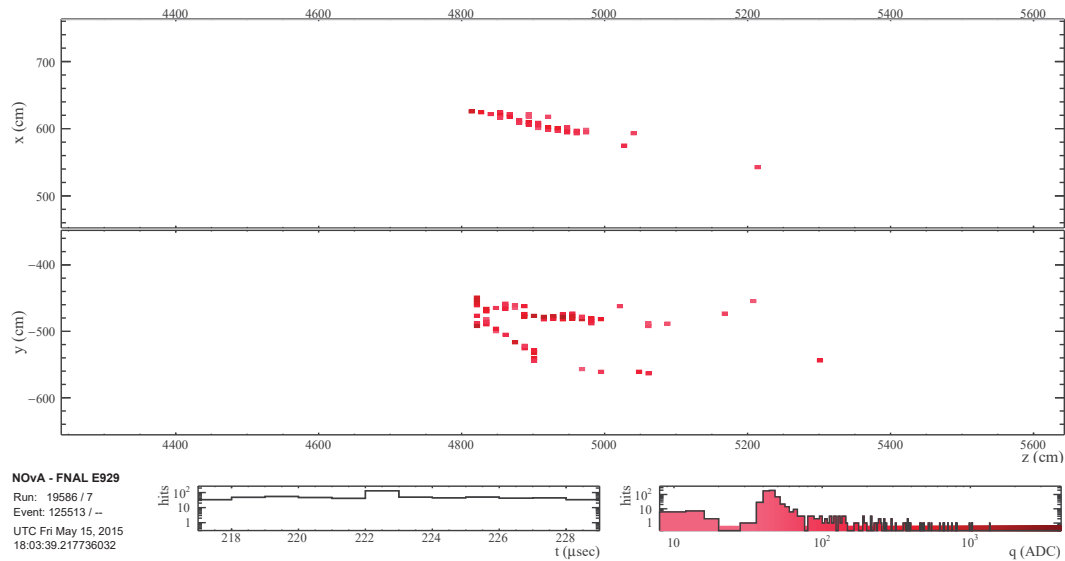


FIGURE B.2: Core sample event: run = 19586, subrun = 07, event number = 125513, slice = 29, hadronic energy = 0.33 (GeV), leptonic energy = 1.73 (GeV) and reconstructed neutrino energy = 2.02 (GeV).

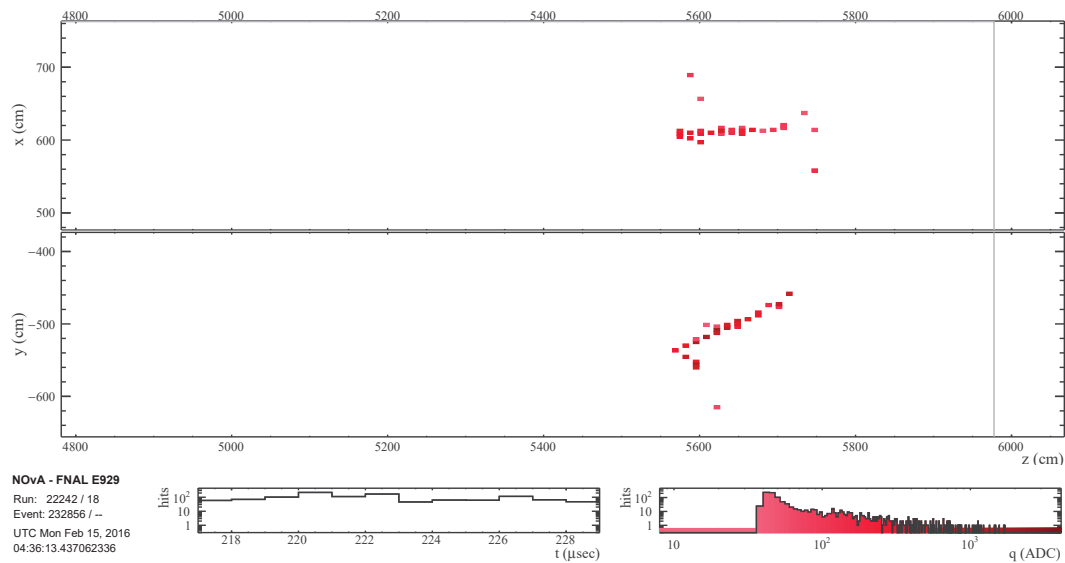


FIGURE B.3: Core sample event: run = 22242, subrun = 18, event number = 232856, slice = 30, hadronic energy = 0.30 (GeV), leptonic energy = 1.30 (GeV) and reconstructed neutrino energy = 1.56 (GeV).

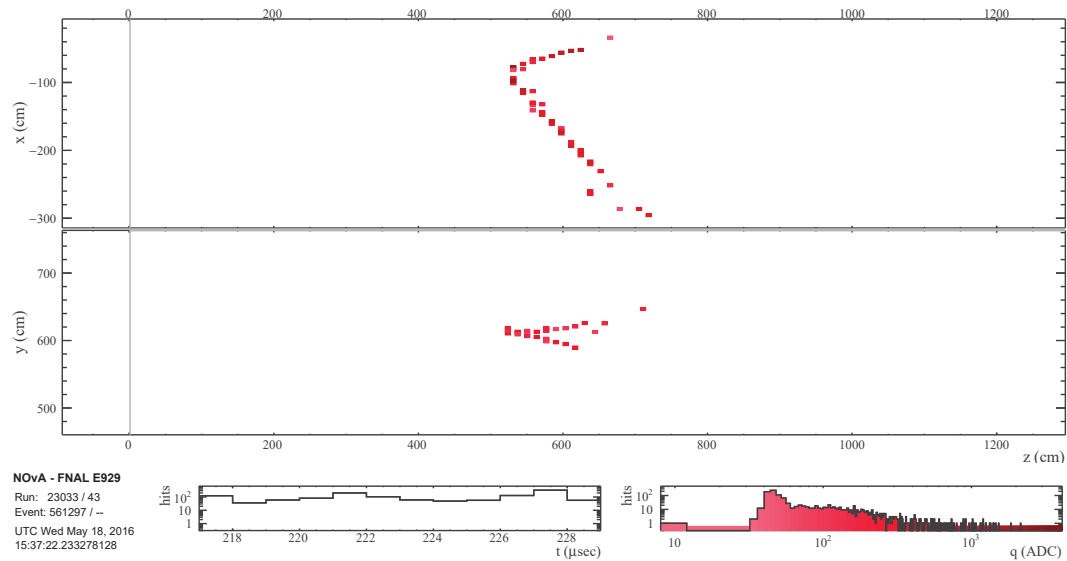


FIGURE B.4: Core sample event: run = 23033, subrun = 43, event number = 561297, slice = 35, hadronic energy = 0.55 (GeV), leptonic energy = 0.89 (GeV) and reconstructed neutrino energy = 1.44 (GeV).

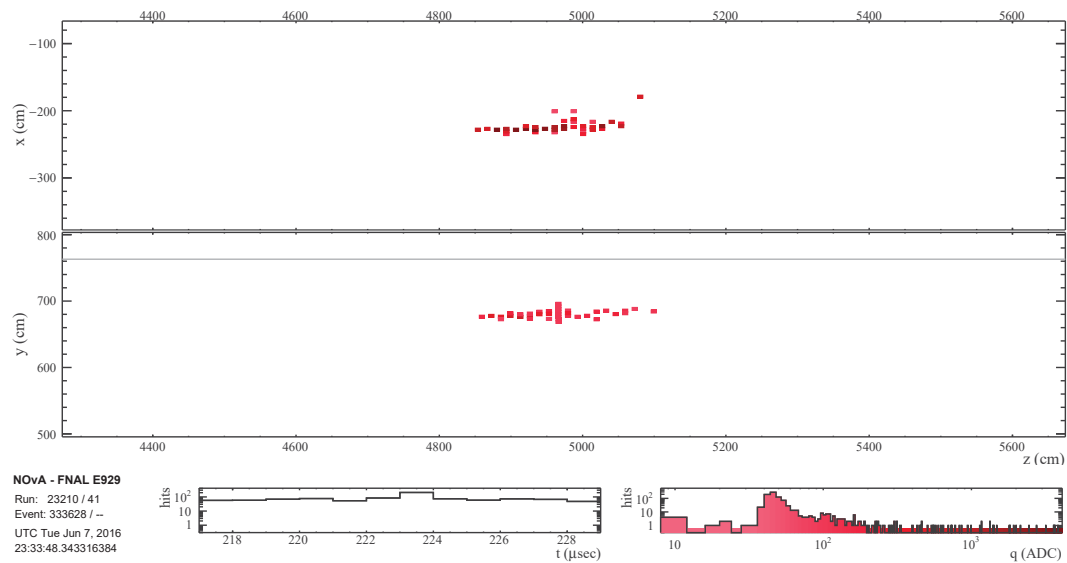


FIGURE B.5: Core sample event: run = 23210, subrun = 41, event number = 333628, slice = 36, hadronic energy = 0.02 (GeV), leptonic energy = 2.17 (GeV) and reconstructed neutrino energy = 2.17 (GeV).

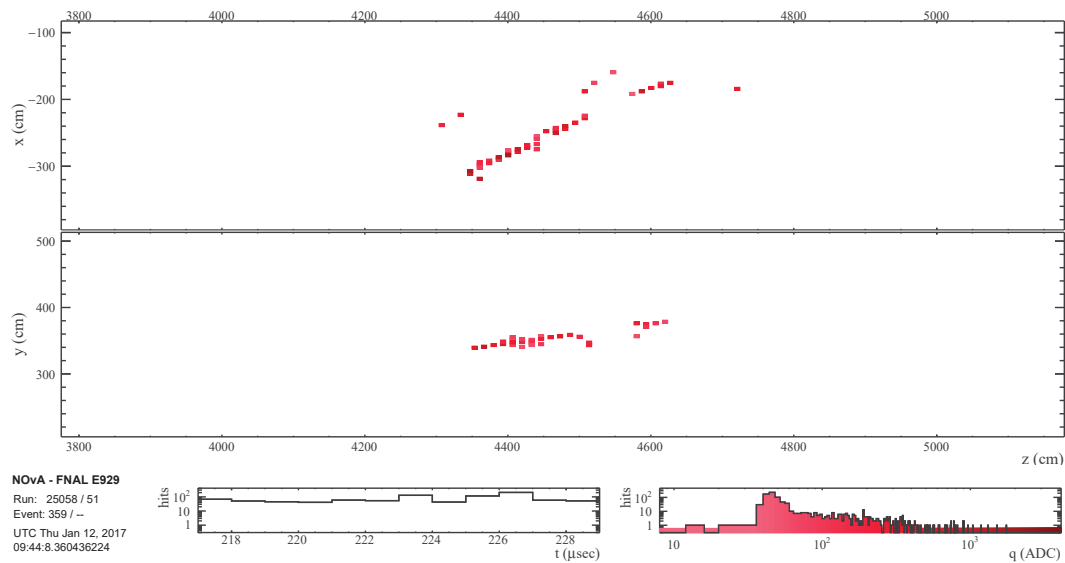


FIGURE B.6: Core sample event: run = 25058, subrun = 51, event number = 359 , slice = 35, hadronic energy = 0.22 (GeV), leptonic energy = 1.57 (GeV) and reconstructed neutrino energy = 1.74 (GeV).

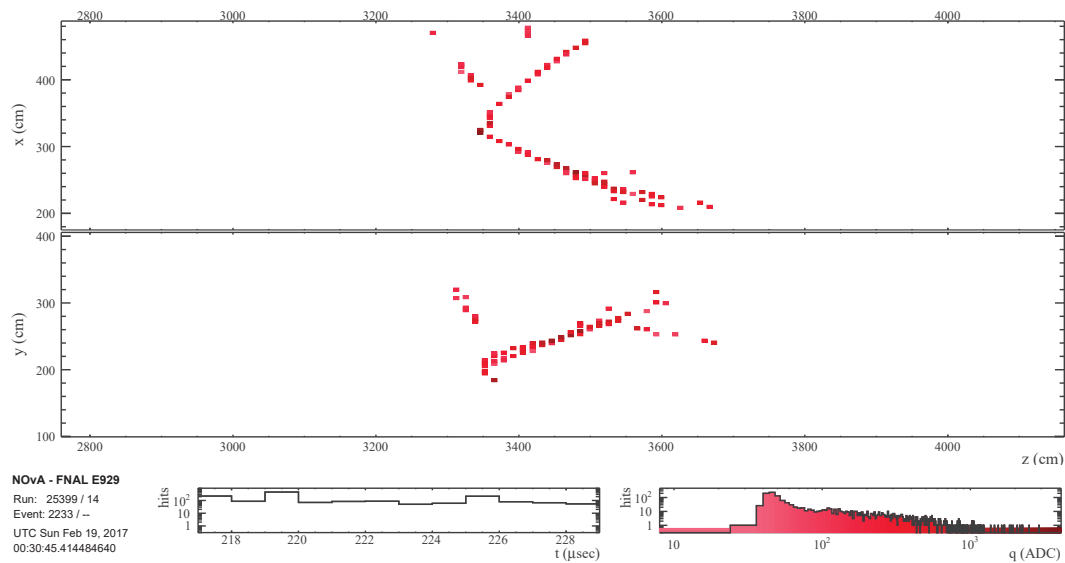


FIGURE B.7: Core sample event: run = 25399, subrun = 14, event number = 2233 , slice = 34, hadronic energy = 0.77 (GeV), leptonic energy = 2.91 (GeV) and reconstructed neutrino energy = 3.85 (GeV).

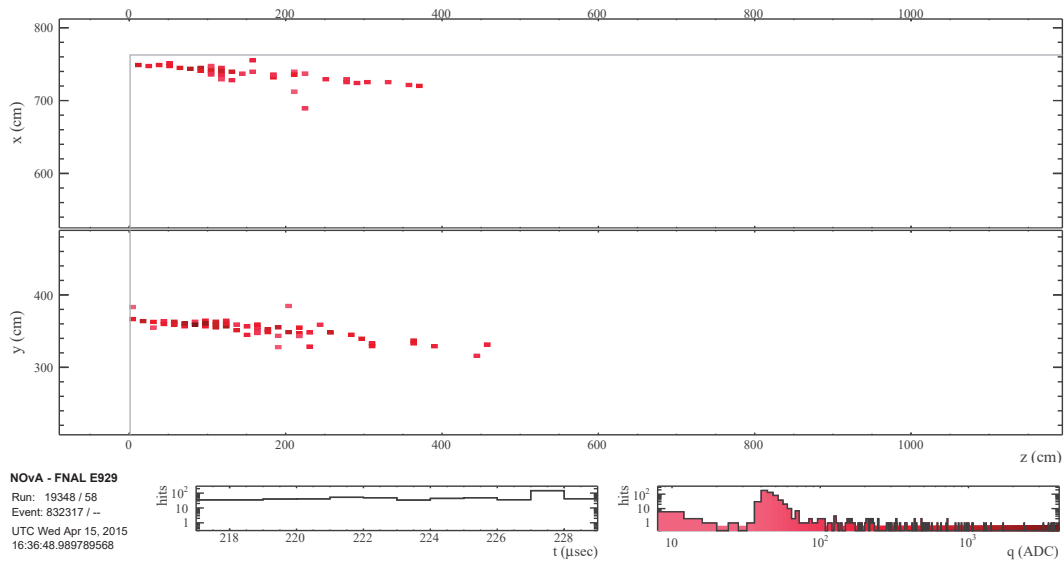


FIGURE B.8: Peripheral sample event: run = 19348, subrun = 58, event number = 832317, slice = 26, hadronic energy = 0.01 (GeV), leptonic energy = 2.30 (GeV) and reconstructed neutrino energy = 2.30 (GeV).

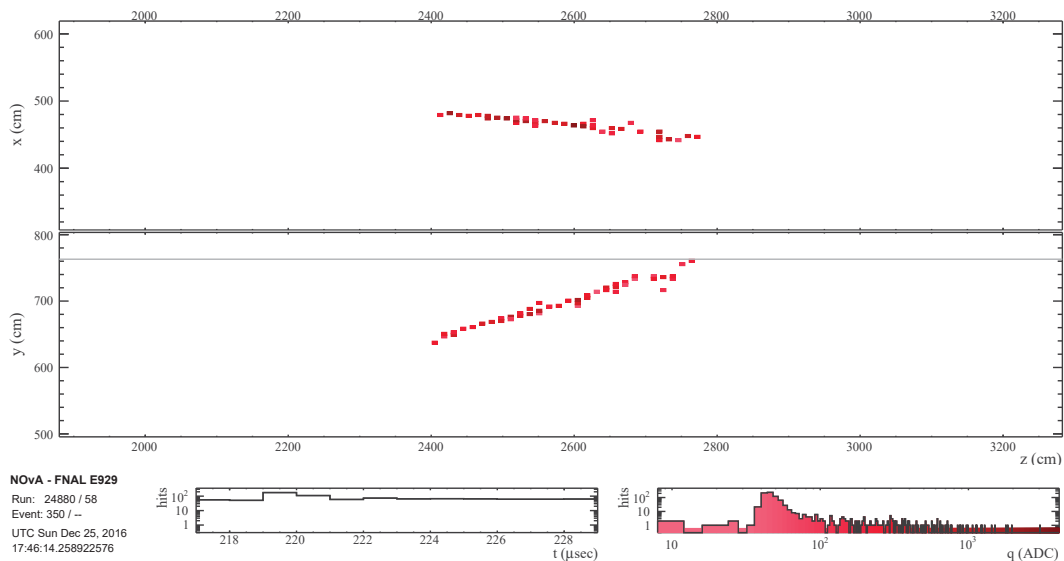


FIGURE B.9: Peripheral sample event: run = 24880, subrun = 58, event number = 350, slice = 29, hadronic energy = 0.004 (GeV), leptonic energy = 1.68 (GeV) and reconstructed neutrino energy = 1.65 (GeV).

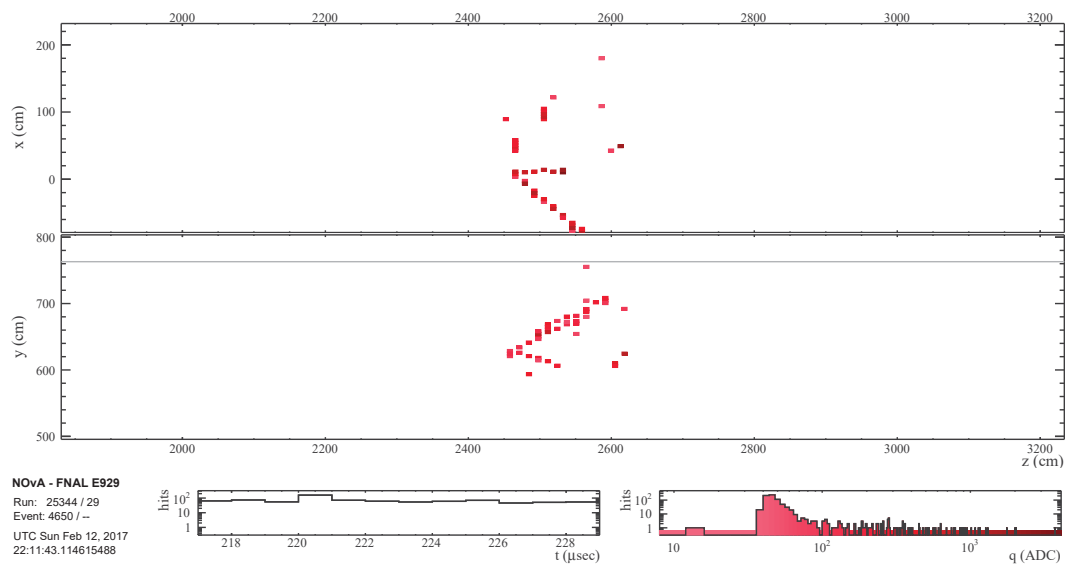


FIGURE B.10: Peripheral sample event: run = 25344, subrun = 29, event number = 4650, slice = 24, hadronic energy = 0.82 (GeV), leptonic energy = 1.16 (GeV) and reconstructed neutrino energy = 2.12 (GeV).

Appendix C

ν_μ Selected FD Data Events

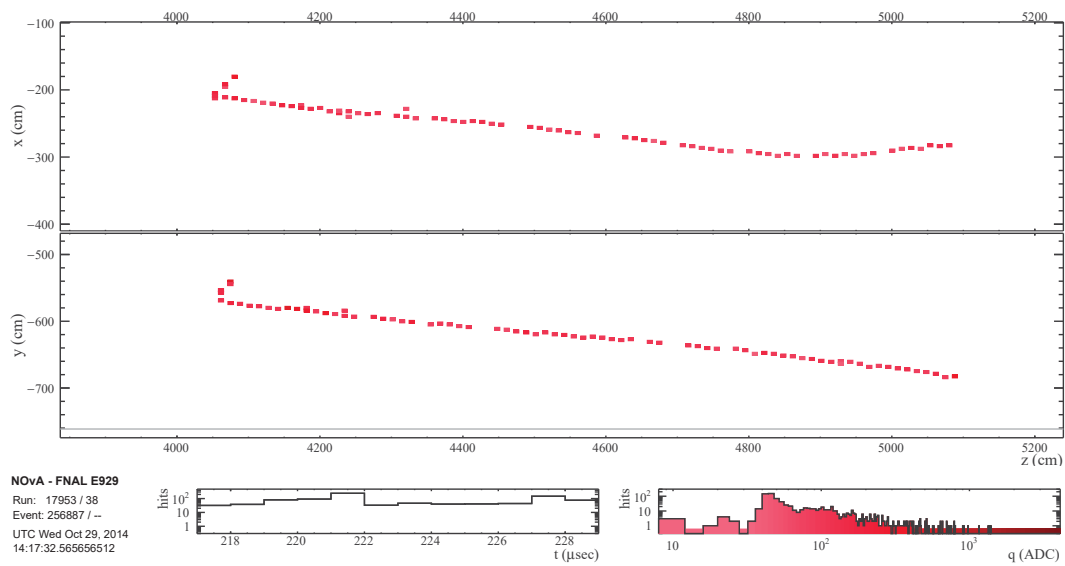


FIGURE C.1: Run = 17953, subrun = 38, event number = 256887, slice = 29, hadronic energy = 0.54 (GeV), leptonic energy = 2.72 (GeV) and reconstructed neutrino energy = 2.81 (GeV).

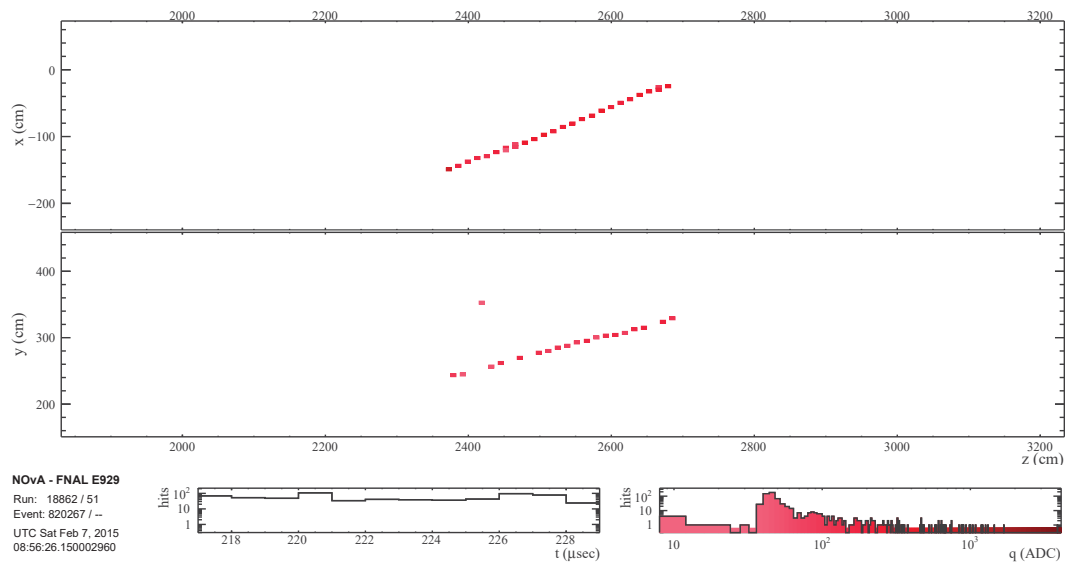


FIGURE C.2: Run = 18862, subrun = 51, event number = 820267, slice = 37, hadronic energy = 0.09 (GeV), leptonic energy = 0.83 (GeV) and reconstructed neutrino energy = 0.92 (GeV).

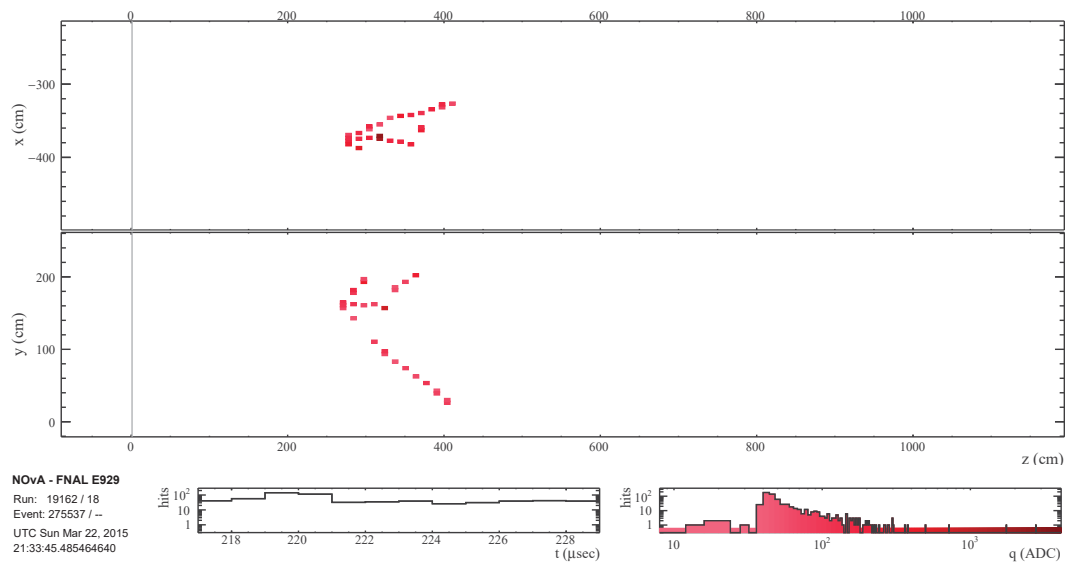


FIGURE C.3: Run = 19162, subrun = 18, event number = 275537, slice = 34, hadronic energy = 1.35 (GeV), leptonic energy = 0.54 (GeV) and reconstructed neutrino energy = 1.89 (GeV).

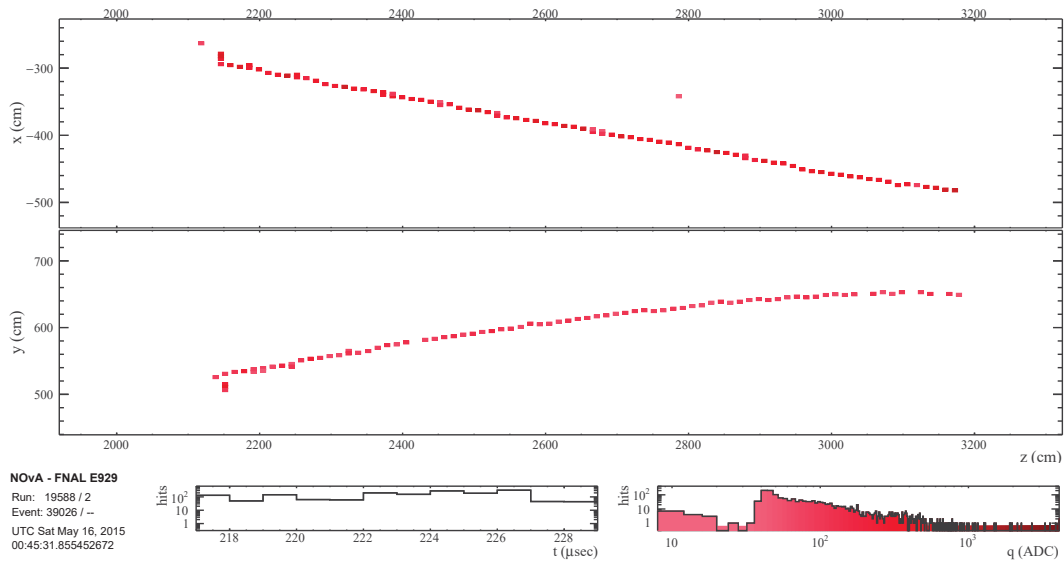


FIGURE C.4: Run = 19588, subrun = 02, event number = 39026 , slice = 33, hadronic energy = 0.51 (GeV), leptonic energy = 2.31 (GeV) and reconstructed neutrino energy = 2.82 (GeV).

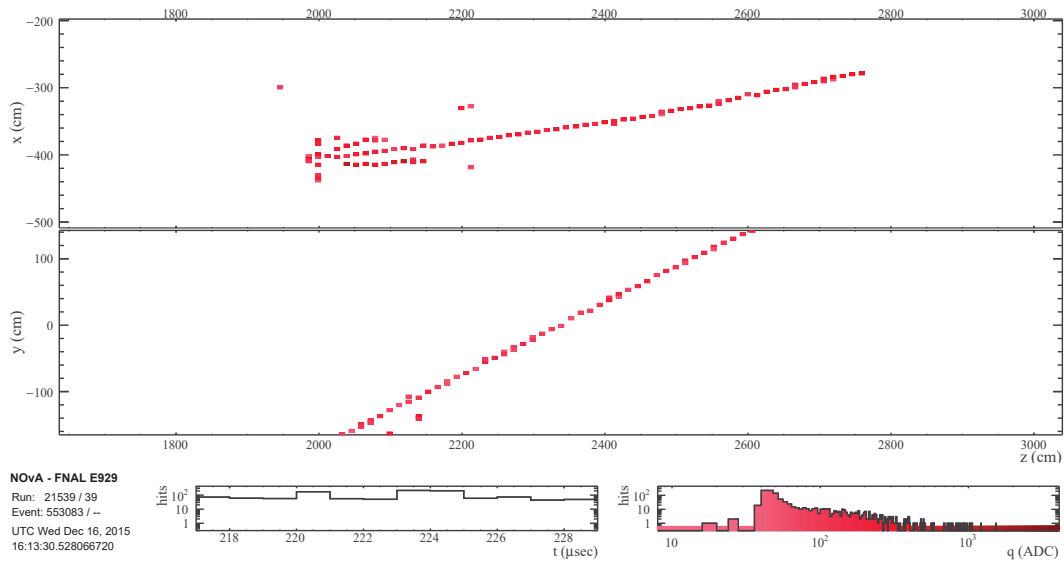


FIGURE C.5: Run = 21539, subrun = 39, event number = 553083, slice = 26, hadronic energy = 2.01 (GeV), leptonic energy = 1.96 (GeV) and reconstructed neutrino energy = 3.97 (GeV).

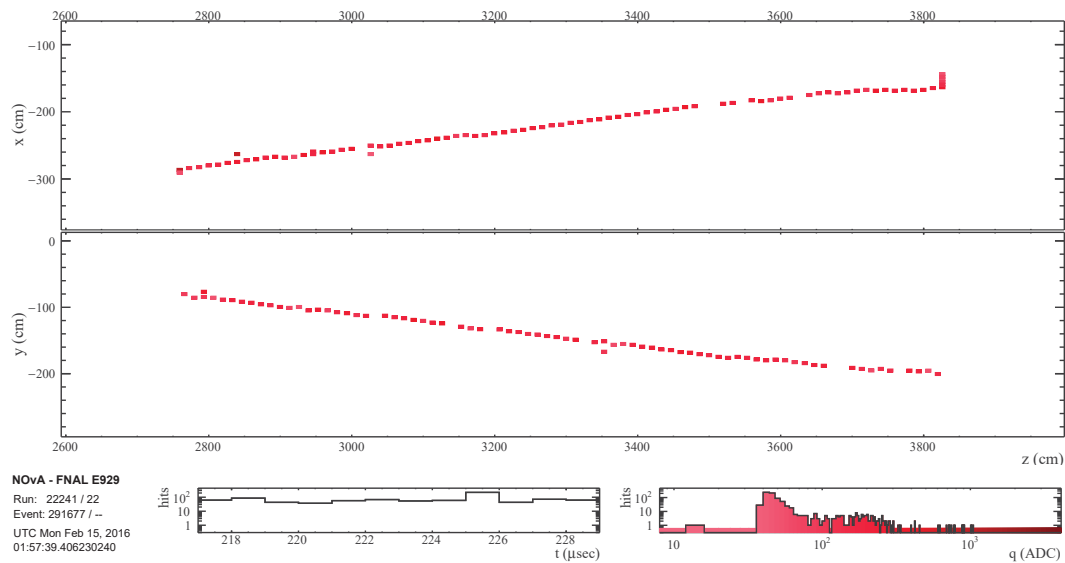


FIGURE C.6: Run = 22241, subrun = 22, event number = 291677, slice = 39, hadronic energy = 0.32 (GeV), leptonic energy = 2.34 (GeV) and reconstructed neutrino energy = 2.65 (GeV).

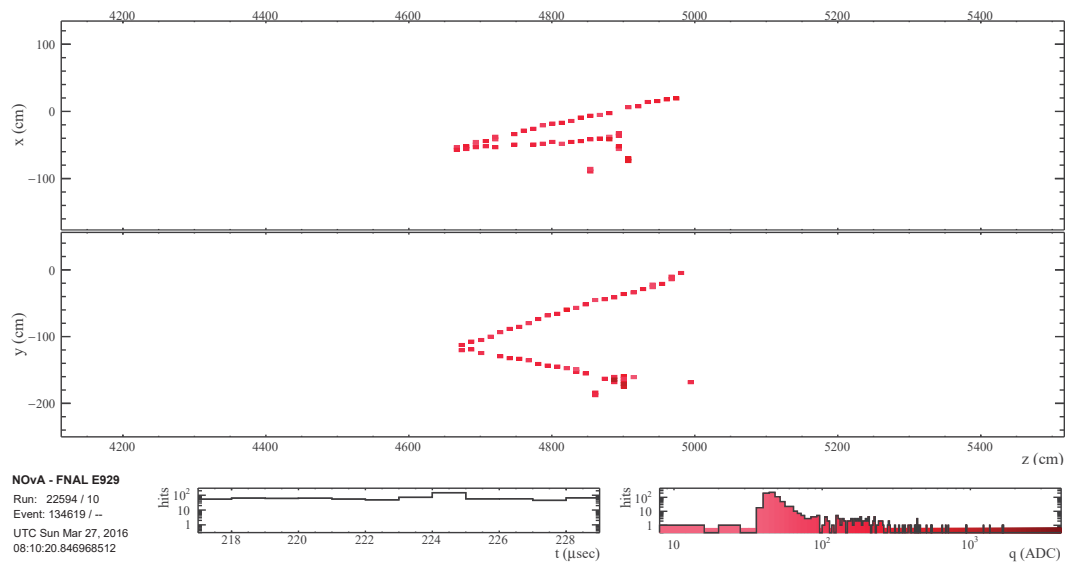


FIGURE C.7: Run = 22594, subrun = 10, event number = 134619, slice = 35, hadronic energy = 1.24 (GeV), leptonic energy = 0.82 (GeV) and reconstructed neutrino energy = 2.06 (GeV).

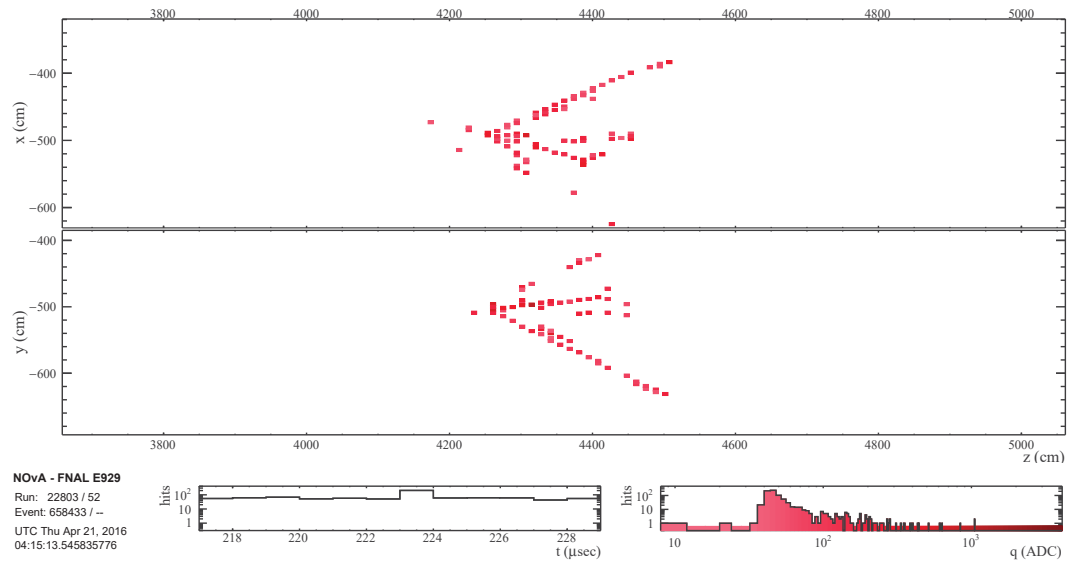


FIGURE C.8: Run = 22803, subrun = 52, event number = 658433, slice = 39, hadronic energy = 2.64 (GeV), leptonic energy = 0.85 (GeV) and reconstructed neutrino energy = 3.49 (GeV).

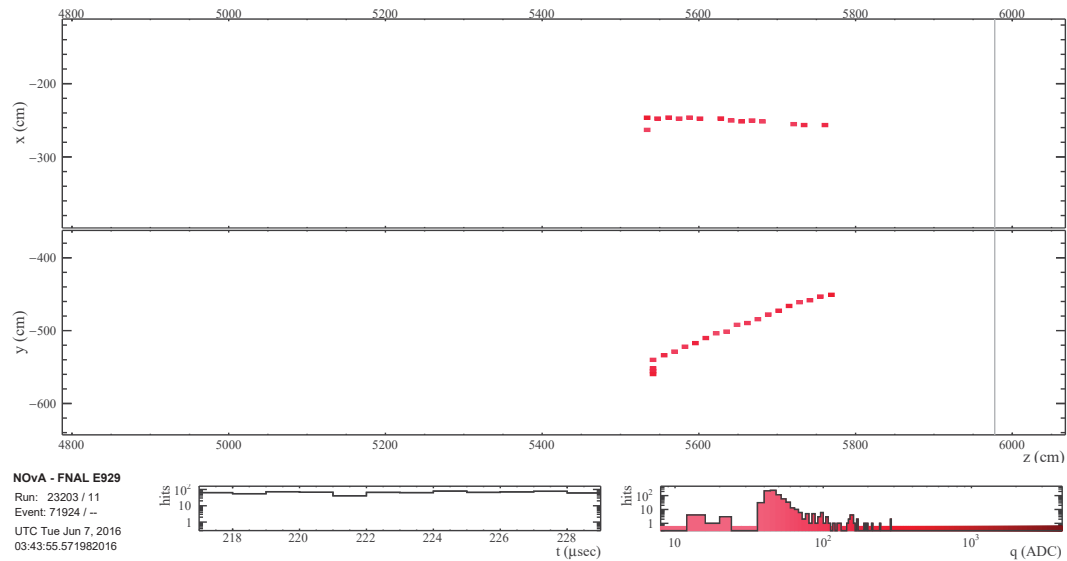


FIGURE C.9: Run = 23203, subrun = 11, event number = 71924, slice = 28, hadronic energy = 0.18 (GeV), leptonic energy = 0.64 (GeV) and reconstructed neutrino energy = 0.82 (GeV).

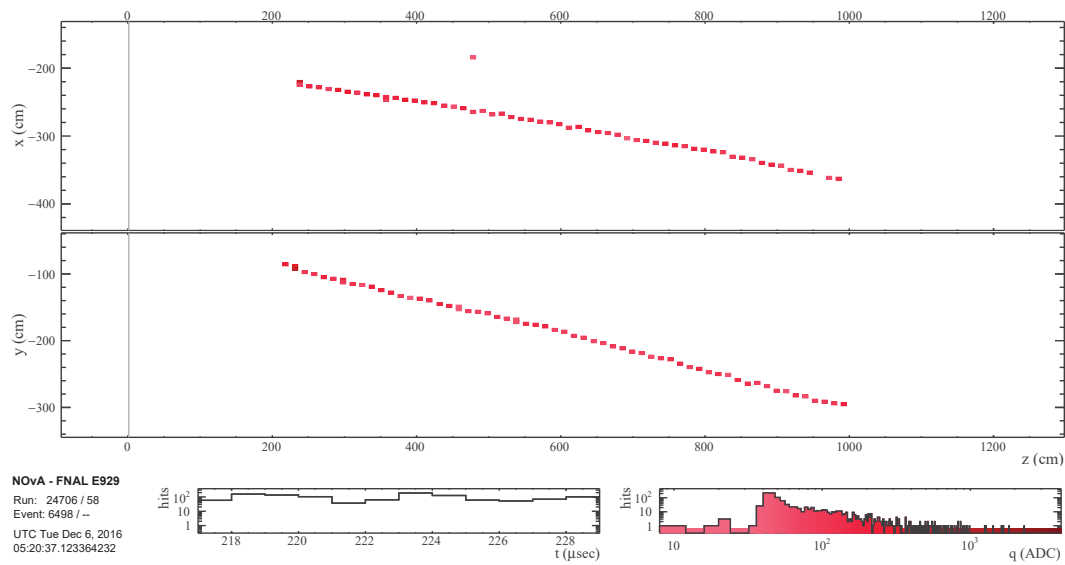


FIGURE C.10: Run = 24706, subrun = 58, event number = 6498 , slice = 30, hadronic energy = 0.44 (GeV), leptonic energy = 1.78 (GeV) and reconstructed neutrino energy = 2.22 (GeV).

Bibliography

- [1] Chee Sheng Fong, Enrico Nardi, and Antonio Riotto. “Leptogenesis in the Universe”. *Advances in High Energy Physics* 2012 (2012), 1–59. DOI: 10.1155/2012/158303.
- [2] K. Abe et al. “Atmospheric neutrino oscillation analysis with external constraints in Super-Kamiokande I-IV”. *Physical Review D* 97.7 (Apr. 2018). DOI: 10.1103/physrevd.97.072001.
- [3] K. Abe et al. “Measurement of neutrino and antineutrino oscillations by the T2K experiment including a new additional sample of ν_e interactions at the far detector”. *Physical Review D* 96.9 (Nov. 2017). DOI: 10.1103/physrevd.96.092006.
- [4] M. A. Acero et al. “New constraints on oscillation parameters from ν_e appearance and $\nu\mu$ disappearance in the NOvA experiment”. *Physical Review D* 98.3 (Aug. 2018). DOI: 10.1103/physrevd.98.032012.
- [5] Laurie M. Brown. “The idea of the neutrino”. *Physics Today* 31.9 (Sept. 1978), 23–28. DOI: 10.1063/1.2995181.
- [6] J. Chadwick. “Possible Existence of a Neutron”. *Nature* 129.3252 (Feb. 1932), 312–312. DOI: 10.1038/129312a0.
- [7] E. Fermi. “Versuch einer Theorie der β -Strahlen. I”. *Zeitschrift für Physik* 88.3-4 (Mar. 1934), 161–177. DOI: 10.1007/bf01351864.
- [8] Fred L. Wilson. “Fermi's Theory of Beta Decay”. *American Journal of Physics* 36.12 (Dec. 1968), 1150–1160. DOI: 10.1119/1.1974382.
- [9] C. L. Cowan et al. “Detection of the Free Neutrino: a Confirmation”. *Science* 124.3212 (July 1956), 103–104. DOI: 10.1126/science.124.3212.103.
- [10] Sheldon L. Glashow. “Partial-symmetries of weak interactions”. *Nuclear Physics* 22.4 (Feb. 1961), 579–588. DOI: 10.1016/0029-5582(61)90469-2.

- [11] Abdus Salam. “Weak and Electromagnetic Interactions”. *Conf. Proc. C680519* (1968), 367–377.
- [12] Steven Weinberg. “A Model of Leptons”. *Phys. Rev. Lett.* 19.21 (Nov. 1967), 1264–1266. DOI: 10.1103/physrevlett.19.1264.
- [13] G. Danby et al. “Observation of High-Energy Neutrino Reactions and the Existence of Two Kinds of Neutrinos”. *Phys. Rev. Lett.* 9.1 (July 1962), 36–44. DOI: 10.1103/physrevlett.9.36.
- [14] B. Pontecorvo. “Electron and Muon Neutrinos”. *Sov. Phys. JETP* 10 (1960). [*Zh. Eksp. Teor. Fiz.*37,1751(1959)], 1236–1240.
- [15] M. Schwartz. “Feasibility of Using High-Energy Neutrinos to Study the Weak Interactions”. *Phys. Rev. Lett.* 4.6 (1960), 306–307. DOI: 10.1103/physrevlett.4.306.
- [16] K. Kodama et al. “Observation of tau neutrino interactions”. *Physics Letters B* 504.3 (Apr. 2001), 218–224. DOI: 10.1016/s0370-2693(01)00307-0.
- [17] John N. Bahcall, M. H. Pinsonneault, and Sarbani Basu. “Solar Models: Current Epoch and Time Dependences, Neutrinos, and Helioseismological Properties”. *The Astrophysical Journal* 555.2 (2001), 990–1012. DOI: 10.1086/321493.
- [18] Y. Fukuda et al. “Evidence for Oscillation of Atmospheric Neutrinos”. *Phys. Rev. Lett.* 81.8 (1998), 1562–1567. DOI: 10.1103/physrevlett.81.1562.
- [19] K. Abe et al. “Solar neutrino measurements in Super-Kamiokande-IV”. *Physical Review D* 94.5 (Sept. 2016). DOI: 10.1103/physrevd.94.052010.
- [20] Q. R. Ahmad et al. “Measurement of the Rate of $\nu_e + d \rightarrow p + p + e^-$ Interactions Produced by ^8B Solar Neutrinos at the Sudbury Neutrino Observatory”. *Phys. Rev. Lett.* 87.7 (2001). DOI: 10.1103/physrevlett.87.071301.
- [21] Carlo Giunti. *Fundamentals of Neutrino Physics and Astrophysics*. Chapter 7. OUP Oxford, 2007. 728 pp. ISBN: 0198508719.
- [22] S. M. Bilenky. “On the phenomenology of neutrino oscillations in vacuum” (2012). arXiv: 1208.2497 [hep-ph].
- [23] Hiroshi Nunokawa, Stephen J. Parke, and Jose W. F. Valle. “CP Violation and Neutrino Oscillations”. *Prog. Part. Nucl. Phys.* 60 (2008), 338–402. DOI: 10.1016/j.ppnp.2007.10.001. arXiv: 0710.0554 [hep-ph].

- [24] Alex Himmel. “New neutrino oscillation results from NOvA”. Slide 8. Jan. 2018. URL: <https://indico.cern.ch/event/696410/>.
- [25] L. Hsu and J. P. Hsu. “The physical basis of natural units and truly fundamental constants”. *The European Physical Journal Plus* 127.1 (Jan. 2012). DOI: 10.1140/epjp/i2012-12011-5.
- [26] L. Wolfenstein. “Neutrino oscillations in matter”. *Physical Review D* 17.9 (May 1978), 2369–2374. DOI: 10.1103/physrevd.17.2369.
- [27] Ivan Esteban et al. “Global analysis of three-flavour neutrino oscillations: synergies and tensions in the determination of θ_{23} , δ_{CP} , and the mass ordering”. *Journal of High Energy Physics* 2019.1 (2019). DOI: 10.1007/jhep01(2019)106.
- [28] Y. Abe et al. “Improved measurements of the neutrino mixing angle θ_{13} with the Double Chooz detector”. *Journal of High Energy Physics* 2014.10 (Oct. 2014). DOI: 10.1007/jhep10(2014)086.
- [29] F. P. An et al. “Measurement of electron antineutrino oscillation based on 1230 days of operation of the Daya Bay experiment”. *Physical Review D* 95.7 (Apr. 2017). DOI: 10.1103/physrevd.95.072006.
- [30] Seon-Hee Seo. “New Results from RENO using 1500 Days of Data”. 15th International Conference on Topics in Astroparticle and Underground Physics (TAUP 2017) Sudbury, Ontario, Canada, July 24-28, 2017. 2017. arXiv: 1710.08204 [hep-ex].
- [31] John N Bahcall and Carlos Peña-Garay. “Solar models and solar neutrino oscillations”. *New Journal of Physics* 6 (June 2004), 63–63. DOI: 10.1088/1367-2630/6/1/063.
- [32] J. N. Bahcall et al. “Solar Neutrino Flux.” *The Astrophysical Journal* 137 (Jan. 1963), 344. DOI: 10.1086/147513.
- [33] M. Tanabashi et al. “Review of Particle Physics”. *Physical Review D* 98.3 (Aug. 2018). ISSN: 1674-1137. DOI: 10.1103/physrevd.98.030001.
- [34] Guido Altarelli and Ferruccio Feruglio. “Discrete flavor symmetries and models of neutrino mixing”. *Reviews of Modern Physics* 82.3 (2010), 2701–2729. DOI: 10.1103/revmodphys.82.2701.
- [35] D.S. Ayres et al. *The NOvA Technical Design Report*. 2007. DOI: 10.2172/935497.

- [36] Fermilab's Creative Services for Fermilab photography. URL: <http://vms.fnal.gov/asset/photogallery>.
- [37] Main Injector Neutrino Oscillation Search. URL: <https://www-numi.fnal.gov>.
- [38] Fermilab's Accelerator Complex. URL: <http://fnal.gov/pub/science/particle-accelerators/accelerator-complex.html>.
- [39] Beam Structure and Delivery Path. URL: <https://ftbf.fnal.gov/beam-delivery-path/>.
- [40] Kanika Sachdev. "Muon Neutrino to Electron Neutrino Oscillation in NOvA". PhD thesis. University of Minnesota, Aug. 2015. URL: <https://lss.fnal.gov/archive/thesis/2000/fermilab-thesis-2015-20.pdf>.
- [41] Evan David Niner. "Observation of Electron Neutrino Appearance in the NuMI Beam with the NOvA Experiment". PhD thesis. Indiana U., 2015. DOI: 10.2172/1221353. URL: <http://lss.fnal.gov/archive/thesis/2000/fermilab-thesis-2015-16.pdf>.
- [42] Shekhar Shukla, John Marriner, and James Griffin. "Slip Stacking in the Fermilab Main Injector" (Mar. 2019). URL: http://www-bd.fnal.gov/lug/tev33/tev33_docs/slip_stacking.pdf.
- [43] NuMI Off-axis ν_e Appearance Experiment. URL: <https://novaexperiment.fnal.gov>.
- [44] Main Injector Experiment for ν -A. URL: <http://minerva.fnal.gov>.
- [45] Micro Booster Neutrino Experiment. URL: <http://microboone.fnal.gov>.
- [46] Muon g-2. URL: <http://muon-g-2.fnal.gov>.
- [47] Muon-to-Electron-Conversion Experiment. URL: <https://mu2e.fnal.gov>.
- [48] Pion interaction length in graphite is 117.8 g cm^{-2} or 53.30 cm. URL: <http://pdg.lbl.gov/2014/AtomicNuclearProperties/>.
- [49] Carlo Giunti and Chung W. Kim. Fundamentals of Neutrino Physics and Astrophysics. OUP Oxford, 2007. ISBN: 978-0-19-850871-7. URL: <http://inspirehep.net/record/747694?ln=en>.
- [50] S. Mufson et al. "Liquid scintillator production for the NOvA experiment". Nuclear Instruments and Methods in Physics Research Section A: Accelerators, Spectrometers, Detectors and Associated Equipment 799 (Nov. 2015), 1–9. DOI: 10.1016/j.nima.2015.07.026.

- [51] J. J. Grudzinski et al. “The Development of PVC Extrusions for a 14,000 Ton Self-Supporting Structure for the Detection of Neutrinos.” (2013). URL: <http://inspirehep.net/record/1280657>.
- [52] Susan M. Lein. “Muon Neutrino Contained Disappearance in NOvA”. PhD thesis. Minnesota U., Sept. 2015. DOI: 10.2172/1221368. URL: <http://lss.fnal.gov/archive/thesis/2000/fermilab-thesis-2015-21.pdf>.
- [53] E Niner et al. “Synchronization of the 14 kTon NOvA neutrino detector with the Fermilab NuMI beam”. *Journal of Physics: Conference Series* 513.1 (2014), 012028. DOI: 10.1088/1742-6596/513/1/012028.
- [54] Christopher J Backhouse. “ND multipoint beam peak”. Nova internal note docdb 11535.
- [55] Luke Vinton. “Measurement of muon neutrino disappearance with a NOvA experiment”. PhD thesis. University of Sussex, Mar. 2018. URL: <http://sro.sussex.ac.uk/id/eprint/74542>.
- [56] Chris Hagmann et al. “Cosmic-ray Shower Library (CRY)”. UCRL-TM-229453 (Mar. 2012). UCRL-TM-229453. URL: https://nuclear.llnl.gov/simulation/doc_cry_v1.7/cry.pdf.
- [57] Brian J. Rebel. “Neutrino - Induced Muons in the MINOS Far Detector”. PhD thesis. Indiana University, Aug. 2004. DOI: 10.2172/15011496. URL: <https://www.osti.gov/biblio/15011496>.
- [58] S. Agostinelli et al. “Geant4—a simulation toolkit”. *Nuclear Instruments and Methods in Physics Research Section A: Accelerators, Spectrometers, Detectors and Associated Equipment* 506.3 (July 2003), 250–303. DOI: 10.1016/S0168-9002(03)01368-8.
- [59] C. Andreopoulos et al. “The GENIE neutrino Monte Carlo generator”. *Nuclear Instruments and Methods in Physics Research Section A: Accelerators, Spectrometers, Detectors and Associated Equipment* 614.1 (Feb. 2010), 87–104. DOI: 10.1016/j.nima.2009.12.009.
- [60] Costas Andreopoulos et al. “The GENIE Neutrino Monte Carlo Generator: Physics and User Manual” (2015). arXiv: 1510.05494 [hep-ph].
- [61] K.A. Olive. “Review of Particle Physics”. *Chinese Physics C* 40.10 (2016). Figure 33.2 in Chapter 33, 100001. DOI: 10.1088/1674-1137/40/10/100001.

- [62] Michael David Baird. “An Analysis of Muon Neutrino Disappearance from the NuMI Beam Using an Optimal Track Fitter”. PhD thesis. Sept. 2015. DOI: 10.2172/1223262. URL: <https://www.osti.gov/biblio/1223262>.
- [63] A. Aurisano et al. “A convolutional neural network neutrino event classifier”. *Journal of Instrumentation* 11.09 (2016), P09001–P09001. DOI: 10.1088/1748-0221/11/09/p09001.
- [64] D. F. Shanno. “Conditioning of quasi-Newton methods for function minimization”. *Mathematics of Computation* 24.111 (1970), 647–647. DOI: 10.1090/s0025-5718-1970-0274029-x.
- [65] Luke Vinton. “Measurement of Muon Neutrino Disappearance with the NOvA Experiment”. PhD thesis. 2018. DOI: 10.2172/1423216.
- [66] Fernanda Psihas. “Measurement of Long Baseline Neutrino Oscillations and Improvements from Deep Learning”. PhD thesis. 2018. DOI: 10.2172/1437288.
- [67] F. James. “MINUIT Function Minimization and Error Analysis: Reference Manual Version 94.1” (1994). URL: <http://inspirehep.net/record/1258343?ln=en>.
- [68] Teppei Katori. “Meson exchange current (MEC) models in neutrino interaction generators”. AIP Publishing LLC, 2015. DOI: 10.1063/1.4919465.
- [69] K.A. Olive. “Review of Particle Physics”. *Chinese Physics C* 40.10 (2016), 100001. DOI: 10.1088/1674-1137/40/10/100001.
- [70] M. A. Acero et al. “First measurement of neutrino oscillation parameters using neutrinos and antineutrinos by NOvA” (2019). arXiv: 1906.04907 [hep-ex].